Computational design and evaluation of novel peptide inhibitors against amyloid aggregation in type 2 diabetes mellitus and Alzheimer's disease

Submitted in the partial fulfilment of the requirements for the degree of

Doctor of Philosophy

in Chemistry

THAPAR INSTITUTE
OF ENGINEERING & TECHNOLOGY
(Deemed to be University)

by

Apneet Kaur

(Reg. No. 901709010)

Under the supervision of

Dr. Bhupesh Goyal Bhupesh Goyal

Department of Chemistry and Biochemistry

Thapar Institute of Engineering and Technology

Patiala, Punjab (India)-147004

February, 2024

Certificate

Certified that the thesis entitled "Computational design and evaluation of novel peptide inhibitors against amyloid aggregation in type 2 diabetes mellitus and Alzheimer's disease" submitted by Ms. Apneet Kaur, Reg. no. 901709010 in the partial fulfilment of the requirements for the award of the degree of Doctor of Philosophy in the Department of Chemistry and Biochemistry, Thapar Institute of Engineering and Technology, Patiala, Punjab is a record of candidate's own independent and original research work carried out by herself under my supervision and guidance. The material embodied in this thesis has not been submitted in part or full to any other University or institute for the award of any degree.

Bhupesh Goyal

Dr. Bhupesh Goyal
(Associate Professor)

Supervisor

Department of Chemistry and Biochemistry

Thapar Institute of Engineering and Technology

Dr. Manmohan Chhibber
(Professor)

Head of Department

Department of Chemistry and Biochemistry

Thapar Institute of Engineering and Technology

CANDIDATE'S DECLARATION

I, hereby declare that the work presented in the thesis entitled "Computational design and evaluation of novel peptide inhibitors against amyloid aggregation in type 2 diabetes mellitus and Alzheimer's disease" in the partial fulfilment of the requirements for the award of the degree of Doctor of Philosophy at Department of Chemistry and Biochemistry, Thapar Institute of Engineering and Technology, Patiala, Punjab is an authentic record of my own work during the period from January 2018 to February 2024, under the supervision of Dr. Bhupesh Goyal, Department of Chemistry and Biochemistry, Thapar Institute of Engineering and Technology. This report has not been submitted for the award of any degree or certificate in this or any other university.

Place: Patiala, Punjab — Apneet Kaur

Date: February, 2024 — (Reg no. 901709010)

Acknowledgement

It is a genuine pleasure to express my gratitude to the individuals without whom this dream wouldn't have converted into a reality. I would like to express my gratitude to my supervisor **Dr. Bhupesh Goyal**, Associate Professor, Department of Chemistry and Biochemistry (DCBC), Thapar Institute of Engineering & Technology, Patiala (Punjab). I sincerely thank him for helping me develop leadership skills and independent thinking capabilities instead of assigning tasks to track my project work. I owe heartfelt thanks to Dr. Bhupesh Goyal for providing such a highly dynamic research environment that pushed me to think with creativity, solve problems and develop myself personally. Your words "eat, drink, and sleep research" motivated my research journey the most.

My sincere gratitude to visionary director of TIET, **Prof. Dr. Padmakumar Nair**, for providing necessary infrastructure and excellent research environment.

I am highly thankful to **Prof. Kamaldeep Paul**, **Prof. Manoj Baranwal**, **Dr. Debashish Mandal** assistant professor, DCBC and for their valuable suggestions and constant encouragement. I am highly obliged to them for their kind support in carrying out present research work.

I would like to thank **Dr. Nitin Kumar Singhal**, Scientist E, National Agri-Food Biotechnology Institute, Mohali, for providing infrastructure support for in vitro assays. I sincerely thank **Dr. Deepti Goyal** for sharing the crucial information and suggestions about characterization of the peptides.

I am grateful to **Dr. Nitesh Priyadarshi** for the cooperation in HPLC and TEM analysis.

I thank Thapar Institute of Engineering & Technology, Patiala (Punjab), Department of Chemistry and Biochemistry, for providing me with financial help under the Contractual Based Lecturer (CBL-S) position.

I thank **Dr. Rajesh Kondabala** Thapar Alumni, School of Chemistry and Biochemistry for their kind guidance, constructive suggestions.

I am indebted to my seniors, **Dr. Rajneet Saini** for the constant help, support, and encouragement. My special thanks to my entire scholar team, Ms. Arushi , Ms. Diksha, Ms. Anisha Manchanda, Ms. Tanishka Mehta, Mr. Ishwar Das Thakur and Ms. Gurmeet Kaur, for

providing such a positive atmosphere in the lab. I extend my heartfelt thanks to all of them for inspiring discussion sessions and treasured moments.

I would also like to acknowledge the care and cooperation of my friends Dr. Rajesh Kondabala, Sheetal Vashisht, Nisha Mallik for their inspiring support. I am incredibly thankful to my landlords, who made me feel at home.

I want to thank my mother and father for seeing that light in me that I never recognized. Their selflessness provided me with the stability and comfort needed to focus on my research. I am truly blessed to have such incredible parents, and I dedicate this achievement to them. Thank you for being my pillars of strength and for making this challenging journey more manageable with your love and support. I sincerely thank my brother and my sister for their endless encouragement and motivation.

A special thanks to my husband Capt. Surinder Singh for being my anchor and encouraging me to achieve better. During times of stress and uncertainty, he stood by me, providing a constant source of motivation and reassurance. His unwavering support allowed me to fully dedicate myself to my research. I am truly fortunate to have a life partner who not only understands the demands of academic life but also actively contributes to my success.

"Above all, my deepest appreciation to my beloved daughter Sharleen Kaur, who, during this Ph.D. pursuit, stayed with her grandparents. Her resilience and support created a stable and nurturing environment for me to focus on my academic endeavors. Despite the physical distance, her presence in my heart was a constant source of inspiration. Her love has been my guiding light, and this achievement is as much hers as it is mine."

I humbly acknowledge the divine guidance and express my profound gratitude to God. The blessings and grace bestowed upon me have been a source of inspiration and comfort during moments of challenge and triumph. I am profoundly grateful for the faith that sustained me and the unwavering belief that, indeed, with faith, all things are possible.

Date: February, 2024

Place: Patiala Apneet Kaur

Abstract

The self-aggregation of normally dissolvable proteins into soluble oligomers and insoluble amyloid filaments characterizes amyloidosis. These aggregates known as amyloid are made up of misfolded proteins with β–sheet structure, have an impact on normal tissue function, and are associated with prevalent amyloidosis diseases such as Alzheimer's disease (AD), Parkinson's disease, and type 2 diabetes (T2D). The human islet amyloid polypeptide (hIAPP, commonly known as amylin) linked to T2D and amyloid−β (Aβ) peptide linked to AD are classic examples of intrinsically disordered proteins (IDPs) that self-assemble to form amyloid fibrils.

The hIAPP (37 amino acid residues hormone) is one of the main secretory components of pancreatic islet β−cells. The self-aggregation of hIAPP into cytotoxic aggregates results in islet β–cells apoptosis and finally leads to T2D. Unfortunately, the underlying molecular mechanism by which hIAPP undergoes structural transition and aggregates into transient oligomers and finally to insoluble amyloid plaques causing T2D symptoms remains unknown. AD is a multifactorial neurodegenerative disease mainly characterized by extracellular accumulation of Aβ peptide. The self-assembly of Aβ peptide generated by the proteolysis of amyloid precursor protein (APP) in the amyloidogenic pathway into toxic oligomers and fibrils is the major event in AD pathogenesis A complete understanding of the underlying process of conformational conversion of functional proteins to toxic oligomers and amyloid fibrils may support the development of medical applications and innovative therapies. Thus, inhibiting the formation of hIAPP and Aβ aggregates has therapeutic benefits for the treatment of T2D, and AD, respectively.

Among various inhibitors, short peptides derived from the amyloidogenic regions of hIAPP have been employed as hIAPP aggregation inhibitors due to their low immunogenicity, biocompatibility, and high chemical diversity. Recently, hexapeptide ANFLVH was identified as a potent inhibitor of hIAPP aggregation among various synthesized peptides derived from the hIAPP sequence. ANFLVH inhibited hIAPP aggregation *in vitro* and in human islet cultures, which significantly enhanced the islet cell viability. However, the molecular mechanism of inhibition of hIAPP aggregation in the presence of ANFLVH remains unclear. Molecular dynamics (MD) simulation analysis highlighted that ANFLVH prevented the conformational transition of hIAPP by stabilizing the native helical conformation. The binding free energy analysis by the molecular mechanics Poisson-Boltzmann surface area (MM-PBSA) method highlighted favourable binding of ANFLVH with hIAPP and depicted a significant

contribution of the van der Waals interaction term in the stability of the hIAPP-ANFLVH complex. The per-residue binding free energy highlighted that ANFLVH strongly interacted with His18 of hIAPP, which has been reported as a key residue in mediating the hIAPP self-assembly process.

The hIAPP fragment $HSSNN_{18\text{-}22}$ was identified as an amyloidogenic sequence and displayed higher antiproliferative activity to RIN-5F cells. Notably, various inhibitors have been designed by chemical modifications of the highly amyloidogenic sequence (NFGAIL) of hIAPP and evaluated for their efficacy against hIAPP aggregation. As HSSNN has been identified as a highly amyloidogenic sequence, thus it can be employed as a lead domain for designing new hIAPP aggregation inhibitors. Hence, a library of pentapeptides based on fragment $HSSNN_{18\text{-}22}$ was designed and assessed for their efficacy in blocking hIAPP aggregation using an integrated computational screening approach. The binding free energy calculations by MM-PBSA method identified HSSQN and HSSNQ that bind to hIAPP monomer with a binding affinity of –21.25 ± 4.90 and –19.73 ± 3.10 kcal/mol, respectively, which is notably higher as compared to HSSNN (–11.90 ± 4.12 kcal/mol). The sampling of the non aggregation-prone helical conformation was notably increased from 23.5 ± 3.0 in hIAPP monomer to 38.1 ± 3.6, and 33.8 ± 3.0% on the incorporation of HSSQN, and HSSNQ, respectively, which indicate reduced aggregation propensity of hIAPP monomer. The computationally designed peptides, HSSQN and HSSNQ, emerged as new, simple, and efficient inhibitors of hIAPP aggregation.

Previous studies reported pentapeptide RIIGL as an effective inhibitor of Aβ aggregation and neurotoxicity induced by Aβ aggregates. A library of 912 pentapeptides based on RIIGL has been designed and assessed for their efficacy in inhibiting $A\beta_{42}$ aggregation using computational techniques. The MD simulations highlighted that the incorporation of proline and arginine in pentapeptides contributed to their strong binding with $A\beta_{42}$ monomer. Furthermore, RVVPI and RIAPA prevented conformational conversion of $A\beta_{42}$ monomer to aggregation-prone structures, which, in turn, resulted in a lower aggregation tendency of $A\beta_{42}$ monomer. Additionally, the disruptive ability of RIIGL, RVVPI, and RIAPA on $A\beta_{42}$ protofibril was examined using MD simulations and *in vitro* studies. Notably, RVVPI displays a more pronounced destabilization effect than other peptides due to higher conformational fluctuations, and disruption of K28-A42 salt bridges in $A\beta_{42}$ protofibril. Among the synthesized peptides, RVVPI exhibited the highest inhibitory activity (Inhibition= 66.2%, IC_{50}= 5.57 ± 0.83 μM) against $A\beta_{42}$ aggregation consistent with the computational results. Remarkably, RVVPI

displayed ~4.5 fold lower IC_{50} value as compared to the RIIGL. The thioflavin T (ThT) and transmission electron microscopy (TEM) studies highlighted the enhanced efficiency of RVVPI (62.4%) in the disassembly of pre-formed $A\beta_{42}$ fibrils than RIIGL and RIAPA. The combined *in silico* and *in vitro* studies in this work identified a new peptide, RVVPI, as an efficient modulator of $A\beta_{42}$ aggregation and disassembly of pre-formed $A\beta_{42}$ aggregates.

The work presented in the thesis illuminates the inhibitory mechanism of the peptide inhibitors against hIAPP and $A\beta_{42}$ aggregation as well as sheds light on the $A\beta_{42}$ protofibril destabilization on the incorporation of peptides. The computational design methodology of the natural peptides against hIAPP and $A\beta_{42}$ aggregation provides an opportunity for the design of more potent inhibitors against T2D and AD. The results of the present studies will help in the structure-based design of more effective and potent novel inhibitors against hIAPP and Aβ aggregation, which will prevent or slow down T2D and AD pathogenesis. In addition, the pentapeptides (RVVPI and RIAPA) identified as potential inhibitors against $A\beta_{42}$ aggregation in this work can be further conjugated with various metal chelating peptides to yield more efficacious and clinically relevant multifunctional modulators possessing abilities to chelate the copper ion and reduce Cu^{2+}-mediated formation of reactive oxygen species. Furthermore, peptides could be used as a template and their affinity, stability, and bioavailability could be improved by the addition of linker molecules/conjugates or could be altered into peptidomimetics with improved stability and cellular delivery.

Table of Contents

List of figures

Figure 4.8: Residue-wise helix and coil content in hIAPP alone and hIAPP-pentapeptide complexes.

Figure 4.9: Hydrogen bonds between hIAPP and pentapeptides during simulation (panel a). Residue-wise hydrogen bonds of the hIAPP with the pentapeptides (panel b).

Figure 4.10: Side chain–side chain contact probability maps for hIAPP (panel a), hIAPP-HSSNN (panel b), hIAPP-HSSQN (panel c), and hIAPP-HSSNQ (panel d).

Figure 4.11: SASA of the hIAPP monomer in different systems (panel a). Residue-wise SASA in hIAPP alone and hIAPP-pentapeptide complexes (panel b).

Figure 4.12: Percentage population and the central member of the highest populated cluster in hIAPP monomer, hIAPP-HSSNN, hIAPP-HSSQN, and hIAPP-HSSNQ complexes.

Figure 4.13: Disorder probability plot and probability of disorder for hIAPP residues is shown in panels a, and, b, respectively.

Figure 4.14: The effect of pentapeptides on the conformational flexibility of hIAPP monomer was analyzed using 2D projection of motion over the first two eigenvectors.

Figure 4.15: The FEL along PC1 and PC2 of hIAPP monomer, hIAPP–HSSNN, hIAPP–HSSQN, and hIAPP–HSSNQ is shown in panels a, b, c, and d, respectively. The purple regions signify the minimum energy basins, whereas wine red represents higher energy basins. The metastable conformational states are represented by cyan and green regions. The conformations extracted from the minimum energy basins are displayed in cartoons.

Figure 5.1: Workflow of computational screening protocol used in this work to identify potential inhibitors of $A\beta_{42}$ aggregation from the pentapeptide library based on reference peptide RIIGL.

Figure 5.2: Sequence of $A\beta_{42}$ peptide with the key regions shown in different colours (panel a). The $A\beta_{42}$ monomer (PDB ID: 1IYT) and the reference peptide RIIGL are shown in the cartoon (panel b) and stick representation (panel c), respectively.

Figure 5.3: Docked pose of reference peptide RIIGL with $A\beta_{42}$ monomer is shown. The hydrogen bonds between $A\beta_{42}$ monomer and RIIGL are shown in the magnified view.

Figure 5.4: Docked poses of the top ten pentapeptides and reference peptide RIIGL with $A\beta_{42}$ monomer (PDB ID: 1IYT). The $A\beta_{42}$ monomer is in cartoon and pentapeptides are in sticks. The binding energy values evaluated using AutoDock Vina are expressed in kcal/mol.

Figure 5.5: Contribution of each residue of $A\beta_{42}$ monomer towards binding with the lead pentapeptides. The $A\beta_{42}$ residues with the most favourable (< –1.0 kcal/mol) and unfavourable (>1.0 kcal/mol) contribution in the binding with pentapeptides are labeled.

Figure 5.6: Correlation between simulated and experimental NMR chemical shifts for Cα, Cβ atoms of $A\beta_{42}$ monomer (panels a, and b, respectively). The unit of chemical shift is ppm. Comparison of computational and experimental NMR *J*-coupling constants ($^3J_{HN\text{-}H\alpha}$) of $A\beta_{42}$ monomer (panel c).

List of tables

List of abbreviations

AD	Alzheimer's disease
ADT	AutoDock Tools
ALS	Amyotrophic Lateral Sclerosis
APP	Amyloid precursor protein
ATB	Automated Topology Builder
$A\beta_{42}$	Amyloid–β_{42}
BBB	Blood brain barrier
BSBHps	β-sheet breaker hybrid peptidomimetics
°C	Degree Celsius
$CDCl_3$	Deuterated chloroform/chloroform–d
CHC	Central hydrophobic core
CVD	Cardiovascular disease
DSSP	Dictionary of secondary structure of proteins
DLS	Dynamic light scattering
FEL	Free energy landscape
FDA	Food and Drug Administration
FPG	Fasting Plasma Glucose
G	Gram(s)
GROMACS	GROningen MAchine for Chemical Simulations
hIAPP	Human islet amyloid polypeptide
HD	Huntington's disease
HPLC	High–performance liquid chromatography
HRMS	High–resolution mass spectrum
Hz	Hertz
$^3J_{NH-H\alpha}$	*J*–coupling
K	Kelvin
LGA	Lamarckian Genetic Algorithm
LINCS	LINear Constraint Solver
MD	Molecular dynamics
mg	Milligram(s)
MHz	Mega hertz
min	Minute
mL	Milliliter
mM	Millimolar
mmol	Millimole
MM–PBSA	Molecular mechanics Poisson–Boltzmann surface area
MPGLT	Multifunctional micelles based on a polymer grafted peptide
MTT	(3-[4,5-dimethylthiazol-2-yl]-2,5 diphenyl tetrazolium bromide)
NaOH	Sodium hydroxide
NDs	Neurodegenerative diseases
nm	Nanometer
NMR	Nuclear magnetic resonance
NPT	Constant number of particles, pressure and temperature
Ns	Nanosecond
NVT	Constant number of particles, volume and temperature
OGTT	Oral Glucose Tolerance Test
PD	Parkinson's disease
PDB	Protein data bank

PME	Particle mesh Ewald
(PDI)	Protein Disulphide Isomrase
(PTMs)	Post-translational modifications
ppm	Parts per million
R_g	Radius–of–gyration
RMSD	Root–mean–square deviation
RMSF	Root–mean–square fluctuation
ROS	Reactive oxidative species
SASA	Solvent accessible surface area
SPC	Simple point–charge
SERS	Surface-enhanced Raman spectroscopy
STD	Saturation-Transfer Difference
t–BuOH	tertiary butanol
TEM	Transmission electron microscopy
ThT	Thioflavin T
UV–Vis	Ultraviolet–visible
VMD	Visual molecular dynamics
vdW	van der Waals

Chapter 1

Sequence based peptide inhibitors: Propitious inhibitor against Aβ and hIAPP aggregation

1.1 Amyloids: Introduction

Amyloids have been recognised and studied for more than 100 years, and their historical identification has been discussed in intervening decades.[1] Amyloid fibrils are filamentous and tubular structures consisting of insoluble accumulations formed from soluble peptides and proteins, capable of undergoing conformational alterations both intracellularly and extracellularly.[2] The global feature of amyloids is their propensity to form β-pleated sheets arranged in an antiparallel fashion.[3] They are frequently associated with the onset of protein misfolding diseases, these include disorders such as Alzheimer's disease (AD), Parkinson's disease (PD), type 2 diabetes (T2D), Prion diseases, Amyotrophic Lateral Sclerosis (ALS), and Huntington's disease.[4] Each disease is linked with a specific protein and aggregates of these proteins are assumed to be the direct or secondary cause of the pathological states associated with the disease. A list of the disorders linked to the formation of extracellular amyloid fibrils and deposition of intracellular aggregates as well as the specific proteins that are main constituents of the deposits are listed in **Table 1.1**.

Misfolding disorders are brought on by conformational changes of protein paired with accumulation of misfolded proteins in extracellular space of fundamental tissues which is associated with the emergence of toxic function,[5] and this process is known as amyloidogenesis. In recent times, there have been reports indicating the existence of soluble aggregates consisting of a small number of protein molecules. The smaller entities, commonly known as oligomers, and the larger counterparts, referred to as protofibrils, have been identified as highly cytotoxic species.[6]

1.1.1 Mechanism of amyloid formation

Protein aggregation can occur in systems that are unfolded or intrinsically disordered, like amyloid-β (Aβ) peptides, as well as in folded globular proteins, where misfolding occurs by generating a partly unfolded state. Typically, the oligomeric entities produced in the amyloidogenic pathway comprise aggregation of individual monomeric units. Such aggregates have the potential to transform into structures that are highly disordered, possess fibrils characterized by well-defined cross-structured patterns (**Figure 1.1**).[7]

Table 1.1: Human disorders linked to the formation of amyloid and their distinctive pathological features.

Disease	Aggregating protein or peptide	Polypeptide length (number of residues)	Characteristic pathology	Structure of protein or peptide
Alzheimer's disease	Amyloid–β peptide	37-43	Neuritic plaques and neurofibrillary tangles	Intrinsically disordered
Spongiform encephalopathies	Prion protein or its fragments	230	Spongiform degeneration, amyloid, other aggregates	Intrinsically disordered and α–helical
Parkinson's disease	α–synuclein	140	Lewy bodies and lewy neurites	Intrinsically disordered
Huntington's disease	Huntingtin fragments	Variable	Intranuclear inclusions and cytoplasmic aggregates	Mostly intrinsically disordered
Amyotrophic lateral sclerosis	Superoxide dismutase 1	153	Bonina bodies and axonal spheroids	β–sheet and immunoglobulin like structure
Type 2 diabetes	Amylin	37	Insulin resistance	Intrinsically disordered

The aggregation mechanism within amyloid structures is influenced by various pathways, determined by the presence of amyloidogenic sequences coexisting together and environmental factors.[8] The aggregation process unfolds over a broad time range, encompassing multiple orders of magnitude, along with conformational alterations occur within milliseconds. The development of aggregates that are observable without the aid of magnification over a period ranging from days to weeks or months.

Understanding the processes that lead to the formation of amyloids and identifying the key molecular species involved in the process are essential for the progression of rational treatment strategies to amyloid diseases.[8] Various aggregation mechanisms, spanning from the transition from the classical nucleation elongation model to the folding funnel concept, have been suggested to facilitate experiments aimed at gaining a comprehensive understanding of the intricate misfolding process.

Experimentally, the progression of fibril development is often described using a sigmoidal curve (**Figure 1.2**). This curve results from the ongoing monitoring of dye binding to cross-

aggregates, enabling the identification of three main phases in the nucleation-dependent aggregation process. The formation of amyloid fibrils is typically elucidated by a nucleation-dependent polymerization mechanism, encompassing nucleation and elongation.[9] The nucleation-elongation polymerization involves three consecutive phases: (1) the nucleation phase, (2) the elongation or fibrillation phase, and (3) the saturation phase.[10]

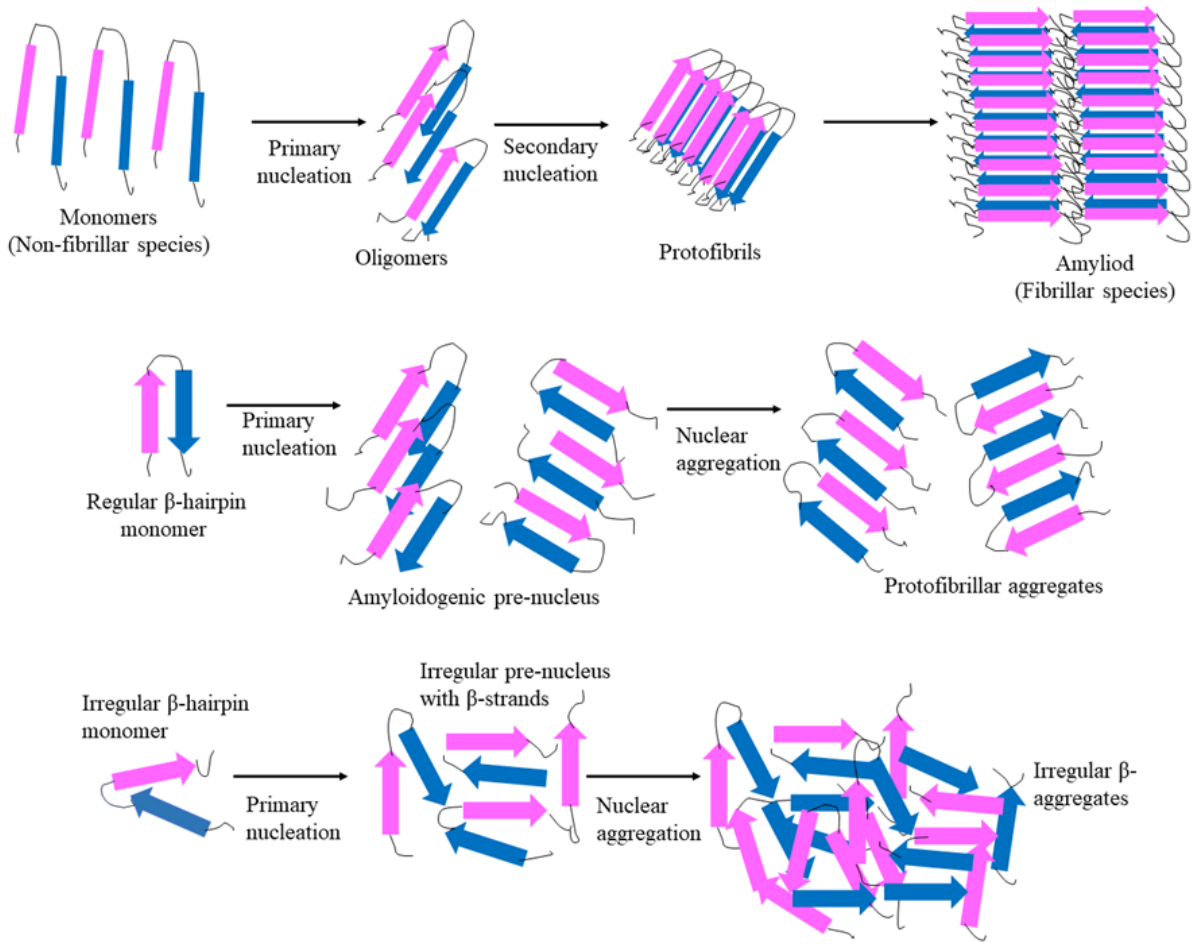

Figure 1.1: A diagram illustrating the diverse conformational states assumed by a protein chain during misfolding process.

The nucleation stage involves the assembly of transient and crucial nuclei, acting as a seed intermediate that attracts additional monomeric subunits, leading to the formation of cross-structured oligomers. During this phase, the rate constants for addition of monomers and dissociation are similar, resulting in a slowdown of the overall nucleation process. This makes nucleation stage the rate-limiting step in formation of fibrils. The nucleation step can be expedited by introducing pre-formed aggregates or fibril species, a phenomenon known as seeding.[11] During the fibrillation phase, monomers, oligomers, and nuclei persist in collaboration, assembling into pre-fibrillar structures that quickly evolve into organized structures known as protofibrils. Finally, in the saturation phase, the concentration of monomer

remains low and relatively constant, and the protofibrils assemble into fully developed amyloid fibrils with diverse morphological shapes and various degrees of polymorphism.[12]

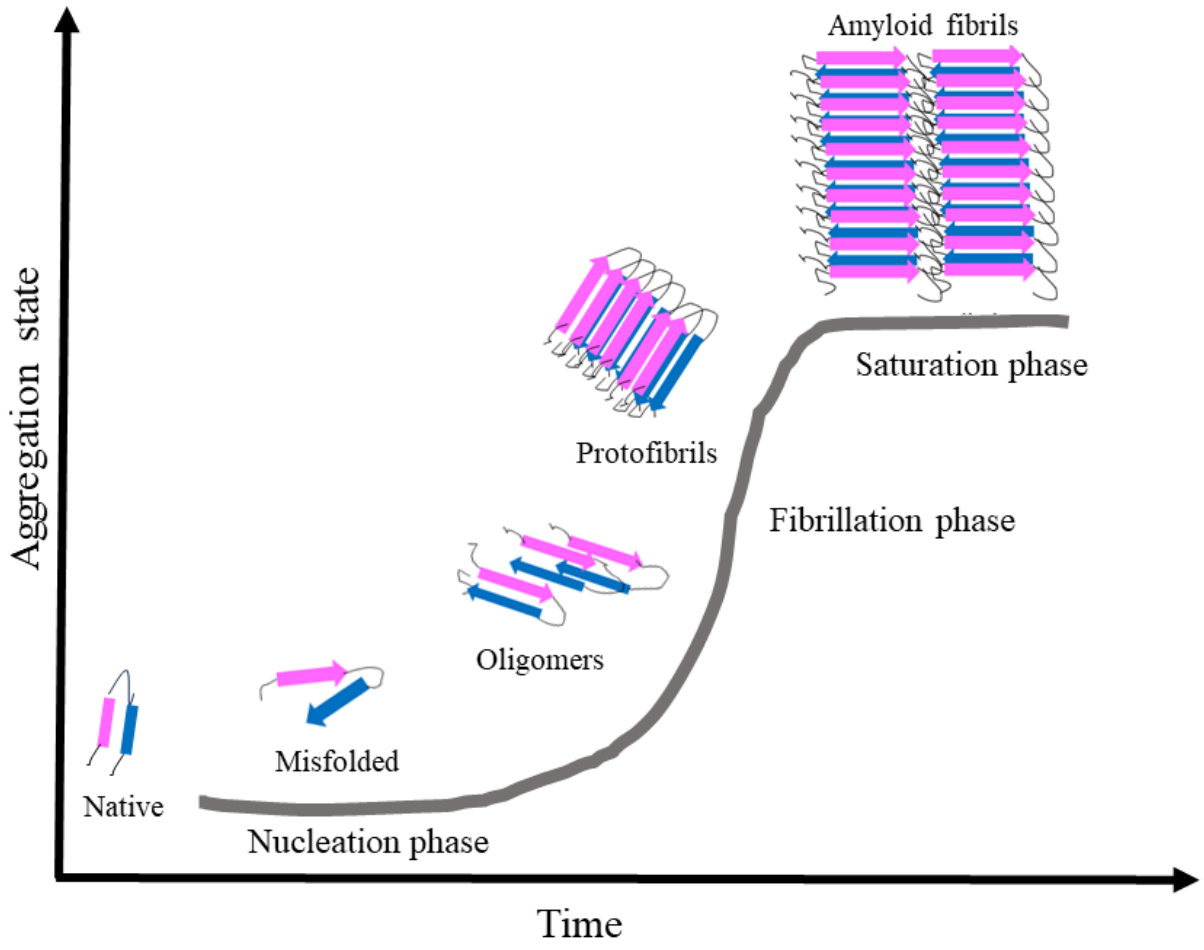

Figure 1.2: Illustration of the nucleation-dependent fibril formation process, comprising the nucleation phase, the fibrillation phase and the saturation phase.

The theory of the free energy landscape (FEL) provides a statistical depiction of the free energies associated with molecular arrangements in protein folding (**Figure 1.3**). The model of the protein folding funnel has been derived from observations obtained through experimentation and theoretical frameworks which rely on simple mechanical models developed by Wolynes, Onuchic, Dill, and their collaborators.[13] In accordance with the FEL theory, the folding funnel of a small protein rapidly adopting an α-helical fold will feature a transition state positioned midway between the native and folded states.[14,15]

The upper area of the funnel illustrates the extensive variety of conformations that exist in the unfolded or extended condition, while its narrower lower section indicates the distinctive inherent structure of the protein. The folding funnel facilitates multiple routes for rapid

transition from the ensemble of unfolded conformations to the global free energy minimum occupied by amyloids. This minimum has recently been refined into a sequence of closely situated local minima, each housing various amyloid structural forms, with crystalline amyloid structures occupying the absolute minimum. The unfolded polypeptide chain at the upper part of the funnel possesses high Gibbs free energy and conformational entropy. Before reaching the metastable local minima, the protein chain undergoes folding into lower energy conformations. Consequently, the protein chain folding results in decrease of entropy and the diversity of conformational states.

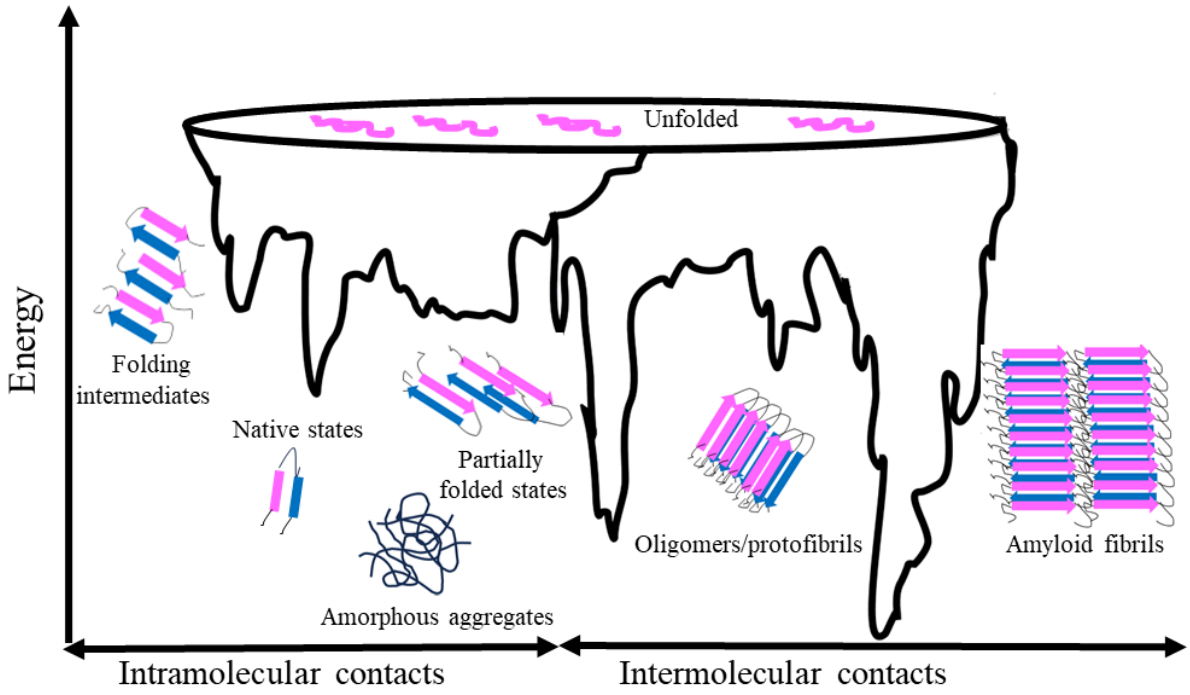

Figure 1.3: The illustration of the FEL associated with the processes of protein folding and aggregation depicting conformations progressing towards amyloid fibrils.

The hydrophobic collapse and the elevated intramolecular contacts collaborate to reduce free energy, steering the system towards the native state. The state, representing the global free energy minimum, leads to the stable folded conformation. In this process, kinetic traps can either impede or facilitate the establishment of native conformations. The outcome depends on the depths of these traps and the barriers separating them from subsequent energy minima. The quantity and intensity of kinetic traps within the funnel landscape are associated with frustration level inherent in the protein sequence.[13a] In accordance with the folding-funnel diagram concept, an off-route aggregation can be represented as a secondary "aggregation funnel."[16] The interaction among multiple non-native protein structures can lead to the creation

of an "amyloidosis formation funnel" via intermolecular interactions, also referred to as intramolecular folding. This phenomenon is primarily propelled by hydrophobic forces, leads in the formation of predominantly amorphous aggregates. Following this, the aggregation process might result in the emergence of amyloid fibrils. Thus, folding funnel models offer a conceptual framework for comprehending the intricate procedure of amyloid production.[17]

1.1.2 Efficacious therapeutics against amyloid

As the number of patients afflicted with diseases associated with amyloidogenesis continues to increase, there is a pressing need for innovative therapeutics. The exploration of inhibiting protein self-aggregation is approached from two perspectives: the formulation of approaches to prevent the protein aggregation process and search for inhibitors that specifically target amyloid aggregates.

Amyloid inhibitors demonstrate the capacity to interact with amyloidogenic aggregates at various stages, either by preventing, hindering, or suppressing amyloid aggregation, or by disassembly of preformed aggregates. In recent decades, active efforts have been made to develop techniques for mitigating amyloidosis, utilizing a range of approaches as inhibitors including utilising peptides,[18] peptidomimetics, monoclonal antibodies,[19]vitamins,[20] osmolytes,[21] non-detergent sulfobetaine,[22] metal chelators,[23] small compounds[24] and more recently organic and inorganic nanoparticles[25] and nanocomposites[26].

1. Small molecule-based inhibitors

Numerous natural products based small molecule, include polyphenols which are abundant in grapes, tea, red wine, and turmeric, have been shown to prevent the aggregation and toxicity of proteins both *in vitro* and *in vivo.*[27] Various studies support the use of curcumin as a viable treatment for AD because it suppresses the production of amyloid and weakens fibrillar or oligomeric forms.[28] Curcumin also binds to monomeric form of α-synuclein reducing aggregation and shows increment in reconfiguration rate.[29] Rosmarinic acid inhibits the formation of Aβ aggregates and human islet amyloid polypeptide (hIAPP) fibrils and can destabilize their preformed fibrils.[28] (-)-Epigallocatechin-gallate (EGCG), a member of flavanols primarily found in green tea, represents another compound showing promising effects in inhibiting amyloid proteins. EGCG demonstrates efficacy in inhibiting amyloid proteins such as Aβ, hIAPP, tau, and α-synuclein.[30]

2. Peptide based inhibitors and peptidomimetics

In recent years, with an accurate understanding of amyloid and fibril structures, peptides designed to inhibit amyloid aggregation have exhibited increased specificity and effectiveness. Rational design methods and peptide screening platforms have resulted in the increase in the number of druggable peptide candidates. The KLVFFA in $A\beta_{42}$ is regarded as the main aggregation-prone location and is frequently referred to as the self-recognition site. KLVFFA-containing peptides are proven to be a reliable class of $A\beta_{42}$ inhibitory drugs through exact binding with the analogous sequence of natural $A\beta_{42}$.[31] Austen et al. examined two peptide inhibitors, OR1 (RGKLVFFGR) and OR2 (RGKLVFFGR-NH2), targeting $A\beta_{42}$.[32] These peptide inhibitors were created by modifying the KLVFF amino acid sequence of $A\beta_{42}$, incorporating RG-/GR residues at the N- and C-terminals. It was noted that both peptide inhibitors successfully prevented the development of Aβ fibrils. The peptide KKLTVWpGKWITVSA (WW2) hinders the formation of amyloids in α-synuclein and IAPP.[33] Peptidomimetics are protein-like compounds with modified small chains that mimic proteins. Recently, peptide-based conjugates have been identified as inhibitors in conditions related to amyloid production. These inhibitors function by impeding protein aggregation.[34]

3. Vitamins

Vitamins are vital organic compounds that are found in the human body, playing a crucial role in ensuring proper bodily functions. Various research groups have reported the involvement of vitamins in preventing protein aggregation. Ono et al. demonstrated that vitamin A has the potential to impede the aggregation of α-synuclein fibrils, which are implicated in Lewy body diseases.[20a] Studies have revealed that vitamin E can stop the aggregation of $A\beta_{42}$.[20b] A significant factor in the aggregation of proteins is oxidative stress (OS),[20c] and these aggregates engage with metal ions and hydrogen peroxide, giving rise to the generation of reactive oxygen species (ROS).[20d] Vitamins A, C, and E limit protein oxidation and reduce ROS through their ability to scavenge free electrons.[20e]

4. Non-detergent sulfobetaine and chaperones

Non-detergent sulfobetaines (NDSBs) are another group of chemicals that are used to prevent aggregation. The osmolyte choline-O-sulphate (2-(trimethylammonio) ethyl sulphate) is one of the choline esters that inhibits amyloid formation.[22e] NDSBs hinder the aggregation of folding

intermediates by binding to them, thereby stabilizing the folded state and preventing protein aggregation.[22b,c] An "artificial chaperone" refers to a non-protein system that exhibits chaperone-like activity, utilizing a combination of cyclodextrins and detergents, both capable of suppressing aggregation. These are frequently employed in combination to reduce the likelihood of aggregation and improve the refolding process efficiency.[35] Furthermore, Jarvela et al. revealed that an *in vitro* experiment suggests that recombinant proSAAS suppress α-synuclein fibrillation.[36]

5. Monoclonal antibodies

Passive immunotherapy strategies known as monoclonal anti-Aβ antibodies (mAbs) have been thoroughly researched as a treatment for AD. The array of accessible monoclonal antibodies (mAbs) differs in their specificity for polymorphic variations, allowing them to recognize epitopes based on either specific regions within the Aβ sequence or various multimeric Aβ conformations. Aducanumab is a humanized monoclonal IgG1 antibody that preferentially binds to soluble and insoluble Aβ amyloid aggregates.[37] It was derived from a library of blood lymphocytes, obtained from a group of elderly individuals in the healthy donor community. These individuals either displayed no signs of cognitive impairment or exhibited an unusually gradual cognitive decline. The mouse monoclonal antibody mAb158 has undergone humanization and is now known as lecanemab.[38] Lecanemab exhibits a preference for binding to large, soluble Aβ protofibrils. It efficiently lowers the levels of pathogenic Aβ, hinders Aβ deposition, and specifically diminishes Aβ protofibrils in both the human brain and animal models.

6. Osmolytes

Osmolytes refer to small organic molecules of low molecular weight that uphold the characteristics of the biological fluid.[39] The most often employed osmolytes for enhancing protein refolding, stability, and preventing protein aggregation and amyloid fibril production are polyols and sugars. According to studies, polyols and sugars alter the solvent's surface tension, viscosity, and hydrogen-bonding pattern in order to stabilise proteins in their natural state through hydration mechanism. The study reported that low concentrations of trehalose prevented the polymerization of α-synuclein *in vitro*, and stabilising α-synuclein folding.[40] It has been found that sucrose has an inhibitory impact on the Aβ peptide, which perturbs aggregation and promotes the helical conformation.[41]

7. Metal chelators

Metal chelators is a promising strategy to lessen redox stress and restore the regular trafficking of metal ions. Recent research has highlighted the potential for the development of more multifunctional chemical compounds with increased effectiveness and selectivity towards metal-induced amyloid production and toxicity. These compounds have the ability to interact with amyloid aggregates and act as a metal chelator.[42] It has been demonstrated that chelators like bathocuproine, tpen (N,N,N′,N′-tetrakis(2-pyridyl-methyl) ethylene diamine), and EGTA can dissolve Aβ plaques.[43] Two copper-zinc chelators, clioquinol and BPT-2, are 8-hydroxyquinoline derivatives that have demonstrated promising *in vitro* outcomes.[44] Meng et al. showed that RK10 (RTHLVFFARK-NH2), a dual-functional peptide consisting of a metal-chelating tripeptide (RTH) and an Aβ aggregation inhibitor, targets both Cu^{2+}-bound and free $A\beta_{40}$ species.[45] It inhibits the aggregation of $A\beta_{40}$, preventing $A\beta_{40}$ from aggregating and reducing the cytotoxicity induced by $A\beta_{40}$ and Cu^{2+}-mediated $A\beta_{40}$ in cultured SH-SY5Y cells.

8. Nanoparticles

Nanoparticles can greatly impact the aggregation and nucleation process of amyloid peptides. Gao et al. reported that the size of nanoparticles and their impact on Aβ aggregation are connected. The small gold nanoparticles (6 nm) and nanoclusters (1.9 nm) considerably slowed down or stopped the aggregation of Aβ peptides.[46] Chan et al. explored the impact of nanoparticles with varying sizes and surface functionalities on the self-assembling fibrillization of the $A\beta_{40}$ peptide. They observed that the small sized quantum dots inhibited the Aβ aggregation and large sized quantum dots promote Aβ aggregation, whereas medium sized particles showed no effect on aggregation.[47] Ghavami et al. examined Aβ aggregation in the absence and presence of hydrophilic silica and hydrophobic polystyrene nanoparticles. At temperature 42°C, silica nanoparticles accelerated the aggregation, and polystyrene nanoparticles impeded the Aβ aggregation process.[48] Zhang and colleagues designed a novel peptide, LK7 (Ac-LVFFARK-NH2), by introducing two positive charged residues into the CHC region segment of $A\beta_{42}$.[49] LK7 exhibited dose-dependent suppression of $A\beta_{42}$ fibrillogenesis but displayed potent cytotoxic self-assembly characteristics. To prevent the self-assembling of LK7, the peptide was conjugated onto nanoparticles named as poly(lactic-co-glycolic acid) (PLGA) and the resulting LK7@PLGA nanoparticle complexes significantly reduced $A\beta_{42}$ fibrillation.

1.2 Type 2 Diabetes

1.2.1 Introduction

Diabetes mellitus is characterized as a series of metabolic disorders manifested by hyperglycemia (elevated blood glucose levels) resulting from abnormalities in insulin secretion and insulin action. Type 1 diabetes involves the destruction of pancreatic β-cells due to an autoimmune response, leading to insulin insufficiency and hyperglycemia. T2D arises from insulin resistance (failure of insulin-sensitive tissues to respond to insulin), reduced β-cell production, and other factors outlined in **Figure 1.4**. Chronic diabetes-related complications impact various organs, including nephropathy, peripheral neuropathy, retinopathy, diabetic foot ulcers, and peripheral arterial disease.[50] T2D patients typically exhibit obesity or an elevated body fat percentage, particularly concentrated in the abdominal region.

While diabetes can remain asymptomatic for an extended period, the diagnosis of T2D often coincides with the presence of another condition. In the absence of symptoms, a T2D diagnosis is established when Fasting Plasma Glucose (FPG) levels reach or exceed 126 mg/dL, Oral Glucose Tolerance Test (OGTT) levels are at or above 200 mg/dL, or HbA1c levels equal or surpass 48 mmol/mol (6.5%). Diabetes is recognized when blood glucose levels are 200 mg/dL or higher, accompanied by symptoms. The rise in the prevalence and incidence of T2D is attributed to factors such as population aging, sedentary lifestyles, high-calorie diets, and the global increase in obesity rates.[51] Insulin resistance in T2D is influenced by adipose tissue through multiple inflammatory mechanisms, including the heightened synthesis of free fatty acids (FFA) and the disruption of adipokine regulation.

The onset of T2D is marked by three factors: diminished insulin secretion by pancreatic β-cells, decreased sensitivity of peripheral tissues to insulin, and the accumulation of aggregates derived from hIAPP.[52] Significant progress has been made in comprehending the cytotoxic mechanism of hIAPP oligomers and aggregates formed both intracellularly and extracellularly over the past two decades. Studies done in primates firmly supported the concept that β-cell apoptosis and islet amyloidosis are two important predictors of islet dysfunction.[53] However, the biological mechanism governing hIAPP turnover and the induction of β-cell apoptosis by hIAPP in human islets remains unclear. Consequently, there are no currently available effective treatments to reduce the aggregation and toxicity of hIAPP in humans.

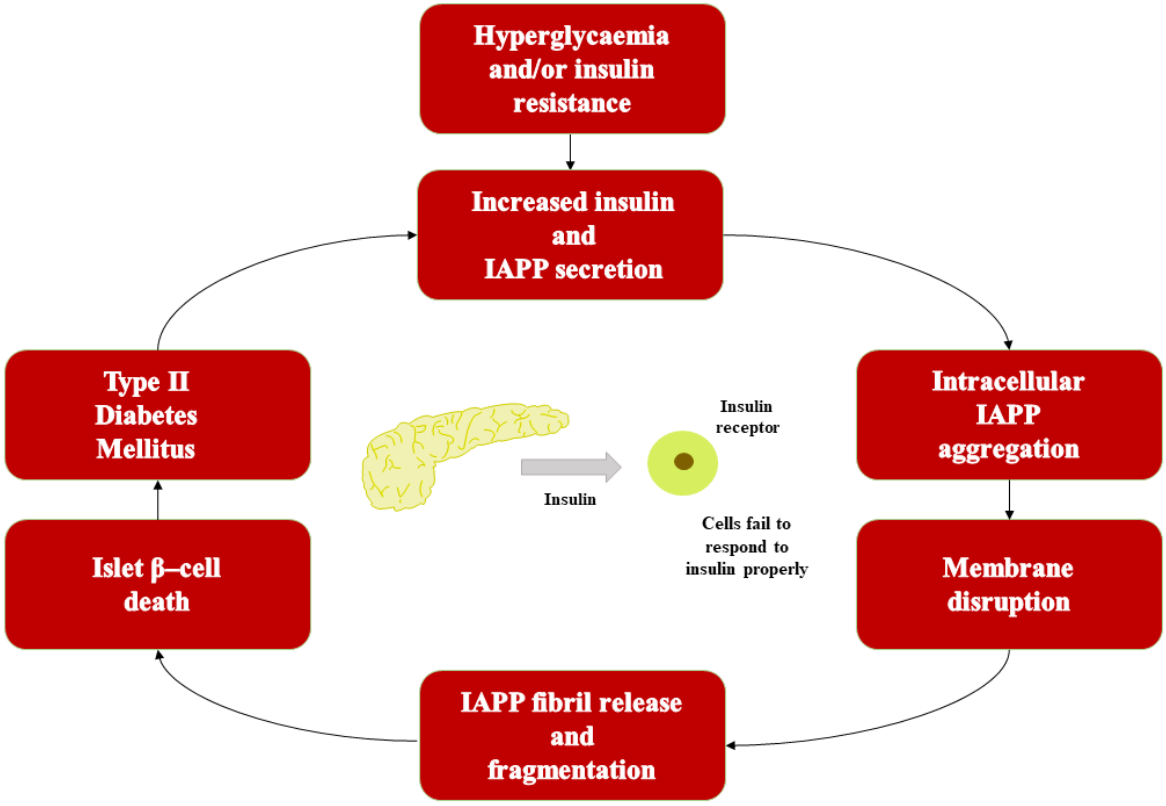

Figure 1.4: Flow chart of events associated with T2D.

1.2.2 Statistics of T2D

The International Diabetes Foundation estimated that in 2021, the global prevalence of diabetes reached a staggering 537 million individuals, with a forecasted surge to an alarming 783 million by the year 2045. The anticipated cost of treating diabetes-related illnesses globally was 966 billion USD in 2021, with expectations of reaching 1,054 billion USD by 2045.[54] The actual disease burden of T2D is likely underestimated, as 1 in 3 diabetic patients were misdiagnosed, equivalent to 232 million people. Individuals most commonly affected by diabetes are between the ages of 40-59 years. The prevalence and incidence of T2D vary by geographic area, with over 80% of affected individuals residing in low and middle-income nations, posing challenges for effective care. Cardiovascular disease (CVD) stands as the leading cause of morbidity and death associated with T2D, with patients facing a 15% higher risk of mortality compared to those without diabetes.[55]

As per the Women's Health Study and the Kuopio Ischemic Heart Disease Risk Factor Study, leading a sedentary lifestyle is identified as another risk factor for T2D. These studies indicated 34% and 56% reduction in the likelihood of developing T2D among participants who engaged

in at least 40 minutes of walking per day and 2-3 hours per week, respectively.[56] Physical activity offers three main advantages in delaying the onset of T2D. Firstly, when skeletal muscle cells contract during exercise, there is increased blood flow into the muscles, enhancing the uptake of glucose from the plasma.[57] Secondly, exercise helps reduce intra-abdominal fat, a confirmed risk factor for insulin resistance.[58] Lastly, moderate exercise has been shown to increase glucose absorption by 40%. Exercise not only enhances insulin sensitivity and glucose uptake but also has the potential to mitigate inflammation and oxidative stress, both of which are risk factors for T2D.[59]

1.2.3 Aggregation mechanism of hIAPP

The two primary pancreatic hormones regulating blood glucose levels are insulin and hIAPP. The hIAPP is encoded by a gene located on chromosome 12, comprising three exons. The first two exons encode the entire Pre-proIAPP protein, which consists of 89 amino acids.[60] In the process of translation, a signal peptide consisting of 22 amino acids is enzymatically removed from the C-terminus, as Pre-proIAPP enters the endoplasmic reticulum. Inside the lumen of the endoplasmic reticulum, a disulfide bond forms between Cys2 and Cys7 of the mature IAPP sequence, catalyzed by the Protein Disulfide Isomerase (PDI) enzyme. The 67-amino acid mature hIAPP is then transported to the Golgi complex, where it is packaged into secretory granules.[61] Within these secretory granules, additional post-translational modifications (PTMs) take place. PC2 and PC3, which are also referred to as furin, are prohormone convertase enzymes that are responsible for the removal of 11 amino acids from the N-terminus and 16 amino acids from the C-terminus of mature hIAPP.[62]

Following the processing by proconvertases, the carboxypeptidase E eliminates the C-terminal dipeptide Lys-Arg. Afterwards, the glycine residue located at the C-terminus is eliminated, and the peptidyl α-amidating monooxygenase enzyme complex facilitates the amidation process of the available carboxyl group of the terminal tyrosine residue in mature hIAPP (**Figure 1.5**).[63] These various post-translational modification events results in formation of an active hIAPP 37-residue peptide hormone. This hormone is secreted alongside insulin, playing a crucial role in the regulation of blood glucose levels.

In 1901, hIAPP deposits were initially observed in post-mortem pancreatic parenchymal cells of T2D patients.[64] Subsequent investigations revealed that these deposits were indeed hIAPP.[65] Elevated concentrations of hIAPP result in an augmented reservoir of partially processed and

fully mature hIAPP protein within the extracellular matrix. These increased levels are adequate to generate the crucial nuclei responsible for instigating the fibrillation process of the hIAPP hormone, ultimately leading to the formation of amyloid. In its physiological state, hIAPP is typically soluble, monomeric, and naturally unfolded in solution. There is a sequence similarity of 89% and 84% between hIAPP and the cat and rodent proteins, respectively.[66] Numerous studies suggest that hIAPP is a highly amyloidogenic peptide capable of adopting various structural states. It is hypothesized that changes in the local environment, particularly alterations in the hydrophobicity of residues 20–29 (the self-recognition region), are crucial for amyloid development.[67]

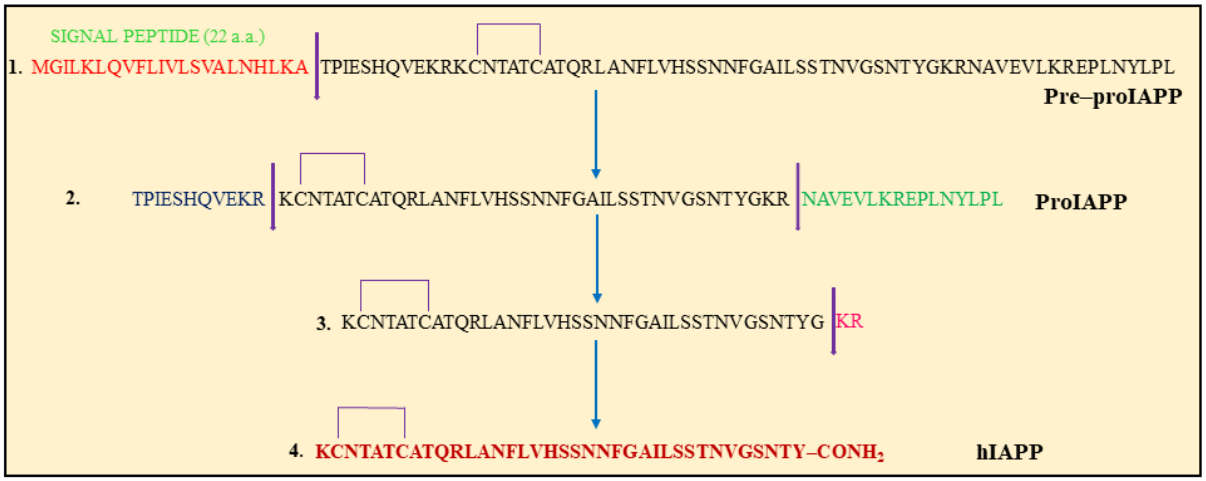

Figure 1.5: Sequential steps involved in the processing of pre-proIAPP to generate mature hIAPP.

1.2.4 Therapeutic strategies to prevent hIAPP aggregation

All critical stages in the pathways leading to the formation of pathogenic species present potential targets for impeding the aggregation process. Despite diverse design approaches for inhibiting hIAPP aggregation, understanding the interactions between hIAPP and inhibitors at various aggregate stages is pivotal in comprehending the hIAPP aggregation process. In order to suppress amyloid aggregation, scientists have developed inhibitors that modify the folding structures, assembly processes, and species populations of amyloid. Broadly, any process influencing the generation, aggregation, or clearance of the hIAPP amyloid peptide can be considered a potential target for inhibiting amyloid development.

The most common inhibition strategies include: (1) reducing hIAPP peptide expression and production; (2) facilitating the elimination of hIAPP peptides and their aggregates; (3) preventing hIAPP peptide interactions with cell membranes; and (4) inhibiting the transformation of the structural conformation to β-structure and subsequent aggregation of hIAPP. The first three inhibitory strategies aim to develop inhibitors targeting specific proteins, enzymes, or receptors (such as the hIAPP protein, insulin receptor, membrane receptors, and the glucagon-like peptide-1 receptor) to hinder the cleavage, or clearance of hIAPP. Inhibiting the activity of protein hormones, receptors, and enzymes may interfere with normal cellular functions, leading to potential side effects.[68] Therefore, strategies that prevent β-sheet formation and disassembly of toxic hIAPP soluble oligomers can be highly effective in treating T2D.

Notably, Lixisenatide, a GLP-1 receptor agonist, and Semaglutide, a GLP-1 analogue, have received FDA approval for managing T2D. Another diabetes medication, ertugliflozin, targeting SGLT2, received approval in 2017.[69] The utilization of GLP-1 receptor agonists is associated with weight loss, and there is ongoing debate regarding whether they increase the risk of heart failure.

1.2.4.1 Peptide based inhibitors against hIAPP aggregation

Approximately 80 peptide medications are presently accessible globally, and ongoing research in the development of new peptide treatments continues at a consistent pace. Currently, over 150 peptides are in various stages of clinical trials, with an additional 400–600 undergoing preclinical studies. We anticipate that the peptide therapeutics market will sustain its momentum and experience growth in the coming years. This growth is attributed to increased investment and research endeavours in peptide synthesis technology, the accomplishments in biologics, and the pharmaceutical industry's imperative to maintain high new drug approval rates. [70,71]

Peptide-based inhibitors for hIAPP offer inherent advantages, including good biocompatibility and minimal immunogenicity. Various design approaches can be employed to create peptide-based hIAPP inhibitors, aiming to hinder the structural changes in hIAPP aggregation. The first approach involves designing inhibitors that stabilize the native folded monomer conformation of hIAPP, preventing further misfolding and aggregation. Secondly, inhibitors may bind to hIAPP oligomers to impede amyloid formation. Third, certain inhibitors act as β-sheet

breakers, disrupting the connections between β-sheets in hIAPP aggregates or breaking up already-formed hIAPP aggregates. Peptide inhibitors can be either designed *de novo* or derived from the hIAPP sequence. The inhibitors are specifically crafted to target amyloidogenic regions, including $hIAPP_{20–29}$, $hIAPP_{22–27}$, $hIAPP_{24–29}$, and $hIAPP_{30–37}$, which are prone to amyloid generation.[72] Inhibitors targeting amyloidogenic regions obstruct the essential active sites required for hIAPP aggregation or structural alterations. The amyloidogenic regions are primarily hydrophobic and feature aromatic residues such as F15, F23, and Y37, allowing inhibitors to bind through hydrophobic contacts or π-π stacking interactions. The following section briefly discusses some noteworthy families of peptide-based inhibitors published in the last decade, while more comprehensive information on peptide-based inhibitors from the past two decades can be found in recent review articles.[73]

I. hIAPPsequence-based peptide inhibitors

Numerous concise peptides, such as NTAT ($hIAPP_{3–6}$), TQRLA ($hIAPP_{9–13}$), FLPNF ($hIAPP_{11–15}$), GAILSS ($hIAPP_{24–29}$), SNNFGA ($hIAPP_{20–25}$), NYGAILSS, NFGAILPP (modified $hIAPP_{22–29}$), and STNVGS ($hIAPP_{29–33}$), have demonstrated the ability to hinder hIAPP aggregation *in vitro*.[73c] These short peptides offer inherent advantages as inhibitors of hIAPP. They exhibit high binding affinities to hIAPP, possess biocompatibility, are straightforward to synthesize and modify, have predictable folding structures, and are easily foldable. Additionally, they can degrade rapidly *in vivo* and exhibit low membrane permeability. Peptide inhibitors, short in length and derived from the hIAPP sequence, exhibit a significant inclination to engage with hIAPP. They compete with hIAPP−hIAPP interactions, effectively hindering the aggregation of hIAPP.

Potter et al. synthesized numerous peptides derived from the sequence of IAPP and identified hexapeptide ANFLVH as a potent inhibitor of IAPP aggregation.[74] The addition of the ANFLVH peptide, at equimolar or higher concentrations, effectively prevented the formation of β-sheets and maintained IAPP in a disordered, random conformation consistently. When ANFLVH was added at a 10-fold molar ratio to full-length IAPP, it completely negated IAPP-induced toxicity in Rin1056A β cells. ANFLVH hexapeptide at a 20-fold molar excess led to a significant decrease in the density of IAPP amyloid. Human islet cultures treated with ANFLVH at concentrations of 200μM exhibited a remarkable reduction in thioflavin S-positive amyloid accumulations compared to untreated cells.

Wang et al. developed D-amino-acid inhibitor derived from the NFGAIL fragment named as D-NFGAIL, with the purpose of inhibiting hIAPP fibrillation.[75] Its inhibitory effectiveness at the phospholipid membrane surface was investigated by specifically targeting helical oligomeric intermediates. The findings indicate that in bulk solution, the D-NFGAIL inhibitor disrupts hIAPP aggregation by halting the formation of β-sheeted oligomeric intermediates. CD results reveal that α-helical oligomers play a crucial role as intermediates in the pathway leading to hIAPP fibrillation at the membrane. MTT ((3-[4,5-dimethylthiazol-2-yl]-2,5 diphenyl tetrazolium bromide)) assay predictions suggest that the D-NFGAIL binds to hIAPP oligomeric intermediates, resulting in the protection of cells from hIAPP-induced toxicity.

Wijesekara et al. conducted a study on the impact of D-ANFLVH by administering it intraperitoneally in a mouse model of hIAPP that mimics the islet amyloid pathology of T2D.[76] The findings reveal that D-ANFLVH significantly reduces islet amyloid accumulation, enhances β-cell survival, and preserves insulin secretion and glucose homeostasis. In another study, Sivanesam et al., demonstrated that both the oligomeric form and the monomeric form of NFGAILSS can impede hIAPP aggregation.[77] The oligomeric form of NFGAILSS prevents the transition from a random coil to β-sheet and serves as a disaggregator for hIAPP β-oligomers. The removal of serine residues from NFGAILSS leads to a reduction in inhibition, underscoring the significance of these residues in the segment's action. CD spectra indicated occurrences resembling α-helix spectra preceding the formation of β-sheet during the amyloidogenesis process. The authors concluded that the β-strand conformation of NFGAILSS acts as the inhibitory feature, interacting with the same sequence in hIAPP and retarding the nucleation of hIAPP amyloid oligomer formation.

Rozniakowski et al. assessed various hIAPP fragments for their aggregation ability and reported that fragments H-HSSNN-OH ($hIAPP_{18–22}$) and H-GSNTY-NH_2 ($hIAPP_{33–37}$) undergo self-aggregation to yield amyloid fibrils.[78] In comparison to other hIAPP fragments, HSSNN displayed the highest antiproliferative activity to RIN-5F cells.

Fraczyk and co-authors explored the inhibitory effects of non-aggregating fragments 1–7, 8–12, 13–17, and 28–32 of hIAPP against the aggregation of the amyloidogenic cores 18–22, 23–27, and 33–37 of hIAPP.[79] Various independent techniques, including spectroscopic and fluorescence assays with indicators, microscopic examinations, and CD studies, were employed to assess the inhibitory capacity of these non-aggregating hIAPP fragments. The

findings indicate that the cyclic fragment H–^{1}KCNTATC^{7}–OH with a disulfide bond serves as an inhibitor capable of preventing the aggregation of all the amyloidogenic cores 18–22, 23–27, and 33–37 of the hIAPP hormone. Furthermore, H–^{1}KCNTATC^{7}–OH hinders the aggregation of insulin hot spots, suggesting its potential utility in preventing the aggregation of hormones crucial for glucose metabolism and directly linked to the onset of diabetes.

II. Rationally designed peptide inhibitors

Andreasen and co-authors studied the effect of a backbone modification at a single site on the self-aggregation tendency of NFGAIL and SNNFGAILSS and examined its impact on the aggregation of hIAPP.[80] Various modifications, including N-methylation, peptoid generation, and replacement of the peptide-bond with a hydroxyethylene and ketomethylene group, were implemented. The modified peptides extended the length of the natural hIAPP fibrils but did not undergo self-aggregation. The findings demonstrated that single-site backbone modifications can modulate hIAPP aggregation.

Mishra et al. developed modified peptide inhibitors, namely NFGAΔFL and FGAΔFL, by incorporating dehydrophenylalanine (ΔF), an unnatural amino acid.[81] ThT experiments indicated that, at a molar ratio of 1:5 for hIAPP (40μM) to inhibitor (200μM), FGAΔFL significantly inhibited hIAPP aggregation (75 ± 8%), demonstrating more effectiveness than NFGAΔFL (7 ± 5%). MTT assay results showed that the presence of FGAΔFL significantly mitigated the cytotoxic effects of hIAPP (1–10μM) on cultured pancreatic rat insulinoma cells (RIN 5fm). Additionally, molecular docking of FGAΔFL with hIAPP (PDB ID: 2KB8) was conducted to explore various modes of interaction, revealing a binding energy of -6.47 kcal/mol. The docking results suggested that FGAΔFL binds to hIAPP in its monomeric helical conformation.

Obasse et al. designed a series of overlapping peptides targeting the 'binding' region RLANFLVHSS (11–20) of hIAPP and investigated their impact on amyloid fibril formation using ThT assay.[82] The designed peptides inhibiting hIAPP aggregation at high concentrations. Among designed peptides, IO5 (H_2N-RGNFLVHGR-$CONH_2$) showed the potent inhibitory ability against hIAPP aggregation. Furthermore, IO5 protected human pancreatic insulin-secreting cells from hIAPP-mediated cytotoxicity. Additionally, two N-methylated peptides, (H_2N-RGAmNFmLVmHGR-$CONH_2$) N1-IO8 and (H_2N-RGANmFLmVHmR-$CONH_2$) N2-IO8, demonstrated a dose-dependent reduction in hIAPP fibril production and sustained

stability in human plasma against various proteolytic enzymes. N1-IO8 and N2-IO8, at a 1:1 and 1:4 molar ratio of peptides to hIAPP, provided protection to human pancreatic 1.4E7 cells against hIAPP-induced toxicity.

Paul et al. reported the successful inhibition of hIAPP aggregation through the utilization of conformationally constrained β-sheet breaker hybrid peptidomimetics (BSBHps) incorporating β, γ, and δ aminobenzoic acids.[83] The study revealed that the inclusion of conformationally constrained aminobenzoic acids enhanced the stability of peptides against proteolytic degradation, making them promising candidates for combating hIAPP aggregation. Modification of the NFGAIL sequence of hIAPP with β(2-aminobenzoic acid), γ(3-aminobenzoic acid), and δ(4-aminobenzoic acid) produced α/β, α/γ, and α/δ peptidomimetics, respectively. Both α/β and α/γ BSBHps demonstrated inhibitory effects on hIAPP aggregation. Moreover, the conformationally constrained BSBHps demonstrated the ability to transform pre-formed amyloids into non-toxic configurations.

Rozniakowski and colleagues explored the inhibitory effects of N-methylated analogs derived from non-aggregating fragments 18–22, 23–27, and 33–37 of hIAPP against hIAPP aggregation.[84] The findings revealed that the peptide H−F(N−Me)GA(N−Me) IL−OH, truncated from the $hIAPP_{23–27}$ amyloidogenic core, did not form fibrous structures. N-methylated H−H(N−Me)SSNN−OH, H−HS(N−Me)SNN−OH, H−H(N−Me)S(N−Me)SNN-OH H−F(N−Me)GAIL−OH, and H−FGA(N−Me)IL−OH peptides exhibited inhibitory activity against the aggregation of the $hIAPP_{18–22}$ fragment. N-methylated peptides derived from the H-$H_{18}SSNN_{22}$-OH fragment, and the HF(N-Me)GA(N-Me)ILOH fragment from the $hIAPP_{23-27}$ hot region, significantly reduced the accumulation of the amyloidogenic core of $hIAPP_{23-27}$. Moreover, N-methylated peptides from the 18-22 fragment and the doubly methylated peptide H-F(NMe)GA(NMe)IL-OH demonstrated inhibitory effects on fragment H-$G_{33}SNTY_{37}$-NH_2 of hIAPP.

Lesma et al. investigated the inhibitory behavior of designed peptides, focusing on structural modifications such as selecting self-recognition elements from the hIAPP amyloidogenic sequence, varying the length of peptide sequences, modifying the N-terminus, and incorporating a diaza-peptide motif.[85] Utilizing mass spectrometry, capillary electrophoresis, TEM, and ThT fluorescence studies, the designed peptides were found to inhibit the oligomerization and fibrillization of hIAPP. Furthermore, these peptides demonstrated the

ability to decelerate the aggregation process in the presence of membrane models and significantly delay membrane leakage caused by hIAPP.

Figueroa et al. examined a range of inhibitors derived from the insulin B-chain sequence HLVEALYLV (10−18) and assessed their effectiveness against hIAPP aggregation and their impact on hIAPP-induced membrane damage.[86] These peptides exhibited the ability to decelerate hIAPP aggregation significantly at high concentrations (10 molar excess), with only EALYLV and VEALYLV among the generated peptides showing inhibitory activity at a 1:1 molar ratio (hIAPP : peptide). DFT calculations revealed that the interaction of EALYLV and VEALYLV with the residues in the Arg11-Phe15 region of hIAPP resulted in the formation of a salt bridge with Arg11. This interaction effectively inhibits a critical amyloidogenic region of hIAPP. Slowing down hIAPP aggregation by these peptides resulted in increased disruption of lipid membranes, suggesting that the fibrillized form of hIAPP was not the primary cause of observed *in vivo* cytotoxicity.

Sivanesam et al. identified potential inhibitors of hIAPP aggregation, namely WW2 and two sequences, cap-WW2 (AcW-KKLTVW-IpGK-WITVSAWTGNH_2) and cyclo-WW2 [cyclo(-GKWITVSIpPKKLTVWIp)].[87] Both cap-WW2 and cyclo-WW2 sequences exhibited more stable and rigid β-hairpin conformations. At a molar ratio of 0.5:1 with cyclo-WW2 (5μM): hIAPP (10μM), cyclo-WW2 was found to be more effective, preventing hIAPP accumulation even at substoichiometric concentrations. No significant increase in fluorescence intensity was observed in the case of cyclo-WW2, indicating the complete absence of hIAPP fibrils at substoichiometric concentrations of cyclo-WW2. β-cap-WW2 and cyclo-WW2 inhibited hIAPP-induced toxicity in the rat insulinoma cell line (RIN 5fm) at a 1:0.5 molar ratio of concentration hIAPP (5μM): peptide (2.5μM).

Shi et al. developed a pentapeptide inhibitor, FLPNF and investigated its efficacy in inhibiting the accumulation of amyloid deposits.[88] ThT staining revealed that FLPNF exhibited an inhibitory effect on the generation of hIAPP amyloid deposits. FLPNF enhanced the cell survival of rat insulinoma cells by mitigating the cytotoxic effects of hIAPP. TEM images demonstrated that the addition of FLPNF (100μM) significantly reduced the quantity of fibril formation after 24 hours of incubation compared to hIAPP (10μM) alone in PBS.

Abioye et al. discovered three tetrapeptides that prevented hIAPP fibrillation: TNGQ, MANT, and YMSV.[89] The authors investigated the potential anti-fibrillation mechanism of

tetrapeptides using various methods, including ThT fluorescence testing, CD spectroscopy, dynamic light scattering (DLS), and molecular docking. The results from TEM, ThT fluorescence kinetics, and microscopy collectively indicated that TNGQ was the effective inhibitor of hIAPP fibrillization. ThT fluorescence kinetics, and TEM collectively demonstrated that TNGQ exhibited superior inhibitory efficacy, evident from the lack of typical hIAPP fibrillar structure. CD spectroscopy further indicated that TNGQ preserved the α-helical configuration of monomeric hIAPP. According to molecular docking, TNGQ and MANT bind to monomeric hIAPP surfaces more strongly than YMSV, which received the highest docking score but primarily interacts with the hIAPP core through hydrophobic contact formation. The highly polar TNGQ peptide proved to be most active as it appeared to prevent hIAPP fibrillation by separating already-formed hIAPP fibrils.

1.3 Alzheimer's disease

1.3.1 Introduction

AD stands as the most prevalent type of dementia and represents a neurodegenerative disorder (ND) characterized by the accumulation of neurotic plaques and neurofibrillary tangles. This accumulation leads to the buildup of Aβ peptide in the most affected region of the brain.[90] AD is marked by impairments in cognitive skills, language difficulties, memory problems, and abnormalities in the pulmonary and circulatory systems. These abnormalities result in a reduced supply of oxygen reaching the brain.[91] Many people with early-stage AD go undetected because of mild cognitive deficits may not noticeably interfere with day-to-day activities. Patients, family members, and healthcare professionals may misinterpret subtle changes as a natural part of ageing.[92] The symptoms of cognitive loss become more noticeable as the condition progresses into AD which interfere with everyday activities more frequently, and may lead individuals to seek medical assistance.[93]

AD typically advances gradually through three distinct phases: mild (initial stage), moderate (intermediate stage), and severe (last stage).[91] Individuals in the early stages of the mild phase often show no apparent symptoms and may appear unaffected. However, during this stage, the hippocampus area of the brain cells begins to deteriorate. Those with mild Alzheimer's dementia are more prone to making mistakes, misplacing items, and experiencing disorientation. In the intermediate stage, individuals may forget events from their own histories and require additional assistance with daily tasks such as dressing appropriately and

maintaining personal hygiene. Changes in personality, including heightened worry, suspicion, or impatience, may manifest. Recognition problems, even with close family members, can become apparent during this phase. The last stage of Alzheimer's dementia sees individuals entirely dependent on others for daily tasks like eating and using the restroom. This severe stage often involves challenges with basic communication skills, impairing the individual's ability to understand others or express their needs. In the advanced stage, complications from infections can become life-threatening. As of now, AD has no known cure, although there are therapies available to help manage the symptoms.

1.3.2 Statistics of AD

Presently, approximately 55 million individuals globally are documented to be living with dementia. By the year 2050, the number of people worldwide affected by AD is projected to reach 139 million, with the majority of those residing in low and middle-income nations.[94] Every three seconds, a new case of dementia is reported somewhere in the world. Globally, up to 75% of individuals with dementia go undiagnosed. One in four people believes that there is no preventive measure for dementia, and nearly 80% of the general public worries about developing dementia at some point. Additionally, approximately 62% of healthcare professionals worldwide mistakenly believe that dementia is an inevitable aspect of aging. According to the study, the projected lifetime risk for Alzheimer's dementia was 1 in 10 (10%) for men and 1 in 5 (20%) for women at the age of 45. The risks slightly increased for both sexes at the age of 65.[95] The analyzed global cost of dementia is estimated to be around US $1.3 trillion, and this figure is expected to double by the year 2030. The social and economic burden of AD is projected to witness a significant increase, primarily attributed to the aging of the global population.[96]

1.3.3 Aggregation mechanism of Aβ

The amyloid hypothesis emerged following extensive research that consistently demonstrated a distinct correlation between dementia and the deposition of β-sheet structures in the central nervous system.[97] As per the amyloid cascade hypothesis, the pathogenic factors in AD are considered to be Aβ aggregates, instigating a series of harmful physiological alterations leading to neurodegeneration, dementia, and ultimately, fatality.[98] The amyloid precursor protein (APP), expressed in various biological tissues and organs, including the brain, is responsible for the generation of Aβ peptides. APP is a type I membrane protein with three distinct splice

variants (APP695, APP751, and APP770), featuring a single transmembrane domain (TMD). The C-terminal domain of APP, referred to as the APP intracellular domain (AICD), is partially situated in the cytoplasm, while the N-terminal domain is located in the extracellular region. The processing of APP can occur through either amyloidogenic or non-amyloidogenic pathways, resulting in distinct outcomes (**Figure 1.6**). In the non-amyloidogenic pathway, the multidomain zinc metalloenzyme α-secretase initiates cleavage of APP between Lys687 and Leu688. This cleavage releases the soluble N-terminal fragment named as sAPP. Subsequently, γ-secretase cleaves the remaining membrane-bound fragment within the TMD of APP at either Val711/Ile712 or Ala713/Thr714, resulting in the production of $A\beta_{17-40}$ or $A\beta_{17-42}$.

Within the amyloidogenic pathway, APP undergoes initial cleavage by β-site amyloid precursor protein cleaving enzyme (BACE1). BACE1 cleaves between Met671 and Asp672, releasing the soluble fragment referred to as sAPPβ. The remaining membrane-bound C-terminal fragment (CTF) is subsequently cleaved by γ-secretase, predominantly yielding the amyloidogenic peptides $A\beta_{1-40}$ and $A\beta_{1-42}$.[99] Aβ peptides play a functional role for neurons. In AD, the fundamental biochemical change involves the abnormal accumulation of Aβ, initially in non-toxic and soluble amyloid peptide forms. This accumulation disrupts proteostasis and leads to the transformation of Aβ into toxic intermediate products, including misfolded soluble Aβs, Aβ dimers, and Aβ oligomers.[100] Both $A\beta_{1-40}$ and $A\beta_{1-42}$ peptides exhibit a propensity to aggregate, often forming oligomers and fibrils. Experimental trials have demonstrated the capacity of soluble Aβ oligomers extracted from AD affected brains to impact synapse plasticity and function.[101] Amyloid fibrils may function as a "reservoir" for oligomers, establishing an equilibrium between cytotoxic soluble oligomers and insoluble Aβ fibrils.[90a] Consequently, AD can be characterized as a "gain-of-toxic function" disorder linked to the toxicity of aggregated Aβ species.

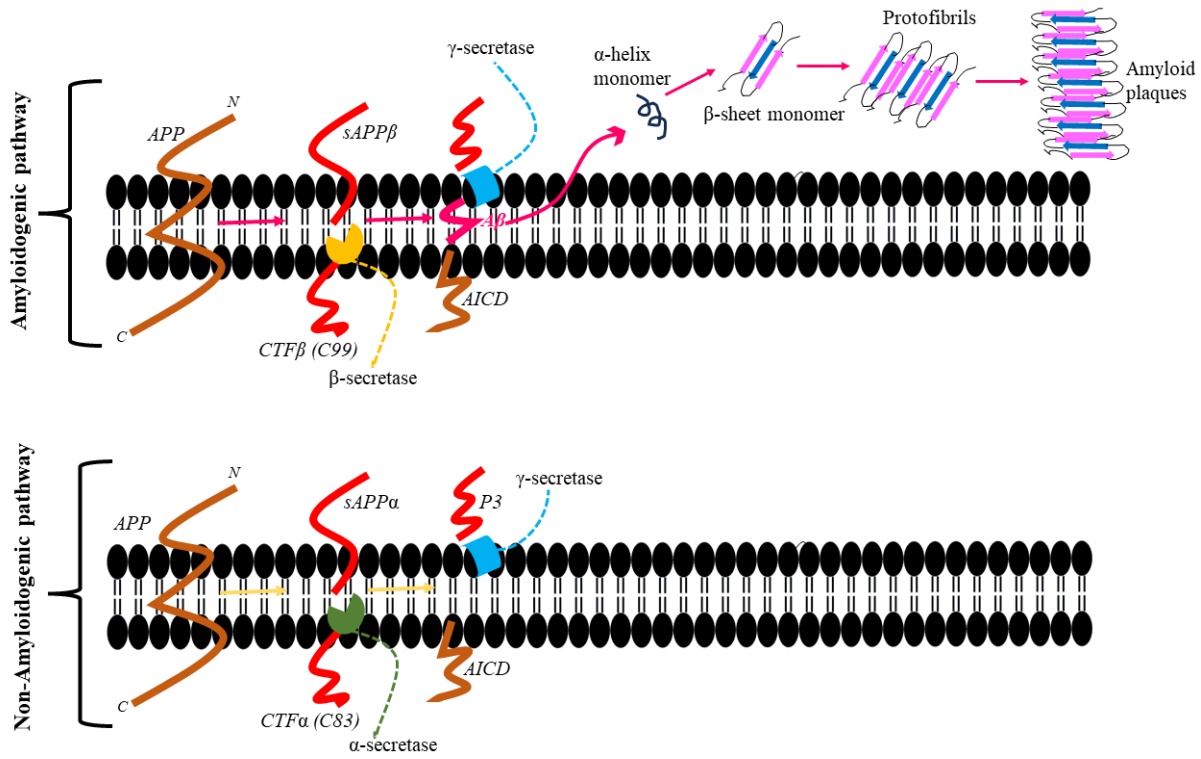

Figure 1.6: Schematic representation of the mechanism leading to the formation of Aβ plaques. The process involves the sequential cleavage of APP through amyloidogenic and non-amyloidogenic pathways.

The monomeric peptides, $A\beta_{1-40}$ and $A\beta_{1-42}$, primarily adopt an unfolded random coil morphology, with a small amount of α-helical and β-sheet content.[102] The Aβ peptide sequence exhibits polarity, featuring a hydrophilic N-terminus and a hydrophobic C-terminus. The residues in the C-terminus and central hydrophobic core (CHC), specifically Leu17−Ala21, are believed to play a crucial role in Aβ aggregation. Aggregated Aβ plaques are more prevalent in $A\beta_{1-42}$ compared to $A\beta_{1-40}$. $A\beta_{1-42}$ is more susceptible to aggregation than $A\beta_{1-40}$, likely due to the presence of two additional hydrophobic C-terminal residues. $A\beta_{1-42}$ is considered more harmful than $A\beta_{1-40}$ because it generates toxic oligomers at a faster rate.[99b]

1.3.4 Therapeutic strategies to prevent Aβ aggregation

The exploration of preventing protein self-assembly involves two main approaches: searching for inhibitors that specifically target amyloid aggregates and devising strategies to prevent protein aggregation in a broader sense. Numerous inhibitors and excipients are employed to eliminate Aβ aggregates using diverse strategies such as stabilizing the native state, destabilizing incorrectly folded states, reducing solvent accessibility, and accelerating protein folding. Currently, a widely researched potential therapeutic approach for AD is focused on

preventing the formation of oligomers and aggregates.[103] The drugs currently prescribed and approved by the Food and Drug Administration (FDA) serve as symptom relievers without offering a cure. Although these medications do not provide a definitive solution, they have shown effectiveness in modestly improving the cognitive abilities of individuals with AD. The only medication approved for modifying AD is aducanumab, an intravenous anti-amyloid antibody, which obtained FDA approval in June 2021.[104] Aducanumab seems to reduce the accumulation of amyloid in the brain, thereby slowing the progression of the disease in terms of both cognition and functionality. The European Medicines Agency, however, declined to approve the medication for use in Europe due to a lack of data supporting the actual efficacy of medication and some safety concerns. Therefore, to treat the pathogenesis of the AD, disease modifying treatments (DMTs) are required for AD.

1.3.4.1 Peptide based therapeutics against Aβ aggregation

Peptide-based approaches exhibit greater adaptability compared to other inhibitor categories, owing to the variety of naturally occurring amino acids, the range of backbone secondary structures, and the ease of modifying termini and side chains. Moreover, the amphiphilic nature of peptides enables easy interaction with the hydrophobic surfaces of amyloid proteins ensures strong water solubility. Peptides serve as biological active compounds, offering increased selectivity due to their ability to establish numerous contacts with their target. The highly selective interactions of peptides contribute to a reduction in cytotoxicity. Interest in peptide science is on the rise due to several factors, including the identification of therapeutic targets, advancements in delivery strategies, the production of extensive peptide libraries, synthetic viability and the development of high-throughput screening techniques.

Proteins and peptides have been explored as potential therapies for AD, although they are currently in the pre-clinical trial stage. An intranasal administration system was utilized to deliver either 20 IU or 40 IU of insulin detemir to adults diagnosed with mild to moderate AD.[105] Significant effects on verbal and visuospatial memory recall were observed for patients who received the higher insulin detemir dose. When administered orally in combination with pravastatin, the Ac-DWFKAFYDKVAEKFKEAF-NH_2 (D-4F) peptide demonstrated the ability to reduce Aβ deposition and activate microglia and astrocytes, while simultaneously enhancing cognitive function in the brains of mice.[106] The progression of peptide inhibitors targeting amyloid fibrils is anticipated to make significant strides in the coming years. Below,

we briefly discuss some of the prominent families of peptide-based inhibitors that have been published in the last decade. Comprehensive details on peptide-based inhibitors can be found in the latest reviews available in literature.[107]

I. Peptide inhibitors derived from Aβ sequences

Harkány et al. reported propionyl-Ile-Ile-Gly-Leu amide (Pr-IIGL) derived from the C-terminal region (31–35) of Aβ peptide as an inhibitor of $A\beta_{42}$ aggregation.[108] Pr-IIGL protected glial cells from cytotoxicity induced by $A\beta_{42}$ aggregates, however, it displayed neurotoxicity. Fülöp et al. modified Pr-IIGL by replacing propionyl with arginine to afford a new pentapeptide $RIIGL_a$, which is not neurotoxic and blocked Aβ amyloid formation as well as reduced the cytotoxicity caused by Aβ aggregates.[109] The transmission electron microscopy (TEM) images depicted the formation of mature fibers of length 2–3 μm when the $A\beta_{42}$ monomer was incubated alone, whereas the fibril formation was completely inhibited when RIIGL was incorporated in $A\beta_{42}$ monomer. Notably, the cell viability of SHSY-5Y neuroblastoma cells was increased from 39% in $A\beta_{42}$ monomer alone to 84% when the $A\beta_{42}$ monomer was co-incubated with RIIGL.

Among the peptide inhibitors derived from the Aβ sequence, ^{16}KLVFF^{20} and its mimics have gained significant popularity. Recent research has focused on modifying KLVFF to enhance its inhibitory effectiveness and explore other functional applications due to its high affinity for Aβ.[110] Austen et al. developed a series of peptides derived from $A\beta_{16\text{-}20}$ with enhanced water solubility, including OR1 (RGKLVFFGR) and OR2 (RGKLVFFGR-NH2).[32] While both peptides were identified as effective inhibitors of fibrillation, only OR2 was able to halt the production of oligomers and prevent amyloidogenic cytotoxicity. Jagota et al. formulated three short synthetic D-peptides based on the CHC region with the aim of diminishing the toxicity and aggregation of $A\beta_{42}$.[111] Thioflavin T (ThT) and turbidity assays illustrated that peptides kklvffa and klvffarrrra reduce fibrillation by encouraging aggregation into insoluble amorphous structures.

Tillett et al. produced N-aminated hexapeptides derived from KLVFFA, demonstrating the ability to impede the fibrillization of.[112] Among designed peptides, a di-aminated derivative of the hexapeptide, Ac-KL-aVF-aFA-NH2, featuring N-amination on Val and a second on Phe, was identified as the most potent inhibitor of $A\beta_{42}$.

Kapadia et al. investigate the effect of sequential amino-acid scan and C-terminus amidation on C-terminus fragment ($VVIA_{39-42}$) of $A\beta_{42}$ sequence.[113] D-FVIA-NH_2 (12c) exhibited high protection against Aβ-mediated neurotoxicity by inhibiting Aβ aggregation in the MTT cell viability and ThT-fluorescence assay. Circular dichroism (CD) studies illustrate the inability of $A\beta_{42}$ to form β-sheet in the presence of 12c. Peptide 12c exhibited 78% inhibition of $A\beta_{42}$ even at a lowest tested dose of 0.1 mM. The peptide 12c exhibits enhanced blood brain barrier (BBB) permeation, no cytotoxicity along with prolonged proteolytic stability. Samani et al. conducted a comparison of the impact of halogenated amino acids on the anti-aggregation properties of peptides.[114] Their findings indicate that an iodinated peptide with an amide at the C-terminus, H_2N-KLVFF(4-I)-$CONH_2$, exhibited superior inhibitory activity against Aβ aggregation compared to the NH_2-KLVFF-COOH peptide.

Subsequently, Kapadia et al. designed and synthesized thirty-eight tetrapeptides derived from the C-terminus segment $A\beta_{39-42}$ of the original Aβ peptide by sequential replacement/modification.[115] The ThT fluorescence assay revealed that F-(4-F)-VIA, V-octahyrdoindole-IA, tert.L-tert.L-IA peptides exhibited significant protection against neurotoxicity induced by $A\beta_{42}$ aggregation in PC-12 cells at dosages ranging from 10μM to 0.1μM. Additionally, CD analysis indicated that F-(4-F)-VIA, V-octahyrdoindole-IA peptides prevented the formation of β-sheets, and electron microscopy confirmed the absence of fibrillar $A\beta_{42}$ structures, supporting the inhibition of $A\beta_{42}$ aggregation.

Mallesh et al. synthesized fourteen hydrophobic peptides each incorporating a single mutation valine with hydrophobic residues such as leucine and proline in the $K^{16}LVFFAE^{22}$ sequence of $A\beta_{42}$.[116] The authors identified the peptides H_2N-KLLFFA-NH_2 (NT-02), H_2N-KLLFF-NH_2 (NT-03), and H_2N-LPFFAE-NH_2 (NT-13), which are more potent than the other peptides. The NT peptides reduce Aβ fibrillation in the range of 60–80% observed in the ThT assay. In the cellular system, the peptides are noncytotoxic and show a significant neuroprotection effect (85–90%) from Aβ-induced toxicity and protects the neurons from Aβ-induced apoptosis. Moreover, the peptides NT-02, NT-03, and NT-13 can cross the BBB, have significant stability in serum, and maintain healthy morphology of PC-12-derived neurons.

Zimbone et al. investigated the efficacy of the Aβ fragment SGYEVHHQKLVFF ($A\beta_{8-20}$) in averting the aggregation and toxicity of $A\beta_{40}$ and $A\beta_{42}$.[117] CD experiments spanning a 96-hour period demonstrate that $A\beta_{8-20}$ assumes a random coil conformation over time. When present

in a 1:1 concentration ratio, $A\beta_{8-20}$ effectively halts $A\beta_{40}$ aggregation and prevents the transition from random coil to β-sheet structure following a 24-hour incubation period. In DLS experiment two distinct populations were observed for $A\beta_{40}$ alone and in the presence of $A\beta_{8-20}$, with mean hydrodynamic diameters centered at 1663 nm and 102.7 nm respectively, for $A\beta_{40}$ alone, and at 850.3 nm and 188.7 nm for $A\beta_{40}$ in the presence of $A\beta_{8-20}$. Furthermore, $A\beta_{8-20}$ demonstrated complete protection, in a dose-dependent manner, of SH-SY5Y cells against the toxicity induced by $A\beta_{42}$ oligomers.

II. Rationally designed peptide inhibitors

Rational design yields highly functional compounds and resulted in the generation of a larger number of synthetic amino acid sequences, peptide-conjugate derivatives and peptidomimetics. Many designs aim to mimic beneficial characteristics of the Aβ sequence, such as hydrophobicity, the tendency to form β-sheet conformation, and the ability to increase selectivity and binding affinity for Aβ.

Xue et al. identified the versatile heptapeptide XD4 (PIKTLPM) through phage screening, with the sequence present in 18 out of 30 positive clones exhibiting high affinity for $A\beta_{42}$.[118] XD4, at a 1:10 ($A\beta_{42}$: XD4) molar ratio, effectively inhibits $A\beta_{42}$-induced cytotoxicity in SH-SY5Y cells and demonstrates dose-dependent binding to $A\beta_{42}$. XD4 also reduces harmful levels of ROS, NO (at a 1:10 molar ratio), and Ca^{2+} (at 1:1 or 1:10 molar ratios). Furthermore, XD4 significantly enhances memory impairments and facilitates Aβ clearance in APP/PS1 transgenic mice.

Li et al. investigated the binding affinity of 8000 tripeptides, representing all possible combinations of amino acids in tripeptides against protofibril model ($6A\beta_{9-40}$) using the Autodock Vina method.[119] The top hits identified through virtual screening were subjected to further analysis using the more precise MM-PBSA method, which indicated that WWW, WPW, WWP, and PWW exhibited the strongest binding ability to Aβ fibrils. The binding and depolymerization abilities of the top leads were demonstrated through *in vitro* studies, such as ThT assays and AFM. The ThT assay revealed the ability of tripeptides selected as top leads (WWW, PWW, WPW, and WWP) to depolymerize Aβ fibrils depends on their concentration. At the highest tripeptide concentration tested (1 mM), a significant decrease in fluorescence intensity compared to that of Aβ fibrils alone was detected. Tripeptides PWW, WWP, and

WWW exhibited the highest disassembly activities, corresponding to the lowest fluorescence intensities, with a depolymerization efficacy of 83%.

Bansal et al. designed 42 new peptides derived from the C-terminus of $A\beta_{32–37}$ underwent a comprehensive peptide scan.[120] This scan entailed substituting all six amino acids with isosterically analogous amino acids of both natural and unnatural origin. Among designed peptides, the N-terminus free hexapeptide, IGLMVG-NH_2 (referred to as peptide 1), was found to effectively shield cells from $A\beta_{40}$-induced toxicity at a concentration of 2μM. In the presence of peptide 1, RFU values of 35.2%, 33.8%, and 38.6% were observed at Aβ:peptide ratios of 1:10, 1:5, and 1:1, respectively, corresponding to approximately 97.6%, 99.7%, and 92.5% inhibition of $A\beta_{40}$ aggregation.

Zhang et al. identified, synthesized, and evaluated a novel Cu^{2+}-binding peptide that specifically hindered Cu-triggered Aβ aggregation using the phage display technique.[121] The Cu^{2+}-binding hexapeptide (S-A-Q-I-A-P-H, named as PCu) discovered from the phage display library was employed to investigate the mechanism of PCu inhibition against Aβ production and Cu^{2+}-mediated Aβ aggregation. *In vitro* results revealed a reduction in Aβ aggregation caused by Cu^{2+} in the presence of PCu, and copper levels were regulated to mitigate biological toxicity. Furthermore, PCu inhibited Cu^{2+}-induced BACE1 expression and enhanced Cu^{2+}-mediated cell oxidative damage to reduce Aβ production.

Yuan and collaborators introduced a novel decapeptide RR (Ac-RYYAAFFAARR-NH_2) designed to disrupt β-sheets synergistically by binding multiple recognition sites along the $A\beta_{40}$ sequence.[122] RR targeted the specific residues His13 and His14 of Aβ, the CHC region, and the salt bridge between Asp23 and Lys28. RR demonstrated highly specific affinity for binding monomeric $A\beta_{40}$, nearly 100 times stronger than the LPFFD peptide (K_D = 1.10 vs. 156μM, respectively). ThT assay results showed that RR efficiently inhibited $A\beta_{40}$ aggregation in a dose-dependent manner. In MTT assay, RR exhibited the ability to protect PC-12 cells against $A\beta_{40}$-mediated cytotoxicity, enhancing cell viability to approximately 95%.

Ghosh et al. engineered NF11 (NAVRWSLMRPF), a nontoxic peptide derived from the modified SARS coronavirus E-protein, known for its inhibition of insulin fibrillation.[123] NF11 demonstrated the ability to dose-dependently suppress the aggregation of $A\beta_{40}$, prolonging the aggregation lag-time. The lag time of $A\beta_{40}$ fibrillation was extended by approximately fourfold in the presence of NF11 at a 1:10 molar ratio. ThT experiment results indicated that NF11

disintegrated Aβ oligomers and fibrils, reducing amyloid-related toxicity in neuronal cells. Incubation with NF11 significantly reduced the extent of Aβ fibrillation, restraining it in its oligomeric state which was observed in the morphology of spherical conglomerates in fluorescence microscopy images.

Jha et al. designed a structurally constrained cyclic peptide by incorporating an unnatural amino acid and a disulfide bond into the sequence β-sheet breaker peptide CVKVDPGLKVC (BHdS).[124] This peptide incorporates the DPro-Gly motif, featuring the unnatural amino acid DPro, strategically positioned to enhance proteolytic stability and induce a turn in the β-hairpin structure. Results from UV-CD spectroscopy indicate that BHdS stabilizes the random coil conformation of $A\beta_{42}$ monomers, preventing their transition into a β-sheet-rich conformation conducive to ordered assembly during aggregation. When $A\beta_{42}$ is co-incubated with BHdS at molar ratios of 1:10, 1:20, and 1:25, the amplitude of ThT fluorescence decreases by approximately 70%, 40%, and 20%, respectively, compared to that observed without BHdS peptide. Additionally, BHdS peptide demonstrates the ability to mitigate the toxicity of soluble $A\beta_{42}$ aggregates towards neuronal cells.

Kapadia et al. investigated the effect of sequential amino-acid scan and C-terminus amidation on C-terminus fragment (VVIA) of Aβ sequence.[125] D-FVIA-NH_2 (12c) exhibited high protection against Aβ-mediated neurotoxicity by inhibiting $A\beta_{42}$ aggregation in the MTT cell viability and ThT-fluorescence assay. CD studies illustrate the inability of Aβ to form β -sheet in the presence of 12c, further confirmed by the absence of $A\beta_{42}$ fibrils in electron microscopy experiments. Peptide 12c exhibited 78% inhibition of $A\beta_{42}$ even at a lowest tested dose of 0.1 mM. The peptide 12c exhibits enhanced BBB permeation, no cytotoxicity along with prolonged proteolytic stability.

Bhattacharyya et al. identified an active peptide fragment derived from the plant *Aristolochia indica* that exhibits inhibitory effects on Aβ aggregation and demonstrates anti-amyloidogenic properties.[126] *In vitro* studies, supported by microscopic images, revealed that the active peptide, denoted as P_{active} (GFLLHQK), hinders the formation of off-route oligomers in the Aβ peptide, thereby preventing their involvement in the cytotoxic fibrillation pathway. Biolayer interferometric tests provided evidence of significant affinity between P_{active} and both $A\beta_{42}$ monomers and Aβ oligomers. MD simulations focusing on the $A\beta_{42}$ monomer structure elucidated substantial conformational changes occurring in the presence of P_{active}. Notably, the

conformational alteration of Tyr10 in the $A\beta_{42}$ structure was observed, rendering it exposed toward the solvent surface. The combined analysis of NMR spectroscopy and MD simulations validated the role of P_{active} in inducing global conformational changes in Aβ monomers during complex formation.

Lei and colleagues strategically designed a polymer-grafted peptide-based multifunctional micelle system, known as MPGLT for the simultaneous clearance of Aβ and ROS.[127] The MPGLT incorporated three functional peptides—a ROS scavenger (tk-GSH), a β-sheet breaker (LP), and an autophagy activator (TK)—each binding to Aβ and promoting Aβ degradation. The tk-GSH on the surface of MPGLT effectively scavenged intracellular ROS, reducing cytotoxicity from both ROS and Aβ. *In vivo* animal studies demonstrated that MPGLT successfully crossed the BBB, reduced Aβ plaque and eliminated ROS in an AD mouse model.

1.4 Recent computational studies related to peptide inhibitor that target Aβ and hIAPP

Over the last two decades, there have been notable advancements in computer techniques for simulating biological macromolecules. In computer-aided drug design (CADD), computational studies play a pivotal role in the rational design and optimization of potential drug candidates.[128] Through the utilization of advanced algorithms and molecular modeling techniques, researchers can analyze the interactions between inhibitors and target proteins at the atomic level. Virtual screening methods allow for the efficient identification of potential drug candidates from large chemical libraries, significantly expediting the drug discovery process. Molecular dynamics simulations provide insights into the dynamic behavior of biomolecular systems, aiding in the understanding of ligand binding mechanisms and predicting the stability of drug-target complexes. Additionally, structure-based drug design enables the modification and refinement of lead compounds to enhance their binding affinity and specificity. Overall, computational studies in computer-aided drug design contribute valuable information to guide experimental efforts, ultimately accelerating the development of novel and effective therapeutic agents. Below, we briefly discuss some well-known families of peptide-based inhibitors generated using CADD that have been published in recent years.

Kanchi et al. engineered the peptide KLVFFP5, comprising two segments: a fragment derived from the self-recognition region $K_{16}LVFF_{20}$ and a β-sheet breaker proline pentamer P5.[129] MD simulations and molecular docking analyses revealed that the KLVFFP5 peptide effectively bound to protofibrils, exerting destabilizing effects by establishing hydrogen bonds and

hydrophobic contacts with greater affinity compared to the KLVFF peptide. The presence of KLVFFP5 led to a significant disruption of the hydrogen bonding network and salt bridges, resulting in a notable reduction in the β-sheet content of Aβ protofibrils.

Wu et al. conducted MD simulations on model mixtures containing $A\beta_{42}$ and $A\beta_{40}$ peptides along with somatostatin-14 (SST14), a cyclic neuropeptide, to investigate the dynamics of early-stage aggregation.[130] Additionally, they explored the aggregation of $A\beta_{42}$ in the presence of arginine vasopressin (AVP), another distinct cyclic neuropeptide. The $A\beta_{42}$-SST14 mixture exhibited the formation of compacted, dynamically stable, yet small aggregates, characterized by the highest exposure of hydrophobic residues to the solvent. SST14 demonstrated inhibitory effects on aggregation in the $A\beta_{42}$-SST14 system, leading to aggregates with a more robust adhesive surface effect.

Jani et al. investigated the destabilization mechanism of various β-sheet breaker peptides on preformed amyloid protofibrils through molecular docking and simulation.[131] Eight BSB peptides with varying lengths (5-mer to 10-mer) were docked onto the Aβ protofibril. Multiple sets of MD simulations were conducted for the Aβ protofibril alone and in the presence of BSB peptides to achieve more comprehensive results. The destabilization of the Aβ protofibril by BSB peptides was evidenced by an increase in root-mean-square deviation (RMSD), a decrease in the number of interchain hydrogen bonds, disruption of significant salt bridge contacts (D23-K28), and destabilization of interchain hydrophobic contacts. To assess the binding affinities of BSB peptides to the Aβ protofibril, the MM-GBSA free energy of binding was computed for each BSB peptide. Additionally, the contribution of the binding free energy was estimated for each residue. The study indicated that, compared to other BSB peptides, 7-mer peptides had a greater tendency to robustly attach to the Aβ protofibril. Among the BSB peptides, the KKLVFFA peptide exhibited a higher potential for destabilizing Aβ protofibrils.

Kanchi et al. designed a β-sheet breaker peptide, LPFFD, and modified it with aromatic amino acids to investigate its impact on Aβ fibrils using MD simulation studies.[132] The modified peptides comprised two sequences: the β-sheet breaker motif LPFFD and aromatic residues at the termini that bind to the fibrils. The findings revealed that LPFFD peptides with tryptophan modifications displayed the highest binding affinities with Aβ fibrils. Additionally, these peptides bound to the region encompassing the CHC region of the Aβ fibrils.

Jarmuła et al. conducted MD simulations of three β-sheet breaker peptides (iaβ6, LPFFFD; iaβ5, LPFFD; and iaβ6_Gly, LPFGFD) with the fibril model of $A\beta_{42}$.[133] They investigated the kinetically probable mechanism of action for these proposed peptides. The suggested mechanism involves the binding of these peptides to the region (LVFFA), which is the CHC region of the Aβ fibril, and the participation of Phe rings in π-π stacking interactions with the Aβ fibril. Extended MD runs of iaβ6 poses demonstrated the disruption of the Aβ fibril and the dissociation of chain A from the fibril model of $A\beta_{42}$. The authors concluded that the presence of three successive Phe residues in the BSB peptide, docked at Phe 20 in the CHC region, enhances the efficacy of dissociating the outer chain.

Roy et al. conducted all-atom MD simulations to investigate the mechanism by which D-nl peptide, derived from the amyloidogenic core of $hIAPP_{22–27}$ and consisting of all D-amino acid residues, prevents hIAPP aggregation.[134] Their findings indicate that the ordered β-sheet structure of $hIAPP_{22–27}$ is completely destabilized upon incorporation of D-nl. In the presence of D-nl peptides, full-length hIAPP is less prone to form β-sheet structures, leading to a more frequently adopted randomly loosely packed structure. The study also explored the impact of $hIAPP_{22–27}$ (L-nl) on the aggregation tendency of full-length hIAPP as a control. D-nl prevents hIAPP-hIAPP association through hydrogen bonding and hydrophobic contacts, supporting the self-aggregation of hIAPP, while L-nl promotes hIAPP aggregation by stabilizing β-sheet-rich aggregates. Additionally, D-nl partially dissolves the hIAPP protofibrils that have already formed.

Roy et al. conducted MD simulations to illustrate that newly designed conformationally restricted BSBHps effectively inhibit hIAPP amyloid production.[135] The BSBHps are peptide sequences consisting of six members, which are derived from the amyloidogenic core of hIAPP ($N_{22}FGAIL_{27}$). These sequences contain one (Ile26) or more (Gly24 and Ile26) residues that can be substituted with one of three isomers of the conformationally restricted aromatic amino acid, aminobenzoic acid (β, γ, and δ). This substitution allows for the generation of the BSBHps. All the different isomeric BSBHps exert divergent effects on the self-assembly of hIAPP. BSBHps containing β- and γ-aminobenzoic acid effectively prevent hIAPP aggregation, while those with the δ-aminobenzoic group stabilize the hIAPP β-sheet-rich aggregates. The planar structure of δ-BSBHps facilitates a distinctive stacking arrangement involving constrained aminobenzoic acids(Abz)/Phe residues of BSBHps and Phe residues of hIAPP, thereby stabilizing the β-sheet structure of hIAPP. Specifically, the double-substituted

δ-BSBHp interacts selectively with the amyloidogenic region of hIAPP, encompassing Ser20-Ser29. This underscores the preference of δ-BSBHp for binding to the β-sheet-prone region of hIAPP.

Mohammed et al. employed molecular docking and MD simulations to investigate how D-Trp-Aib inhibits the early oligomerization and destabilizes preformed Aβ protofibrils.[136] MD simulations unveiled that D-Trp-Aib binds to the aggregation-prone region (Lys16-Glu22), leading to the stabilization of the Aβ monomer through π-π stacking interactions between Tyr10 and the indole ring of D-Trp-Aib. This interaction results in a decrease in β-sheet content and an increase in α-helices. Additionally, the binding of Lys28 of the Aβ monomer to D-Trp-Aib is likely responsible for obstructing initial nucleation, potentially impeding fibril growth and elongation. The robust binding of D-Trp-Aib to the aromatic region and the basic residue Lys28 of the Aβ monomer hinders the formation of a crucial salt bridge (Asp23-Lys28), a significant step in fibril formation.

1.5 References

1. Willbold, D.; Strodel, B.; Schröder, G. F.; Hoyer, W.; Heise, H. Amyloid-type protein aggregation and prion-like properties of amyloids. *Chem. Rev.* **2021**, *121*, 8285–8307.

2. (a) Ilie, I. M.; Caflisch, A. Simulation studies of amyloidogenic polypeptides and their aggregates. *Chem. Rev.* **2019**, *119*, 6956–6993; (b)Riek, R.; Eisenberg, D. S. The activities of amyloids from a structural perspective. *Nature* **2016**, *539*, 227−235.

3 Merlini, G.; Bellotti, V. Molecular mechanisms of amyloidosis. *N. Engl. J. Med.* **2003**, *349*, 583−596.

4. (a) Chiti, F.; Dobson, C. M. Protein misfolding, functional amyloid, and human disease. *Annu. Rev. Biochem*. **2006**, *75*, 333−366; (b) Benson, M. D.; Buxbaum, J. N.; Eisenberg, D. S.; Merlini, G.; Saraiva, M. J. M.; Sekijima, Y.; Sipe, J. D.; Westermark, P. Amyloid nomenclature 2018: recommendations by the International Society of Amyloidosis (ISA) nomenclature committee. *Amyloid* **2018**, *25*, 215−219; (c) Breydo, L.; Wu, J. W.; Uversky, V. N., α-Synuclein misfolding and Parkinson's disease. *Biochim. Biophys. Acta* **2012**, *1822*, 261−285.

5. (a) Cohen, F. E.; Kelly, J. W. Therapeutic approaches to protein-misfolding diseases. *Nature* **2003**, *426*, 905−909; (b) Rochet, J. C.; Lansbury Jr, P. T. Amyloid fibrillogenesis: themes and variations. *Curr. Opin. Struct. Biol.* **2000**, *10*, 60–68.

6. (a) Haass, C.; Selkoe, D. J. Soluble protein oligomers in neurodegeneration: lessons from the Alzheimer's amyloid β-peptide. *Nat. Rev. Mol. Cell Biol.* **2007**, *8*, 101–112; (b) Benilova, I.; Karran, E.; De Strooper, B. The toxic Aβ oligomer and Alzheimer's disease: an emperor in need of clothes. *Nat. Neurosci.* **2012**, *15*, 349–357; (c) Flagmeier, P.; De, S.; Wirthensohn, D. C.; Lee, S. F.; Vincke, C.; Muyldermans, S.; Knowles, T. P.; Gandhi, S.; Dobson, C. M.; Klenerman, D. Ultrasensitive measurement of Ca^{2+} influx into lipid vesicles induced by protein aggregates. *Angew. Chem. Int. Ed.* **2017**, *56*, 7750–7754; (d) Fusco, G.; Chen, S. W.; Williamson, P. T.; Cascella, R.; Perni, M.; Jarvis, J. A.; Cecchi, C.; Vendruscolo, M.; Chiti, F.; Cremades, N.; Ying, L. Structural basis of membrane disruption and cellular toxicity by α- synuclein oligomers. *Science* **2017**, *358*, 1440–1443.

7. (a) Dobson, C.M. Protein misfolding, evolution and disease. *Trends Biochem. Sci.* **1999**, *24*, 329–332; (b) Dobson, C.M. Protein folding and misfolding. *Nature* **2003**, *426*, 884–890.

8. (a) Frieden, C. Protein aggregation processes: in search of the mechanism. *Protein Sci.* **2007**, *16*, 2334–2344; (b) Buell, A. K.; Dobson, C. M.; Knowles, T. P. J. The physical chemistry of the amyloid phenomenon: thermodynamics and kinetics of filamentous protein aggregation. *Essays Biochem.* **2014**, *56*, 11–39; (c) Jarrett, J. T.; Lansbury, P. T. Amyloid fibril formation requires a chemically discriminating nucleation event: studies of an amyloidogenic sequence from the bacterial protein OsmB. *Biochemistry* **1992**, *31*, 12345–12352; (d) Gosal, W. S.; Morten, I. J.; Hewitt, E. W.; Smith, D. A.; Thomson, N. H.; Radford, S. E. Competing pathways determine fibril morphology in the self-assembly of 2-microglobulin into amyloid. *J. Mol. Biol.* **2005**, *351*, 850–864.

9. (a) Cohen, S. I. A.; Vendruscolo, M.; Dobson, C. M.; Knowles, T. P. J. From macroscopic measurements to microscopic mechanisms of protein aggregation. *J. Mol. Biol.* **2012**, *421*, 160–171; (b) So, M.; Hall, D.; Goto, Y. Revisiting supersaturation as a factor determining amyloid fibrillation. *Curr. Opin. Struct. Biol.* **2016**, *36*, 32–39; (c) Djikaev, Y. S.; Ruckenstein, E. Model for the nucleation mechanism of protein folding. *J. Phys. Chem. B* **2007**, *111*, 886–897; (d) Serio, T. R.; Cashikar, A. G.; Kowal, A. S.; Sawicki, G. J.; Moslehi, J. J.; Serpell, L.; Arnsdorf, M. F.; Lindquist, S. L. Nucleated conformational conversion and the replication of conformational information by a prion determinant. *Science* **2000**, *289*, 1317–1321.

10. (a) Ferrone, F. Analysis of protein aggregation kinetics. *Methods Enzymol.* **1999**, *309*, 256–274; (b) Morris, A. M.; Watzky, M. A.; Finke, R. G. Protein aggregation kinetics, mechanism, and curve-fitting: a review of the literature. *Biochim. Biophys. Acta* **2009**, *1794*, 375–397.

11. (a) Arosio, P.; Knowles, T. P. J.; Linse, S. On the lag phase in amyloid fibril formation. *Phys. Chem. Chem. Phys*. **2015**, *17*, 7606–7618; (b) Harper, J. D.; Lansbury, P. T. Models of amyloid seeding in Alzheimer's disease and scrapie: mechanistic truths and physiological consequences of the time-dependent solubility of amyloid proteins. *Annu. Rev. Biochem.* **1997**, *66*, 385–407; (c) O'Nuallain, B.; Shivaprasad, S.; Kheterpal, I.; Wetzel, R. Thermodynamics of Aβ(1-40) amyloid fibril elongation. *Biochemistry* **2005**, *44*, 12709–12718.

12. (a) Jarrett, J. T.; Lansbury, P. T. Seeding 'one-dimensional crystallization' of amyloid: a pathogenic mechanism in Alzheimer's disease and scrapie? *Cell* **1993**, *73*, 1055−1058; (b) Come, J. H.; Lansbury, P. T. Predisposition of prion protein homozygotes to Creutzfeldt-Jakob disease can be explained by a nucleation-dependent polymerization mechanism. *J. Am. Chem. Soc.* **1994**, *116*, 4109−4110.

13. (a) Onuchic, J. N.; Wolynes, P. G. Theory of protein folding. *Curr. Opin. Struct. Biol.* **2004**, *14*, 70–75; (b) Bryngelson, J. D.; Onuchic, J. N.; Socci, N. D.; Wolynes, P. G. Funnels, pathways, and the energy landscape of protein folding: a synthesis. *Proteins* **1995**, *21*, 167–195; (c) Dill, K. A.; Chan, H. S. From Levinthal to pathways to funnels. *Nat. Struct. Mol. Biol.* **1997**, *4*, 10–19.

14. Onuchic, J. N.; Socci, N. D.; Luthey-Schulten, Z.; Wolynes, P. G. Protein folding funnels: the nature of the transition state ensemble. *Fold. Des.* **1996**, *1*, 441**–**450.

15. Hartl, F.; Hayer-Hartl, M. Converging concepts of protein folding *in vitro* and *in vivo. Nat. Struct. Mol. Biol*. **2009**, *16*, 574–581.

16. Clark, P. L. Protein folding in the cell: reshaping the folding funnel. *Trends Biochem. Sci.* **2004,** *29*, 527–534.

17. (a) Reynolds, N. P.; Adamcik, J.; Berryman, J. T.; Handschin, S.; Zanjani, A. A. H.; Li, W.; Liu, K.; Zhang, A.; Mezzenga, R. Competition between crystal and fibril formation in molecular mutations of amyloidogenic peptides. *Nat. Commun.* **2017**, *8*, 1338–1348; (b)Adamcik, J.; Mezzenga, R. Angew. Amyloid polymorphism in the protein folding and

aggregation energy landscape. *Angew. Chem. Int. Ed.***2018**, *57*, 8370–8382; (c) Ke, P. C.; Zhou, R.; Serpell, L. C.; Riek, R.; Knowles, T. P.; Lashuel, H. A.; Gazit, E.; Hamley, I. W.; Davis, T. P.; Fändrich, M.; Otzen, D. E. Half a century of amyloids: past, present and future. *Chem. Soc. Rev.* **2020**, *49*, 5473–5509.

18. (a) Popiel, H. A.; Takeuchi, T.; Burke, J. R.; Strittmatter, W. J.; Toda, T.; Wada, K.; Nagai, Y. Inhibition of protein misfolding/aggregation using polyglutamine binding peptide QBP1 as a therapy for the polyglutamine diseases. *Neurotherapeutics* **2013**, *10*, 440–446; (b) Rajasekhar, K.; Suresh, S. N.; Manjithaya, R.; Govindaraju, T. Rationally designed peptidomimetic modulators of Aβ toxicity in Alzheimer's disease. *Sci. Rep.* **2015**, *5*, 8139–8148; (c) Loureiro, J. A.; Crespo, R.; Börner, H.; Martins, P. M.; Rocha, F. A.; Coelho, M.; Pereira, M. C.; Rocha, S. Fluorinated beta-sheet breaker peptides. *J. Mater. Chem. B* **2014**, *2*, 2259–2264.

19. Lansbury, P. T.; Lashuel, H. A. A century-old debate on protein aggregation and neurodegeneration enters the clinic. *Nature* **2006**, *443*, 774–779.

20. (a) Ono, K.; Yamada, M. Vitamin A potently destabilizes preformed alpha-synuclein fibrils *in vitro*: implications for Lewy body diseases. *Neurobiol. Dis.* **2007**, *25*, 446–454; (b) Yatin, S. M.; Varadarajan, S.; Butterfield, D. A. Vitamin E prevents Alzheimer's amyloid β-peptide(1-42)-induced neuronal protein oxidation and reactive oxygen species production. *J. Alzheimer's Dis.* **2000**, *2*, 123–131; (c) Liu, Z.; Zhou, T.; Ziegler, A.C.; Dimitrion, P.; Zuo, L. Oxidative stress in neurodegenerative diseases: from molecular mechanisms to clinical applications. *Oxid. Med. Cell. Longev.* **2017**, *2017*, 2525967; (d) Brieger, K.; Schiavone, S.; Miller, F.J.; Krause, K. H. Reactive oxygen species: from health to disease. *Swiss Med. Wkly.* **2012**, *142*, w13659; (e) Lobo, V.; Patil, A.; Phatak, A.; Chandra, N. Free radicals, antioxidants and functional foods: impact on human health. *Pharmacogn. Rev.* **2010**, *4*, 118–126.

21. (a) Choudhary, S.; Kishore, N.; Hosur, R. V. Inhibition of insulin fibrillation by osmolytes: Mechanistic insights. *Sci. Rep.* **2015**, *5*, 17599–17609; (b) Dasgupta, M.; Kishore, N. Selective inhibition of aggregation/fibrillation of bovine serum albumin by osmolytes: Mechanistic and energetics insights. *PLoS One* **2017**, *12*, e0172208; (c) Venkatraman, A.; Murugan, E.; Lin, S. J.; Peh, G. S. L.; Rajamani, L.; Mehta, J. S. Effect of osmolytes on *in-vitro* aggregation properties of peptides derived from TGFBIp. *Sci. Rep.* **2020**, *10*, 4011–4023.

22. (a) Goldberg, M. E.; Expert-Bezançon, N.; Vuillard, L.; Rabilloud, T. Non-detergent sulphobetaines: a new class of molecules that facilitate *in vitro* protein renaturation. *Fold. Des.* **1996**, *1*, 21–27; (b) Vuillard, L.; Rabilloud, T.; Goldberg, M. E. Interactions of non-detergent sulfobetaines with early folding intermediates facilitate *in vitro* protein renaturation. *Eur. J. Biochem.* **1998**, *256*, 128–135; (c)Wangkanont, K.; Forest, K. T.; Kiessling, L. L. The non-detergent sulfobetaine-201 acts as a pharmacological chaperone to promote folding and crystallization of the type II TGF-β receptor extracellular domain. *Protein Expr. Purif.* **2015**, *115*, 19–25; (d) Expert-Bezançon, N.; Rabilloud, T.; Vuillard, L.; Goldberg, M. E. Physical–chemical features of non-detergent sulfobetaines active as protein-folding helpers. *Biophys. Chem.* **2003**, *100*, 469–479; (e) Hagihara, M.; Takei, A.; Ishii, T.; Hayashi, F.; Kubota, K.; Wakamatsu, K.; Nameki, N. Inhibitory effects of choline-O-sulfate on amyloid formation of human islet amyloid polypeptide. *FEBS Open Bio.* **2012**, *2*, 20–25.

23. (a) Gaeta, A.; Hider, R. C. The crucial role of metal ions in neurodegeneration: the basis for a promising therapeutic strategy. *Br. J. Pharmacol.* **2005**, *146*, 1041–1059; (b) Di Vaira, M.; Bazzicalupi, C.; Orioli, P.; Messori, L.; Bruni, B.; Zatta, P. Clioquinol, a drug for Alzheimer's disease specifically interfering with brain metal metabolism: structural characterization of its zinc (II) and copper (II) complexes. *Inorg. Chem.* **2004**, *43*, 3795–3797.

24. (a) Sgarbossa, A. Natural biomolecules and protein aggregation: emerging strategies against amyloidogenesis. *Int. J. Mol. Sci.* **2012**, *13*, 17121–17137; (b) Folch, J.; Ettcheto, M.; Petrov, D.; Abad, S.; Pedrós, I.; Marin, M.; Olloquequi, J.; Camins, A. Review of the advances in treatment for Alzheimer disease: strategies for combating β-amyloid protein. *Neurologia* **2018**, *33*, 47–58; (c) Ringman, J. M.; Frautschy, S. A.; Cole, G. M.; Masterman, D. L.; Cummings, J. L. A potential role of the curry spice curcumin in Alzheimer's disease. *Curr. Alzheimer Res.* **2005**, *2*, 131–136; (d) Cádiz-Gurrea, M .D. L. L.; Fernández-Arroyo, S.; Segura-Carretero, A. Pine bark and green tea concentrated extracts: antioxidant activity and comprehensive characterization of bioactive compounds by HPLC–ESI-QTOF-MS. *Int. J. Mol. Sci.* **2014**, *15*, 20382–20402; (e) Betts, J. W.; Sharili, A. S.; Phee, L. M.; Wareham, D. W. *In vitro* activity of epigallocatechin gallate and quercetin alone and in combination versus clinical isolates of methicillin-resistant Staphylococcus aureus. *J. Nat. Prod.* **2015**, *78*, 2145–2148; (f) Yao, Y.; Tang, Y.; Wei, G. Epigallocatechin gallate destabilizes α-synuclein fibril by disrupting the E46–K80 salt-bridge and inter-protofibril interface. *ACS Chem. Neurosci.* **2020**, *11*, 4351–4361; (g) Saha, S.; Deep, S. Glycerol inhibits the primary pathways and transforms the secondary pathway of insulin aggregation. *Phys. Chem. Chem. Phys*. **2016**, *18*, 18934-18948.

25. (a) Cabaleiro-Lago, C.; Lynch, I.; Dawson, K. A.; Linse, S. Inhibition of IAPP and IAPP (20− 29) fibrillation by polymeric nanoparticles. *Langmuir* **2010**, *26*, 3453–3461; (b) Bellova, A.; Bystrenova, E.; Koneracka, M.; Kopcansky, P.; Valle, F.; Tomasovicova, N.; Timko, M.; Bagelova, J.; Biscarini, F.; Gazova, Z. Effect of Fe_3O_4 magnetic nanoparticles on lysozyme amyloid aggregation. *Nanotechnology* **2010**, *21*, 65103; (c) Yoo, S. I.; Yang, M.; Brender, J. R.; Subramanian, V.; Sun, K.; Joo, N. E.; Jeong, S. H.; Ramamoorthy, A.; Kotov, N. A. Inhibition of amyloid peptide fibrillation by inorganic nanoparticles: functional similarities with proteins. *Angew. Chem. Int. Ed.* **2011**, *50*, 5110–5115; (d) John, T.; Gladytz, A.; Kubeil, C.; Martin, L. L.; Risselada, H. J.; Abel, B. Impact of nanoparticles on amyloid peptide and protein aggregation: a review with a focus on gold nanoparticles. *Nanoscale* **2018**, *10*, 20894–20913.

26. Ke, P. C.; Pilkington, E. H.; Sun, Y.; Javed, I.; Kakinen, A.; Peng, G.; Ding, F.; Davis, T. P. Mitigation of amyloidosis with nanomaterials. *Adv. Mater.* **2020**, *32*, 1901690.

27. Ngoungoure, V. L. N.; Schluesener, J.; Moundipa, P. F.; Schluesener, H. Natural polyphenols binding to amyloid: a broad class of compounds to treat different human amyloid diseases. *Mol. Nutr. Food Res.* **2015**, *59*, 8–20.

28. Yang, F.; Lim, G.P.; Begum, A. N.; Ubeda, O. J.; Simmons, M. R.; Ambegaokar, S. S.; Chen, P. P.; Kayed, R.; Glabe, C. G.; Frautschy, S. A.; Cole, G. M. Curcumin inhibits

formation of amyloid beta oligomers and fibrils, binds plaques, and reduces amyloid *in vivo*. *J. Biol. Chem.* **2005**, *280*, 5892–5901.

29. Singh, P. K.; Kotia, V.; Ghosh, D.; Mohite, G. M.; Kumar, A.; Maji, S. K. Curcumin modulates α-synuclein aggregation and toxicity. *ACS Chem. Neurosci.* **2013**, *4*, 393–407.

30. (a) Ehrnhoefer, D. E.; Bieschke, J.; Boeddrich, A.; Herbst, M.; Masino, L.; Lurz, R.; Engemann, S.; Pastore, A.; Wanker, E. E. EGCG redirects amyloidogenic polypeptides into unstructured, off-pathway oligomers. *Nat. Struct. Mol. Biol.* **2008**, *15*, 558–566; (b)Wobst, H. J.; Sharma, A.; Diamond, M. I.; Wanker, E. E.; Bieschke, J. The green tea polyphenol (−)-epigallocatechin gallate prevents the aggregation of tau protein into toxic oligomers at substoichiometric ratios. *FEBS Lett.***2015**, *589*, 77–83; (c) Cao, P.; Raleigh, D.P. Analysis of the inhibition and remodelling of islet amyloid polypeptide amyloid fibers by flavanols. *Biochemistry* **2012**, *51*, 2670–2683.

31. (a) Ahmed, M.; Davis, J.; Aucoin, D.; Sato, T.; Ahuja, S.; Aimoto, S.; Elliott, J. I.; Van Nostrand, W. E.; Smith, S. O. Structural conversion of neurotoxic amyloid-β1–42 oligomers to fibrils. *Nat. Struct. Mol. Biol.* **2010**, *17*, 561–567; (b) Lu, J. X.; Qiang, W.; Yau, W. M.; Schwieters, C. D.; Meredith, S. C.; Tycko, R. Molecular structure of β-amyloid fibrils in Alzheimer's disease brain tissue. *Cell* **2013**, *154*, 1257–1268.

32. Austen, B. M.; Paleologou, K. E.; Ali, S. A.; Qureshi, M. M.; Allsop, D.; El-Agnaf, O. M. Designing peptide inhibitors for oligomerization and toxicity of Alzheimer's β-amyloid peptide. *Biochemistry* **2008**, *47*, 1984–1992.

33. Huggins, K. N.; Bisaglia, M.; Bubacco, L.; Tatarek-Nossol, M.; Kapurniotu, A.; Andersen, N. H. Designed hairpin peptides interfere with amyloidogenesis pathways: fibril formation and cytotoxicity inhibition, interception of the pre-amyloid state. *Biochemistry* **2011**, *50*, 8202–8212.

34. Song, Y.; Moore, E. G.; Guo, Y.; Moore, J. S. Polymer–peptide conjugates disassemble amyloid β fibrils in a molecular-weight dependent manner. *J. Am. Chem. Soc.* **2017**, *139*, 4298–4301.

35. Horwich, A. Protein aggregation in disease: a role for folding intermediates forming specific multimeric interactions. *J. Clin. Invest.* **2002**, *110*, 1221–1232.

36. Jarvela, T. S.; Lam, H. A.; Helwig, M.; Lorenzen, N.; Otzen, D. E.; McLean, P. J.; Maidment, N. T.; Lindberg, I. The neural chaperone proSAAS blocks alpha-synuclein fibrillation and neurotoxicity. *Proc. Natl. Acad. Sci. U. S. A.* **2016**, *113*, 4708–4715.

37. Arndt, J. W.; Qian, F.; Smith, B. A.; Quan, C.; Kilambi, K. P.; Bush, M. W.; Walz, T.; Pepinsky, R. B.; Bussière, T.; Hamann, S.; Cameron, T. O. Structural and kinetic basis for the selectivity of aducanumab for aggregated forms of amyloid-β. *Sci. Rep.* **2018**, *8*, 6412.

38. (a) Logovinsky, V.; Satlin, A.; Lai, R.; Swanson, C.; Kaplow, J.; Osswald, G.; Basun, H.; Lannfelt, L. Safety and tolerability of BAN2401 - a clinical study in Alzheimer's disease with a protofibril selective Aβ antibody. *Alzheimer's Res. Ther.* **2016**, *8*, 1–10; (b) Tucker, S.; Möller, C.; Tegerstedt, K.; Lord, A.; Laudon, H.; Sjödahl, J.; Söderberg,

L.; Spens, E.; Sahlin, C.; Waara, E. R.; Satlin, A. The murine version of BAN2401 (mAb158) selectively reduces amyloid-β protofibrils in brain and cerebrospinal fluid of tg-ArcSwe mice. *J. Alzheimer's Dis.* **2015**, *43*, 575–588; (c) Söllvander, S.; Nikitidou, E.; Gallasch, L.; Zyśk, M.; Söderberg, L.; Sehlin, D.; Lannfelt, L.; Erlandsson, A. The Aβ protofibril selective antibody mAb158 prevents accumulation of Aβ in astrocytes and rescues neurons from Aβ-induced cell death. *J. Neuroinflammation* **2018**, *15*, 1–15.

39. (a) Gekko, K.; Timasheff, S. N. Mechanism of protein stabilization by glycerol: preferential hydration in glycerol-water mixtures. *Biochemistry* **1981**, *20*, 4667–4676; (b) Kaushik, J. K.; Bhat, R. Thermal stability of proteins in aqueous polyol solutions: role of the surface tension of water in the stabilizing effect of polyols. *J. Phys. Chem. B* **1998**, *102*, 7058–7066.

40. Ruzza, P.; Hussain, R.; Biondi, B.; Calderan, A.; Tessari, I.; Bubacco, L.; Siligardi, G. Effects of trehalose on thermodynamic properties of alpha-synuclein revealed through synchrotron radiation circular dichroism. *Biomolecules* **2015**, *5*, 724–734.

41. Ueda, T.; Nagata, M.; Monji, A.; Yoshida, I.; Tashiro, N.; Imoto, T. Effect of sucrose on formation of the β-amyloid fibrils and D-Aspartic acids in Aβ1-42. *Biol. Pharm. Bull.* **2002**, *25*, 375–378.

42. Savelieff, M. G.; DeToma, A. S.; Derrick, J. S.; Lim, M. H. The ongoing search for small molecules to study metal-associated amyloid-β species in Alzheimer's disease. *Acc. Chem. Res.* **2014**, *47*, 2475–2482.

43. Cherny, R. A.; Legg, J. T.; McLean, C. A.; Fairlie, D. P.; Huang, X.; Atwood, C. S.; Beyreuther, K.; Tanzi, R. E.; Masters, C. L.; Bush, A. I. Aqueous dissolution of Alzheimer's disease Aβ amyloid deposits by biometal depletion. *J. Biol. Chem.* **1999**, *274*, 23223–23228.

44. Bush, A. I.; Tanzi, R. E. Therapeutics for Alzheimer's disease based on the metal hypothesis. *Neurotherapeutics* **2008**, *5*, 421–432.

45. Meng, J.; Zhang, H.; Dong, X.; Liu, F.; Sun, Y. RTHLVFFARK-NH_2: A potent and selective modulator on Cu^{2+}-mediated amyloid-β protein aggregation and cytotoxicity. *J. Inorg. Biochem.* **2018**, *181*, 56–64.

46. Gao, G.; Zhang, M.; Gong, D.; Chen, R.; Hu, X.; Sun, T. The size-effect of gold nanoparticles and nanoclusters in the inhibition of amyloid-β fibrillation. *Nanoscale* **2017**, *9*, 4107–4113.

47. Chan, H. M.; Xiao, L.; Yeung, K. M.; Ho, S. L.; Zhao, D.; Chan, W. H.; Li, H. W. Effect of surface-functionalized nanoparticles on the elongation phase of beta-amyloid(1–40) fibrillogenesis. *Biomaterials* **2012**, *33*, 4443–4450.

48. Ghavami, M.; Rezaei, M.; Ejtehadi, R.; Lotfi, M.; Shokrgozar, M. A.; Abd Emamy, B.; Raush, J.; Mahmoudi, M. Physiological temperature has a crucial role in amyloid β in the absence and presence of hydrophobic and hydrophilic nanoparticles. *ACS Chem. Neurosci.* **2013**, *4*, 375–378.

49. Zhang, H.; Dong, X.; Liu, F.; Zheng, J.; Sun, Y. Ac-LVFFARK-NH_2 conjugation to β-cyclodextrin exhibits significantly enhanced performance on inhibiting amyloid β-protein fibrillogenesis and cytotoxicity. *Biophys. Chem.* **2018**, *235*, 40–47.

50. American Diabetes Association. Diagnosis and classification of diabetes mellitus. *Diabetes Care* **2014**, *37*, S81−S90.

51. (a) Chatterjee, S.; Khunti, K.; Davies, M. J. Type 2 diabetes. *Lancet* **2017**, *389*, 2239–2251;(b) NCD Risk Factor Collaboration. Worldwide trends in diabetes since 1980: A pooled analysis of 751 population-based studies with 4.4 million participants. *Lancet* **2016**, *387*, 1513–1530.

52. Westermark, P.; Andersson, A.; Westermark, G. T. Islet amyloid polypeptide, islet amyloid, and diabetes mellitus. *Physiol. Rev.* **2011**, *91*, 795–826.

53. (a) Nakamura, S.; Okabayashi, S.; Ageyama, N.; Koie, H.; Sankai, T.; Ono, F.; Fujimoto, K.; Terao, K. Transthyretin amyloidosis and two other aging-related amyloidoses in an aged vervet monkey. *Vet. Pathol.* **2008**, *45*, 67–72; (b) Guardado-Mendoza, R.; Davalli, A. M.; Chavez, A. O.; Hubbard, G. B.; Dick, E. J.; Majluf-Cruz, A.; Tene-Perez, C. E.; Goldschmidt, L.; Hart, J.; Perego, C.; Comuzzie, A. G. Pancreatic islet amyloidosis, β-cell apoptosis, and α-cell proliferation are determinants of islet remodeling in type-2 diabetic baboons. *Proc. Natl. Acad. Sci. U.S.A.* **2009**, *106*, 13992–13997.

54. Sun, H.; Saeedi, P.; Karuranga, S.; Pinkepank, M.; Ogurtsova, K.;Duncan, B. B.; Stein, C.; Basit, A.; Chan, J. C. N.; Mbanya, J. C.; Pavkov, M. E.; Ramachandaran, A.; Wild, S. H.; James, S.; Herman, W. H.; Zhang, P.; Bommer, C.; Kuo, S.; Boyko, E. J.; Magliano, D. J. IDF Diabetes Atlas: Global, regional and country-level diabetes prevalence estimates for 2021 and projections for 2045. *Diabetes Res. Clin. Pract.* **2022**, *183*, 109119–109132.

55. Gaede, P.; Vedel, P.; Larsen, N.; Jensen, G.V.; Parving, H. H.; Pedersen, O. Multifactorial intervention and cardiovascular disease in patients with type 2 diabetes. *N. Engl. J. Med.* **2003**, *348*, 383–393.

56. (a) Weinstein, A. R.; Sesso, H. D.; Lee, I. M.; Cook, N. R.; Manson, J. E.; Buring, J. E.; Gaziano, J. M. Relationship of physical activity vs body mass index with type 2 diabetes in women. *JAMA* **2004**, *292*, 1188–1194; (b) Lynch, J.; Helmrich, S. P.; Lakka, T. A.; Kaplan, G. A.; Cohen, R. D.; Salonen, R.; Salonen, J. T. Moderately intense physical activities and high levels of cardiorespiratory fitness reduce the risk of non-insulin-dependent diabetes mellitus in middle-aged men. *Arch. Intern. Med.* **1996**, *156*, 1307–1314.

57. Venkatasamy, V. V.; Pericherla, S.; Manthuruthil, S.; Mishra, S.; Hanno, R. Effect of physical activity on insulin resistance, inflammation and oxidative stress in diabetes mellitus. *J. Clin. Diagn. Res.* **2013**, *7*, 1764–1766.

58. Strasser, B. Physical activity in obesity and metabolic syndrome. *Ann. N. Y. Acad. Sci.* **2013**, *1281*, 141–159.

59. Ross, R. Does exercise without weight loss improve insulin sensitivity? *Diabetes Care* **2003**, *26*, 944–945.

60. (a) Wimalawansa, S. J. Amylin, calcitonin gene-related peptide, calcitonin, and adrenomedullin: A peptide superfamily. *Crit. Rev. Neurobiol.* **1997**, *11*, 167–239; (b) Christmanson, L.; Rorsman, F.; Stenman, G.; Westermark, P.; Betsholtz, C. The human islet amyloid polypeptide (IAPP) gene: organization, chromosomal localization and functional identification of a promoter region. *FEBS Lett.* **1990**, *267*, 160–166.

61. Abedini, A.; Raleigh, D. P.; Islet Amyloid Polypepide, in: Ramirez-Alvarado, M.; Kelly, J. W.; Dobson, C. M. (Eds.) Protein misfolding diseases: current and emerging principles and therapies, John Wiley & Sons, Place Published, **2010**, 517–541.

62. (a) Wang, J.; Xu, J.; Finnerty, J.; Furuta, M.; Steiner, D. F.; Verchere, C. B. The prohormone convertase enzyme2 (PC2) is essential for processing pro-islet amyloid polypeptide at the NH_2-terminal cleavage site. *Diabetes* **2001**, *50*, 534–539; (b) Higham, C. E.; Hull, R. L.; Lawrie, L.; Shennan, K. I.; Morris, J. F.; Birch, N. P.; Docherty, K.; Clark, A. Processing of synthetic pro-islet amyloid polypeptide (proIAPP) 'amylin' by recombinant prohormone convertase enzymes, PC2 and PC3, *in vitro*. *Eur. J. Biochem.* **2000**, *267*, 4998–5004.

63. (a) Halban, P.A.; Irminger, J.C. Sorting and processing of secretory proteins. *Biochem. J.* **1994**, *299*, 1; (b) Marzban, L.; Verchere, C. B. The role of islet amyloid polypeptide in type 2 diabetes. *Can. J. Diabetes* **2004**, *28*, 39–47; (c) Sanke, T.; Bell, G. I.; Sample, C.; Rubenstein, A. H.; Steiner, D. F. An islet amyloid peptide is derived from an 89-amino acid precursor by proteolytic processing. *J. Biol. Chem.* **1988**, *263*, 17243–17246.

64. Opie, E. L. The relation of diabetes mellitus to lesions of the pancreas. Hyaline degeneration of the islands of Langerhans. *J. Exp. Med.* **1901**, *5*, 527–540.

65. (a) Westermark, P.; Wernstedt, C.; Wilander, E.; Hayden, D. W.; O'Brien, T. D.; Johnson, K. H. Amyloid fibrils in human insulinoma and islets of Langerhans of the diabetic cat are derived from a neuropeptide-like protein also present in normal islet cells. *Proc. Natl. Acad. Sci. U.S.A.* **1987**, *84*, 3881–3885; (b) Cooper, G. J.; Willis, A. C.; Clark, A.; Turner, R. C.; Sim, R. B.; Reid, K. B. Purification and characterization of a peptide from amyloid-rich pancreases of type 2 diabetic patients. *Proc. Natl. Acad. Sci. U.S.A.* **1987**, *84*, 8628–8632.

66. Asthana, S.; Mallick, B.; Alexandrescu, A. T.; Jha, S. IAPP in type II diabetes: Basic research on structure, molecular interactions, and disease mechanisms suggests potential intervention strategies. *Biochim. Biophys. Acta Biomembr.* **2018**, *1860*, 1765–1782.

67. Chakraborty, S.; Chatterjee, B.; Basu, S. A mechanistic insight into the amyloidogenic structure of hIAPP peptide revealed from sequence analysis and molecular dynamics simulation. *Biophys. Chem.* **2012**, *168*, 1–9.

68. Härd, T.; Lendel, C. Inhibition of amyloid formation. *J. Mol. Biol.* **2012**, *421*, 441−465.

69. Bhutani, P.; Joshi, G.; Raja, N.; Bachhav, N.; Rajanna, P. K.; Bhutani, H.; Paul, A. T.; Kumar, R. US FDA approved drugs from 2015–June 2020: a perspective. *J. Med. Chem.* **2021**, *64*, 2339–2381.

70. Dahlén, A. D.; Dashi, G.; Maslov, I.; Attwood, M. M.; Jonsson, J.; Trukhan, V.; Schiöth, H. B. Trends in antidiabetic drug discovery: FDA approved drugs, new drugs in clinical trials and global sales. *Front. Pharmacol.* **2022**, *12*, 4119–4135.

71. Muttenthaler, M.; King, G.F.; Adams, D.J.; Alewood, P.F. Trends in peptide drug discovery. *Nat. Rev. Drug Discov.***2021**, *20*, 309–325.

72. Nilsson, M. R.; Raleigh, D. P. Analysis of amylin cleavage products provides new insights into the amyloidogenic region of human amylin. *J. Mol. Biol.* **1999**, *294*, 1375−1385.

73. (a) Tang, Y.; Zhang, D.; Zhang, Y.; Liu, Y.; Gong, X.; Chang, Y.; Ren, B.; Zheng, J. Introduction and fundamentals of human islet amyloid polypeptide inhibitors. *ACS Appl. Bio Mater.* **2020**, *3*, 8286−8308; (b) Mitra, A.; Sarkar, N. Sequence and structure-based peptides as potent amyloid inhibitors: A review. *Arch. Biochem. Biophys.* **2020**, *695*, 108614–108624; (c)Saini, R. K.; Goyal, D.; Goyal, B. Targeting human islet amyloid polypeptide aggregation and toxicity in type 2 diabetes: an overview of peptide-based inhibitors. *Chem. Res. Toxicol.* **2020**, *33*, 2719−2738.

74. Potter, K.J.; Scrocchi, L.A.; Warnock, G.L.; Ao, Z.; Younker, M.A.; Rosenberg, L.; Lipsett, M.; Verchere, C.B.; Fraser, P.E. Amyloid inhibitors enhance survival of cultured human islets. *Biochim. Biophys. Acta, Gen. Subj.* **2009**, *1790*, 566–574.

75. Wang, L.; Lei, L.; Li, Y.; Wang, L.; Li, F. A hIAPP-derived all-D-amino-acid inhibits hIAPP fibrillation efficiently at membrane surface by targeting α-helical oligomeric intermediates. *FEBS Lett.* **2014**, *588*, 884−891.

76. Wijesekara, N.; Ahrens, R.; Wu, L.; Ha, K.; Liu, Y.; Wheeler, M. B.; Fraser, P. E. Islet amyloid inhibitors improve glucose homeostasis in a transgenic mouse model of type 2 diabetes. *Diabetes Obes. Metab.* **2015**, *17*, 1003−1006.

77. Sivanesam, K.; Andersen, N. H. Inhibition of human amylin amyloidogenesis by human amylin-fragment peptides: Exploring the effects of serine residues and oligomerization upon inhibitory potency. *Biochemistry* **2017**, *56*, 5373−5379.

78. Rozniakowski, K.; Fraczyk, A.; Galecki, K.; Wietrzyk, J.; Filip-Psurska, B.; Fraczyk, J.; Kaminski, Z.J.; Kolesinska, B. New human islet amyloid polypeptide fragments susceptible to aggregation. *Chem. Biodivers*. **2020**, *17*, e2000501.

79. Fraczyk, A.; Janczewski, L.; Wasko, J.; Rozniakowski, K.; Galecki, K.; Kaminski, Z. J.; Kolesinska, B. Non-aggregating amylin fragments as an inhibitor of the aggregation process of susceptible to aggregation fragments 18–22, 23–27, and 33–37 of hormone. *Chem. Biodivers.* **2021**, *18*, e2100034.

80. Andreasen, M.; Nielsen, S. B.; Mittag, T.; Bjerring, M.; Nielsen, J. T.; Zhang, S.; Nielsen, E. H.; Jeppesen, M.; Christiansen, G.; Besenbacher, F.; Dong, M. Modulation of

fibrillation of hIAPP core fragments by chemical modification of the peptide backbone. *Biochim. Biophys. Acta Proteins Proteom.* **2012**, *1824*, 274−285.

81. Mishra, A.; Misra, A.; Vaishnavi, T.S.; Thota, C.; Gupta, M.; Ramakumar, S.; Chauhan, V.S. Conformationally restricted short peptides inhibit human islet amyloid polypeptide (hIAPP) fibrillization. *Chem. Comm.* **2013**, *49*, 2688−2690.

82. Obasse, I.; Taylor, M.; Fullwood, N. J.; Allsop, D. Development of proteolytically stable N-methylated peptide inhibitors of aggregation of the amylin peptide implicated in type 2 diabetes. *Interface Focus* **2017**, *7*, 20160127-20160138.

83. Paul, A.; Kalita, S.; Kalita, S.; Sukumar, P.; Mandal, B. Disaggregation of amylin aggregate by novel conformationally restricted aminobenzoic acid containing α/β and α/γ hybrid peptidomimetics. *Sci. Rep.* **2017**, *7*, 40095.

84. Rozniakowski, K.; Galecki, K.; Wietrzyk, J.; Filip-Psurska, B.; Fraczyk, J.; Kaminski, Z. J.; Kolesinska, B. N-methylated analogs of hIAPP fragments 18–22, 23–27, 33–37 inhibit aggregation of the amyloidogenic core of the hormone. *Chem. Biodivers.* **2021**, *18*, e2000842.

85. Lesma, J.; Bizet, F.; Berardet, C.; Tonali, N.; Pellegrino, S.; Taverna, M.; Khemtemourian, L.; Soulier, J. L.; van Heijenoort, C.; Halgand, F.; Ha-Duong, T. β-hairpin peptide mimics decrease human islet amyloid polypeptide (hIAPP) aggregation. *Front. Cell Dev. Biol.* **2021**, *9*, 2531–2555.

86. Figueroa, H.; Peddi, D.; Osborne, J. M.; Wilson, B. M.; Pesaru, R. R.; Kurva, B.; Ramaraju, S.; Milletti, M. C.; Heyl, D. L. Modeling the interface between islet amyloid polypeptide and insulin-based aggregation inhibitors: correlation to aggregation kinetics and membrane damage. *J. Chem. Inf. Model.* **2012**, *52*, 1298−1307.

87. Sivanesam, K.; Shu, I.; Huggins, K. N.; Tatarek-Nossol, M.; Kapurniotu, A.; Andersen, N. H. Peptide Inhibitors of the amyloidogenesis of IAPP: verification of the hairpin-binding geometry hypothesis. *FEBS Lett.* **2016**, *590*, 2575−2583.

88. Shi, Y.; Lv, W.; Jiao, A.; Zhang, C.; Zhang, J. A novel pentapeptide inhibitor reduces amyloid deposit formation by direct interaction with hIAPP. *Internet. J. Endocrinol.* **2019**, *2019*, 9062032.

89. Abioye, R. O.; Okagu, O. D.; Udenigwe, C. C. Disaggregation of islet amyloid polypeptide fibrils as a potential anti-fibrillation mechanism of tetrapeptide TNGQ. *Int. J. Mol. Sci.* **2022**, *23*, 1972−1985.

90. (a) Jakob-Roetne, R.; Jacobsen, H. Alzheimer's Disease: from pathology to therapeutic approaches. *Angew. Chem. Int. Ed.* **2009**, *48*, 3030−3059; (b) Savelieff, M. G.; Lee, S.; Liu, Y.; Lim, M. H. Untangling Amyloid-β, tau, and metals in Alzheimer's Disease. *ACS Chem. Biol.* **2013**, *8*, 856−865.

91. (a) Terry, R. D.; Davies, P. Dementia of the Alzheimer type. *Annu. Rev. Neurosci.* **1980**, *3*, 77–95; (b) Rathmann, K. L.; Conner, C. S. Alzheimer's disease: Clinical features, pathogenesis, and treatment. *Drug Intell. Clin. Pharm.* **1984**, *18*, 684–691.

92. Gerontological Society of America. The Gerontological Society of America workgroup on cognitive impairment detection and earlier diagnosis: Report and recommendations. Washington, DC. **2015**.

93. Alzheimer's Association 2019 Alzheimer's disease facts and figures. *Alzheimers Dement*. **2019**, *15*, 321–387.

94. Gauthier, S.; Webster C.; Servaes, S.; Morais, J. A.; Rosa-Neto, P. World Alzheimer Report 2022: Life after diagnosis: Navigating treatment, care and support. London, England: Alzheimer's Disease International. **2022**.

95. Chêne, G.; Beiser, A.; Au, R.; Preis, S. R.; Wolf, P. A.; Dufouil, C.; Seshadri, S. Gender and incidence of dementia in the Framingham Heart Study from mid-adult life. *Alzheimers Dement.* **2015**, *11*, 310–320.

96. Alzheimer's Association 2022 Alzheimer's disease facts and figures. *Alzheimer's Dement.* **2022**, *18*, 700–789.

97. Hardy, J. A.; Higgins, G. A. Alzheimer's disease: The amyloid cascade hypothesis. *Science* **1992**, *256*, 184–185.

98. Rauk, A. The chemistry of Alzheimer's disease. *Chem. Soc. Rev.* **2009**, *38*, 2698−2715;

99. (a) Hamley, I. W. The amyloid beta peptide: a chemist's perspective. Role in Alzheimer's and fibrillization. *Chem. Rev.* **2012**, *112*, 5147−5192; (b) Kepp, K. P. Bioinorganic chemistry of Alzheimer's disease. *Chem. Rev.* **2012**, *112*, 5193−5239; (c) DeToma, A. S.; Salamekh, S.; Ramamoorthy, A.; Lim, M. H. Misfolded proteins in Alzheimer's disease and type II diabetes. *Chem. Soc. Rev.* **2012**, *41*, 608−621.

100. Abramov, E.; Dolev, I.; Fogel, H.; Ciccotosto, G. D.; Ruff, E.; Slutsky, I. Amyloid-β as a positive endogenous regulator of release probability at hippocampal synapses. *Nat. Neurosci.* **2009**, *12*, 1567–1576.

101. (a) Lesné, S.; Koh, M. T.;Kotilinek, L.; Kayed, R.; Glabe, C. G.; Yang, A.; Gallagher, M.; Ashe, K. H. A specific amyloid-β protein assembly in the brain impairs memory. *Nature* **2006**, *440*, 352−357; (b) Shankar, G. M.; Li, S.;Mehta, T. H.; Garcia-Munoz, A.; Shepardson, N. E.; Smith, I.; Brett, F. M.; Farrell, M. A.; Rowan, M. J.; Lemere, C. A.; Regan, C. M.; Walsh, D. M.; Sabatini, B. L.; Selkoe, D. J. Amyloid-β protein dimers isolated directly from Alzheimer's brains impair synaptic plasticity and memory. *Nat. Med.* **2008**, *14*, 837−842.

102. Vivekanandan, S.; Brender, J. R.; Lee, S. Y.; Ramamoorthy, A. A partially folded structure of amyloid-β(1−40) in an aqueous environment. *Biochem. Biophys. Res. Commun.* **2011**, *411*, 312−316.

103. Hardy, J.; Selkoe, D. J. The amyloid hypothesis of Alzheimer's disease: progress and problems on the road to therapeutics. *Science* **2002**, *297*, 353–356.

104. Vaz, M.; Silva, V.; Monteiro, C.; Silvestre, S. Role of aducanumab in the treatment of Alzheimer's Disease: Challenges and opportunities. *Clin. Interv. Aging* **2022**, *17*, 797–810.

105. (a) Claxton, A.; Baker, L. D.; Hanson, A.; Trittschuh, E. H.; Cholerton, B.; Morgan, A.; Callaghan, M.; Arbuckle, M.; Behl, C.; Craft, S. Long-acting intranasal insulin Detemir improves cognition for adults with mild cognitive impairment or early-stage Alzheimer's disease dementia. *J. Alzheimers Dis.* **2015**, *44*, 897–906; (b) Hallschmid, M. Intranasal insulin for Alzheimer's disease. *CNS Drug* **2021**, *35*, 21–37.

106. Handattu, S. P.; Garber, D. W.; Monroe, C. E.; vanGroen, T.; Kadish, I.; Nayyar, G.; Cao, D.; Palgunachari, M. N.; Li, L.; Anantharamaiah, G. M. Oral apolipoprotein a-i mimetic peptide improves cognitive function and reduces amyloid burden in a mouse model of Alzheimer's disease. *Neurobiol. Dis.* **2009**, *34*, 525–534.

107. (a) Ryan, P.; Patel, B.; Makwana, V.; Jadhav, H. R.; Kiefel, M.; Davey, A.; Reekie, T. A.; Rudrawar, S.; Kassiou, M. Peptides, peptidomimetics, and carbohydrate–peptide conjugates as amyloidogenic aggregation inhibitors for Alzheimer's disease. *ACS Chem. Neurosci.* **2018**, *9*,1530–1551; (b) Goyal, D.; Shuaib, S.; Mann, S.; Goyal, B. Rationally designed peptides and peptidomimetics as inhibitors of amyloid-β (Aβ) aggregation: potential therapeutics of Alzheimer's disease. *ACS Comb. Sci.* **2017**, *19*, 55–80.

108. Harkany, T.; Abraham, I.; Laskay, G.; Timmerman, W.; Jost, K.; Zarandi, M.; Penke, B.; Nyakas, C.; Luiten, P. G. Propionyl-IIGL tetrapeptide antagonizes β-amyloid excitotoxicity in rat nucleus basalis. *Neuroreport* **1999**, *10*, 1693–1698.

109. Fülöp, L.; Zarándi, M.; Datki, Z.; Soós, K.; Penke, B. β-Amyloid-derived pentapeptide RIIGLa inhibits $A\beta_{1\text{-}42}$ aggregation and toxicity. *Biochem. Biophys. Res. Commun*. **2004**, *324*, 64–69.

110. Xiong, N.; Dong, X. Y.; Zheng, J.; Liu, F. F.; Sun, Y. Design of LVFFARK and LVFFARK-functionalized nanoparticles for inhibiting amyloid β-protein fibrillation and cytotoxicity. *ACS Appl. Mater. Interfaces* **2015**, *7*, 5650–5662.

111. Jagota, S.; Rajadas, J. Synthesis of D-amino acid peptides and their effect on β-amyloid aggregation and toxicity in transgenic *Caenorhabditis elegans*. *Med. Chem. Res.* **2013**, *22*, 3991–4000.

112. Tillett, K. C.; Del Valle, J. R. N-Amino peptide scanning reveals inhibitors of $A\beta_{42}$ aggregation. *RSC Adv.* **2020**, *10*, 14331–14336.

113. Kapadia, A.; Patel, A.; Sharma, K. K.; Maurya, I. K.; Singh, V.; Khullar, M.; Jain, R. Effect of C-terminus amidation of Aβ(39-42) fragment derived peptides as potential inhibitors of Aβ aggregation. *RSC Adv.* **2020**, *10*, 27137–27151.

114. Khalili Samani, E.; Mofid, M.R.; Malakoutikhah, M. The effect of terminal groups and halogenation of KLVFF peptide on its activity as an inhibitor of β-amyloid aggregation. *J. Pept. Sci*. **2020**, *26*, e3227.

115. Kapadia, A.; Sharma, K. K.; Maurya, I. K.; Singh, V.; Khullar, M.; Jain, R. Structural and mechanistic insights into the inhibition of amyloid-β aggregation by Aβ39-42 fragment derived synthetic peptides. *Eur. J. Med. Chem.* **2021**, *212*, 113126–113144.

116. Mallesh, R.; Juhee khan; Gharai, P. K.; Gupta, V.; Roy, R.; Ghosh, S. Controlling amyloid-β peptide aggregation and toxicity by protease-stable ligands. *ACS Bio Med Chem Au* **2023**, *3*, 158−173.

117. Zimbone, S.; Giuffrida, M. L.; Sabatino, G.; Di Natale, G.; Tosto, R.; Consoli, G. M.; Milardi, D.; Pappalardo, G.; Sciacca, M. F. $A\beta_{8\text{-}20}$ fragment as an anti-fibrillogenic and neuroprotective agent: Advancing toward efficient Alzheimer's Disease treatment. *ACS Chem. Neurosci*. **2023**, *14*, 1126–1136.

118. Xue, D.; Zhao, M.; Wang, Y. J.; Wang, L.; Yang, Y.; Wang, S. W.; Zhang, R.; Zhao, Y.; Liu, R. T. A multifunctional peptide rescues memory deficits in Alzheimer's disease transgenic mice by inhibiting $A\beta_{42}$-induced cytotoxicity and increasing microglial phagocytosis. *Neurobiol. Dis.* **2012**, *46*, 701–709.

119. Viet, M. H.; Siposova, K.; Bednarikova, Z.; Antosova, A.; Nguyen, T. T.; Gazova, Z.; Li, M. S. *In silico* and *in vitro* study of binding affinity of tripeptides to amyloid β fibrils: Implications for Alzheimer's disease. *J. Phys. Chem. B* **2015**, *119*, 5145–5155.

120. Bansal, S.; Maurya, I. K.; Yadav, N.; Thota, C. K.; Kumar, V.; Tikoo, K.; Chauhan, V. S.; Jain, R. C-terminal fragment, $A\beta_{32\text{–}37}$, analogues protect against Aβ aggregation-induced toxicity. *ACS Chem. Neurosci*. **2016**, *7*, 615–623.

121. Zhang, X.; Zhang, X.; Zhong, M.; Zhao, P.; Guo, C.; Li, Y.; Xu, H.; Wang, T.; Gao, H. A novel Cu (II)-binding peptide identified by phage display inhibits Cu^{2+}-mediated Aβ aggregation. *Int. J. Mol. Sci.* **2021**, *22*, 6842.

122. Liu, J.; Wang, W.; Zhang, Q.; Zhang, S.; Yuan, Z. Study on the efficiency and interaction mechanism of a decapeptide inhibitor of β-amyloid aggregation. *Biomacromolecules* **2014**, *15*, 931–939.

123. Ghosh, A.; Pradhan, N.; Bera, S.; Datta, A.; Krishnamoorthy, J.; Jana, N. R.; Bhunia, A. Inhibition and degradation of amyloid beta ($A\beta_{40}$) fibrillation by designed small peptide: a combined spectroscopy, microscopy, and cell toxicity study. *ACS Chem. Neurosci*. **2017**, *8*, 718–722.

124. Jha, A.; Kumar, M. G.; Gopi, H. N.; Paknikar, K. M. Inhibition of β-amyloid aggregation through a designed β-hairpin peptide. *Langmuir* **2018**, *34*, 1591-1600.

125. Kapadia, A.; Patel, A.; Sharma, K. K.; Maurya, I. K.; Singh, V.; Khullar, M.; Jain, R. Effect of C-terminus amidation of $A\beta_{39\text{–}42}$ fragment derived peptides as potential inhibitors of Aβ aggregation. RSC advances, 2020, 10, 27137–27151.

126. Bhattacharyya, R.; Bhattacharjee, S.; Pathak, B. K.; Sengupta, J. Heptameric peptide interferes with amyloid-β aggregation by structural reorganization of the toxic oligomers. *ACS Omega* **2020**, *5*, 16128–16138.

127. Lei, L.; Zou, Z.; Liu, J.; Xu, Z.; Fu, Y.; Tian, Y.; Zhang, W. Multifunctional peptide-assembled micelles for simultaneously reducing amyloid-β and reactive oxygen species. *Chem. Sci.* **2021**, *12*, 6449–6457.

128. Bharatam, P.V. Computer-Aided Drug Design. In: Poduri, R. (eds) *Drug Discovery and Development*, Singapore *Springer*, **2021**, 137–210.

129. Kanchi, P. K.; Dasmahapatra, A. K. Destabilization of the Alzheimer's amyloid-β peptide by a proline-rich β-sheet breaker peptide: a molecular dynamics simulation study. *J. Mol. Model.* **2021**, *27*, 1–15.

130. Wu, M.; Dorosh, L.; Schmitt-Ulms, G.; Wille, H.; Stepanova, M. Aggregation of Aβ40/42 chains in the presence of cyclic neuropeptides investigated by molecular dynamics simulations. *PLoS Comput. Biol.* **2021**, *17*, e1008771.

131. Jani, V.; Sonavane, U.; Joshi, R. Destabilization potential of beta sheet breaker peptides on Aβ fibril structure: an insight from molecular dynamics simulation study. *RSC advances* **2021**, *11*, 23557−23573.

132. Kanchi, P. K.; Dasmahapatra, A. K. Enhancing the binding of the β-sheet breaker peptide LPFFD to the amyloid-β fibrils by aromatic modifications: A molecular dynamics simulation study. *Comput. Biol. Chem.* **2021**, *92*, 107471.

133. Jarmuła, A.; Ludwiczak, J.; Stępkowski, D. β-sheet breakers with consecutive phenylalanines: Insights into mechanism of dissolution of β-amyloid fibrils. *Proteins: Struct. Funct. Genet.* **2021**, *89*, 762−780.

134. Roy, R.; Paul, S. hIAPP-amyloid-core derived D-peptide prevents hIAPP aggregation and destabilizes its protofibrils. *J. Phys. Chem. B* **2022**, *126*, 822−839.

135. Roy, R.; Paul, S. Disparate effect of hybrid peptidomimetics containing isomers of aminobenzoic acid on hIAPP aggregation. *J. Phys. Chem. B* **2022**, *126*, 10427−10444.

136. Mohammed, A. A.; Barale, S. S.; Kamble, S. A.; Paymal, S. B.; Sonawane, K. D. Molecular insights into the inhibition of early stages of Aβ peptide aggregation and destabilization of Alzheimer's Aβ protofibril by dipeptide D-Trp-Aib: A molecular modelling approach. *Int. J. Biol. Macromol*. **2023**, *242*, 124880.

Chapter 2

Computational approaches and biophysical evaluation

2.1 Docking

Docking is molecular modelling method that involves fitting one or multiple molecular structures into a designated target (such a protein), and predicting the binding affinity of resulting complex (**Figure 2.1**). The process involves fitting a ligand within a binding site, examining each pose for hydrophobic and steric interactions, and prioritizing the outcomes using a scoring system that compares the results of different binding poses. The advantage of using docking in the drug development process is ability to screen millions of molecules against a specific target. The docking process consists of two stages: configurational sampling and the assessment of the scoring function. Configurational sampling in docking refers to the process of exploring various possible conformations or configurations of a ligand molecule within the binding site of a target protein. The goal is to predict the most energetically favorable binding pose of a ligand within the protein's active site, which is crucial for understanding the ligand-protein interaction and designing potential drug candidates. Sampling can be categorized as rigid, where neither the ligand nor the receptor undergoes movement (analogous to key-lock imposition in some comparisons), semi-flexible, where the ligand exhibits some degree of movement, and flexible, allowing freedom of movement for both the ligand and the protein. In the rigid and semi-flexible approaches, only the atomic coordinates of the receptor are deemed capable of interacting with the ligand.

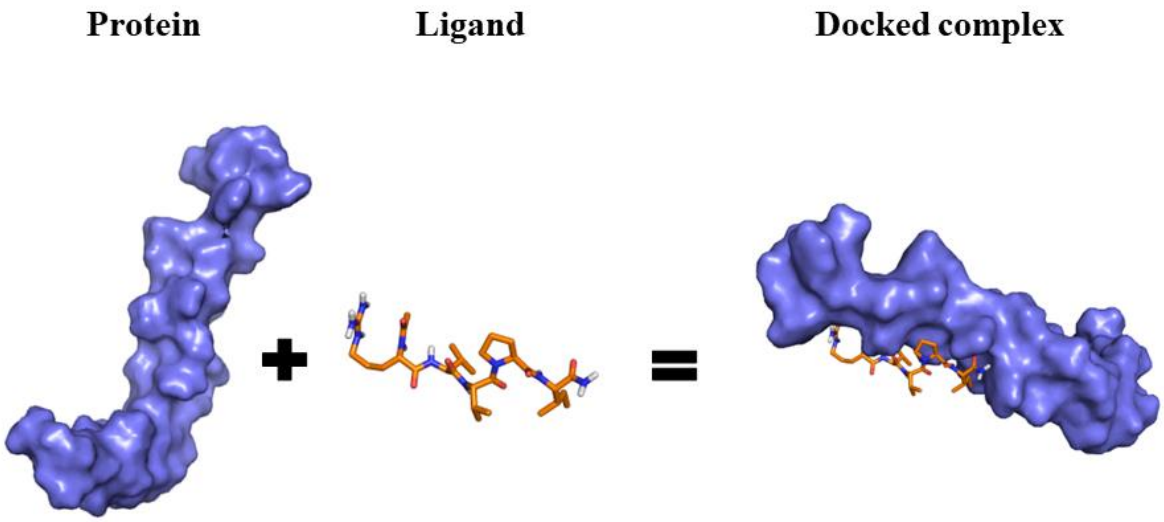

Figure 2.1: Peptide binding with protein using AutoDock.

2.2 Molecular dynamics

Molecular dynamics (MD) is a computational chemistry technique to simulate the movement of atoms by applying Newton's law of motion through integration. For biological processes including ligand-target contact, conformational change, and protein folding/unfolding, MD simulations provide essential atomistic insights into the mechanism. This is accomplished by giving the position of every atom simulated with time resolution at the femtosecond scale.[1] MD was first employed in 1957 to determine the equilibrium properties of system to examine particle collisions within a rectangular box.[2] McCammon et al. studied the dynamics of the Bovine Pancreatic Trypsin Inhibitor (BPTI) protein, consisting of 58 residues, over a total duration of 9.2 picoseconds for the first time on a biological system in 1977.[3] Due to the advancement of force fields, and super computers has substantially expanded the applicability of MD over the last few decades, transforming it into a powerful tool for comprehending chemical and biological processes.[4]

The conventional MD simulation method involves the generation of set of atomic coordinates by iteratively integrating the following Newton's law of motion equation:

$$\frac{d^2 r_i(t)}{dt^2} = \frac{F_i(t)}{m_i} \qquad (1)$$

where F_i (t) represents the force acting on atom i with mass m at time t, and r_i (t) represent the position vector of the atom i.

For the execution of MD simulations, we need to take various steps, which are outlined below:

Initial conditions: Specification of the initial atomic coordinates of system for simulation. This step is crucial for the MD simulation to be successful, particularly for biological systems such as proteins. Generally, the initial coordinates are derived from experimental findings, such as NMR, X-ray crystallography, and Cryo-EM. Experimentally determined structures of biomolecules, in the form of Protein Data Bank (PDB) files, can be accessed on the Research Collaboratory for Structural Bioinformatics (RCSB) website, where the initial coordinates for atoms can be found.

Numerical integration*:* Following the definition of the initial positions and velocities of atoms, it is necessary to perform numerical integration of Newton's equations of motion. Various integration algorithms have been developed for this purpose, one of the simplest and efficient algorithms is the Verlet algorithm, along with its variations.[5]

$$r_{n+1} = r_n + v\Delta t + \frac{F_n}{2m}\Delta t^2 \qquad (2)$$

$$v_{n+1} = v_n \frac{+F_{n+1}+F_n}{2m} \Delta t \qquad (3)$$

Velocity Verlet algorithm is common integration algorithm in which it calculates the velocity and position are at the same timestep. In the velocity Verlet algorithm, the new positions are computed before the new velocities, which are subsequently used to determine the forces.

Integration timestep (∆t)*:* The accuracy and convergence of MD simulations depend on the choice of the timestep (t) for the numerical integration. Simulations become more precise with smaller time steps, but this improvement comes at the cost of increased computational expense. Although a greater timestep results in more sampling of the conformational space, the simulation becomes unstable. To obtain accuracy and convergence in the simulations, it is crucial to choose the timestep.[6]

Force field: The force field is a crucial collection of parameters named as FF. A parametric function of atomic coordinates called force field which calculates the potential energy of system. The potential energy is formulated as the summation of different terms utilized for representing both bonded and non-bonded interactions. Bond stretching, rotation around a dihedral and torsional angle, collectively contribute to bonded interactions, while non-bonded interactions consist of Van der Waals and electrostatic interactions. Both experimental investigation and *ab initio* calculations can be used to determine the value for each of these parameters. AMBER (Assisted Model Building with Energy Refinement),[7] GROMOS (GROenigen Molecular Simulation),[8] OPLS (Optimized Parameters for Large-scale Simulations),[9] and CHARMM (Chemistry at HARvard using Molecular Mechanics)[10] are a few well-known force field algorithms. I used the GROMOS and AMBER force field for most of the work in my thesis.

Boundary conditions: Boundary conditions in molecular dynamics (MD) simulations refer to the specifications regarding how the system behaves at its edges or boundaries. These conditions are crucial for accurately modeling the behavior of atoms or molecules within the simulation environment. There are several types of boundary conditions commonly used in MD simulations.[11] Periodic boundary conditions is the most commonly used boundary condition in MD simulations. With periodic boundary conditions, the simulation box is replicated infinitely in all three dimensions. When a particle moves out of one side of the simulation box, it re-enters from the opposite side, maintaining the continuity of the system.

periodic boundary conditions effectively eliminates edge effects and allows for the simulation of bulk systems.[12] In my work, I ran all MD simulations using periodic boundary conditions.

Water model: The availability of possible models that can provide an precise picture of the system is crucial for MD simulations of any biomolecular system. For a multi-body system such as water, the model should be computationally efficient, physically plausible, and capable of estimating most experimental parameters for real water across a wide range of state points.[13] The precision of the model can be confirmed by comparing simulation results with experimental data since the outcomes of a molecular simulation are solely determined by the nature of the theoretical model employed. The following four considerations can be applied to categorise the main differences between various water models[14]:

- Parametrization values: Depending on the accessibility of experimental data and the scope of the application of model, different models employ different target quantities for parametrization.
- The arrangement of interaction sites and the charge distribution. Different water models situate negative charge in different locations in relation to where the oxygen atom is located. As a result, there are water models for three, four, five, and six sites.
- Internal degrees of freedom: While many water models neglect internal degrees of freedom, some models incorporate flexible geometry, accounting for the stretching of the O-H covalent bond and the bending of the O-H-O angle.
- Non-additive interaction terms: For non-additive interactions including polarisation, charge redistribution, and higher order interactions, etc., only a few water models are available. The computing effort is significantly increased by the inclusion of all these new interactions.

One of the earliest water models is the simple point charge (SPC) model. In 1981, Berendsen et al. proposed the three-site model. The model is more computationally economical and simple to implement in protein water potential, and it averages many-body interactions. Electrostatic contact and the Lennard-Jones term combine to form the intermolecular potential.

$$u = 4 \in \sum_i \sum_{j \neq i} \left[\left(\frac{\sigma}{r^{00}{}_{ij}} \right)^{12}_{-} \left(\frac{\sigma}{r^{00}{}_{ij}} \right)^{6} \right] + \frac{e^2}{4\Pi\epsilon_0} \sum_i \sum_{j \neq i} \frac{q_i q_j}{r_{ij}} \qquad (5)$$

Where $r^{00}{}_{ij}$ and r_{ij} are the distances between the oxygen sites and charged sites of two molecules respectively, e is the proton charge, $\varepsilon_{\circ}$ is the permittivity of vacuum. The SPC model gives

enthalpy of vaporisation value 44,213 kJ/mol·K (44.0451), isobaric heat capacity value 72.264 J/mol·K (75.312), and isothermal compressibility value 0.461 1/Gpa (0.458) that align well with experimental observations values enclosed in parentheses.[15] Due to the absence of two lone electron pairs, the SPC water molecule can travel more quickly than "actual water." However, as one of the original water models, SPC provided a solid foundation for the creation of subsequent water models.

Jorgensen et al. proposed the TIP3P (transferable intermolecular potential three point) model in 1983. In comparison to the SPC model, this model is three-site model having O-H bond length and H-OH angle are shorter. The Lennard-Jones constants and the charge associated with hydrogen atom, which are model parameters, were determined by reproducing the vaporisation enthalpy and liquid density of water under natural conditions. When compared to experimental values, TIP3P yields too high thermal expansion and self-diffusion coefficients, as well as too low viscosity values. On the O-O radial distribution function, it also shows a second peak with a very low intensity. However, as recently demonstrated (Mao and Zhang, 2012), the TIP3P water model offers an estimate of isochoric heat capacity at room conditions with an error from the experimental value of less than 1%. Due to its computational efficiency, this model is still frequently employed for biological molecules.[16]

Energy minimization: Even when preliminary structures are found through experimental effort, residues could still lack hydrogen atoms or other atoms. Therefore, it is essential to perform energy minimization on the initial coordinates to resolve any potential steric conflicts among atoms. Additionally, missing atoms are introduced during the initial structure preparation. Prior to doing MD simulations in my study, I either used conjugate gradient methods or steepest descents method for energy minimization.

Temperature Pressure control*:* MD simulations are normally collaborated with thermostats and barostats. In the case of a thermostat, the volume (V) and the temperature (T) are maintained constant (NVT, also referred to as a canonical ensemble), while a barostat controls the pressure (P) while maintaining a constant value for V (NPT). Thermostats such velocity rescaling,[17] Andersen,[18] Nosé-Hoover,[19] Berendsen,[20] and Langevin[21] have all been used in MD simulations. In the present thesis I applied the Berendsen thermostat and Parrinello-Rahman barostat as implemented in GROMACS software.

Berendsen thermostat also called proportional thermostat corrects the deviations of the actual temperature T (instantaneous temperature) from the prescribed one T_0 (desired temperature) by

multiplying the velocities by a certain factor λ (coupling parameter) in order to move the system dynamics towards the one corresponding to T_0. One benefit of the Berendsen thermostat is that it permits temperature fluctuations, rather than constraining it to a constant value. This method gives an exponential decay of the system towards the desired temperature.

$$\frac{dT(t)}{dt} = \frac{1}{\lambda}\left(T_0 - T(t)\right) \qquad (6)$$

In the Parrinello-Rahman barostat the box vectors represented by the matrix b which follow the matrix equation:

$$\frac{db^2}{dt^2} = vw^{-1}b'^{-1}\left(P - P_{ref}\right) \qquad (7)$$

V stands for the volume of box, while W stands for a matrix parameter that controls the strength of coupling. The current and reference pressures are represented by the matrices P and Pref, respectively.

Analysis of MD simulations: In addition to $A\beta_{42}$ monomer-peptide complex and $A\beta_{42}$ protofibril-peptide complex, MD simulation of $A\beta_{42}$ monomer and $A\beta_{42}$ protofibril alone was performed in order to analyse the effect of designed peptide ligand on the monomeric as well as protofibrillar structure. MD simulations were conducted using the GROMACS 5.0.1 package employing the GROMOS96 54a7 force field. The GROMOS96 force field has been extensively employed for the investigation of protein conformational dynamics. The necessary number of counterions was introduced into the cubic box, and periodic boundary conditions were implemented for all simulations. The protonation states of all amino acids in the MD simulations were determined according to physiological pH. The final MD simulations has been performed for 200 ns each for the designed peptides with different $A\beta_{42}$ monomer structures and different $A\beta_{42}$ protofibril structures.

The GROMACS tools were used along with visual molecular dynamics (VMD)[22] and PyMOL[23] to visualize and analyze MD trajectories. The conformational clustering analysis of the MD ensemble was performed using a cut-off over the backbone atoms.[24] The structural analysis of the conformational ensemble involved assessing root-mean-square deviation (RMSD), radius-of-gyration (R_g), and Cα root-mean-square fluctuation (RMSF) using the tools gmx rms, gmx gyrate, and gmx rmsf, respectively. The RMSD was evaluated for the backbone atoms of the protein. The structure obtained after NVT and NPT equilibration was used as a reference structure to evaluate the RMSD. The dictionary of the secondary structure of proteins

(DSSP) program[25] was utilized to assess the secondary structure content of the during simulation by employing gmx do_dssp tool.

Elucidation of the inhibitory mechanism of peptides against hIAPP and Aβ$_{42}$ aggregation
The molecular docking and MD simulations has been employed to elucidate the binding mode and key interactions of the peptide inhibitors with hIAPP and Aβ monomer and protofibril model structure. The MD simulations in explicit water provides insights into the molecular mechanism of inhibition of hIAPP and Aβ aggregation by peptide inhibitors. The key interactions and inhibitory mechanism of peptide inhibitors against hIAPP and Aβ$_{42}$ aggregation has been evaluated using computational techniques.

Library generation: The amino acids are grouped into several classes based upon the similarity in their side chains. The general chemical properties and nature of the side chain are considered while grouping amino acids as depicted in **Table 2.1**. We designed peptide libraries by replacing amino acids of hIAPP sequence-based peptides [hIAPP$_{18-22}$ (HSSNN)] and Aβ$_{42}$ sequence-based peptides [Aβ$_{32-35}$ (RIIGL)] with amino acids present in the similar group.

Screening of designed peptide libraries: The Aβ$_{32-35}$ (RIIGL) based pentapeptide library has been generated and screened using AutoDock Vina and PyRx tools. MD simulations in explicit water was performed to elucidate the structural changes in Aβ$_{42}$ monomer/protofibril upon top hit pentapeptide binding. The inhibitory mechanism of the pentapeptides was evaluated against Aβ$_{42}$ aggregation using computational techniques.

Table 2.1: The grouping of amino acids based upon similarity in their side chains. The amino acids are categorized as nonpolar aliphatic, polar uncharged, aromatic, positively charged, and negatively charged. The hydrophobicity index is mentioned for each amino acid.

Amino acid	Symbol	Hydropathy index
Glycine (nonpolar, aliphatic)	G	–0.4
Alanine (nonpolar, aliphatic)	A	1.8
Valine (nonpolar, aliphatic)	V	4.2
Isoleucine (nonpolar, aliphatic)	I	4.5
Leucine (nonpolar, aliphatic)	L	3.8
Proline (nonpolar, aliphatic)	P	1.6
Methionine (nonpolar, aliphatic)	M	1.9
Serine (polar, uncharged)	S	–0.8
Threonine (polar, uncharged)	T	–0.7
Cysteine (polar, uncharged)	C	2.5
Asparagine (polar, uncharged)	N	–3.5

Glutamine (polar, uncharged)	Q	–3.5
Phenylalanine (aromatic)	F	2.8
Tyrosine (aromatic)	Y	–1.3
Tryptophan (aromatic)	W	–0.9
Lysine (positively charged)	K	–3.9
Arginine (positively charged)	R	–4.5
Histidine (positively charged)	H	–3.2
Aspartic acid (negatively charged)	D	–3.5
Glutamic acid (negatively charged)	E	–3.5

The molecular docking based virtual screening has been performed using AutoDock Vina and PyRx tools to screen an $hIAPP_{18-22}$ (HSSNN) based pentapeptide library. The top ten leads were subjected to more extensive screening based on the binding free energies between hIAPP monomer and designed pentapeptides using MM-PBSA method. Finally, MD simulations in explicit water has been performed to elucidate the structural changes in hIAPP monomer upon pentapeptide binding.

2.3 Validation of the simulation data with experiment

To validate the results of the MD simulations, the computational data has been compared with the experimental data. A comprehensive comparison of simulation data with the available experimental results that include the comparison between primary Cα, Cβ NMR chemical shifts, as well as the computational three bond *J*–coupling ($^3J_{NH\text{-}H\alpha}$) data has been done to check the accuracy of the simulation data. The NMR chemical shifts of Cα and Cβ atoms of the central member of the conformational cluster with the highest population were calculated by SHIFTX2[26] and compared with experimental chemical shifts. The scalar *J*–coupling ($^3J_{NH\text{-}H\alpha}$) constants were calculated by evaluating the dihedral angles ϕ and ψ using the Karplus equation.[27] The parameter set was used in which A= 6.4, B= –1.4, and C= 1.9.[28]

2.4 Solid phase peptide synthesis

Solid phase peptide synthesis (SPPS) was initially invented by Robert Bruce Merrifield.[29] The process of solid phase peptide synthesis begins with reaction of polystyrene resin with the carboxy terminal of Fmoc (Fluorenyloxymethylcarbonyl) protected amino acid (**Figure 2.2**). There are two types of protecting groups that are accessible, named as Fmoc and Boc (tertbutyloxycarbonyl). Most peptide synthesis currently use Fmoc-protected amino acids since the Boc approach needs a powerful cleaving agent, such as, hydrogen fluoride. Additionally,

the Fmoc protective group is eliminated using a solution of 20% piperidine (v/v) in dimethylformamide (DMF), a basic deprotecting agent. Subsequently, the unbound N-terminus of an amino acid attached to the solid resin support participates in a reaction with another amino acid possessing a free C-terminus and a protected N-terminus with Fmoc. The necessary sequence was finally be synthesised after several rounds of deprotection, washing, and coupling. Then, the peptide is separated from the resin, causing any side chain protective groups to be eliminated. Generally, trifluoroacetic acid (TFA) is utilised as a cleaving agent. The manual solid phase synthesis of the designed peptides has been performed. The synthesized peptides was purified by HPLC and characterized by various techniques: HRMS.

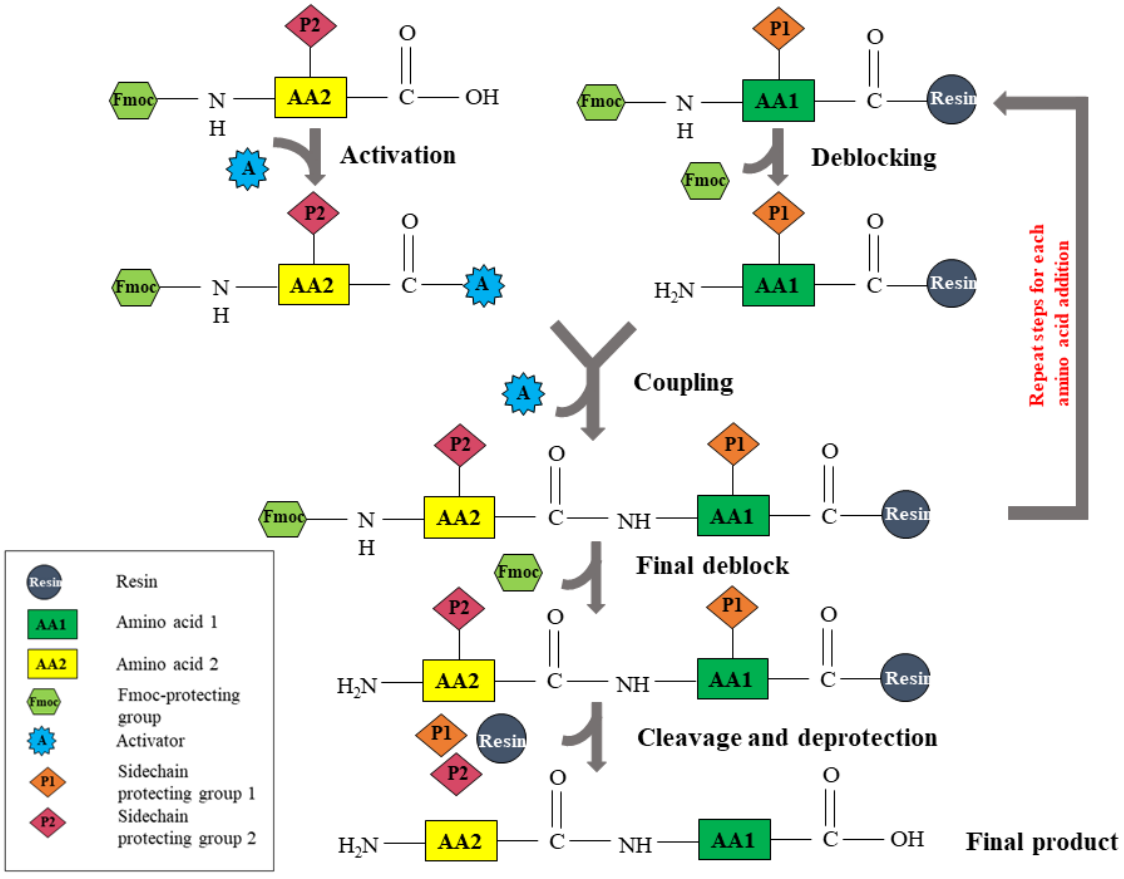

Figure 2.2: General scheme of steps involved in Solid phase peptide synthesis.

General method for the synthesis of pentapeptides: All pentapeptides were synthesized was conducted through the solid-phase peptide synthesis methodology using Rink amide resin (mesh size: 100-200) as the solid support, employing Fmoc-protection-deprotection cycles.[30] The synthesis of the pentapeptide started from the 5th amino acid (amidated C-terminus) and

proceeded towards the 1st amino acid (uncapped N-terminus). The Rink amide resin solid support was initially loaded with the 5th amino acid. The 5th amino acid was the first to become bonded to the resin. All the pentapeptides were made using Fmoc-protected Rink amide resin, which is commercially available. The resin was treated with 35% piperidine in DMF for 30 minutes, followed by three washes with DCM, DMF, and DCM for Fmoc deprotection. Three equivalents of Fmoc-protected amino acids, DIPEA, and HOBt were employed as an activator base, in addition to DMF serving as the solvent to couple each successive amino acid. The accomplishment of each coupling reaction was regularly confirmed through Kaiser's test.

Peptide Cleavage: To release the synthesized peptides from the resin, a mixture of 5% water, 5% thioanisole, 82% TFA, 5% phenol, and 2.5% EDT (1,2-ethanedithiol) was used. The reaction proceeded with continuous shaking for 3 h using a vibrax shaker. After completion of the reaction, the resin suspension underwent filtration, and the collected filtrate was gradually added to cold diethyl ether to achieve thorough precipitation. Ultimately, the resulting precipitate was isolated through centrifugation at 4°C with a speed of 6000 rpm. To ensure purity, all peptides underwent purification utilizing a C-18 reversed-phase high-performance liquid chromatography (RP-HPLC) column. Characterization of the peptides was achieved through HRMS, and they were then stored in a freezer at -20°C for future applications.

Peptide Purification: The preliminary purification of peptides (1 mg/mL) included dissolving them in a mixture of water and methanol (1:1; v/v), which was subsequently introduced into a preparative RP-HPLC system (Agilent Technologies 1260 Infinity series system). This process operated at 210 nm with a flow rate of 1 mL/min. The mobile-phase solvents A and B consisted of 0.1% TFA in acetonitrile (CH_3CN) and 0.1% TFA in water, respectively. The system was programmed to operate for 30 minutes, employing a linear gradient spanning from 10% to 70% of mobile-phase B. The pure peptide fractions were gathered and subsequently dissolved in a minimal amount of t-butanol/water solution. The resulting solution underwent lyophilization, yielding a white powder with a fluffy texture.

Lyophilization of peptides: Lyophilization was carried out using a freeze drier to improve the stability of peptides. The peptides were dissolved in a mixture of butanol in water (4:1), pre-frozen at -80°C, and then lyophilized at -100°C at 0–10 mTorr until a fluffy appearance was observed (approx. 24 hours). Peptides were kept at -80°C.

Peptide analysis: Analytical RP-HPLC (Agilent Technologies 1260 Infinity series system) was employed to assess the purity of peptides. This operated at 210 nm with a flow rate of 1 mL/min, employing the same mobile-phase solvent system as previously described. The system was operated for 10 minutes with a gradient ranging from 10% to 60% of mobile-phase B (0.1% TFA in water). The purity of the peptides was assessed and found to be in the range of 92% to 100%. Subsequently, the peptides underwent characterization through high-resolution mass spectrometry (HRMS). The molecular weights of the synthesized pentapeptides are shown in Table 3.

2.5 Inhibition of $A\beta_{42}$ fibrillar aggregates and disassembly of preformed $A\beta_{42}$ fibrils

$A\beta_{42}$ fibril inhibition and disassembly properties of the synthesized peptides has been evaluated using *in situ* kinetic Thioflavin T (ThT) fluorescence assay. ThT (a cationic benzothiazole dye) binds to β-sheet-rich structures to yield a shifted and enhanced fluorescent signals.[31] As a result, it can be used to detect selectively β-sheet aggregates of Aβ. Fluorescence was measured at an excitation wavelength of 435 nm and emission was measure at 485 nm by using fluorescence spectrophotometer. Inhibitor (synthesized peptides) generally works by binding to Aβ and they have the potential to disrupt the binding of ThT to aggregate structure, which can render false positive results. Thus, it is necessary to first evaluate whether peptide competes for binding site with ThT. Hence, a competitive ThT binding assay has been performed by adding synthesized peptides to a solution of preformed Aβ fibrils. Later, aggregation assays has been performed to assess the ability of the synthesized peptides to inhibit Aβ aggregation and to disaggregate the preformed Aβ fibrils. The inhibition/disaggregation activity has been calculated by the percentage reduction in the amyloid-bound ThT fluorescence of the Aβ-inhibitor mixture as compared to that of the Aβ alone. Further, transmission electron microscopy (TEM) (give the morphological changes of aggregates formed in a mixture of Aβ and inhibitor) has been employed to support the results obtained from ThT fluorescence assay.

2.6 References

1. J. Harvey, Computational Chemistry. Oxford University Press, 2018.
2. Alder, B. J.; Wainwright, T. E. Studies in molecular dynamics. II. Behavior of a small number of elastic spheres. *J. Chem. Phys.* **1960**, *33*, 1439-1451.
3. McCammon, J.A.; Gelin, B.R.; Karplus, M. Dynamics of folded proteins. *Nature* **1977**, *267*, 585–590.
4. Karplus, M.; McCammon, J.A. Molecular dynamics simulations of biomolecules. *Nat. Struct. Biol.* **2002**, *9*, 646–652.
5. Daan Frenkel and Berend Smit. *Understanding Molecular Simulation*. Academic Press, Inc. 6277 Sea Harbor Drive Orlando, FL, United States, 2001.
6. Schlick, T.; Barth, E.; Mandziuk, M. Biomolecular dynamics at long timesteps: bridging the timescale gap between simulation and experimentation. *Ann. Rev. Biophys. Biomol. Struct.* **1997**, *26*, 181–222.
7. Cornell, W.D.; Cieplak, P.; Bayly, C.I.; Gould, I.R.; Merz, K.M.; Ferguson, D.M.; Spellmeyer, D.C.; Fox, T.; Caldwell, J.W.; Kollman, P.A. A second generation force field for the simulation of proteins, nucleic acids, and organic molecules. *J. Am. Chem. Soc.* **1995**, *117*, 5179–5197.
8. Oostenbrink, C.; Villa, A.; Mark, A.E.; Van Gunsteren, W.F. A biomolecular force field based on the free enthalpy of hydration and solvation: the GROMOS force-field parameter sets 53A5 and 53A6. *J. Comput. Chem.* **2004**, *25*, 1656–1676.
9. Jorgensen, W.L.; Tirado-Rives, J. The OPLS [optimized potentials for liquid simulations potential functions for proteins, energy minimizations for crystals of cyclic peptides and crambin. *J. Am. Chem. Soc.* **1988**, *110*, 1657–1666.
10. MacKerell Jr, A.D.; Bashford, D.; Bellott, M.L.D.R.; Dunbrack Jr, R.L.; Evanseck, J.D.; Field, M.J.; Fischer, S.; Gao, J.; Guo, H.; Ha, S.; Joseph-McCarthy, D. All-atom empirical potential for molecular modeling and dynamics studies of proteins. *J. Phys. Chem. B* **1988**, *102*, 3586–3616.
11. van Gunsteren, W.F.; Huenenberger, P.H.; Mark, A.E.; Smith, P.E.; Tironi, I.G. Computer simulation of protein motion. *Comput. Phys. Commun.* **1995**, *91*, 305–319.
12. Schlick, T. Molecular modeling and simulation: an interdisciplinary guide; Springer: New York, NY, **2002**.
13. (a) Guillot, B.; Guissani, Y. How to build a better pair potential for water. *J. Chem. Phys.* **2001**, *114*, 6720–6733; (b) Kiss, P.T.; Baranyai, A. A systematic development of a polarizable potential of water. *J. Chem. Phys.* **2013**, *138*, 204507; (c) Kiss, P.T.; Baranyai, A. Clusters of classical water models. *J. Chem. Phys.* **2009**, *131*, 204310.
14. Yigzawe, T. M. Molecular dynamics simulation of the thermodynamic properties of water and atomistic fluids. Dissertation, Swinburne University of Technology: Melbourne, **2012**.
15. Wu, Y.; Tepper, H. L.; Voth, G. A. Flexible simple point-charge water model with improved liquid-state properties. *J. Chem. Phys.* **2006**, *124*, 024503.

16. Mao, Y.; Zhang, Y. Thermal conductivity, shear viscosity and specific heat of rigid water models. *Chem. Phys. Lett*, **2012**, *542*, 37-41.

17. Bussi, G.; Donadio, D.; Parrinello, M. Canonical sampling through velocity rescaling. *J. Chem. Phys.* **2007**, *126*, 014101.

18. Andersen, H. C. Molecular dynamics simulations at constant pressure and/or temperature. *J. Chem. Phys*. **1980**, *72*, 2384–2393.

19. (a) Nosé, S. A unified formulation of the constant temperature molecular dynamics methods. *J. Chem. Phys*. **1984**, *81*, 511–519; (b) Hoover, W. G. Canonical dynamics: Equilibrium phase-space distributions," *Phys. Rev. A* **1985**, *31*, 1695–1697.

20. Berendsen, H.J.C.; Postma, J.P.M.; Van Gunsteren, W.F.; Dinola, A.; Haak, J. R. Molecular dynamics with coupling to an external bath. *J. Chem. Phys*. **1984**, *81*, 3684–3690.

21. Lemons, D. S.; Gythiel, A. Paul langevin's 1908 paper "on the theory of brownian motion"["sur la théorie du mouvement brownien," cr acad. sci.(paris) 146, 530–533 (1908)]. *Am. J. Phys.* **1997**, *65*, 1079-1081.

22. Humphrey, W.; Dalke, A.; Schulten, K. VMD: visual molecular dynamics. *J. Mol. Graph*. **1996**, *14*, 33–38.

23. DeLano, W. L. The PyMol Molecular Graphics System; DeLano Scientific: San Carlos, CA, USA, 2002.

24. Daura, X.; Gademann, K.; Jaun, B.; Seebach, D.; van Gunsteren, W.F.; Mark, A.E. Peptide folding: when simulation meets experiment. *Angew. Chem. Int. Ed*. **1999**, *38*, 236–240.

25. Kabsch, W.; Sander, C. Dictionary of protein secondary structure: pattern recognition of hydrogen-bonded and geometrical features. *Biopolymers* **1983**, *22*, 2577–2637.

26. (a) Han, B.; Liu, Y.; Ginzinger, W. S.; Wishart, S. D. SHIFTX2: Significantly improved protein chemical shift prediction. *J. Biomol. NMR* **2011**, *50*, 43–57; (b) Neal, S.; Nip, A. M.; Zhang, H.; Wishart, D. S. Rapid and accurate calculation of protein ^{1}H, ^{13}C and ^{15}N chemical shifts. *J. Biomol. NMR* **2003**, *26*, 215–240.

27. Karplus, M. Vicinal proton coupling in nuclear magnetic resonance. *J. Am. Chem. Soc.* **1963**, *85*, 2870–2871.

28. Pardi, A.; Billeter, M.; Wüthrich, K. Calibration of the angular dependence of the amide proton-Cα proton coupling constants, ^{3}JHNα, in a globular protein: use of ^{3}JHNα for identification of helical secondary structure. *J. Mol. Biol*. **1984**, *180*, 741−751.

29. (a) Chan, W. C.; White, P. D., Eds. Fmoc solid phase peptide synthesis: a practical approach; Oxford University Press: New York, **2000**; (b) Samisetti, S. M. S. Thesis, Eastern Michigan University, Michigan, USA, **2007**.

30. (a) Sabatino, G.; Papini, A.M. Advances in automatic, manual and microwave-assisted solid-phase peptide synthesis. *Curr. Opin. Drug Discov. Dev.* **2008**, *11*, 762–770; (b)

Fields, G.B.; Noble, R.L. Solid phase peptide synthesis utilizing 9-fluorenylmethoxycarbonyl amino acids. *Int. J. Pep. Protein Res.* **1990**, *35*, 161–214.

31. Gade Malmos, K.; Blancas-Mejia, L. M.; Weber, B.; Buchner, J.; Ramirez-Alvarado, M.; Naiki, H.; Otzen, D. ThT 101: a primer on the use of thioflavin T to investigate amyloid formation. *Amyloid* **2017**, *24*, 1-16.

Chapter 3

Deciphering the inhibitory mechanism of hIAPP-derived fragment peptide against hIAPP aggregation in Type 2 Diabetes

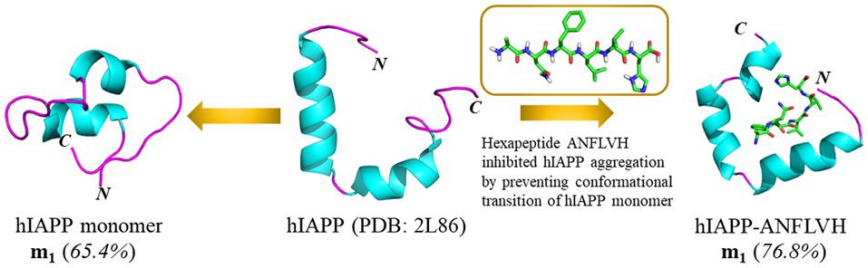

The molecular mechanism by which human islet amyloid polypeptide (hIAPP)-derived fragment peptide (ANFLVH) blocked the hIAPP aggregation. The conformational clustering analysis highlighted an increase in the percentage population of microstate 1 ($\mathbf{m_1}$) of the hIAPP-ANFLVH complex, which depicts higher conformational homogeneity of hIAPP in the presence of ANFLVH. The MD simulations demonstrated that ANFLVH inhibited hIAPP aggregation by stabilizing the non-aggregation-prone helical conformation of the hIAPP monomer.

Kaur, A.; Goyal, B. Deciphering the inhibitory mechanism of hIAPP-derived fragment peptide against hIAPP aggregation in type 2 diabetes. *ChemistrySelect* **2020**, *5*, 13341–13350.

3.1 Introduction

Protein misfolding diseases (PMDs) are diseases in which peptide or protein in some ways tend to misfold, aggregate, and accumulate in tissues of the human body.[1] PMDs include several systemic disorders like type 2 diabetes (T2D), familial amyloid polyneuropathy, secondary amyloidosis, and a diverse range of neurodegenerative diseases such as Parkinson's disease, Alzheimer's disease, Huntington disease, and transmissible spongiform encephalopathies.[2] T2D is a critical metabolic disease described by insulin resistance condition and gradual failure of β-cell function, which ultimately leads to hyperglycemia and disturbed insulin secretion. An estimated 463 million adults are living with diabetes worldwide.[3] This number will increase to 700 million by 2045 and the number of people with diabetes will significantly increase in low- and middle-income countries.[3,4]

One of the pathological hallmarks of T2D is the presence of fibrillar amyloid deposits[5] and soluble oligomers formed by the aggregation of human islet amyloid polypeptide (hIAPP).[6] The hIAPP, also known as human amylin, is a neuropancreatic soluble hormone secreted along with insulin and plays a major role in controlling the blood glucose level in the human body.[7] The mature hIAPP consists of 37 residues with an amidated C-terminus and possesses a disulfide bond between Cys2 and Cys7. In the pancreatic tissues of T2D patients, oligomers and fibrillar amyloid deposits of hIAPP were found. The increasing shreds of evidence demonstrated that the low molecular weight soluble oligomers are the most toxic agents, which are formed during the early stages of hIAPP aggregation.[6a] The toxic aggregates of hIAPP are believed to contribute to the loss of pancreatic β-cells and eventually T2D. However, the molecular mechanism by which hIAPP monomer forms soluble oligomers and subsequently fibrillar amyloid deposits remain unclear due to the transient nature of the species involved in the aggregation pathway.

The characterization of a monomeric form of hIAPP in solution and its molecular mechanism of aggregation is important to understand its cellular toxicity and role in T2D.[6a,d] This will help in the design of inhibitors that can slow down hIAPP aggregation or redirect it to a pathway, which results in nontoxic aggregates, and may present a new therapeutic strategy for the treatment of T2D. Various inhibitors comprising natural compounds[8] and small-molecules[9] have been reported as inhibitors of hIAPP aggregation. However, small-molecule

inhibitors lack specificity, undergo rapid metabolism, and are unable to block interactions involving large protein-protein interfaces, which, in turn, hinder their clinical applications.

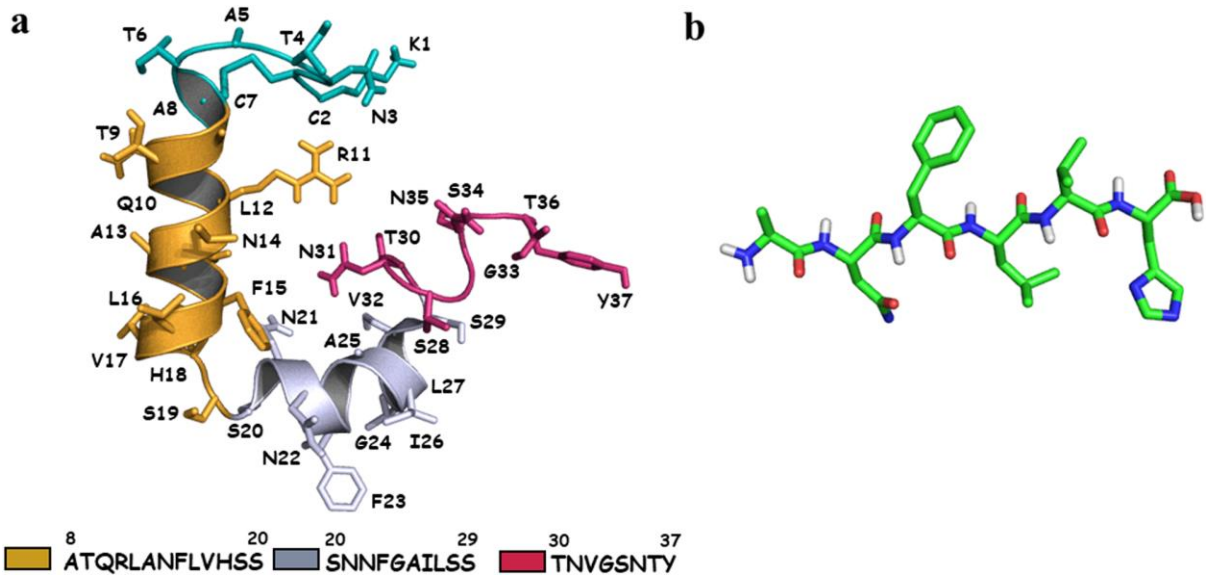

Figure 3.1: The initial structures of hIAPP (PDB ID: 2L86) and ANFLVH are shown in panel a, and b, respectively. The hIAPP is shown in the cartoon representation with key amyloidogenic regions (8–20, 20–29, and 30–37) in different colours and ANFLVH is shown in the stick representation. The residues of hIAPP are shown in the stick representation.

The peptide-based inhibitors provide an alternative option against hIAPP aggregation due to their biocompatibility, the feasibility of synthesis and modification, and weak immunogenicity.[10] A large number of peptides derived from the amyloidogenic fragments of hIAPP or by slight structural changes in these fragments have been evaluated as inhibitors of hIAPP aggregation and hIAPP-induced cytotoxicity.[11] In addition to peptides derived from the amyloidogenic fragments of hIAPP, several other peptide-based inhibitors have been tested against hIAPP aggregation and hIAPP-induced cytotoxicity.[12] Potter et al. synthesized numerous peptides derived from the sequence of IAPP and identified hexapeptide ANFLVH as a potent inhibitor of IAPP aggregation.[13] ANFLVH inhibited IAPP aggregation *in vitro* and in human islet cultures, which significantly enhanced the islet cell viability. However, the molecular mechanism of inhibition of hIAPP aggregation in presence of ANFLVH remains unclear. In this regard, MD simulations have been conducted in the current study to elucidate the inhibitory mechanism of ANFLVH against hIAPP aggregation.

3.2 Computational details

3.2.1 Molecular docking

AutoDock Vina[14] was utilized for conducting the molecular docking. In this study, the protein was kept rigid and the ligand was kept flexible. The protein was prepared by retrieving the NMR structure of hIAPP from Protein Data Bank (PDB: 2L86) and this was used as the receptor for molecular docking.[15] The hexapeptide (ANFLVH) was drawn using Maestro software.[16] For molecular docking, the PDBQT files for the hIAPP and ANFLVH were prepared. The grid spacing was kept as default and grid box measurements were taken as 36 × 34 × 20 Å with grid center at x = 3.067, y = 1.521 and z = 0.034 to cover the hIAPP-ANFLVH complex. The configuration file used for the docking process was also prepared along with the addition of hydrogens and the Gasteiger charges.

Table 3.1: The binding energy (kcal/mol) between hIAPP and ANFLVH. The residues of hIAPP involved in the hydrophobic contacts and hydrogen bonds with ANFLVH are listed.

Model system	AutoDock binding energy (kcal/mol)	Residue involved in hydrophobic contacts	Residues participating in intermolecular hydrogen bonds with ANFLVH		
			Residue and atom of hIAPP monomer	Residue and atom of ANFLVH	Hydrogen bond distance
hIAPP monomer	–6.0	Asn3, Thr4, Leu12, Phe15, Asn21, Val32, Ser34	Arg11 (SC[a]: H) Asn31 (SC: H) Asn35 (MC: H)	Phe3 (MC[b]: O) Asn2 (SC: O) His6 (MC: O)	0.29 nm 0.27 nm 0.30 nm

[a] SC: side chain; [b] MC: main chain

3.2.2 Molecular dynamics (MD) simulations

The MD simulations were executed using the GROMACS 5.0.7 version[17] including the GROMOS 54A7 force field[18] and a simple point charge (SPC) water model.[19] The GROMOS force field has been extensively utilized for the conformational analysis of hIAPP and amyloid-β peptide.[20] The hIAPP and best-docked pose complex of hIAPP-ANFLVH were selected for MD simulations and these two systems are named as hIAPP and hIAPP-ANFLVH complex, respectively. The systems were placed within a cubic box of dimensions 5.5 nm × 5.5 nm × 5.5 nm and neutralized by adding sufficient Cl^- ions as per the literature.[21] Both systems were solvated in a cubic box of water molecules with a minimum distance of 1.5 nm from the wall. A total number of 5279 and 5211 water molecules were added in the

simulation box of hIAPP and hIAPP-ANFLVH complex, respectively. Both systems underwent protonation according to the physiological pH. The N-terminal and C-terminal of the hIAPP were kept protonated and deprotonated, respectively. The particle mesh Ewald method was employed for calculating the electrostatic energy.[22] The cut-off distances for the calculation of Coulomb and van der Waals interaction were 1.0 nm and 1.0 nm, respectively. The LINCS algorithm was employed to constrain bond lengths, while energy minimization utilized the steepest descent algorithm with a maximum step size of 0.01 nm and a tolerance of 1000 kJ/mol/nm.[23] The systems were equilibrated under NVT for 500 ps at 300 K and the second phase of equilibration under NPT for 500 ps at 1 bar. In all MD simulations, the temperature was maintained at 300 K using a modified Berendsen thermostat,[24] and the pressure was maintained at 1 bar using Parrinello–Rahman barostat.[25] Finally, the systems were subjected to 200 ns MD simulation and the atom coordinates were recorded every 10 ps during the simulation for later analyses. To ensure the precision of MD simulations, both simulations were repeated for 200 ns with different initial velocities and the atom coordinates were recorded during the simulation for comparison purposes.

GROMACS tools were employed in conjunction with Visual Molecular Dynamics (VMD)[26] and PyMOL[27] for visualization and analysis of MD trajectories. The conformational clustering analysis of the MD ensemble was conducted utilizing a cut-off of 0.15 nm over the backbone atoms.[28] The structural analysis of the conformational ensemble involved assessing root-mean-square deviation (RMSD), radius-of-gyration (R_g), and Cα root-mean-square fluctuation (RMSF) using tools gmx rms, gmx gyrate, and gmx rmsf, respectively. The RMSD was evaluated for the backbone atoms of the protein. The structure obtained after NVT and NPT equilibration was used as a reference structure to evaluate the RMSD. The secondary structure of proteins was analyzed using the Dictionary of Secondary Structure of Proteins (DSSP) program[29] to estimate the secondary structure content of the hIAPP and hIAPP-ANFLVH complex. Further, the smallest distance between residue pairs was calculated based on the distance matrices generated using g_mdmat built-in function in the GROMACS package. The graphs obtained from various analyses were plotted using Origin 9.0 software. The $^{3}J_{NH\text{-}H\alpha}$ coupling constants were computed from the dihedral angles ϕ and ψ using parameters as reported by Vogeli et al.[30] in the Karplus equation.[31]

3.2.3 Evaluation of binding free energy and free energy landscape (FEL) analysis

The binding free energy calculations for hIAPP-ANFLVH complex and FEL analysis were performed in accordance with our previously reported study.[32] The $\Delta G_{binding}$ reported is the relative binding free energy with the contribution of conformational entropy was ignored aligning with earlier studies.[33] The binding free energy was assessed through molecular mechanics Poisson−Boltzmann surface area (MM-PBSA) calculations utilizing the g_mmpbsa.[34] The FEL maps were constructed using the GROMACS tool gmx sham.

3.3 Results and discussion

3.3.1 Molecular docking of ANFLVH with hIAPP to predict the binding energy and key interactions

In the present study, the molecular docking of ANFLVH with hIAPP monomer was conducted using the AutoDock Vina program (**Figure 3.1**). The binding energy of the most stable binding pose between ANFLVH and hIAPP was found to be –6.0 kcal/mol (**Table 3.1**). The negative binding energy favour the binding of ANFLVH with hIAPP.

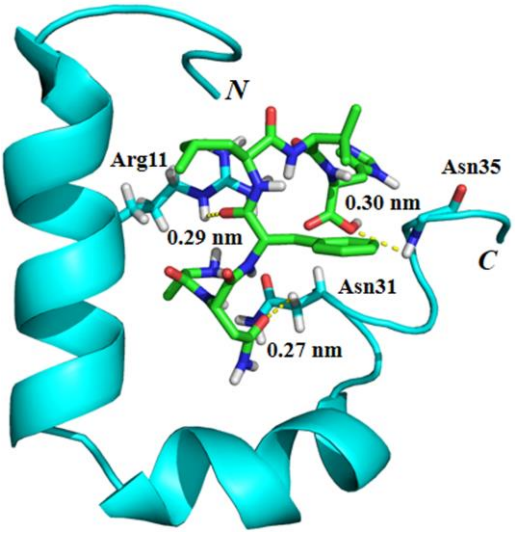

Figure 3.2: The most stable binding pose of hIAPP with ANFLVH is shown. ANFLVH displayed three hydrogen bonds with hIAPP residues. The hydrogen bonds are depicted as dashed lines, indicating their distance in nm.

The best-docked binding pose displayed three hydrogen bonds between ANFLVH and hIAPP (**Figure 3.2**). The Asn and His residues of ANFLVH were involved in the hydrogen bonding interactions with Asn31 and Asn35 residues of hIAPP with a hydrogen bond distance of 0.27 nm and 0.30 nm, respectively (**Figure 3.2**). The third hydrogen bond (0.29 nm) was formed

between the Phe of ANFLVH and Arg11 of hIAPP (**Figure 3.2**). The Asn3, Thr4, Leu12, Phe15, Asn21, Val32, and Ser34 residues of hIAPP display hydrophobic contacts with ANFLVH (**Figure 3.3**). To elucidate the structural stability of hIAPP in the presence of ANFLVH and to understand the interactions of ANFLVH with hIAPP at the atomic level, MD simulations of hIAPP and hIAPP-ANFLVH complex have been performed. The MD simulations demonstrated that ANFLVH inhibited hIAPP aggregation by stabilizing the non-aggregation-prone helical conformation of the hIAPP monomer.

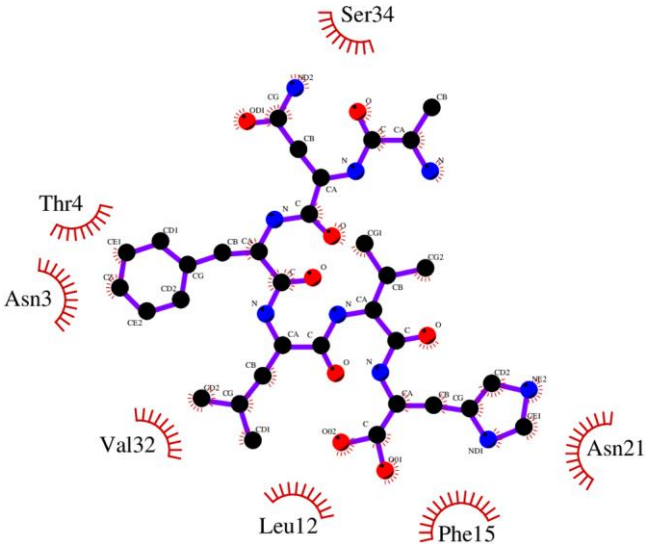

Figure 3.3: The 2D interaction map illustrates the hydrophobic contacts between hIAPP residues and ANFLVH.

3.3.2 Comparison between experimental and simulated NMR data

The NMR chemical shifts for the amide NH and Hα atoms of simulated MD ensembles of hIAPP monomer were compared with experimental data using the SHIFTX2 program.[35] The average experimental chemical shift values of amide NH and Hα for hIAPP were noted to be 8.09 Hz and 4.19 Hz, respectively,[15] which are comparable with the simulated average chemical shift values of amide NH (8.20 Hz) and Hα (4.30 Hz) (**Figure 3.4**). Therefore, the calculated chemical shift accessed from MD simulated data is comparable with experimental amide NH and Hα chemical shifts of hIAPP reported by Nanga et al.[15]

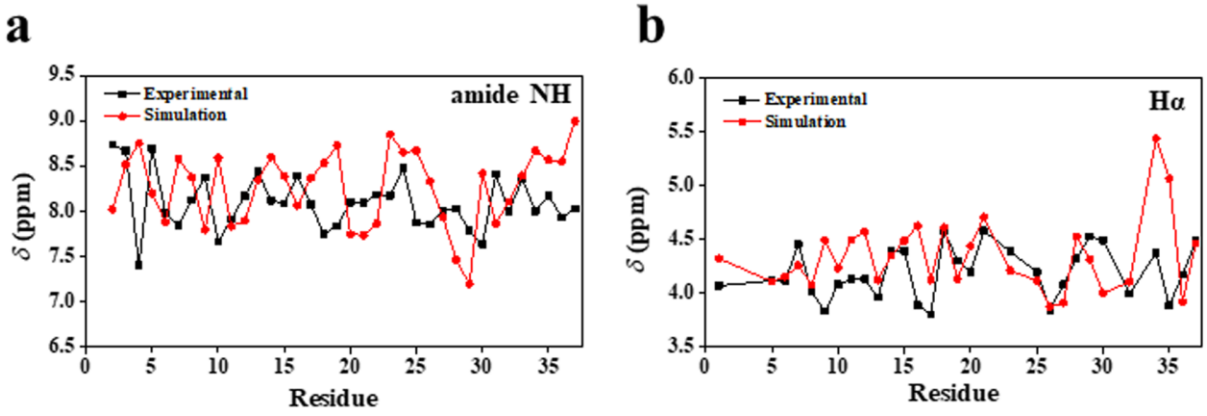

Figure 3.4: The comparison of computational (δ_{sim}) and experimental (δ_{exp}) NMR chemical shifts of amide NH and Hα atoms of hIAPP are shown in panel a, and b, respectively.

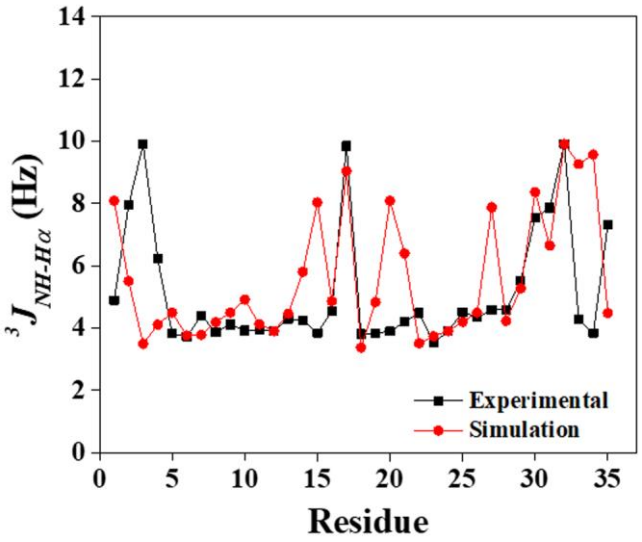

Figure 3.5: Comparison of simulated $^3J_{NH\text{-}H\alpha}$ coupling constants of hIAPP residues (red) with experimental measurements (black).

The three-bond coupling interaction between amide NH and Hα protons provides a more reflective measure of peptide conformations compared to primary chemical shifts.[36] Therefore, ensemble-averaged $^3J_{NH\text{-}H\alpha}$ constants of the hIAPP residues were computed and compared with experimental data (**Figure 3.5**). The $^3J_{NH\text{-}H\alpha}$ coupling constant values for hIAPP exhibit a strong correlation with experimental values. The average value of $^3J_{NH\text{-}H\alpha}$ coupling constant value generated from experimental hIAPP structure is noted to be 5.12 Hz which shows a good similarity with the average $^3J_{NH\text{-}H\alpha}$ coupling constant value of 5.57 Hz for MD simulation data. The agreement between computational and experimental NMR chemical shifts, as well as $^3J_{NH\text{-}H\alpha}$ coupling constant values, suggests that the generated MD

ensembles align well with the experimental data, affirming their suitability for subsequent structural analysis.

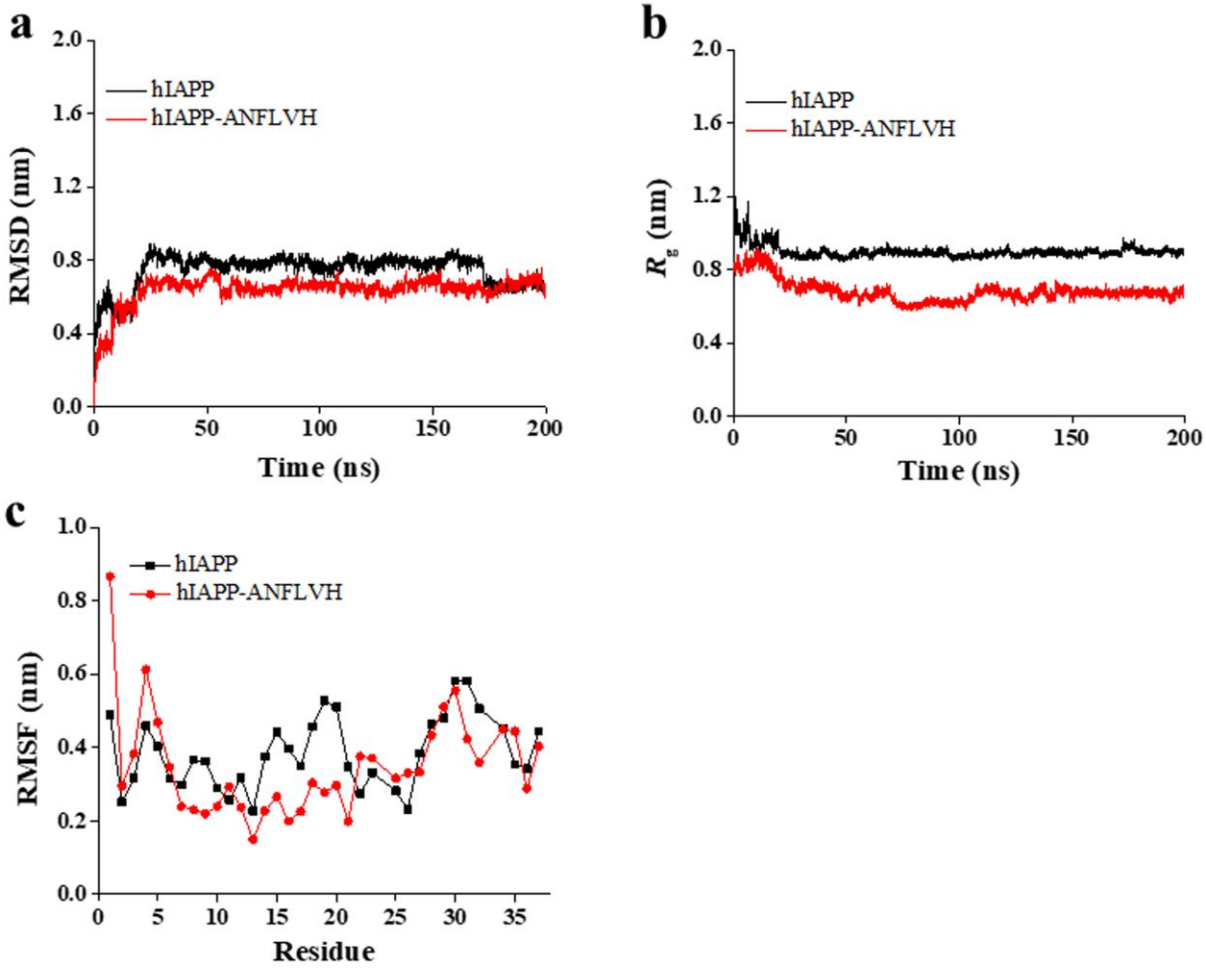

Figure 3.6: The root-mean-square deviation (RMSD) (panel a) and radius-of-gyration (R_g) (panel b) for hIAPP and hIAPP-ANFLVH complex as a function of simulation time in ns are shown. The root-mean-square fluctuation (RMSF) of each residue in hIAPP and hIAPP-ANFLVH are shown in panel c.

3.3.3 Structural stability of hIAPP in the presence of ANFLVH

The structural stability of hIAPP in the presence of ANFLVH was evaluated by root-mean-square deviation (RMSD) and radius-of-gyration (R_g) analysis (**Figure 3.6**). The average RMSD of hIAPP alone was 0.75 nm, whereas the average value was noted to be 0.63 nm for the hIAPP-ANFLVH complex (**Figure 3.6a**), which depicts higher structural stability of hIAPP-ANFLVH complex as compared to hIAPP. The RMSD values converge well within 200 ns simulation time for both the systems (**Figure 3.6a**), which indicated the convergence

of MD simulations. The RMSD has been considered as indicative of the convergence of MD simulations.[37]

The average R_g value for hIAPP and hIAPP-ANFLVH during the simulation was noted to be 0.90 nm and 0.68 nm, respectively (**Figure 3.6b**). A significant decrease in the R_g in the presence of ANFLVH indicates more compactness of the hIAPP structure. The compactness of hIAPP in the presence of ligand is consistent with the results of Patel et al.,[38] which depicted a lower value of R_g in the presence of various small molecules as compared to hIAPP alone. The study reported that catechins and the identified hit compounds (CID636525, CID44589219, Molport-001-806-035, and Molport-002-693-913) significantly affect the level of compactness of hIAPP. The previous studies highlighted that more extended hIAPP conformations with β-sheet rich structures are responsible for the aggregation of hIAPP into amyloid fibrils.[39]

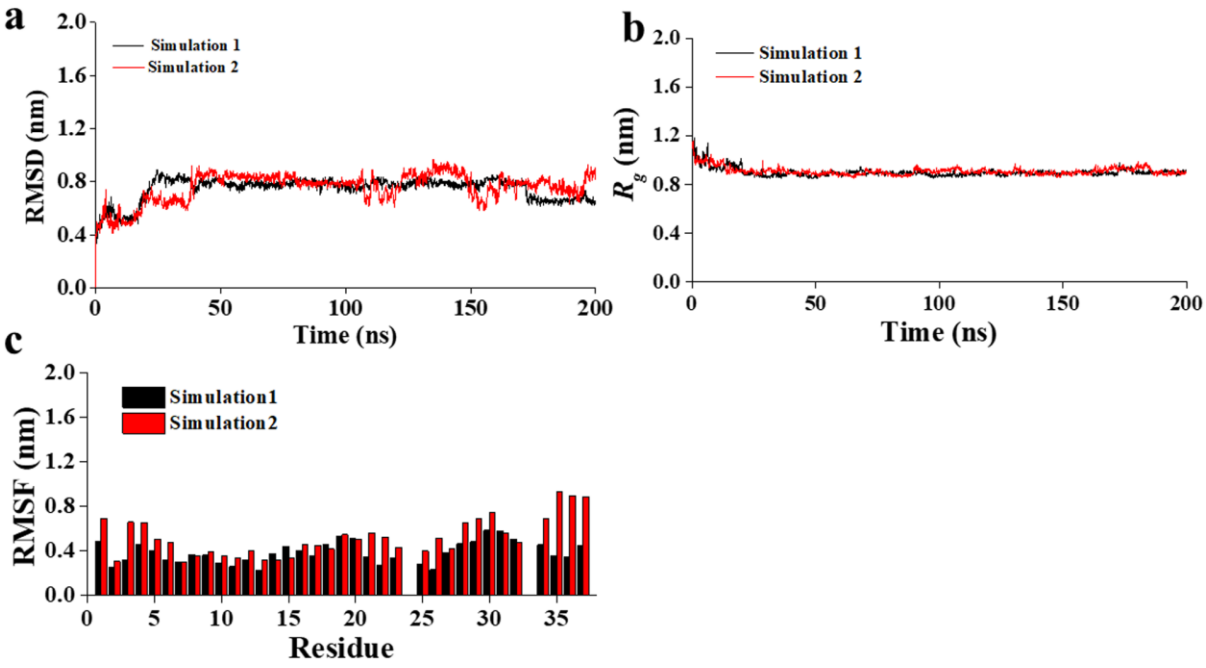

Figure 3.7: The root-mean-square deviation, RMSD, (panel a) and radius-of-gyration, R_g, (panel b) are plotted as a function of simulation time in ns for simulation 1 and simulation 2.

The root-mean-square fluctuation (RMSF) analysis highlighted that hIAPP residues fluctuate at a higher value for hIAPP alone as compared to the hIAPP-ANFLVH complex (**Figure 3.6c**). The region spanning residues 8–20 (ATQRLANFLVHSS) was identified as the key amyloidogenic region of hIAPP and undergo self-fibrillation into β-sheet fibrils with identical

morphology to *in vivo* amyloids.[40] A significant reduction in the RMSF value of hIAPP residues in the region (13–21) was observed in the presence of ANFLVH (**Figure 3.6c**), which highlights the higher structural stability of the amyloidogenic region in the presence of ANFLVH. These results are consistent with Patel et al.,[38] which highlighted the lower flexibility of hIAPP residues (region 15–23) in the presence of EGCG (Epigallocatechin gallate), GCG (Gallocatechin gallate), CID636525, CID44589219, Molport-001-806-035, and Molport-002-693-913. The RMSD and R_g distributions were evaluated for hIAPP monomer repeat simulations (**Figure 3.7**). The hIAPP monomer exhibited identical distributions of RMSD and R_g across simulations with different initial velocities, underscoring the repeatability and reliability of the MD simulations (**Figure 3.7a, b**). In addition, Cα RMSF of hIAPP residues displays almost identical fluctuations for both simulations (**Figure 3.7c**).

3.3.4 Conformational clustering analysis of hIAPP and hIAPP-ANFLVH complex

To characterize the conformational ensembles of hIAPP in the absence and presence of ANFLVH, the conformations obtained from MD simulations were clustered and relative population distributions of microstates are listed in **Table 3.2**.

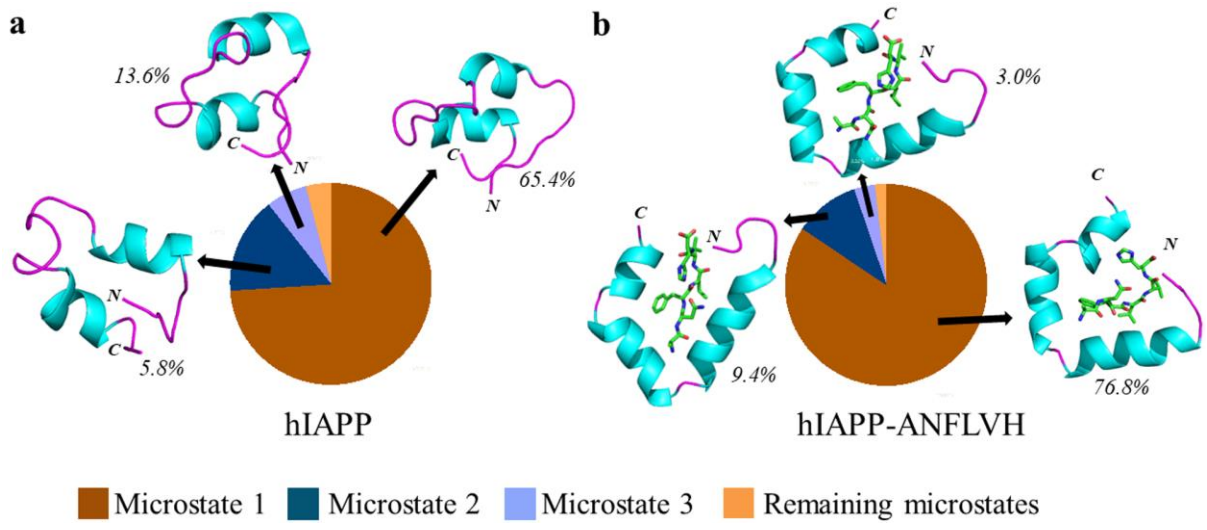

Figure 3.8: The representative conformations of the three most-populated microstates (**m_1**, **m_2**, and **m_3**) of hIAPP and hIAPP-ANFLVH complex are shown in the cartoon representation. The percentage population of corresponding microstates is shown underneath the structure.

The model systems were observed to reach equilibrium and stabilize with defined populations in the microstates. The representative member of the three highest-populated microstates of hIAPP and hIAPP-ANFLVH are shown in **Figure 3.8**. The MD ensemble of hIAPP consists of 76 microstates as compared to only 31 for the hIAPP-ANFLVH complex, which indicated enhanced conformational homogeneity of hIAPP monomer in the presence of ANFLVH. A large number of microstates observed in the conformational ensemble of hIAPP monomer is consistent with that of Dupuis et al.,[41] which reported diversified structural families in the clustering analysis indicating the sampling of helical and β-hairpin structures in the conformational ensemble of hIAPP monomer generated by all-atom replica exchange molecular dynamics (REMD) simulations. The percentage population of the three highest-populated microstates for hIAPP was 65.4%, 13.6%, and 5.8% as compared to 76.8%, 9.4%, and 3.0%, respectively, in the hIAPP-ANFLVH complex (**Figure 3.8**). An increase in the percentage population of $\mathbf{m_1}$ of the hIAPP-ANFLVH complex was observed, which highlights higher conformational homogeneity of hIAPP in the presence of ANFLVH. Notably, higher sampling of helix conformation was observed in the three most-populated microstates of hIAPP-ANFLVH as compared to hIAPP alone (**Figure 3.8**).

Table 3.2: The total number of microstates and percentage population of the three most-populated microstates ($\mathbf{m_1}$, $\mathbf{m_2}$, and $\mathbf{m_3}$) of hIAPP and hIAPP-ANFLVH during MD simulation in explicit water.

Model system	Number of microstates	Percentage population		
		$\mathbf{m_1}$	$\mathbf{m_2}$	$\mathbf{m_3}$
hIAPP	76	65.4	13.6	5.8
hIAPP-ANFLVH	31	76.8	9.4	3.0

3.3.5 Secondary structure analysis of hIAPP and hIAPP-ANFLVH complex

The secondary structure analysis of the hIAPP and hIAPP-ANFLVH complex was performed to characterize the effect of ANFLVH on the secondary structure of hIAPP (**Figure 3.9** and **Figure 3.10**). For hIAPP, the percentage population of helix, β-sheet, turn, coil, and bend conformations were noted to be 37 ± 3.05%, 8 ± 1.14%, 12 ± 1.76%, 29 ± 4.14%, and 13 ± 1.9%, respectively (**Table 3.3**).

In hIAPP, the N-terminal region (4–10) and region (23–27) mainly adopt helix conformation, which is in agreement with earlier reported experimental results.[15] The sampling of helical

conformation at the N-terminal residues in hIAPP monomer (**Figure 3.10a**) is consistent with that of Qiao et al.,[42] which reported that residues 4–7 in the N-terminal region of hIAPP monomer displayed notable α-helical propensity in the conformational ensemble generated by extensive MD simulations.

Table 3.3: The secondary structural component statistics for hIAPP and hIAPP-ANFLVH during MD simulation. The standard errors of the mean were evaluated by dividing the MD trajectory into four long, non-overlapping blocks.

Model system	Helix[a]	β–sheet[b]	turn	coil	bend
hIAPP	37 ± 3.05	8 ± 1.14	12 ±1.76	29 ± 4.14	13 ± 1.9
hIAPP-ANFLVH	41 ± 3.37	0 ± 0.02	18 ± 1.5	30 ± 2.52	9 ± 0.79

[a] helix is the sum of α–, π–, and 3_{10}–helix ; [b] β–sheet is the sum of β–strand and β-bridge

After 60 ns, the β-sheet conformation was mainly observed in N-terminal (region 2–4) and C-terminal residues (Ser34 and Asn35), which is consistent with the results reported by Tran et al.[43] In the hIAPP-ANFLVH complex, the percentage population of the helix, turn, coil, and bend conformations were 41 ± 3.37%, 18 ± 1.5%, 30 ± 2.52%, and 9 ± 0.79%, respectively, and complete absence of β-sheet was observed (**Figure 3.9**, **Table 3.3**). The absence of β-sheet structures in the conformational ensemble of the hIAPP-ANFLVH complex is consistent with circular dichroism (CD) results, which highlighted the prevention of the formation of β-sheet in hIAPP on the addition of ANFLVH peptide at equimolar or higher concentrations.[13] The results of the secondary structure analysis are consistent with Xuan et al., which reported that LA12 (LTPHKHHKHLHA) stabilized hIAPP in a random coil conformation, which, in turn, prevented the conformational transition to aggregation-prone β-sheet conformation and formation of hIAPP fibrils.[12d] Further, Lao et al. also highlighted the prevention of the formation of β-sheet conformation by hIAPP dimer in the presence of dopamine by employing replica-exchange MD simulations.[44] Dopamine displayed preferential binding with Arg11, Leu12, Phe15, His18, Phe23, Ile26, Leu27, and Tyr37 residues of hIAPP and prevented the β-sheets formation in the amyloidogenic regions of hIAPP.

In the presence of ANFLVH, helix content was increased and notably, no β-sheet content was sampled, which highlights the overall destabilization of the β-sheet structure and decreased aggregation tendency of hIAPP in the presence of ANFLVH. By employing MD simulations

and infrared experiments, Reddy et al. highlighted that the hIAPP monomer can adopt α-helical, random coil, and β-hairpin conformations in solution,[45] whereas rat IAPP sampled only α-helical, random coil conformations.[46] The study proposed that β-hairpin is a key intermediate in the hIAPP fibril formation pathway and the tendency of hIAPP monomer to adopt a stable β-hairpin facilitates the formation of hIAPP fibrils. The results of the present study are consistent with that of Reddy et al.,[45] as no β-sheet conformations were sampled in the presence of ANFLVH, which, in turn, depict reduced aggregation propensity of the hIAPP-ANFLVH complex as compared to hIAPP alone. This observation is also consistent with earlier studies by Dupuis et al.,[47] which highlighted that the β-strand content dominates in the early oligomeric species formed by hIAPP aggregation. Further, Guo et al. reported the formation of an intermediate structure displaying transient β-sheet character in the early oligomerization process of hIAPP, which later forms a stabilized hIAPP dimer structure.[48]

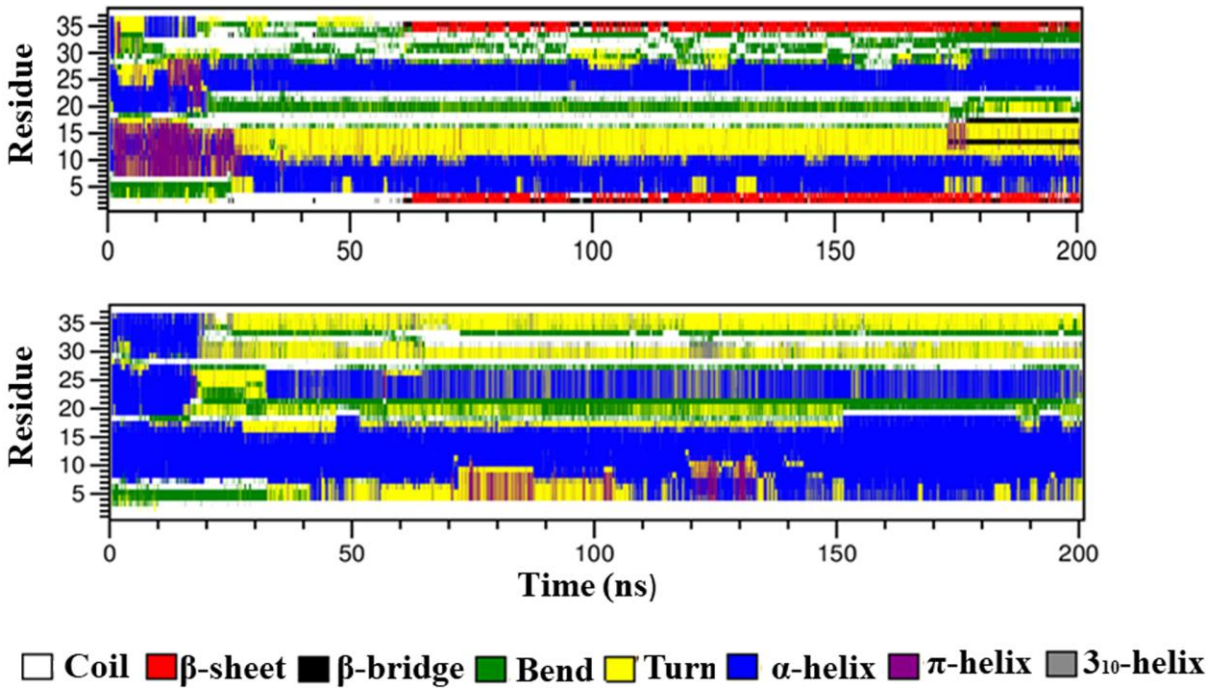

Figure 3.9: The evolution of the secondary structure component as a function of simulation time (ns) for hIAPP and hIAPP-ANFLVH are shown in the upper and lower panel, respectively. The secondary structure components are colour coded as shown underneath.

The per-residue secondary structure analysis was performed to get more information about secondary structure preferences of each residue in hIAPP alone and in the presence of ANFLVH. The helix, β-sheet, turn, coil, and bend content for each residue of hIAPP was shown in the absence and presence of ANFLVH (**Figure 3.10**). A substantial increase in the

helical content of residues spanning the region Thr6–Asn14 of hIAPP was observed in the presence of ANFLVH (**Figure 3.10a**). Notably, the number of residues adopting overall helix conformation increases significantly from 18 residues located in regions Lys1–Leu12, His18–Phe23 in hIAPP to 25 residues located in regions Lys1–Ala13, Val17–Asn21, Ala25–Asn31 in the hIAPP-ANFLVH complex (**Figure 3.10a**).

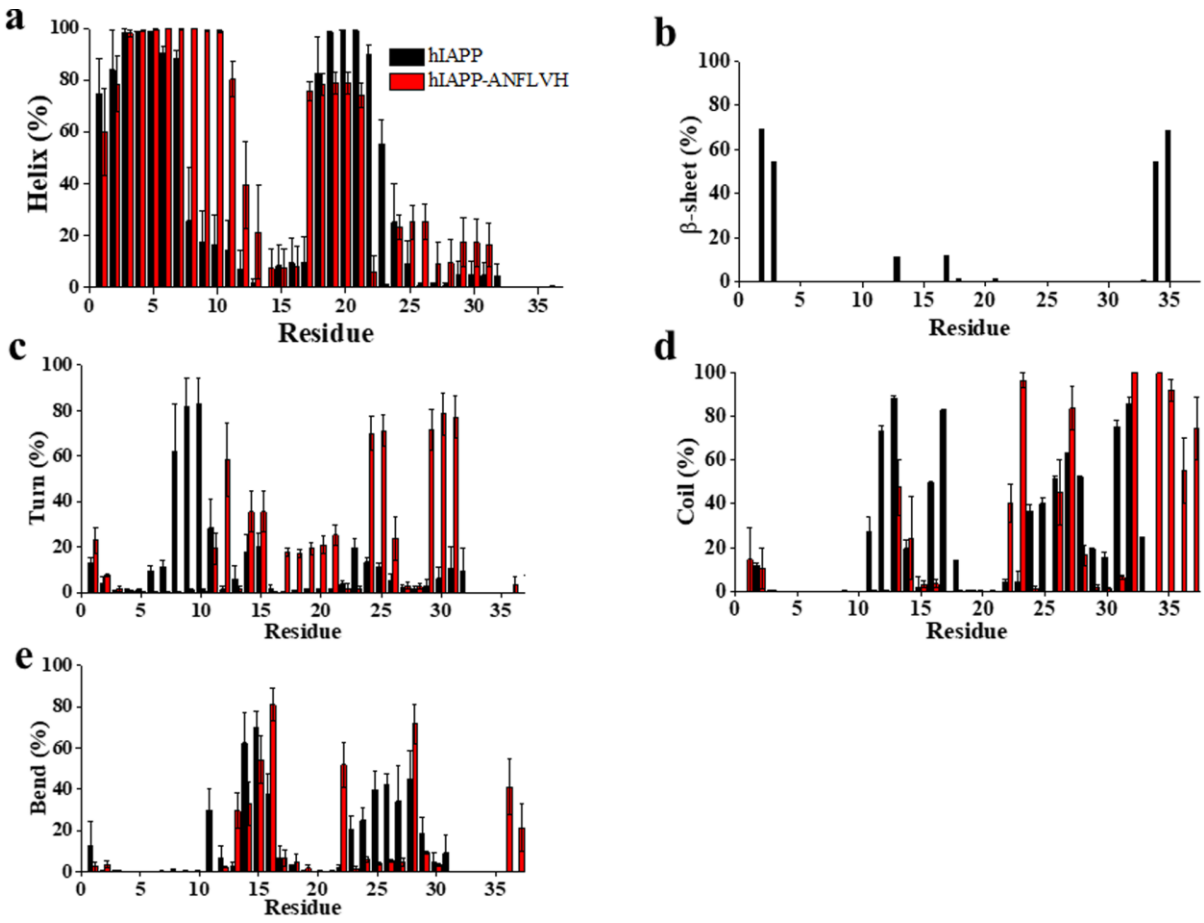

Figure 3.10: The per-residue helix, β-sheet, turn, coil, and bend content for hIAPP (black) and hIAPP-ANFLVH (red) are shown in panel a, b, c, d, and e, respectively. The standard errors of the mean were evaluated by dividing the MD trajectory into four long, non-overlapping blocks.

The β-sheet conformation prone to aggregation was observed at the N-terminal residues (Cys2 and Asn3) and C-terminal residues (Ser34 and Asn35) of hIAPP (**Figure 3.10b**), whereas no β-sheet conformation content was observed in presence of ANFLVH. The β-sheet content in C-terminus residues (Ser34 and Asn35) of hIAPP was converted to the coil in the hIAPP-ANFLVH complex (**Figure 3.10b, d**). A notable decrease in turn content was observed for Thr6–Arg11 residues in the presence of ANFLVH (**Figure 3.10c**). In the

presence of ANFLVH, the coil content at C-terminal residues (Val32–Thr36) was increased (**Figure 3.10d**).

The per-residue secondary structure analysis indicated that ANFLVH significantly reduces the β-sheet content and enhances the helical content in hIAPP. These results are consistent with the observation made by Wu et al.[49] By comparing the hIAPP, cat IAPP, rat IAPP, and pig IAPP, Wu et al. reported that helix and coil conformations contribute to the normal functioning of hIAPP, whereas β-rich conformations of hIAPP promote aggregation and responsible for the toxicity of hIAPP along with other mechanisms.

Table 3.4: The different components of the binding free energy (kcal/mol) between hIAPP and ANFLVH evaluated using the MM-PBSA method.

Energy terms (kcal/mol)	hIAPP-ANFLVH complex
ΔE_{vdW}	–46.33 ± 0.32
ΔE_{elec}	–11.68 ± 0.12
ΔE_{MM}[a]	–58.01 ± 0.44
ΔG_{ps}	17.26 ± 0.21
ΔG_{nps}	–9.15 ± 0.98
ΔG_{solv}[b]	8.11 ± 1.19
$\Delta G_{binding}$[c]	–49.90 ± 0.67

[a] $\Delta E_{MM} = \Delta E_{vdW} + \Delta E_{elec}$; [b] $\Delta G_{solv} = \Delta G_{ps} + \Delta G_{nps}$; [c] $\Delta G_{binding} = \Delta E_{MM} + \Delta G_{solv}$

3.3.6 Binding free energy analysis between hIAPP and ANFLVH

The binding affinity and key binding interactions between hIAPP and ANFLVH were investigated using MM-PBSA (**Table 3.4**). The binding free energy was noted to be –49.90 ± 0.67 kcal/mol for the hIAPP-ANFLVH complex. As listed in **Table 3.4**, the polar electrostatic (ΔE_{elec} = –11.68 ± 0.12 kcal/mol) and nonpolar van der Waals (ΔE_{vdW} = –46.33 ± 0.32 kcal/mol) terms were found to be favourable for the binding of ANFLVH with hIAPP. The nonpolar solvation (ΔG_{nps} = –9.15 ± 0.98 kcal/mol) dominate over the polar solvation (ΔG_{ps} = 17.26 ± 0.21 kcal/mol) and contribute maximum to the solvation term. The intermolecular van der Waals interaction was noted to be a governing force that was involved in the stabilization of the hIAPP-ANFLVH complex. The overall binding free energy analysis confirms a robust affinity of ANFLVH with hIAPP.

Further, the contribution of each residue of hIAPP to the binding free energy was assessed. The residues Cys2, Cys7, Ala8, Thr9, Ala13, His18, Ser19, Asn21, Asn22, and Asn35 of hIAPP contribute maximally to the binding of ANFLVH with hIAPP (**Figure 3.11**). The strong binding affinity (–6.29 kcal/mol) of ANFLVH with His18 of hIAPP results in the blocking of interactions mediated by His18 in promoting hIAPP aggregation. These results are consistent with earlier studies, which highlighted the key role of His18 in hIAPP amyloid formation[50] as well as in the promotion of reactive oxidative stress in the copper-ion mediated hIAPP aggregation.[51] Wei et al. highlighted that polyphenol resveratrol displayed strong binding with His18 of hIAPP and inhibited its oligomerization and amyloid formation, which is consistent with the observation that His18 is crucial for on-pathway oligomer formation by hIAPP.[52]

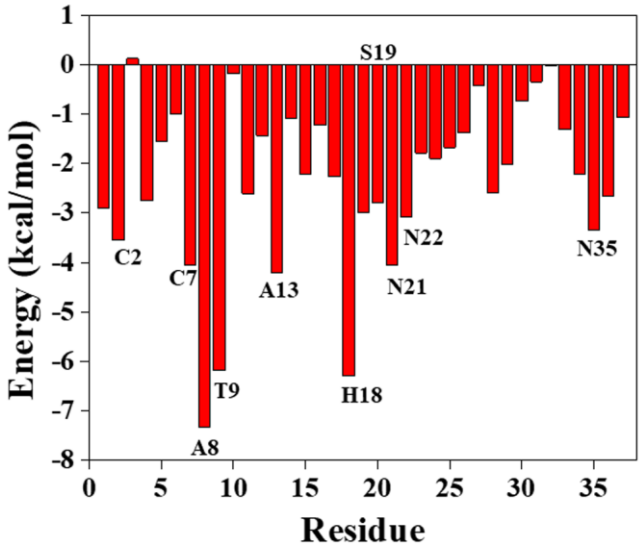

Figure 3.11: The binding free energy (kcal/mol) contribution of each residue of hIAPP in the hIAPP-ANFLVH complex is shown.

3.3.7 Impact of ANFLVH on the tertiary contacts in hIAPP

A comparison between the interaction pattern of the side chain tertiary contacts of hIAPP and hIAPP-ANFLVH highlights significant changes within 20–30 region (**Figure 3.12**). The residues 20–29 (SNNFGAILSS) of hIAPP can independently undergo self-aggregation and are recognized as the key amyloidogenic region of hIAPP.[53] The critical role of this region in the formation of fibrillar amyloid deposits was elucidated by the structure-activity studies.[40,53b,54,] Based on proline substitutions in rodent IAPP, the decapeptide

(SNNFGAILSS) region of hIAPP was shown as an important region for the formation of fibrillar amyloid deposits.[53,55]

In hIAPP, the interactions between residues spanning 20–30 region were observed (**Figure 3.12a**), which were significantly reduced in the hIAPP-ANFLVH complex (**Figure 3.12b**). This illustrated that ANFLVH interacted with the amyloidogenic region of hIAPP and lowered the probability of hIAPP self-aggregation. This is consistent with earlier results, which reported that hIAPP aggregation was mainly driven by the hydrophobic contacts among the hydrophobic core region (residues $F^{23}GAIL^{27}$) of hIAPP.[56]

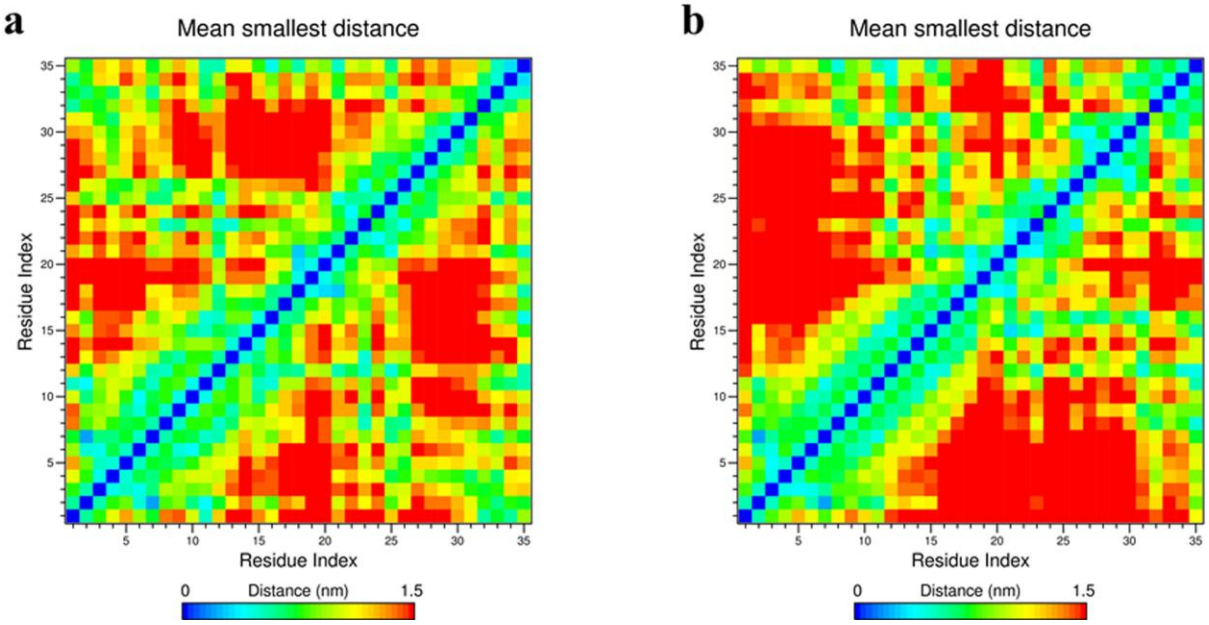

Figure 3.12: The side chain contacts in hIAPP and hIAPP-ANFLVH are shown in panel a, and b, respectively. The colour scale corresponds to the distance between the side chain atoms being ≤1.5 nm from each other.

3.3.8 Free energy landscape (FEL) of hIAPP and hIAPP-ANFLVH complex

The FEL was plotted to gain insights into the conformational states corresponding to various free energy states. The FEL was plotted for hIAPP and hIAPP-ANFLVH complex utilizing the first two PCs (PC1 and PC2) (**Figure 3.13**). The wine region depicts conformations with high energy. The blue region represents free energy minima while cyan and green regions indicate meta-stable conformational states. The FEL of hIAPP and hIAPP-ANFLVH complex depicts two defined minimum energy basins associated with its conformational states however, the representative conformations extracted from minimum energy basins

were noted to be more ordered in the hIAPP-ANFLVH complex as compared to hIAPP (**Figure 3.13**).

Table 3.5: The secondary structure component statistics for the representative conformations extracted from the minimum energy basins in the FEL of hIAPP and hIAPP-ANFLVH complex.

Model system	Conformation	Helix[a]	β-sheet[b]	turn	coil	bend
hIAPP	*i*	30	4	23	28	15
	ii	31	3	24	25	17
hIAPP-ANFLVH complex	*i*	46	0	16	20	18
	ii	45	1	20	21	13

[a] helix is the sum of α–, π–, and 3_{10}–helix ; [b] β–sheet is the sum of β-strand and β-bridge

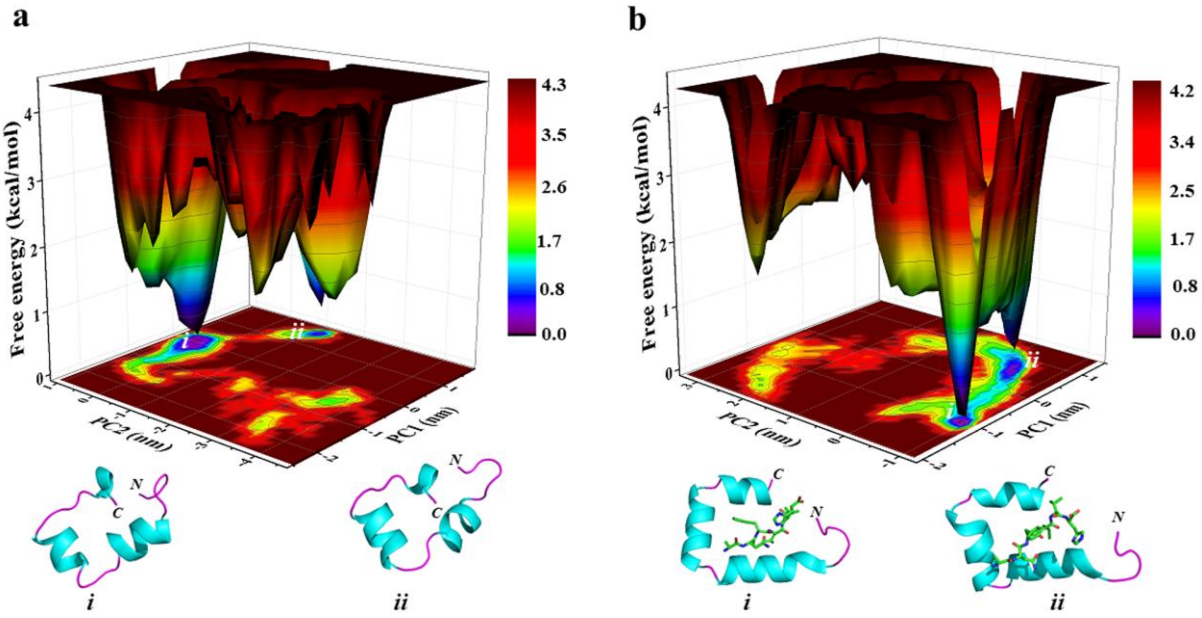

Figure 3.13: The free energy landscapes (FEL) generated by projecting the first two principal components, PC1, and PC2, are shown for hIAPP and hIAPP-ANFLVH complex in panel a, and b, respectively. The representative conformations extracted from the minimum energy basins are shown in the cartoon representation.

The secondary structure content of the representative conformations was evaluated (**Table 3.5**). For hIAPP, the representative conformation extracted from the minimum energy basin *i* sampled 30% helical, 23% turn, 28% coil, and 15% bend content, whereas a significantly higher helical (46%) and lower turn (16%), coil (20%) content was observed in the conformation extracted from the minimum energy basin *i* of hIAPP-ANFLVH (**Table 3.5**).

Notably, the content of the aggregation-prone β-sheet conformation diminished from 3–4 % in hIAPP to 0–1 % in hIAPP-ANFLVH. The representative conformations extracted from the minimum energy basins of the hIAPP-ANFLVH complex highlight a significant increase in the helical content and a concomitant decrease in the coil and turn content as compared to hIAPP, which, in turn, depict higher structural stability of the hIAPP-ANFLVH complex.

3.4 Conclusion

The current study explored the inhibitory mechanism of the hexapeptide ANFLVH against hIAPP aggregation through molecular docking and MD simulations. The RMSD and R_g analysis depicted higher structural stability and compactness of the hIAPP monomer in the presence of ANFLVH. The RMSF analysis highlighted reduced fluctuations of ~57 % residues of hIAPP in the presence of ANFLVH, which lead to the enhanced structural stability of the hIAPP-ANFLVH complex as compared to hIAPP alone. The conformational clustering of the conformational ensemble and secondary structure analysis highlighted that ANFLVH significantly inhibited the formation of aggregation-prone β-sheet conformation by reducing β-sheet content and stabilizing the helical conformation in the hIAPP monomer. Secondary structure analysis depicted enhancement of the helical content from 37% to 41% and stabilizes native hIAPP structure in the presence of ANFLVH. The per-residue secondary structure analysis emphasized an increased helical content in the Thr6–Asn14 region of hIAPP in presence of ANFLVH, which leads to the stabilization of non-aggregation-prone hIAPP conformation.

The side chain tertiary contact analysis highlighted the reduction of tertiary contacts in the amyloidogenic region spanning 20–30 of hIAPP in the presence of ANFLVH. The per-residue binding free energy analysis depicted that Cys2, Cys7, Ala8, Thr9, Ala13, His18, Ser19, Asn21, Asn22, and Asn35 of hIAPP contribute significantly to the binding of ANFLVH with hIAPP monomer. The representative conformations extracted from the minimum energy basins in the FEL of hIAPP-ANFLVH complex depicted significantly higher helical content as compared to conformations extracted from the FEL of hIAPP. The MD simulations demonstrated that ANFLVH inhibited hIAPP aggregation by stabilizing the non-aggregation-prone helical conformation of the hIAPP monomer. The findings from this

study will aid drug discovery scientists in modifying peptides for the future design of more potent inhibitors against hIAPP aggregation in T2D.

3.5 References

1. (a) Chiti, F.; Dobson, C.M. Protein misfolding, amyloid formation, and human disease: a summary of progress over the last decade. *Annu. Rev. Biochem,* **2017**, *86*, 27–68; (b) Ladanza, M.G.; Jackson, M.P.; Hewitt, E.W.; Ranson, N.A.; Radford, S.E. A new era for understanding amyloid structures and disease. *Nat. Rev. Mol. Cell Biol.* **2018**, *19*, 755–773.

2. Ke, P.C.; Sani, M.A.; Ding, F.; Kakinen, A.; Javed, I.; Separovic, F.; Davis, T.P.; Mezzenga, R. Implications of peptide assemblies in amyloid diseases. *Chem. Soc. Rev.* **2017**, *46*, 6492–6531.

3. IDF Diabetes Atlas, 9th ed., International Diabetes Federation, Brussels, Belgium, 2019.

4. Cho, N.H.; Shaw, J.E.; Karuranga, S.; Huang, Y.; da Rocha Fernandes, J.D.; Ohlrogge, A.W.; Malanda, B.I.D.F. IDF Diabetes Atlas: Global estimates of diabetes prevalence for 2017 and projections for 2045. *Diabetes Res. Clin. Pract.* **2018**, *138*, 271–281.

5. (a) Cooper, G.J.; Willis, A.C.; Clark, A.; Turner, R.C.; Sim, R.B.; Reid, K.B. Purification and characterization of a peptide from amyloid-rich pancreases of type 2 diabetic patients. *Proc. Natl. Acad. Sci.* U. S. A. **1987**, *84*, 8628–8632; (b) Westermark, P.; Wernstedt, C.; Wilander, E.; Hayden, D.W.; O'Brien, T.D.; Johnson, K.H. Amyloid fibrils in human insulinoma and islets of Langerhans of the diabetic cat are derived from a neuropeptide-like protein also present in normal islet cells. *Proc. Natl. Acad. Sci.* U. S. A. **1987**, *84*, 3881–3885.

6. (a) Cao, P.; Abedini, A.; Raleigh, D.P. Aggregation of islet amyloid polypeptide: from physical chemistry to cell biology. *Curr. Opin. Struct. Biol.* **2013**, *23*, 82–89; (b) Clark, A.; Wells, C.A.; Buley, I.D.; Cruickshank, J.K.; Vanhegan, R.I.; Matthews, D.R.; Cooper, G.J.; Holman, R.R.; Turner, R.C. Islet amyloid, increased A-cells, reduced B-cells and exocrine fibrosis: quantitative changes in the pancreas in type 2 diabetes. *Diabetes Res.* **1988**, *9*, 151–159; (c) Konarkowska, B.; Aitken, J.F.; Kistler, J.; Zhang, S.; Cooper, G.J. The aggregation potential of human amylin determines its cytotoxicity towards islet β-cells. *FEBS J.* **2006**, *273*, 3614–3624; (d) Lorenzo, A.; Razzaboni, B.; Weir, G.C.; Yankner, B.A. Pancreatic islet cell toxicity of amylin associated with type-2 diabetes mellitus. *Nature* **1994**, *368*, 756–760.

7. Westermark, P.; Andersson, A.; Westermark, G.T. Islet amyloid polypeptide, islet amyloid, and diabetes mellitus. *Physiol. Rev.* **2011**, *91*, 795–826.

8. (a) Dhouafli, Z.; Cuanalo-Contreras, K.; Hayouni, E.A.; Mays, C.E.; Soto, C.; Moreno-Gonzalez, I. Inhibition of protein misfolding and aggregation by natural phenolic compounds. *Cell. Mol. Life Sci.* **2018**, *75*, 3521–3538; (b) Dubey, R.; Patil, K.; Dantu, S.C.; Sardesai, D.M.; Bhatia, P.; Malik, N.; Acharya, J.D.; Sarkar, S.; Ghosh, S.; Chakrabarti, R.; Sharma, S. Azadirachtin inhibits amyloid formation, disaggregates pre-formed fibrils and protects pancreatic β-cells from human islet amyloid

polypeptide/amylin-induced cytotoxicity. *Biochem. J.* **2019**, *476*, 889–907; (c) Ma, L.; Yang, C.; Zheng, J.; Chen, Y.; Xiao, Y.; Huang, K. Non-polyphenolic natural inhibitors of amyloid aggregation. *Eur. J. Med. Chem.* **2020**, *192*, 112197; (d) Pang, B.; Bian, X.; Xing, J.; Liu, S.; Liu, Z.; Song, F. Effects of lithospermic acid on hIAPP aggregation and amyloid-induced cytotoxicity by multiple analytical methods. *Biophys. Acta* Proteins *Proteom.* **2020**, *1868*, 140283; (e) Ren, B.; Liu, Y.; Zhang, Y.; Cai, Y.; Gong, X.; Chang, Y.; Xu, L.; Zheng, J. Genistein: a dual inhibitor of both amyloid β and human islet amylin peptides. *ACS Chem. Neurosci.* **2018**, *9*, 1215–1224; (f) Sequeira, I.R.; Poppitt, S.D. Unfolding novel mechanisms of polyphenol flavonoids for better glycaemic control: Targeting pancreatic islet amyloid polypeptide (IAPP). *Nutrients* **2017**, *9*, 788; (g) Velander, P.; Wu, L.; Henderson, F.; Zhang, S.; Bevan, D.R.; Xu, B. Natural product-based amyloid inhibitors. *Biochem. Pharmacol.* **2017**, *139*, 40–55; (h) Xin, Y.; Wang, X.; Luo, L.; Meng, F. Conformation-dependent manipulation of human islet amyloid polypeptide fibrillation by shiitake-derived lentinan. *ACS Appl. Mater. Interfaces* **2018**, *10*, 31069–31079; (i) Xu, Z.X.; Ma, G.L.; Zhang, Q.; Chen, C.H.; He, Y.M.; Xu, L.H.; Zhou, G.R.; Li, Z.H.; Yang, H.J.; Zhou, P. Inhibitory mechanism of epigallocatechin gallate on fibrillation and aggregation of amidated human islet amyloid polypeptide. *ChemPhysChem* **2017**, *18*, 1611–1619.

9. (a) Kumar, S.; Vogel, M.C.; Hamilton, A.D. Teaching an old scaffold new recognition tricks: oligopyrrolamide antagonists of IAPP aggregation. *Org. Biomol. Chem.* **2018**, *16*, 733–741; (b) Mishra, R.; Bulic, B.; Sellin, D.; Jha, S.; Waldmann, H.; Winter, R. Small-molecule inhibitors of islet amyloid polypeptide fibril formation. *Angew. Chem.* **2008**, *47*, 4679–4682; (c) Nath, A.; Schlamadinger, D.E.; Rhoades, E.; Miranker, A.D. Structure-based small molecule modulation of a pre-amyloid state: pharmacological enhancement of iapp membrane-binding and toxicity. *Biochemistry* **2015**, *54*, 3555–3564; (d) Saravanan, M.S.; Ryazanov, S.; Leonov, A.; Nicolai, J.; Praest, P.; Giese, A.; Winter, R.; Khemtemourian, L.; Griesinger, C.; Killian, J.A. The small molecule inhibitor anle145c thermodynamically traps human islet amyloid peptide in the form of non-cytotoxic oligomers. *Sci. Rep.* **2019**, *9*, 19023; (e) Xu, J.; Zhao, C.; Huang, X.; Du, W. Tetracycline derivatives resist the assembly behavior of human islet amyloid polypeptide. *Biochimie* **2020**, *174*, 95–106; (f) Xu, J.; Zhao, C.; Huang, X.; Du, W. Regulation of artemisinin and its derivatives on the assembly behavior and cytotoxicity of amyloid polypeptides hIAPP and Aβ. *ACS Chem. Neurosci.* **2019**, *10*, 4522–4534; (g) Zou, Y.; Qian, Z.; Sun, Y.; Wei, G.; Zhang, Q. Orcein-related small molecule O4 destabilizes hIAPP protofibrils by interacting mostly with the amyloidogenic core region. *J. Phys. Chem. B* **2017**, *121*, 9203–9212.

10. (a) Armiento, V.; Spanopoulou, A.; Kapurniotu, A. Peptide-Based Molecular Strategies To Interfere with Protein Misfolding, Aggregation, and Cell Degeneration. *Angew. Chem. Int. Ed.* **2020**, *59*, 3372–3384; (b) Goyal, D.; Shuaib, S.; Mann, S.; Goyal, B. Rationally designed peptides and peptidomimetics as inhibitors of amyloid-β (Aβ) aggregation: potential therapeutics of Alzheimer's disease. *ACS Comb. Sci.* **2017**, *19*, 55–80; (c) Henninot, A.; Collins, J.C.; Nuss, J.M. The current state of peptide drug discovery: back to the future? *J. Med. Chem.* **2018**, *61*, 1382−1414.

11. (a) Muthusamy, K.; Arvidsson, P.I.; Govender, P.; Kruger, H.G.; Maguire, G.E.; Govender, T. Design and study of peptide-based inhibitors of amylin cytotoxicity. *Bioorg. Med. Chem. Lett.* **2010**, *20*, 1360–1362; (b) Scrocchi, L.A.; Chen, Y.; Waschuk, S.; Wang, F.; Cheung, S.; Darabie, A.A.; McLaurin, J.; Fraser, P.E. Design of peptide-based inhibitors of human islet amyloid polypeptide fibrillogenesis. *J. Mol. Biol.* **2002**, *318*, 697–706; (c) Sivanesam, K.; Andersen, N.H. Inhibition of human amylin amyloidogenesis by human amylin-fragment peptides: Exploring the effects of serine residues and oligomerization upon inhibitory potency. *Biochemistry* **2017**, *56*, 5373–5379.

12. (a) Ghosh, A.; Pithadia, A.S.; Bhat, J.; Bera, S.; Midya, A.; Fierke, C.A.; Ramamoorthy, A.; Bhunia, A. Self-assembly of a nine-residue amyloid-forming peptide fragment of SARS corona virus E-protein: mechanism of self aggregation and amyloid-inhibition of hIAPP. *Biochemistry* **2015**, *54*, 2249–2261; (b) Shaykhalishahi, H.; Mirecka, E.A.; Gauhar, A.; Grüning, C.S.; Willbold, D.; Härd, T.; Stoldt, M.; Hoyer, W. A β-Hairpin-Binding Protein for Three Different Disease-Related Amyloidogenic Proteins. *ChemBioChem* **2015**, *16*, 411–414; (c) Xin, Y.; Zhang, H.; Hu, Q.; Tian, S.; Wang, C.; Luo, L.; Meng, F. Oligotyrosines inhibit amyloid formation of human islet amyloid polypeptide in a tyrosine-number-dependent manner. *ACS Biomater. Sci. Eng.* **2019**, *5*, 1092−1099; (d) Xuan, Q.; He, J.; Li, M.; Chai, R.; Wang, C.; Wang, Y.; Wang, P. Monomer-targeting affinity peptide inhibitors of amyloid with no self-fibrillation and low cytotoxicity. *Chem. Commun.* **2020**, *56*, 1633–1636.

13. Potter, K.J.; Scrocchi, L.A.; Warnock, G.L.; Ao, Z.; Younker, M.A.; Rosenberg, L.; Lipsett, M.; Verchere, C.B.; Fraser, P.E. Amyloid inhibitors enhance survival of cultured human islets. *Biochim. Biophys. Acta, Gen. Subj.* **2009**, *1790*, 566–574.

14. Trott, O.; Olson, A.J. AutoDock Vina: improving the speed and accuracy of docking with a new scoring function, efficient optimization, and multithreading. *J. Comput. Chem.* **2010**, *31*, 455–461.

15. Nanga, R.P.R.; Brender, J.R.; Vivekanandan, S.; Ramamoorthy, A. Structure and membrane orientation of IAPP in its natively amidated form at physiological pH in a membrane environment. *Biochim. Biophys. Acta*. **2011**, *1808*, 2337–2342.

16. Schrödinger Release 2018-1: Maestro, Schrödinger, LLC, New York, NY, 2018.

17. Abraham, M.J.; Murtola, T.; Schulz, R.; Páll, S.; Smith, J.C.; Hess, B.; Lindahl, E. GROMACS: High performance molecular simulations through multi-level parallelism from laptops to supercomputers. *SoftwareX* **2015**, *1–2*, 19–25.

18. Lin, Z.; van Gunsteren, W.F. Refinement of the application of the GROMOS 54A7 force field to β-peptides. *J. Comput. Chem.* **2013**, *34*, 2796–2805.

19. Berendsen, H. J. C.; Postma, J. P. M.; van Gunsteren, W. F.; Hermans, J. *Intermolecular forces, In B. Pullman Ed.*, Reidel Publishing Company, Dordrecht, **1981**, 331–342.

20. (a) Asthana, S.; Sahu, M.; Nayak, P.S.; Mallick, B.; Jha, S. The smaller heparin fragments bind non-specifically through the IAPP sequence: An in silico study. *Int. J. Biol. Macromol.* **2018**, *113*, 1092–1104; (b) Autiero, I.; Langella, E.; Saviano, M. Insights into the mechanism of interaction between trehalose-conjugated beta-sheet breaker peptides and Aβ (1–42) fibrils by molecular dynamics simulations. *Mol. Biosyst.* **2013**, *9*, 2835–2841; (c) D'Urso, L.; Condorelli, M.; Puglisi, O.; Tempra, C.; Lolicato, F.; Compagnini, G.; La Rosa, C. Detection and characterization at nM concentration of oligomers formed by hIAPP, Aβ (1–40) and their equimolar mixture using SERS and MD simulations. *Phys. Chem. Chem. Phys.* **2018**, *20*, 20588–20596; (d) La Rosa, C.; Condorelli, M.; Compagnini, G.; Lolicato, F.; Milardi, D.; Do, T.N.; Karttunen, M.; Pannuzzo, M.; Ramamoorthy, A.; Fraternali, F.; Collu, F. Symmetry-breaking transitions in the early steps of protein self-assembly. *Eur. Biophys. J.* **2020**, *49*, 175–191.

21. Guo, A.Z.; Fluitt, A.M.; de Pablo, J.J. Early-stage human islet amyloid polypeptide aggregation: Mechanisms behind dimer formation. *J. Chem. Phys.* **2018**, *149*, 025101.

22. (a) Darden, T.; York, D.; Pedersen, L. Particle mesh Ewald: An W log (N) method for Ewald sums in large systems. *J. Chem. Phys.* **1993**, *98*, 10089–10092; (b) Essmann, U.; Perera, L.; Berkowitz, M.L.; Darden, T.; Lee, H.; Pedersen, L.G. A smooth particle mesh Ewald method. *J. Chem. Phys.* **1995**, *103*, 8577–8593.

23. Hess, B.; Bekker, H.; Berendsen, H.J.; Fraaije, J.G. LINCS: A linear constraint solver for molecular simulations. *J. Comput. Chem.* **1997**, *18*, 1463–1472.

24. (a) Berendsen, H.J.; Postma, J.V.; van Gunsteren, W.F.; DiNola, A.R.H.J.; Haak, J.R. Molecular dynamics with coupling to an external bath. *J. Chem. Phys.* **1984**, *81*, 3684–3690; (b) Bussi, G.; Donadio, D.; Parrinello, M. Canonical sampling through velocity rescaling. *J. Chem. Phys.* **2007**, *126*, 014101.

25. Parrinello, M.; Rahman, A. Polymorphic transitions in single crystals: A new molecular dynamics method. *J. Appl. Phys.* **1981**, *52*, 7182–7190.

26. Humphrey, W.; Dalke, A.; Schulten, K. VMD: visual molecular dynamics. *J. Mol. Graph.* **1996**, *14*, 33–38.

27. DeLano, W. L. The PyMol Molecular Graphics System; DeLano Scientific: San Carlos, CA, USA, 2002.

28. Daura, X.; Gademann, K.; Jaun, B.; Seebach, D.; van Gunsteren, W.F.; Mark, A.E. Peptide folding: when simulation meets experiment. *Angew. Chem. Int. Ed.* **1999**, *38*, 236–240.

29. Kabsch, W.; Sander, C. Dictionary of protein secondary structure: pattern recognition of hydrogen-bonded and geometrical features. *Biopolymers* **1983**, *22*, 2577–2637.

30. Vögeli, B.; Ying, J.; Grishaev, A.; Bax, A. Limits on variations in protein backbone dynamics from precise measurements of scalar couplings. *J. Am. Chem. Soc*. **2007**, *129*, 9377–9385.

31. Karplus, M. Contact electron-spin coupling of nuclear magnetic moments. *J. Chem. Phys*. **1959**, *30*, 11–15.

32. Kaur, A.; Shuaib, S.; Goyal, D.; Goyal, B. Interactions of a multifunctional di-triazole derivative with Alzheimer's $A\beta_{42}$ monomer and $A\beta_{42}$ protofibril: a systematic molecular dynamics study. *Phys. Chem. Chem. Phys*. **2020**, *22*, 1543–1556.

33. (a) Best, R.B.; Buchete, N.V.; Hummer, G. Are current molecular dynamics force fields too helical? *Biophys. Chem*. **2008**, *95*, L07–L09; (b) Zhang, T.; Xu, W.; Mu, Y.; Derreumaux, P. Atomic and dynamic insights into the beneficial effect of the 1, 4-naphthoquinon-2-yl-l-tryptophan inhibitor on Alzheimer's Aβ1–42 dimer in terms of aggregation and toxicity. *ACS Chem. Neurosci*. **2014**, *5*, 148–159.

34. Kumari, R.; Kumar, R. Open Source Drug Discovery Consortium; Lynn, A. g_mmpbsa–A GROMACS tool for high-throughput MM-PBSA calculations. *J. Chem. Inf. Model*. **2014**, *54*, 1951–1962.

35. Han, B.; Liu, Y.; Ginzinger, S.W.; Wishart, D.S. SHIFTX2: significantly improved protein chemical shift prediction. *J. Biomol. NMR* **2011**, *50*, 43−57.

36. Nasica-Labouze, J.; Nguyen, P.H.; Sterpone, F.; Berthoumieu, O.; Buchete, N.V.; Cote, S.; De Simone, A.; Doig, A.J.; Faller, P.; Garcia, A.; Laio, A. Amyloid β protein and Alzheimer's disease: When computer simulations complement experimental studies. *Rev*. **2015**, *115*, 3518–3563.

37. (a) Lyman, E.; Zuckerman, D.M. Ensemble-based convergence analysis of biomolecular trajectories. *Biophys. J.* **2006**, *91*, 164–172; (b) Ng, H.W.; Laughton, C.A.; Doughty, S.W. Molecular dynamics simulations of the adenosine A2a receptor: structural stability, sampling, and convergence. *J. Chem. Inf. Model.* **2013**, *53*, 1168–1178; (c) Smith, L.J.; Daura, X.; van Gunsteren, W.F. Assessing equilibration and convergence in biomolecular simulations. *Proteins: Struct. Funct. Genet.* **2002**, *48*, 487–496.

38. Patel, P.; Parmar, K.; Vyas, V.K.; Patel, D.; Das, M. Combined *in silico* approaches for the identification of novel inhibitors of human islet amyloid polypeptide (hIAPP) fibrillation. *J. Mol. Graphics Modell.* **2017**, *77*, 295–310.

39. (a) Lee, S.J.C.; Choi, T.S.; Lee, J.W.; Lee, H.J.; Mun, D.G.; Akashi, S.; Lee, S.W.; Lim, M.H.; Kim, H.I. Structure and assembly mechanisms of toxic human islet amyloid polypeptide oligomers associated with copper. *Chem. Sci.* **2016**, *7*, 5398−5406; (b) Young, L.M.; Cao, P.; Raleigh, D.P.; Ashcroft, A.E.; Radford, S.E. Ion mobility spectrometry–mass spectrometry defines the oligomeric intermediates in amylin amyloid formation and the mode of action of inhibitors. *J. Am. Chem. Soc.* **2014**, *136*, 660–670.

40. Jaikaran, E.T.; Higham, C.E.; Serpell, L.C.; Zurdo, J.; Gross, M.; Clark, A.; Fraser, P.E. Identification of a novel human islet amyloid polypeptide β-sheet domain and factors influencing fibrillogenesis. *J. Mol. Biol.* **2001**, *308*, 515–525.

41. Dupuis, N.F.; Wu, C.; Shea, J.E.; Bowers, M.T. Human islet amyloid polypeptide monomers form ordered β-hairpins: a possible direct amyloidogenic precursor. *J. Am. Chem. Soc.* **2009**, *131*, 18283–18292.

42. Qiao, Q.; Bowman, G.R.; Huang, X. Dynamics of an intrinsically disordered protein reveal metastable conformations that potentially seed aggregation. *J. Am. Chem. Soc.* **2013**, *135*, 16092–16101.

43. Tran, L.; Ha-Duong, T. Effect of post-translational amidation on islet amyloid polypeptide conformational ensemble: implications for its aggregation early steps. *Int. J. Mol. Sci.* **2016**, *17*, 1896.

44. Lao, Z.; Chen, Y.; Tang, Y.; Wei, G. Molecular dynamics simulations reveal the inhibitory mechanism of dopamine against hIAPP aggregation and its destabilization effect on hIAPP protofibrils. *ACS Chem. Neurosci.* **2019**, *10*, 4151–4159.

45. Reddy, A.S.; Wang, L.; Singh, S.; Ling, Y.L.; Buchanan, L.; Zanni, M.T.; Skinner, J.L.; de Pablo, J.J. Stable and metastable states of human amylin in solution. *Biophys. J.* **2010**, *99*, 2208–2216.

46. Reddy, A.S.; Wang, L.; Lin, Y.S.; Ling, Y.; Chopra, M.; Zanni, M.T.; Skinner, J.L.; de Pablo, J.J. Solution structures of rat amylin peptide: simulation, theory, and experiment. *Biophys. J.* **2010**, *98*, 443–451.

47. Dupuis, N.F.; Wu, C.; Shea, J.E.; Bowers, M.T. The amyloid formation mechanism in human IAPP: dimers have β-strand monomer− monomer interfaces. *J. Am. Chem. Soc.* **2011**, *133*, 7240–7243.

48. Guo, A.Z.; Fluitt, A.M.; de Pablo, J.J. Early-stage human islet amyloid polypeptide aggregation: Mechanisms behind dimer formation. *J. Chem. Phys.* **2018**, *149*, 025101.

49. Wu, C.; Shea, J.E. Structural similarities and differences between amyloidogenic and non-amyloidogenic islet amyloid polypeptide (IAPP) sequences and implications for the dual physiological and pathological activities of these peptides. *PLoS Comput. Biol.* **2013**, *9*, e1003211.

50. Abedini, A.; Raleigh, D.P. The role of His-18 in amyloid formation by human islet amyloid polypeptide. *Biochemistry* **2005**, *44*, 16284–16291.

51. Huo, G.; Chen, W.; Wang, J.; Chu, X.; Xu, W.; Li, B.; Zhang, Y.; Xu, B.; Zhou, X. His18 promotes reactive oxidative stress production in copper-ion mediated human islet amyloid polypeptide aggregation. *RSC Adv.* **2020**, *10*, 5566–5571.

52. Wei, L.; Jiang, P.; Xu, W.; Li, H.; Zhang, H.; Yan, L.; Chan-Park, M.B.; Liu, X.W.; Tang, K.; Mu, Y.; Pervushin, K. The molecular basis of distinct aggregation pathways of islet amyloid polypeptide. *J. Biol. Chem.* **2011**, *286*, 6291–6300.

53. (a) Glenner, G.G.; Eanes, E.D.; Wiley, C.A. Amyloid fibrils formed from a segment of the pancreatic islet amyloid protein. *Biochem. Biophys. Res. Commun.* **1988**, *155*, 608–614; (b) Westermark, P.; Engström, U.; Johnson, K.H.; Westermark, G.T.; Betsholtz, C. Islet amyloid polypeptide: pinpointing amino acid residues linked to amyloid fibril formation. *Proc. Natl. Acad. Sci.* U. S. A. **1990**, *87*, 5036–5040.

54. Azriel, R. Gazit, E. Analysis of the minimal amyloid-forming fragment of the islet amyloid polypeptide. *J. Biol. Chem.* **2001**, *276*, 34156–34161.

55. Moriarty, D.F.; Raleigh, D.P. Effects of sequential proline substitutions on amyloid formation by human amylin$_{20-29}$. *Biochemistry* **1999**, *38*, 1811–1818.

56. (a) Rivera, E.; Straub, J.; Thirumalai, D.J.B.J. Sequence and crowding effects in the aggregation of a 10-residue fragment derived from islet amyloid polypeptide. *Biophys. J.* **2009**, *96*, 4552–4560; (b) Wu, C.; Lei, H.; Duan, Y. Elongation of ordered peptide aggregate of an amyloidogenic hexapeptide NFGAIL observed in molecular dynamics simulations with explicit solvent. *J. Am. Chem. Soc.* **2005**, *127*, 13530–13537.

Chapter 4

In silico design and identification of new peptides for mitigating hIAPP aggregation in type 2 diabetes

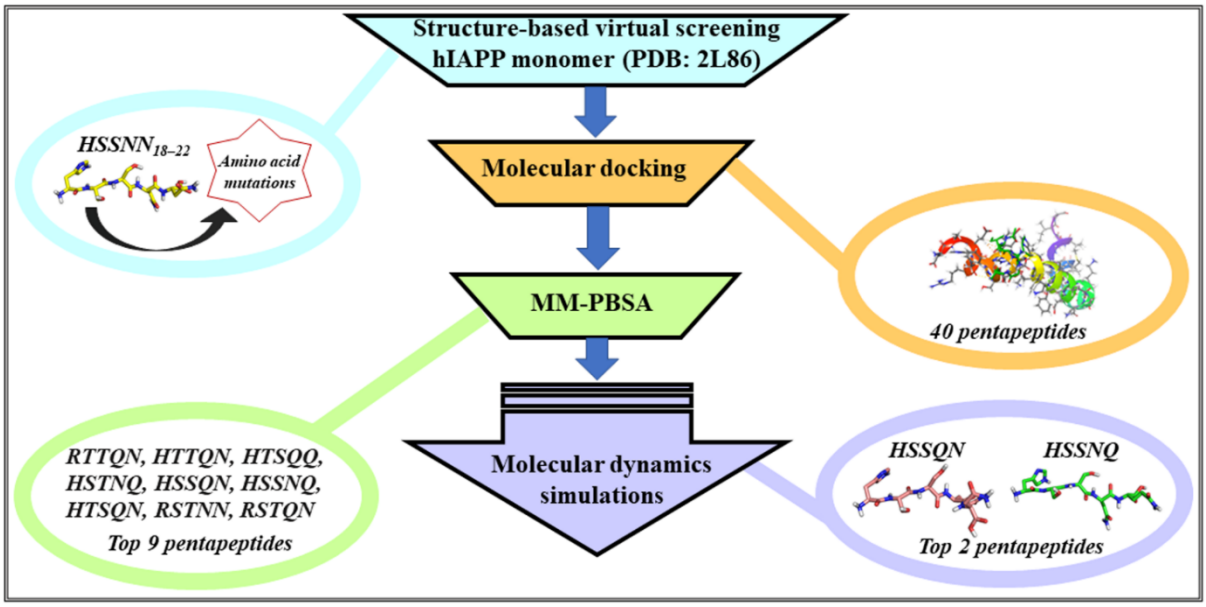

In our present study we investigated the effect of modifying the HSSNN peptide up to the five positions with similar amino acids. The model of the amyloid hIAPP protein used in the present study is an L-shaped monomer. We performed molecular docking of forty pentapeptide analogues of HSSNN followed by MM-PBSA calculations of best 9 peptides from docking. The best inhibitors have been chosen from MD were those containing glutamine i.e. HSSQN and HSSNQ contributed strong binding with hIAPP monomer than the reference peptide HSSNN. These two chosen peptides resulting in increase in helical content of hIAPP monomer structure.

Kaur, A.; Goyal, B. *In silico* design and identification of new peptides for mitigating hIAPP aggregation in type 2 diabetes. *J. Biomol. Struct. Dyn.* **2023**. doi: 10.1080/07391102.2023.2254411.

4.1 Introduction

The self-aggregation of normally dissolvable proteins into insoluble amyloid filaments characterizes amyloidosis.[1] These aggregates, known as amyloid are made up of misfolded proteins with β–sheet structure, have an impact on normal tissue function, and are associated with prevalent amyloidosis diseases such as Alzheimer's disease (AD), Parkinson's disease, and type 2 diabetes (T2D).[2] The amyloid−β (Aβ) peptide linked to AD[3] and human islet amyloid polypeptide (hIAPP, commonly known as amylin) linked to T2D are classic examples of intrinsically disordered proteins (IDPs) that self-assemble to form amyloid fibrils.[4] hIAPP (37 amino acid residues hormone) is one of the main secretory components of pancreatic islet β−cells.[5] The self-aggregation of hIAPP into cytotoxic aggregates results in islet β–cells apoptosis and finally leads to T2D.[6] Thus, inhibiting the formation of hIAPP aggregates has therapeutic benefits for the treatment of T2D.

The hIAPP undergoes a conformational transition from the initial random coil or helical to aggregation-prone β−sheet conformation and exhibits a high proclivity to aggregate into oligomers and amyloid plaques in a nucleation-dependent manner.[7] Increasing evidence suggested small, dynamic, and transient oligomers as toxic species compared to mature amyloid fibrils.[4c, 8] Unfortunately, the underlying molecular mechanism by which hIAPP undergoes structural transition and aggregates into transient oligomers and finally to insoluble amyloid plaques causing T2D symptoms remains unknown. Monomer, as the beginning point, plays a crucial part in understanding the initial stage aggregation mechanism.[9] The characterization of hIAPP monomer through experimental studies is very challenging due to its fast aggregation propensity. The hIAPP monomer has been extensively investigated experimentally[10] and computationally[11] as the aggregation starting point. The hIAPP monomer is predominantly randomly coiled as an IDP, with a slight fraction of α–helix and β–hairpin structures in the monomer ensemble.[12] The circular dichroism (CD) and solid-state NMR have revealed that monomeric hIAPP can sample random coil, α–helical and β−hairpin conformations.[13] A complete understanding of the underlying process of conformational conversion of functional proteins to toxic oligomers and amyloid fibrils may support the development of medical applications and innovative therapies.[14]

A wide range of inhibitors, including composite materials,[15] inorganic nanomaterials,[16] and natural compounds[17] have been identified as prospective therapeutic candidates against hIAPP

aggregation for T2D management. Multiple considerations, such as fast metabolism, removal, and high cytotoxicity, prevent these inhibitors from being used in clinical trials against hIAPP aggregation. Among various inhibitors, peptide-based inhibitors are currently one of the most effective amyloid inhibitors due to their high chemical diversity, biocompatibility, low immunogenicity, high potency and selectivity, thus peptides are frequently used as hIAPP aggregation inhibitors.[17b, 18] Numerous studies reported short peptides as inhibitors of hIAPP aggregation and provided insights into the molecular mechanism of its aggregation.[18c-d, 19] Recently, Roy et al. investigated the molecular mechanism of inhibition of hIAPP aggregation by D-NFGAIL (D-nl) derived from $hIAPP_{22–27}$ sequence using molecular dynamics (MD) simulations.[20]

Rozniakowski et al. assessed various hIAPP fragments for their aggregation ability and reported that fragments H-HSSNN-OH ($hIAPP_{18–22}$) and H-GSNTY-NH_2 ($hIAPP_{33–37}$) undergo self-aggregation to yield amyloid fibrils.[21] In comparison to other hIAPP fragments, HSSNN displayed the highest antiproliferative activity to RIN-5F cells. Various inhibitors have been designed by chemical modifications of the highly amyloidogenic sequence (NFGAIL) of hIAPP and evaluated for their efficacy against hIAPP aggregation.[17b, 18c-d] Thus, HSSNN can be employed as a lead domain for designing new hIAPP aggregation inhibitors.

The peptides derived from hIAPP sequence are altered by substituting with other amino acid residues which promote the interaction of hIAPP with these modified peptides over itself.[17b] The hIAPP fragment (residues 20-29, SNNFGAILSS) was reported as a key amyloidogenic sequence of hIAPP by species-specific proline replacement in rodent IAPP.[22] The proline substitutions yielded β-sheet breaker peptides, which prevented hIAPP misfolding and subsequent aggregation.[23] It is noteworthy to mention that two patents have been granted for the peptide derivatives of hIAPP that can prevent hIAPP aggregation and hIAPP-mediated cytotoxicity.[24] However, none of the peptide derivatives has been advanced into the clinical trials. This motivated us to design, screen, and evaluate peptide library with the aim to identify new peptides as potent inhibitors against hIAPP fibrillation in T2D. The objective of the present study is to determine whether the alterations in the amyloid-forming fragment (HSSNN) of $hIAPP_{18-22}$ are capable of interacting with full-length hIAPP and modulating its aggregation pathway. The strategy of designing new peptide inhibitors by chemical modifications in the

native sequences has proved successful in the development of therapeutic candidates against Aβ aggregation in AD.[18b, 25]

Recent studies utilized computational techniques to identify and examine the binding mechanism of potential inhibitors against various biological targets.[26] The computational design and evaluation of potential peptides as inhibitors of druggable targets by employing computational techniques without experimental validation have been reported in recent studies.[27] In this work, a library of pentapeptides was generated from the reference peptide HSSNN by mutating each amino acid of its sequence with a similar amino acid. Various computational techniques including virtual screening, molecular mechanics Poisson-Boltzmann surface area (MM-PBSA), and MD simulations have been employed to identify potential inhibitors from the designed library against hIAPP aggregation. The present work yielded computationally designed peptides with completely new sequences rather than sequences derived from hIAPP that have been explored previously[18c, d] as hIAPP aggregation inhibitors. The results of the present study will provide direction for the synthesis and biological assessment of putative inhibitors against hIAPP aggregation.

4.2 Computational methodology

4.2.1 Computational design of the pentapeptide library

To demonstrate the effect of substituting a different amino acid at a specific position in a peptide, a selected site in the sequence is systematically changed with a different amino acid. A library of pentapeptides was generated by replacing each amino acid in the HSSNN sequence with a similar kind of amino acid (**Table 4.1–4.5**). All pentapeptides were drawn using Maestro software[28] and the geometry was optimized using Maestro inbuilt package. After optimization, all pentapeptides were subjected to molecular docking studies.

Table 4.1: Pentapeptide sequences generated by mutating one amino acid in the reference peptide HSSNN extracted from the region 18-22 of hIAPP monomer.

Reference peptide amino acids	Nature of side chain	Amino acids with similar side chains	Peptides with one amino acid mutation
H	Basic, polar	K, R	**R**SSNN**, K**SSNN
S	Uncharged, polar	T	H**T**SNN**,** HS**T**NN
N	Uncharged, polar	Q	HSS**Q**N**,** HSSN**Q**

Table 4.2: Pentapeptide sequences generated by mutating two amino acid residues in HSSNN.

Combination	Mutant peptides
1,2	**RT**SNN, **KT**SNN
1,3	**RST**NN, **KST**NN
1,4	**RSSQ**N, **KSSQ**N
1,5	**RSSNQ**, **KSSNQ**
2,3	H**TT**NN
2,4	H**TSQ**N
2,5	H**TSNQ**
3,4	HS**TQ**N
3,5	HS**TNQ**
4,5	HSS**QQ**

Table 4.3: Pentapeptide sequences generated by mutating three amino acid residues in HSSNN.

Combination	Mutant peptides
1,2,3	**RTT**NN, **KTT**NN
1,3,4	**RSTQ**N, **KSTQ**N
1,4,5	**RSSQQ**, **KSSQQ**
2,3,4	H**TTQ**N
2,4,5	H**TSQQ**
3,4,5	HS**TQQ**

Table 4.4: Pentapeptide sequences generated by mutating four amino acid residues in HSSNN.

Combination	Mutant peptides
1,2,3,4	**RTTQ**N, **KTTQ**N
1,3,4,5	**RSTQQ**, **KSTQQ**
2,3,4,5	H**TTQQ**

Table 4.5: Pentapeptide sequences generated by mutating five amino acid residues in HSSNN.

Combination	Mutant peptides
1,2,3,4,5	**RTTQQ**, **KTTQQ**

4.2.2 Virtual screening of the pentapeptide library

The single amino acid in HSSNN was mutated with other amino acids belonging to the same group, which results in the generation of six single amino acid mutated pentapeptides (**Table 4.1**). To assess the binding affinity for the hIAPP monomer, the HSSNN, and single amino acid mutated pentapeptides were docked to hIAPP monomer (PDB ID: 2L86).[29] The initial structure of hIAPP monomer along with its sequence and reference peptide HSSNN are shown in **Figure 4.1**. Similarly, two, three, four, and five amino acids were replaced in HSSNN to produce a library of mutated pentapeptides, and all pentapeptides were docked with hIAPP monomer.

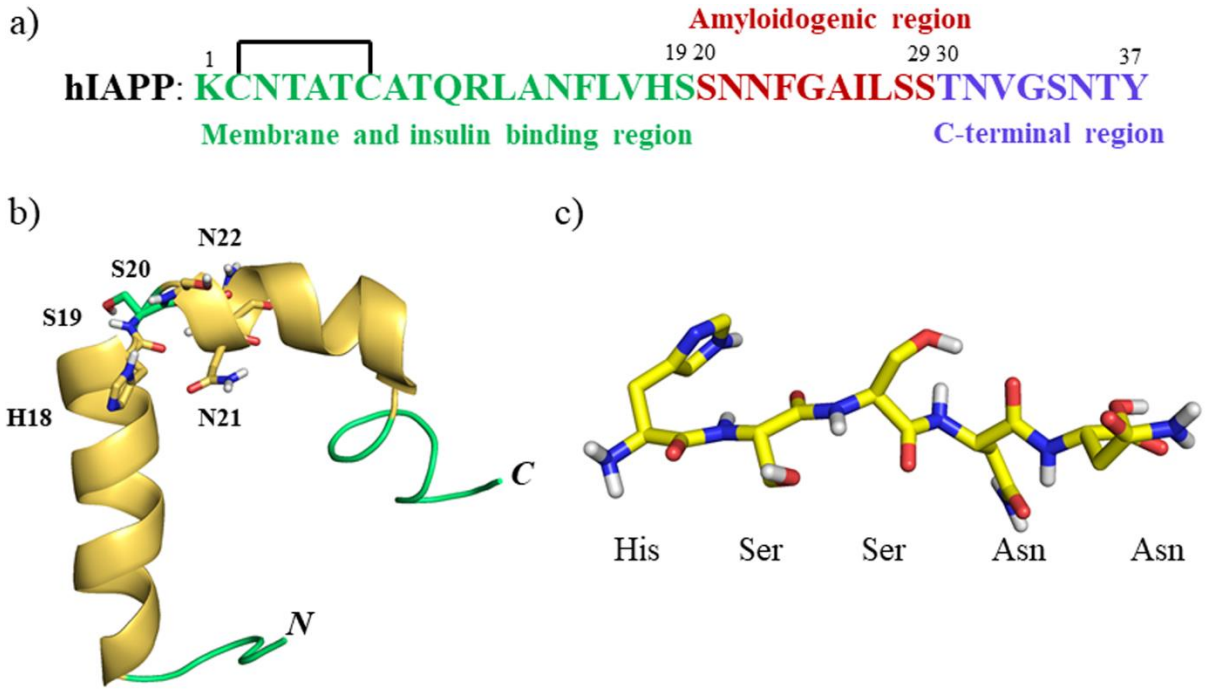

Figure 4.1: Amino acid sequence of hIAPP depicting the important regions (panel a). The disulfide linkage between hIAPP residues C2 and C7 is shown (panel a). hIAPP monomer (PDB ID: 2L86) in the cartoon with N- and C-termini labeled (panel b). The residues of the reference peptide (HSSNN) are shown in sticks. The initial structure of the fragment $HSSNN_{18-22}$ of hIAPP (panel c).

The designed library was screened for potential inhibitors of hIAPP aggregation using AutoDock Vina[30] assembled in the PyRx virtual screening tool.[31] In molecular docking, the peptides were shortlisted based on two criteria: the first was the binding energy of the peptides with hIAPP, and the second was the interaction of the peptides with the aggregation-prone region of hIAPP. The grid was calculated at about 20 Å to cover all the residues of hIAPP monomer and other parameters were used as default. To ensure the exhaustiveness of the global search space kept at a value of 10000. The binding energies of computationally designed peptides with hIAPP monomer were determined and then compared against the reference

peptide HSSNN. The top nine peptides were shortlisted based on interaction with a higher number of residues in the amyloidogenic core region S20-S29 of hIAPP monomer in the resulting docked poses. Meticulous visual inspection and analysis of the binding poses revealed nine pentapeptides with better overall docking profiles as compared to HSSNN.

4.2.3 Binding free energy evaluation using MM–PBSA method

The binding free energy was analyzed to further screen the topmost pentapeptides attained from the molecular docking studies. The binding free energy was evaluated by the MM−PBSA method using the g_mmpbsa tool (http://rashmikumari.github.io/g_mmpbsa).[32, 33] The top nine docked hIAPP-pentapeptide complexes were subjected to energy minimization and 500 ps *NVT* followed by *NPT* equilibration. The MD simulation was used to produce a conformational ensemble for the binding free energy calculations for the top nine and reference peptides. The binding free energy analysis was performed as reported in the previous studies.[34] MM-PBSA overestimates the absolute binding free energy, whereas relative binding affinities are acceptable.[35] Thus, the contribution of conformational entropy has not been taken into account for the evaluation of the binding free energy.[36] Numerous studies depicted that MM-PBSA still achieves satisfactory accuracy in ranking ligand affinities without taking into account conformational entropy.[37]

Table 4.6: Detail of the systems chosen for MD simulations.

System	Simulation length (ns)[b]	Simulation box parameters (nm)	N_w[c]
hIAPP monomer[a]	300	5.5 × 5.5 × 5.5	5264
hIAPP–HSSNN	300	5.5 × 5.5 × 5.5	5227
hIAPP–HSSQN	300	5.5 × 5.5 × 5.5	5229
hIAPP–HSSNQ	300	5.5 × 5.5 × 5.5	5229

[a]hIAPP monomer (PDB ID: 2L86); [b]The Amber99SB-ILDN force field and TIP3P water model are used for MD simulations. [c]Number of water molecules

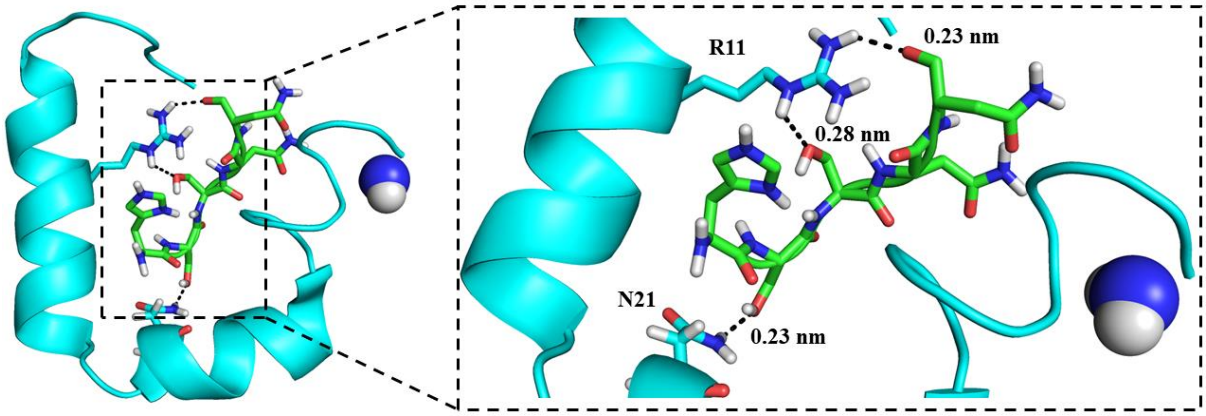

Figure 4.2: Docked pose of reference peptide HSSNN with hIAPP monomer (PDB ID: 2L86). The hydrogen bonds between hIAPP monomer and HSSNN are shown in the magnified view.

4.2.4 Details of MD simulation setup

MD simulations were performed to visualize the conformational changes in the hIAPP monomer on the incorporation of pentapeptides using GROMACS 5.0.7.[38] The coordinate and topology files were generated using the Amber99SB-ILDN force field[39] in GROMACS. The Amber99SB-ILDN force field was chosen for MD simulations as it provides a better energetic balance between helix and coil conformations and depicts good agreement with experimental NMR scalar coupling data.[39, 40] The details of all the systems used for MD simulations are presented in **Table 4.6**. The hIAPP-pentapeptide complexes were soaked with TIP3P[41] water molecules in a cubic box of dimension 5.5 nm × 5.5 nm × 5.5 nm. The four systems hIAPP monomer, hIAPP monomer–HSSNN, hIAPP monomer–HSSQN, and hIAPP monomer–HSSNQ were solvated with 5264, 5227, 5229, and 5229 TIP3P water molecules, respectively (Table 2). To neutralize the solvated system, counter Cl^- ions were introduced in the cubic box. Furthermore, NaCl was introduced to maintain the ionic strength of the systems at 150 mM followed by energy minimization using the steepest descent minimization algorithm. Each system was subjected to periodic boundary conditions, and equilibrated for 500 ps at 310 K under *NVT*, and then for 500 ps in *NPT* conditions. To calculate the long-range Coulomb interactions, the particle mesh Ewald (PME) technique was used.[42] The V-scaling method[43] and Parrinello-Rahman barostat[44] were employed to preserve the temperature and pressure of the systems, respectively. The MD simulations of hIAPP and hIAPP-pentapeptide complexes were performed at 310 K and 1 bar. The repeat simulations of 300 ns with varying initial velocities have been performed for hIAPP monomer. Random initial velocities for the atoms were

generated following a Maxwell distribution at a specified temperature using random seeds (gen_vel = yes, gen_seed = -1). The sequence of pseudo-random numbers utilized to set these initial random velocities is governed by the seed value. Therefore, altering the seed can introduce variability to a specific structure.

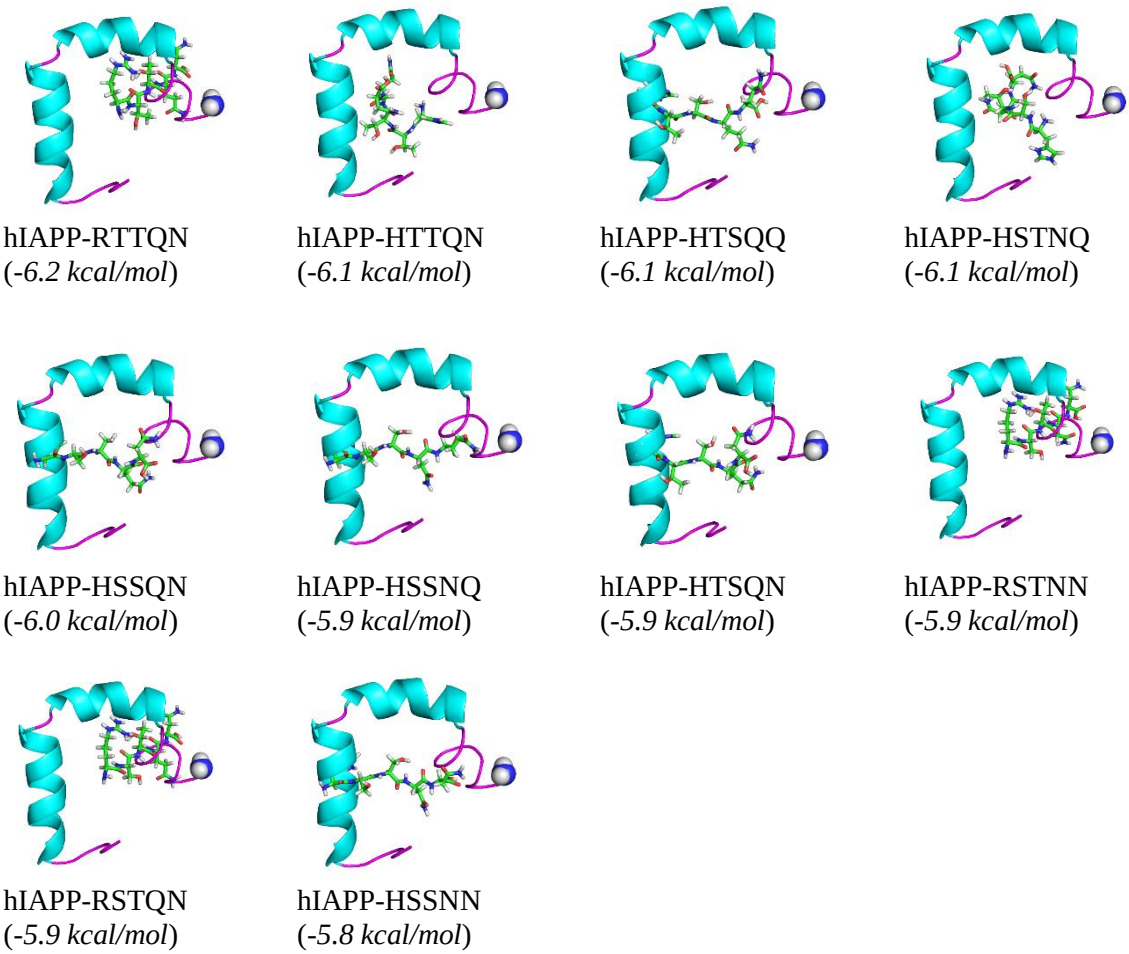

Figure 4.3: Docked poses of the top nine pentapeptides and reference peptide HSSNN with hIAPP monomer (PDB ID: 2L86). The hIAPP monomer is in cartoon and pentapeptides are in sticks. The binding energy evaluated using AutoDock Vina is expressed in kcal/mol.

The GROMACS tools, visual molecular dynamics (VMD),[45] and PyMOL[46] were employed to analyze the conformational ensembles from MD simulations. The root-mean-square deviation (RMSD) and radius-of-gyration (R_g) were evaluated by employing gmx rms, and gmx gyrate, respectively. The conformational changes in hIAPP monomer on the incorporation of pentapeptides were analysed by the Dictionary of Secondary Structure of Proteins (DSSP) analysis.[47] A hydrogen bond was counted when the donor(D)-acceptor(A) distance was within 3.5 Å and the H-D-A angle was within 30°.[48] The MD ensembles were clustered using a cut-off of 0.19 nm over the backbone atoms by employing Daura et al. algorithm.[49] The impact of

pentapeptides on the intramolecular side chain contacts in hIAPP monomer was calculated using gmx mdmat.

4.3 Result and discussion

4.3.1 Molecular docking of designed pentapeptides with hIAPP monomer

Molecular docking was performed to examine the binding affinity and key interactions of designed pentapeptides with hIAPP monomer. The pentapeptides bind to hIAPP monomer with a binding energy ranging from −4.5 to −6.2 kcal/mol. HSSNN depicts binding energy of –5.8 kcal/mol and displayed hydrogen bonds with Arg11 and Asn21 of hIAPP monomer with the hydrogen bond distances of 0.23 nm, 0.28 nm, and 0.23 nm, respectively (**Figure 4.2**). The pentapeptides RTTQN, HTTQN, HTSQQ, HSTNQ, HSSQN, HSSNQ, HTSQN, RSTNN, and RSTQN displayed interactions with the residues of amyloidogenic core region S20-S29 of hIAPP in the docked poses and displayed a higher binding affinity as compared to HSSNN (**Figure 4.3**). Thus, the top nine ranked pentapeptides along with HSSNN are selected for the binding free energy analysis.

4.3.2 Estimation of binding free energy between hIAPP monomer and screened pentapeptides using MM–PBSA method

To provide insight into the key interactions between hIAPP monomer and the top nine pentapeptides, the binding free energies of hIAPP-pentapeptide complexes were calculated. The pentapeptides HSSQN and HSSNQ bind to hIAPP monomer with a binding free energy of –21.25 ± 4.90 and –19.73 ± 3.10 kcal/mol, respectively, which is notably higher as compared to hIAPP-HSSNN complex (–11.90 ± 4.12 kcal/mol) (**Table 4.7**).

Table 4.7: Binding free energies (kcal/mol) of the top hit pentapeptides with hIAPP monomer.

Pentapeptide	Binding free energy (kcal/mol)						
	$\Delta G_{binding}$[a]	ΔE_{vdW}	$\Delta E_{elec.}$	ΔE_{MM}[b]	ΔG_{ps}	ΔG_{nps}	ΔG_{solv}[c]
HSSNN	–11.90 ± 4.12	–31.07 ± 8.77	–10.50 ± 5.21	–41.57 ± 13.98	33.41 ± 11.23	–3.74 ± 0.60	29.67 ± 11.83
HSSQN	–21.25 ± 4.90	–38.13 ± 7.21	–17.18 ± 5.09	–55.31 ± 12.30	37.93 ± 8.44	–3.94 ± 0.57	33.99 ± 9.01
HSSNQ	–19.73 ± 3.10	–36.21 ± 3.40	–8.05 ± 3.79	–44.26 ± 7.19	28.71 ± 4.04	–4.17 ± 0.30	24.54 ± 4.34
HTSQN	–14.50 ± 4.98	–24.85 ± 3.60	–11.63 ± 5.32	–36.48 ± 8.92	24.89 ± 5.36	–2.90 ± 0.37	21.99 ± 5.73

HTSQQ	–13.70 ± 4.72	–28.44 ± 4.61	–5.90 ± 5.31	–34.34 ± 9.92	24.02 ± 6.31	–3.30 ± 0.45	20.72 ± 6.76
HSTNQ	–5.60 ± 4.85	–9.70 ± 12.50	–3.13 ± 1.30	–12.83 ± 14.80	8.08 ± 8.13	–0.94 ± 5.37	7.14 ± 13.50
HTTQN	–3.90 ± 5.29	–9.81 ± 10.56	–3.35 ± 1.07	–13.16 ± 11.63	10.46 ± 8.41	–1.22 ± 2.98	9.24 ± 11.39
RTTQN	+3.63 ± 8.29	–28.68 ± 22.01	9.18 ± 3.96	–19.5 ± 25.97	26.81 ± 18.42	–3.04 ± 2.30	23.77 ± 20.72
RSTQN	+8.72 ± 6.26	–8.82 ± 11.03	11.84 ± 3.96	3.02 ± 14.9	6.88 ± 9.30	–1.18 ± 1.36	5.70 ± 10.66
RSTNN	+10.60 ± 4.10	–1.86 ± 5.98	11.90 ± 4.50	10.04 ± 10.48	0.90 ± 5.74	–0.31 ± 0.78	0.59 ± 6.52

[a] $\Delta G_{binding} = \Delta E_{MM} + \Delta G_{solv}$; [b] $\Delta E_{MM} = \Delta E_{vdW} + \Delta E_{elec}$; [c] $\Delta G_{solv} = \Delta G_{ps} + \Delta G_{nps}$

The binding free energy analysis revealed that the pentapeptides containing histidine bind more strongly to hIAPP monomer as compared to arginine-containing pentapeptides due to electrostatic repulsions of arginine with the positively charged residues of hIAPP monomer. The pentapeptides RSTNN (10.60 ± 4.10 kcal/mol), RSTQN (8.72 ± 6.26 kcal/mol), and RTTQN (3.63 ± 8.29 kcal/mol) depict unfavourable binding to hIAPP. Notably, RSTNN, RSTQN, and RTTQN displayed favourable binding to hIAPP using AutoDock Vina as it does not take into account the electrostatic interactions (**Figure 4.3**),[30] which, in turn, depicts the importance of screening potential inhibitors using MM-PBSA method. The electrostatic interactions are unfavourable for the pentapeptides containing arginine and favourable for histidine-containing pentapeptides (**Table 4.7**).

To examine the contribution of the residues of hIAPP monomer in binding to pentapeptides, the residue-wise binding free energy was evaluated (**Figure 4.4**). HSSNN preferentially binds to V17 (−1.08 kcal/mol) and S34 (−1.08 kcal/mol) of hIAPP monomer (**Figure 4.4a**). The hIAPP residues L12 (−2.82 kcal/mol), F15 (−1.43 kcal/mol), and Y37 (−1.56 kcal/mol) contribute significantly to binding with HSSQN (**Figure 4.4b**). HSSNQ binds to L12 (−3.14 kcal/mol), A13 (−0.92 kcal/mol), L16 (−1.03 kcal/mol), and T30 (−1.49 kcal/mol) of hIAPP monomer (**Figure 4.4c**).

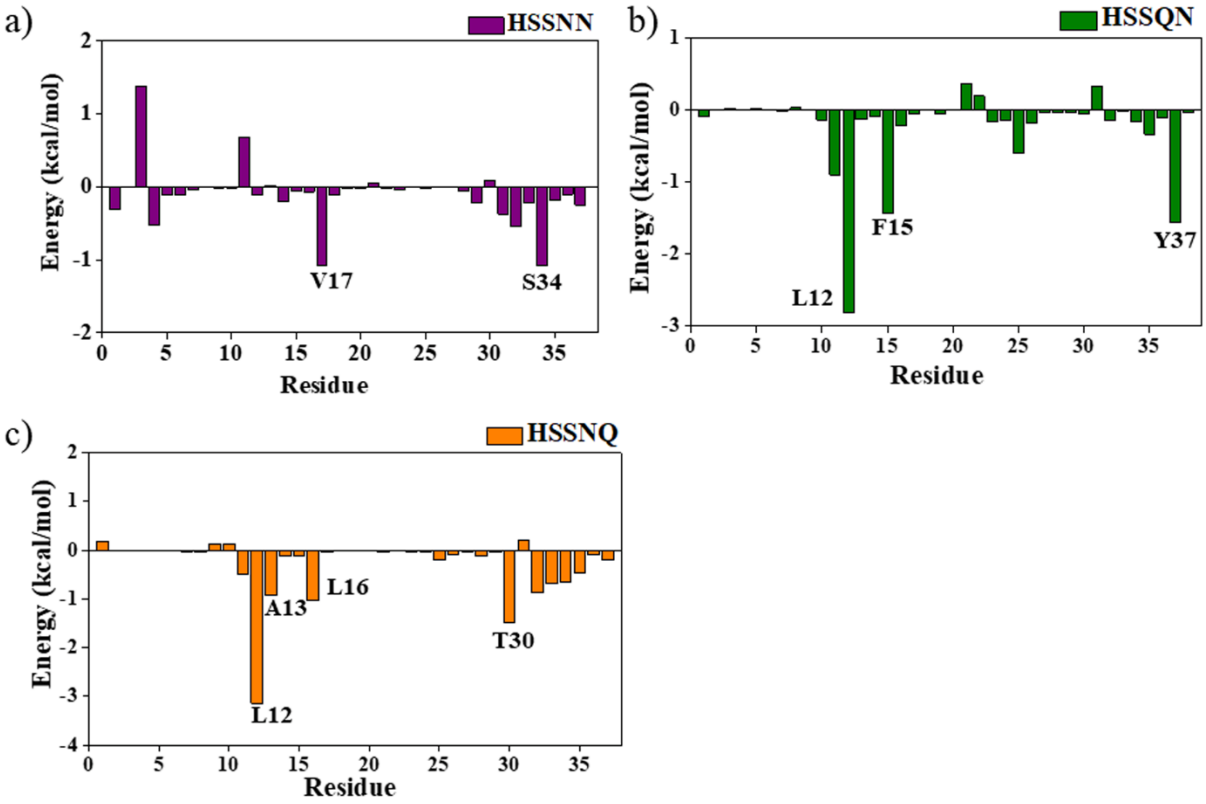

Figure 4.4: Residue-wise binding free energy of hIAPP with HSSNN (panel a), HSSQN (panel b), and HSSNQ (panel c). The hIAPP residues with the most favourable (< –1.0 kcal/mol) contribution in the binding with pentapeptides are labeled.

HSSQN displayed strong interactions with L12, F15, and Y37 of hIAPP monomer, which is consistent with Lao et al. that reported the preferential binding of dopamine to R11, L12, F15, H18, F23, I26, L27, and Y37 residues of hIAPP dimer.[50] The hIAPP residues F15, H18, F23, and Y37 play a critical role in hIAPP aggregation[51] and MD simulations depicted that the residue pairs F15–F15 and F15–Y37 have large contact numbers in hIAPP homodimer.[52] Thus, the binding of HSSQN with the key residues (F15 and Y37) of hIAPP monomer involved in its aggregation highlights the inhibitory potential of the designed pentapeptide. Furthermore, MD simulations of hIAPP-pentapeptide complexes have been performed to scrutinize the conformational dynamics and structural changes in hIAPP on the incorporation of pentapeptides.

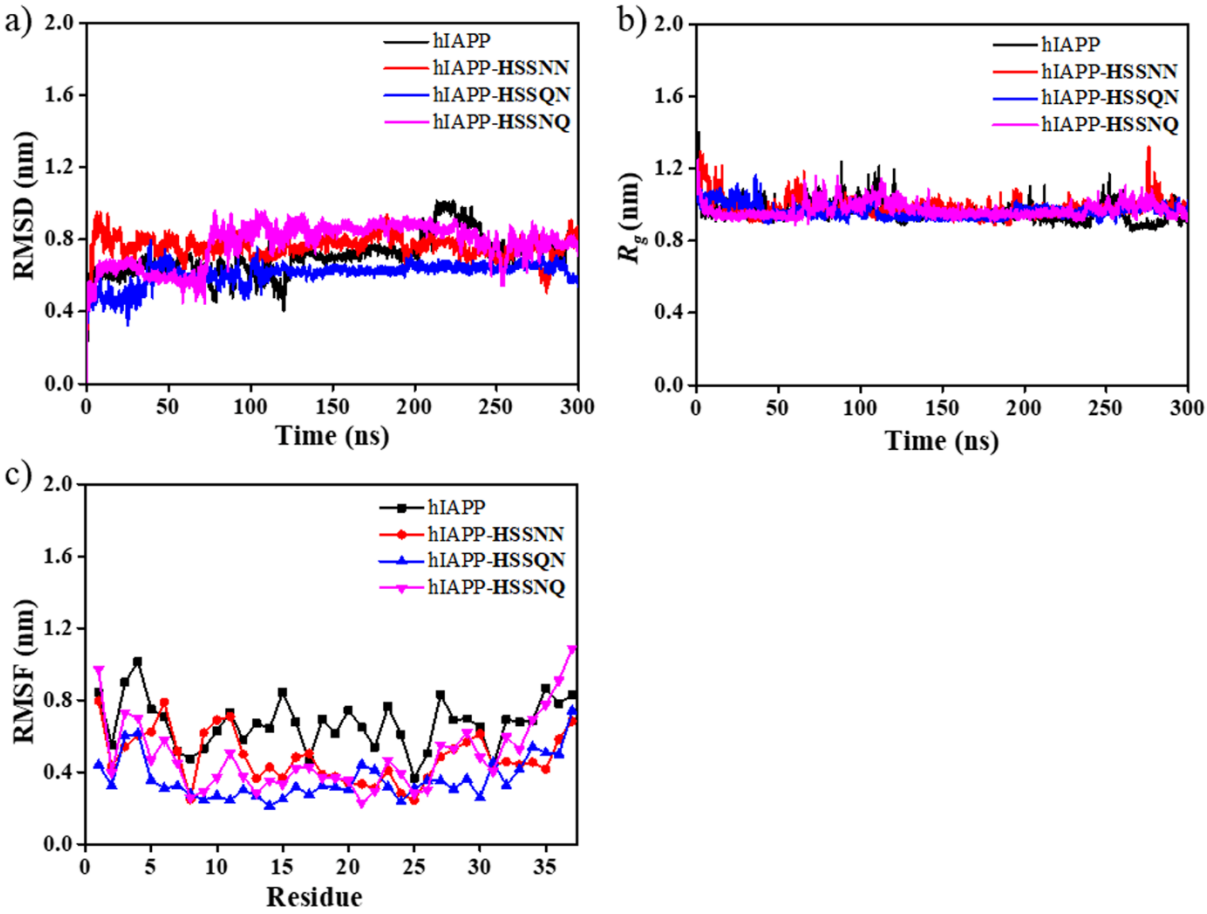

Figure 4.5: RMSD and radius-of-gyration (R_g) of hIAPP monomer (black), hIAPP-HSSNN (red), hIAPP-HSSQN (blue), and hIAPP-HSSNQ (pink) are shown in panels a, and, b, respectively. Average Cα RMSF of hIAPP alone and in the presence of pentapeptides (panel c).

4.3.3 Pentapeptides bind to hIAPP monomer to form a stable complex

The structural stability of the hIAPP-pentapeptide complexes was investigated using the backbone RMSDs of hIAPP in all systems (**Figure 4.5a**). The average RMSD of hIAPP monomer displays a limited change in the presence of pentapeptides that indicates stable binding of the pentapeptides with hIAPP monomer. The average RMSD of hIAPP monomer, hIAPP-HSSNN, and hIAPP-HSSNQ complex is noted to be 0.76 ± 0.02, 0.76 ± 0.06, and 0.77 ± 0.05 nm, respectively. The average RMSD was significantly decreased to 0.60 ± 0.07 nm in hIAPP-HSSQN, which indicates higher structural stability of hIAPP-HSSQN complex.

The stable R_g during simulation depicts the stability of hIAPP-pentapeptide complexes (**Figure 4.5b**). The average R_g for hIAPP monomer was noted to be 0.95 ± 0.04 nm, which is consistent with Kumari et al. that reported the average R_g of hIAPP monomer as ~1.0 nm.[53] The average

R_g for hIAPP−HSSNN, hIAPP−HSSQN, and hIAPP−HSSNQ complexes is noted to be 0.98 ± 0.04, 0.94 ± 0.08, and 0.97 ± 0.07 nm, respectively (**Figure 4.5b**). The R_g of hIAPP monomer depicts a marginally lower value on the addition of HSSQN, which indicates the stability of hIAPP-HSSQN complex. Triplicate simulations of hIAPP monomer have been performed to check the reliability of the MD simulation data (**Figure 4.6**). An almost similar pattern was noted in the RMSD and R_g during simulation that indicates the reproducibility of the simulation data.

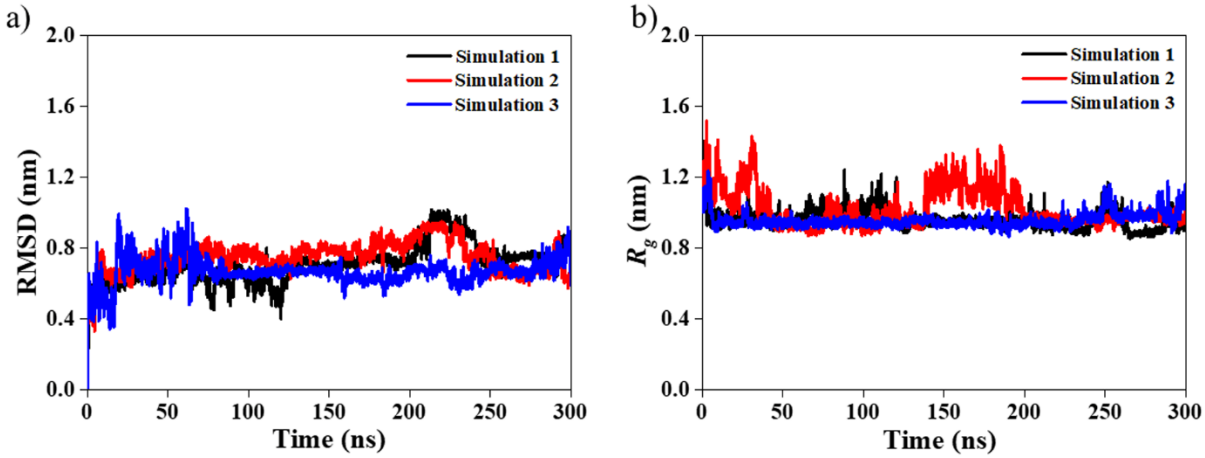

Figure 4.6: Root–mean–square deviation (RMSD) and radius-of-gyration (R_g) of simulations with different initial velocities for hIAPP monomer is shown in panels a, and b, respectively.

The residue-based RMSF for Cα atoms of hIAPP monomer in the absence and presence of pentapeptides was evaluated to analyze the flexibility and localized dynamics of hIAPP monomer (**Figure 4.5c**). The average RMSF for hIAPP monomer, hIAPP−HSSNN, hIAPP−HSSQN, and hIAPP−HSSNQ are noted to be 0.67 ± 0.04, 0.48 ± 0.03, 0.36 ± 0.06, and 0.49 ± 0.03 nm, respectively. The lowest RMSF in hIAPP−HSSQN as compared to the other systems depicted higher structural and conformational stability of hIAPP monomer on the incorporation of HSSQN. In comparison to hIAPP monomer, a substantial difference in RMSF was noted in residues K1−A5, A8, R11−T30, and V32−Y37 for hIAPP−HSSNN, K1−T30, V32−Y37 for hIAPP−HSSQN, and C2−G33, N35 for hIAPP−HSSNQ. Notably, reduced conformational fluctuations were observed within the residues of the aggregation-prone regions A8−S20 and S20−S29 of hIAPP monomer[54] in the presence of pentapeptides (**Figure 4.5c**), which stabilizes hIAPP monomer. Remarkably, the residues of the aggregation-prone regions ($hIAPP_{8–20}$ and $hIAPP_{20–29}$) of hIAPP monomer fluctuate at markedly lower

values in the presence of HSSQN as compared to other pentapeptides (**Figure 4.5c**), which indicates the higher conformational stability of hIAPP−HSSQN complex.

5.3.4 Effect of pentapeptides on the secondary structure of hIAPP monomer

To investigate the inhibitory effect of pentapeptides on the conformational conversion of hIAPP monomer, the secondary structure analysis of hIAPP monomer with and without pentapeptides was performed (**Figure 4.7**, **Table 4.8**). The helix structure was gradually decreasing in hIAPP monomer (Figure 4a) which is consistent with Tran et al., which reported that amidated hIAPP monomer rapidly lost its helices and unfolded during MD simulation.[55] The helix, β–sheet, coil, bend, and turn conformations in hIAPP monomer were noted to be 23.5 ± 3.0, 0.0 ± 0.0, 31.1 ± 1.9, 20.3 ± 3.1, and 25.1 ± 1.6%, respectively (**Table 4.8**).

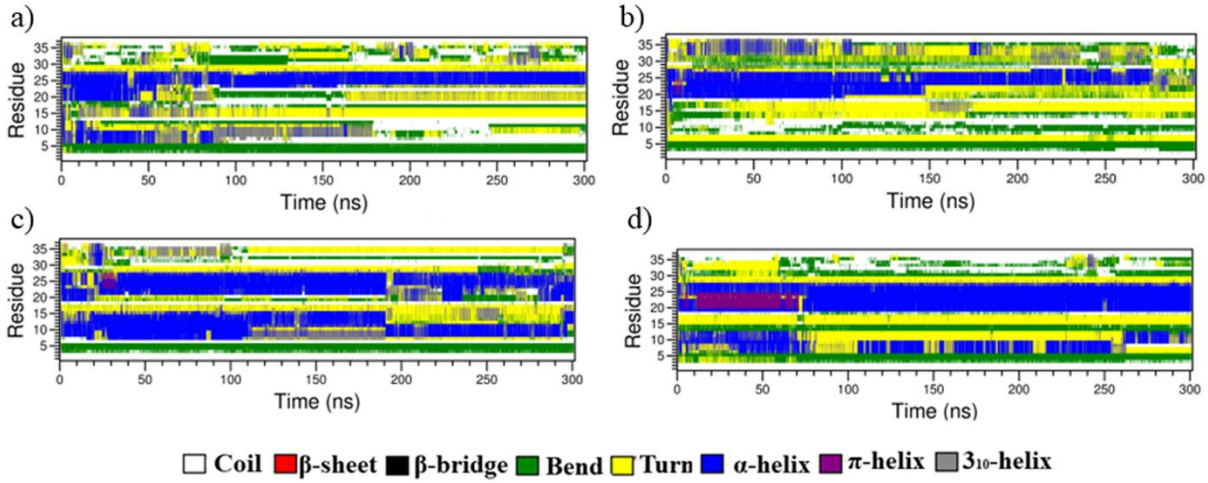

Figure 4.7: Evolution of secondary structure during simulation for hIAPP (panel a), hIAPP-HSSNN (panel b), hIAPP-HSSQN (panel c), and hIAPP-HSSNQ (panel d).

Additionally, the intrinsic disorder propensity of hIAPP monomer was analyzed using an ODiNPred webserver.[56] The disorder plot analysis highlighted that the C-terminal residues displayed a higher probability to exist in the coil conformation as compared to the N-terminal residues of hIAPP monomer (**Figure 4.13**). This is consistent with previous studies that highlight a sampling of the coil conformation in the C-terminal region of hIAPP monomer.[57]

The helical content was significantly increased from 23.5 ± 3.0 in hIAPP monomer to 38.1 ± 3.6, and 33.6 ± 3.0% on the incorporation of HSSQN, and HSSNQ, respectively, which indicates reduced aggregation propensity of hIAPP monomer on the incorporation of pentapeptides. Concomitantly, the coil content was decreased from 31.1 ± 1.9 in hIAPP monomer to 25.2 ± 2.4, and 21.5 ± 2.0% on the incorporation of HSSQN, and HSSNQ,

respectively. The secondary structure analysis depicted that HSSQN and HSSNQ dramatically impede the coil conformation and induce the formation of helix structures in hIAPP monomer, which, in turn, suggested a lower aggregation probability of hIAPP monomer in the presence of HSSQN and HSSNQ.

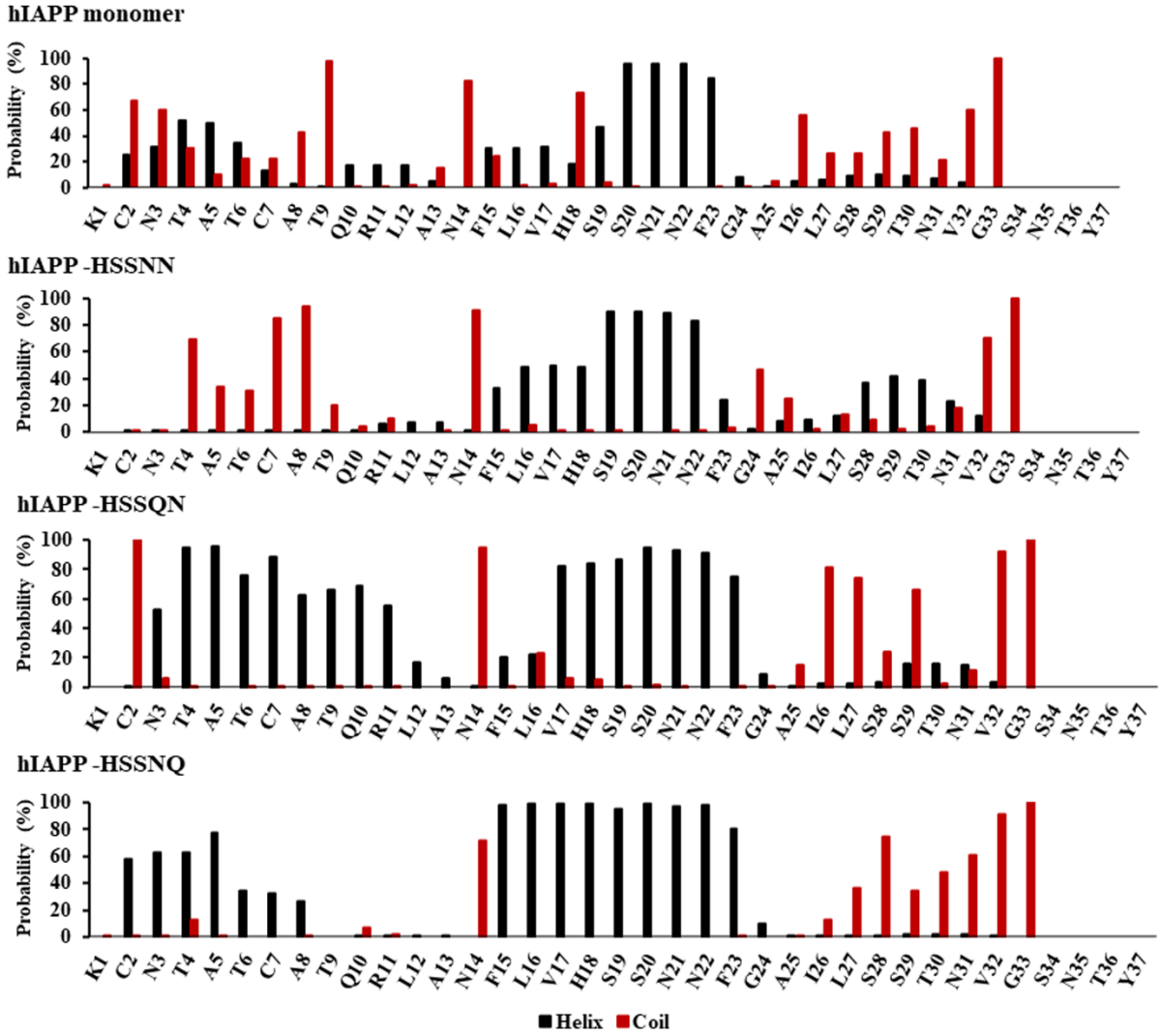

Figure 4.8: Residue-wise helix and coil content in hIAPP alone and hIAPP-pentapeptide complexes.

To determine the influence of pentapeptides on the secondary structure of each residue of hIAPP monomer, the residue-wise helix and coil content were evaluated (**Figure 4.8**). In the hIAPP monomer, residues T4–T6, F15−V17, and S19–F23 mainly adopt helical conformation (**Figure 4.8a**). The sampling of helical structures was noted in the N-terminal residues A13–V17 in an all-atom replica exchange molecular dynamics (REMD) study on hIAPP(11–25) monomer.[58] The hIAPP residues C2, N3, C7−T9, N14, H18, and I26−G33 displayed high

probabilities to adopt coil conformation that is consistent with the previous experiments, which highlighted that C−terminal residues (S28−Y37) of hIAPP monomer predominantly sample coil conformations.[59] The probability of helical content was slightly increased in the residues F15−S19 and L27–V32 of hIAPP monomer on the addition of HSSNN (**Figure 4.8b**). A remarkable increase in the helical content in the residues N3−L12 and V17−F23 of hIAPP monomer was observed on the incorporation of HSSQN (**Figure 4.8c**). Upon HSSNQ binding, the propensity of residues C2−A8 of hIAPP monomer to sample coil conformation was significantly decreased and the probability of helical content was increased in the F15−F23 region of hIAPP monomer (**Figure 4.8d**). An overall increase in helical content in the amyloidogenic region A8−S20 was observed in presence of HSSQN and HSSNQ. Thus, a lower sampling of the coil and notably higher helical content in hIAPP residues on the incorporation of HSSQN and HSSNQ highlights the role of pentapeptides in stabilizing hIAPP monomer structure.

Table 4.8: Secondary structural component statistics for hIAPP monomer and hIAPP-pentapeptide complexes.

System	helix[a]	β–sheet[b]	coil	bend	turn
hIAPP	23.5 ± 3.0	0.0 ± 0.0	31.1 ± 1.9	20.3 ± 3.1	25.1 ± 1.6
hIAPP-HSSNN	20.4 ± 2.6	0.0 ± 0.0	26.6 ± 2.4	23.8 ± 2.8	29.2 ± 0.7
hIAPP-HSSQN	38.1 ± 3.6	0.0 ± 0.0	25.2 ± 2.4	14.4 ± 4.7	22.3 ± 1.6
hIAPP-HSSNQ	33.6 ± 3.0	0.0 ± 0.0	21.5 ± 2.0	20.4 ± 2.2	24.5 ± 1.1

[a]helix comprises α–, π–, and 3_{10} helix ; [b]β–sheet comprises β–strand and β–bridge

To analyze the stability of the hIAPP-pentapeptide complexes, hydrogen bond analysis was performed (**Figure 4.9a**). The average hydrogen bonds were observed to be 6.0, 5.7, and 7.4, for hIAPP-HSSNN, hIAPP-HSSQN, and hIAPP-HSSNQ, respectively, which indicate the stability of the hIAPP-pentapeptide complexes. A relatively large hydrogen bond between hIAPP monomer and HSSNQ suggests its stronger binding, which, in turn, depicts its potential to block the self-aggregation of hIAPP.

The residue-wise hydrogen bond analysis depicted a significant contribution of hIAPP residues Q10−L12, N14, F15, and N35−Y37 in binding to HSSNN (**Figure 4.9b**). HSSQN displayed hydrogen bond interactions with K1, Q10, N14, N21, S28, and T30 of hIAPP. The residues N14, V17–S19, N22, and S34–N35 of hIAPP displayed hydrogen bonds with HSSNQ. Roy and Paul reported that hydrogen bonds between the residues of the regions N3-Q10, N14-N22,

and S28-Y37, enhance the aggregation between the amyloidogenic regions of hIAPP.[20] Interestingly, pentapeptides displayed hydrogen bonds with the residues of the regions N3-Q10, N14-N22, and S28-Y37of hIAPP, which, in turn, decreases the intramolecular contacts between amyloidogenic regions of hIAPP and thus, lower the aggregation propensity of hIAPP.

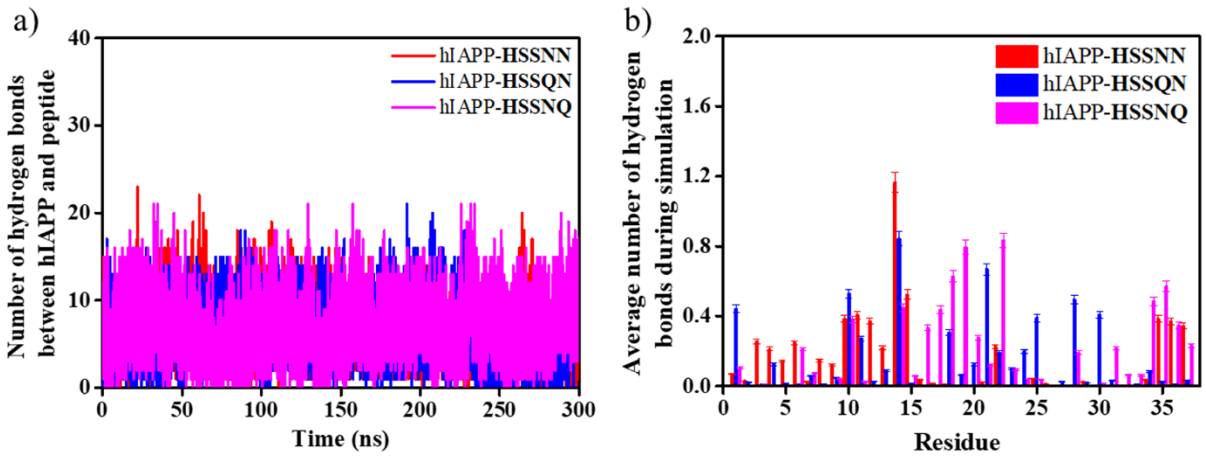

Figure 4.9: Hydrogen bonds between hIAPP and pentapeptides during simulation (panel a). Residue-wise hydrogen bonds of the hIAPP with the pentapeptides (panel b).

5.3.5 Effect of pentapeptides on the intramolecular side chain contacts in hIAPP monomer

A comparison between the intramolecular side chain contacts in hIAPP monomer with and without pentapeptides highlights significant changes in the side chain contacts of the residues of N-terminal, amyloidogenic (residues 20-29, SNNFGAILSS) and C-terminal regions of hIAPP monomer (**Figure 4.10**). The protein side chain−side chain contact map has been widely used to characterize intrachain hydrophobic contacts.[60] In hIAPP monomer, several contacts between the side chains of hIAPP residues were observed that attributed to intrachain hydrophobic contacts keeping the N−terminal and C−terminal of hIAPP monomer close to each other (**Figure 4.10a**). In comparison to hIAPP monomer, the side chain contacts between N−terminal residues (K1−A8) and C-terminal residues (L27−N35) was notably reduced in the presence of HSSNN (**Figure 4.10b**). The contacts between the side chains of N−terminal residues (K1−T6) and A13−L27 residues were significantly disrupted in the presence of HSSQN (**Figure 4.10c**). On the incorporation of HSSNQ, the side chain contacts between N−terminal (K1−T9) and C−terminal (V32−Y37) residues in hIAPP monomer was greatly reduced (**Figure 4.10d**). The side chain-side chain contact maps highlighted that HSSQN

inhibited long-range intra hIAPP side chain-side chain contacts between the regions containing $hIAPP_{20-29}$ (SNNFGAILSS) amyloid core segment which is crucial for hIAPP aggregation.[22]

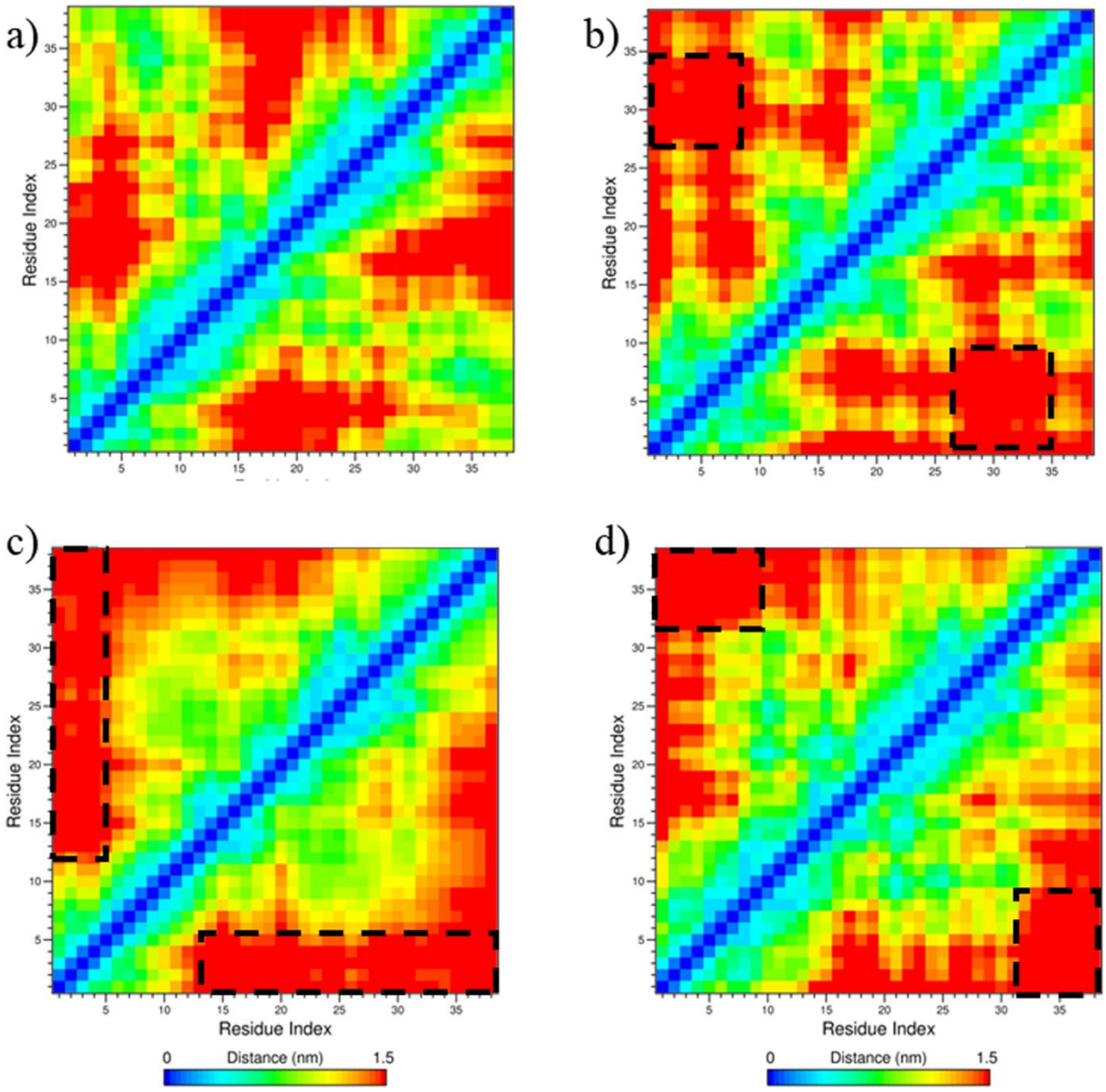

Figure 4.10: Side chain–side chain contact probability maps for hIAPP (panel a), hIAPP-HSSNN (panel b), hIAPP-HSSQN (panel c), and hIAPP-HSSNQ (panel d).

The average solvent accessible surface area (SASA) of hIAPP−monomer, hIAPP−HSSNN, hIAPP−HSSQN, and hIAPP−HSSNQ was noted to be 31.6 ± 1.6 nm^2, 32.1 ± 1.2 nm^2, 30.4 ± 0.9 nm^2, and 30.9 ± 0.6 nm^2, respectively (**Figure 4.11a**). The SASA remain stable during simulation for the hIAPP-pentapeptide complexes, which indicate the stable binding of pentapeptides to hIAPP monomer.

The residue-wise SASA analysis highlighted lower SASA of the hydrophobic residues of hIAPP monomer in the presence of pentapeptides (**Figure 4.11b**). In comparison to hIAPP monomer alone, the following hydrophobic residues displayed lower SASA in the hIAPP monomer–pentapeptides complexes: (*i*) G24, V32 for hIAPP monomer–HSSNN (*ii*) A5, V32 for hIAPP monomer–HSSQN, and (*iii*) A8, F15, G24, A25 for hIAPP monomer–HSSNQ. A lower SASA for the hydrophobic residues of hIAPP monomer on the incorporation of pentapeptides suggests a lower aggregation tendency of hIAPP monomer.

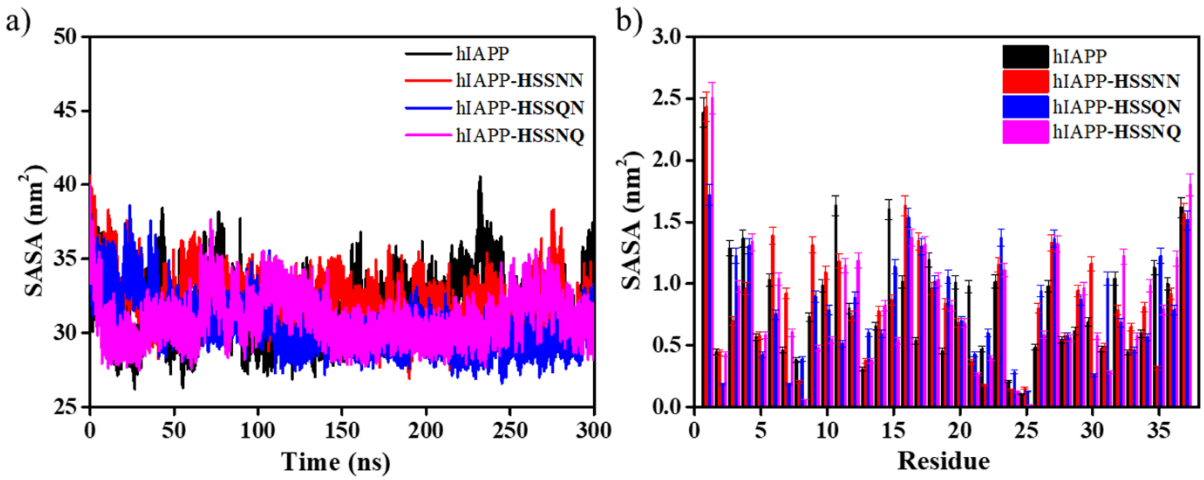

Figure 4.11: SASA of the hIAPP monomer in different systems (panel a). Residue-wise SASA in hIAPP alone and hIAPP-pentapeptide complexes (panel b).

5.3.6 Effect of pentapeptides on the conformational transitions of hIAPP monomer

The clustering analysis was performed to explore the impact of pentapeptides on the conformational sampling of hIAPP monomer. A total of 70 clusters were noted in hIAPP monomer and the number significantly decreased to 20, 25, and 15, for hIAPP monomer–HSSNN, hIAPP monomer–HSSQN, and hIAPP monomer–HSSNQ, respectively, which indicates higher conformational stability of hIAPP monomer in the presence of pentapeptides (**Table 4.9**).

The most-populated cluster constitutes 44.85%, 85.86%, 97.40%, and 75.30% of all the sampled conformations in hIAPP monomer alone, hIAPP−HSSNN, hIAPP−HSSQN, and hIAPP−HSSNQ, respectively, which indicate higher homogeneity in the hIAPP monomer conformational ensemble on the incorporation of pentapeptides (**Table 4.9**, **Figure 4.12**).

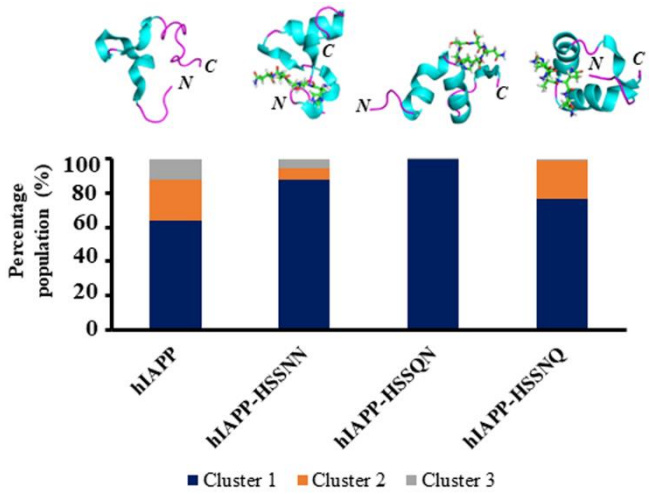

Figure 4.12: Percentage population and the central member of the highest populated cluster in hIAPP monomer, hIAPP-HSSNN, hIAPP-HSSQN, and hIAPP-HSSNQ complexes.

Specifically, the most-populated cluster in hIAPP−HSSQN constituted 97.40% population and sampled helical conformations in the regions T6−L16, H18−S28, and N31−N35 of hIAPP monomer. The visual inspection depicts that hIAPP monomer sampled coiled conformation with short helix structures (**Figure 4.12**). Increased sampling of the helix conformation in the central member of the highest populated cluster of hIAPP-pentapeptide complexes was observed, which matches with the secondary structure analysis.

Table 4.9: Total number of clusters and the population of the three highest populated clusters (C_1, C_2, and C_3) of hIAPP monomer and hIAPP-pentapeptide complexes during MD simulation.

System	No. of clusters	Population of the three highest populated clusters		
		C_1	C_2	C_3
hIAPP monomer	70	44.85	17.24	8.50
hIAPP–HSSNN	20	85.86	6.42	5.71
hIAPP–HSSQN	25	97.30	0.14	0.12
hIAPP–HSSNQ	15	75.30	22.80	0.76

a)

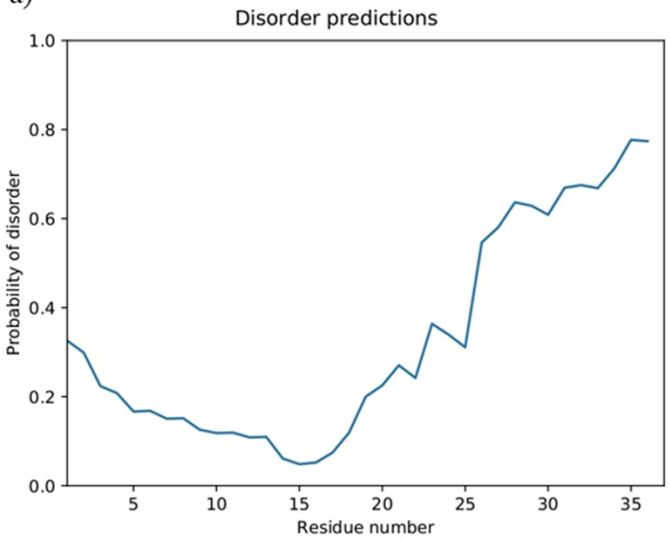

b)

Residue number	Residue code	Probability of disorder
1	K	0.38
2	C	0.32
3	N	0.29
4	T	0.22
5	A	0.20
6	T	0.16
7	C	0.16
8	A	0.15
9	T	0.15
10	Q	0.12
11	R	0.11
12	L	0.11
13	A	0.10
14	N	0.10
15	F	0.06
16	L	0.04
17	V	0.05
18	H	0.07
19	S	0.11
20	S	0.19
21	N	0.22
22	N	0.27
23	F	0.24
24	G	0.36
25	A	0.33
26	I	0.31
27	L	0.54
28	S	0.58
29	S	0.63
30	T	0.62
31	N	0.60
32	V	0.66
33	G	0.67
34	S	0.66
35	N	0.71
36	T	0.77
37	Y	0.77

Figure 4.13: Disorder probability plot and probability of disorder for hIAPP residues is shown in panels a, and, b, respectively.

To determine the physicochemical, ADME, and toxicity properties of the top hit peptides as well as well-known small molecule [epigallocatechin gallate (EGCG) and quercetin] inhibitors of hIAPP aggregation, ADMETboost was employed.[61] The ADMET characteristics of the top hit peptides were interpreted based on the criteria described in ADMETlab 2.0 platform.[62] The top hit peptides displayed comparable ADMET parameters as noted for EGCG and Quercetin (**Table 4.10**).

Table 4.10: Comparison of ADMET properties of top hit peptides and small molecule (EGCG and Quercetin) inhibitors of hIAPP aggregation.

Category	Property (unit)	HSSNN	HSSQN	HSSNQ	EGCG	Quercetin	References range
	Caco-2 permeability log(cm/s)	-5.81	-5.81	-5.81	-5.64	-5.30	Optimal: Higher than -5.15
Absorption	P-Glycoprotein inhibition (%)	38.69	37.37	37.35	48.73	49.54	Optimal:<=30%; Medium:30%-70%; Poor:>=70%

	HIA/Human Intestinal Absorption (%)	47.21	46.91	46.91	70.37	72.56	Optimal:>=80%; Medium:30%-80%; Poor:<=30%
Distribution	Blood brain barrier penetration (%)	23.07	25.36	25.30	20.63	32.22	Optimal:<=30%; Medium:30%-70%; Poor:>=70%
	PPB/Plasma protein binding (%)	47.18	47.13	46.84	45.81	43.33	Optimal:<=90%; Poor:>90%
Metabolism	CYP2C9 Substrate	Low	Low	Low	Low	Low	>0.5: A substrate; <0.5: Non substrate
	CYP2C9 Inhibition (%)	47.14	47.11	47.86	61.05	67.96	
	CYP3A4 Substrate	Low	Low	Low	Low	Low	>0.5: A substrate; <0.5: Non substrate
	CYP3A4 Inhibition (%)	38.61	39.61	39.32	38.82	37.23	
Excretion	Clearance (ml/ min/Kg)	0.47	0.47	0.47	0.47	0.34	High: >15 ml/ min/kg; Moderate: 5-15 ml/min/kg; Low: <5 ml/min/kg
	T1/2/Half-life (h)	114.9	115.21	115.21	68.35	67.42	Long half-life: >3 h; Short half-life: <3 h
Toxicity	hERG blockers (%)	43.02	43.29	43.29	43.38	37.47	Optimal:<=30%; Medium:30%-70%; Poor:>=70%
	AMES (Ames mutagenicity) (%)	39.21	39.24	39.36	44.81	43.40	Optimal:<=30%; Medium:30%-70%; Poor:>=70%
	DILI/Drug Induced Liver Injury (%)	64.56	63.84	63.84	53.88	56.07	Optimal:<=30%; Medium:30%-70%; Poor:>=70%

4.3.7 PCA and FEL analyses of hIAPP monomer and hIAPP-pentapeptide complexes

PCA was performed to analyze the effect of pentapeptides on the conformational fluctuations and atomic movements in hIAPP monomer (**Figure 4.14**). The first two eigenvectors represent an essential conformational subspace with noteworthy concerted motions [49.3, 46.2, 71.0, and 67.6% in hIAPP monomer, hIAPP–HSSNN, hIAPP–HSSQN, and hIAPP–HSSNQ, respectively, and thus was chosen for the analysis of the conformational dynamics (**Figure 4.14**). The flexibility of systems was assessed using trace of the diagonalized covariance matrix of the Cα atomic positional fluctuations. The trace values were noted to be 7.5, 5.4, 3.4, and, 6.9 nm^2 for hIAPP monomer, hIAPP–HSSNN, hIAPP–HSSQN, and hIAPP–HSSNQ, respectively. A noteworthy lower trace value in hIAPP–HSSQN depicted lower fluctuations in

hIAPP monomer on the addition of HSSQN and highlight the preservation of the native conformation of hIAPP monomer.

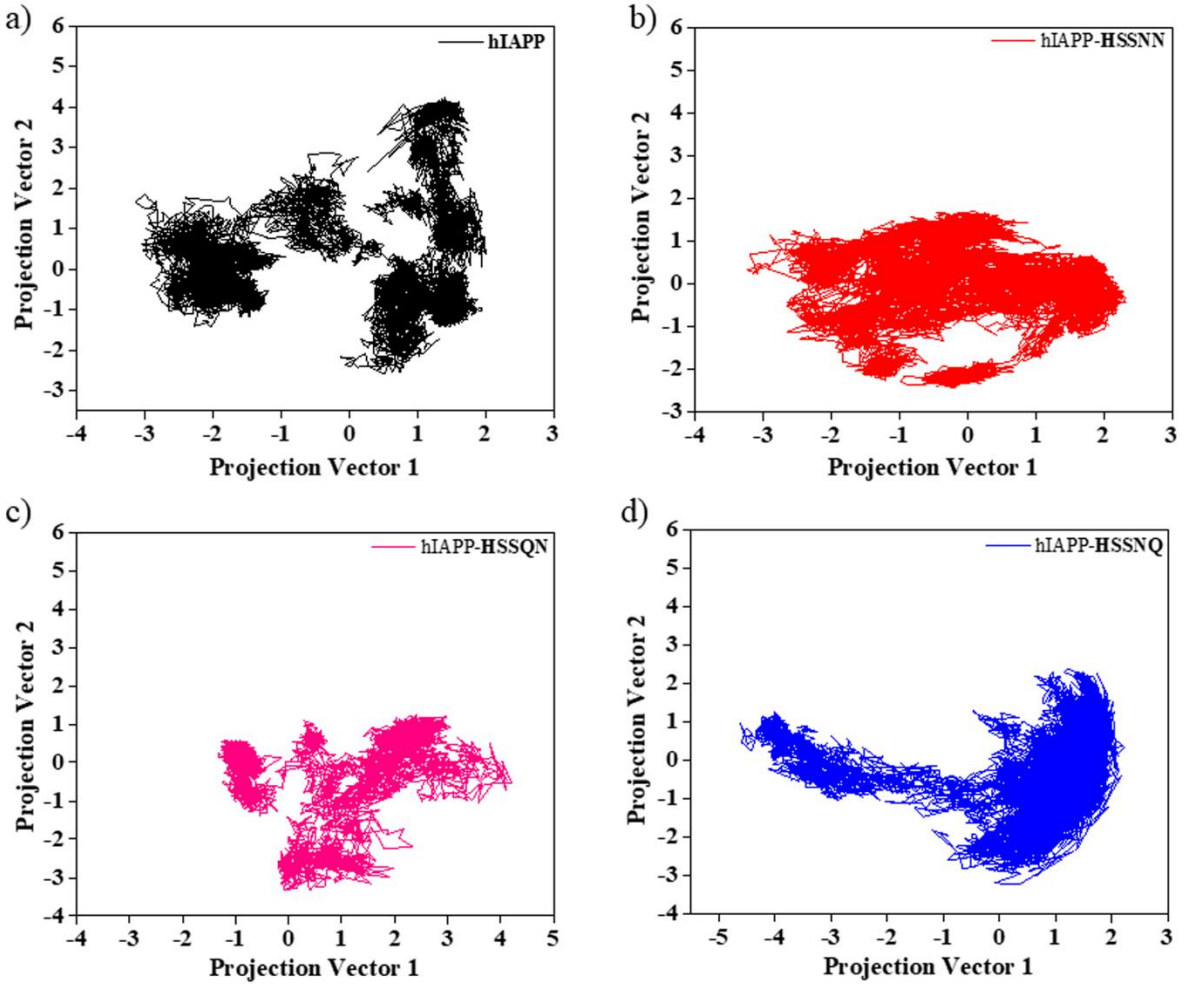

Figure 4.14: The effect of pentapeptides on the conformational flexibility of hIAPP monomer was analyzed using 2D projection of motion over the first two eigenvectors.

Furthermore, the conformational states of the hIAPP monomer and hIAPP–pentapeptide complexes were evaluated using FEL (**Figure 4.15**). Only one free energy minima were noted in hIAPP–HSSQN as compared to multiple minima in other systems, which highlights higher conformational homogeneity in hIAPP monomer in the presence of HSSQN. The sampling of helix conformation in the minimum energy conformation extracted from FEL was noted to increase from 19 to 24% in hIAPP monomer on the incorporation of HSSNN (**Table 4.11**). A noteworthy increase in the helix content from 19% in hIAPP monomer to 38–44% on the addition of HSSQN and HSSNQ depicts the prevention of conformational transition to aggregation-prone structures.

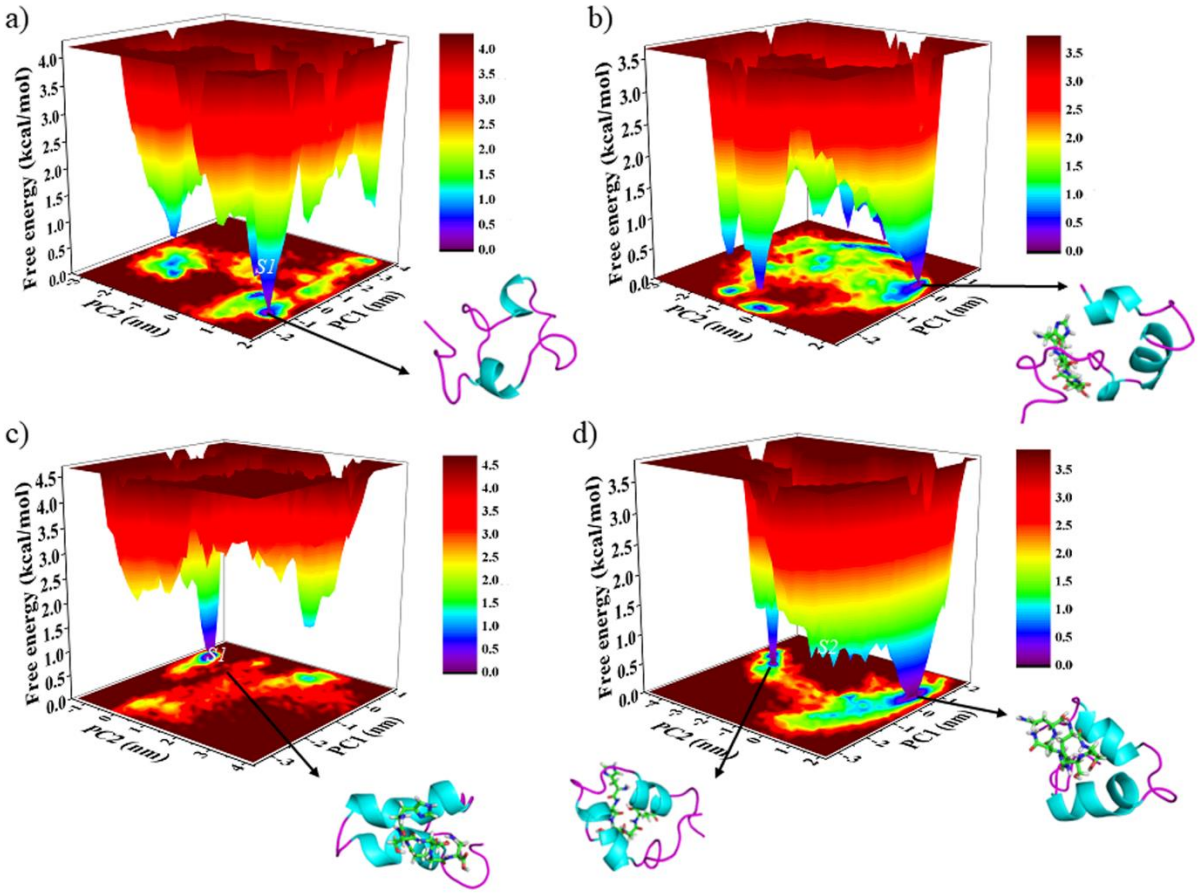

Figure 4.15: The FEL along PC1 and PC2 of hIAPP monomer, hIAPP–HSSNN, hIAPP–HSSQN, and hIAPP–HSSNQ is shown in panels a, b, c, and d, respectively. The purple regions signify the minimum energy basins, whereas wine red represents higher energy basins. The metastable conformational states are represented by cyan and green regions. The conformations extracted from the minimum energy basins are displayed in cartoons.

Table 4.11: Secondary structure composition of the representative conformations extracted from the FEL of simulated systems.

System	conformation	helix[a]	coil	bend	turn
hIAPP monomer	*S1*	19	27	22	32
hIAPP–HSSNN	*S1*	24	24	14	38
hIAPP–HSSQN	*S1*	44	16	14	27
	S2	41	11	14	35
hIAPP–HSSNQ	*S1*	38	24	14	24

[a]helix is the sum of α–, π– and 3_{10} helix

The MD simulations highlighted that HSSQN and HSSNQ displayed higher binding affinity to hIAPP monomer and induces significantly higher helical conformations in hIAPP monomer as compared to the reference peptide HSSNN. Furthermore, the top hit peptides identified using computational techniques need to be assessed for their inhibitory potential against hIAPP

aggregation using experimental studies. With the improvement in the current force fields by taking into account the charge polarizability and enhanced sampling methods, MD simulations can be employed to screen potential druggable candidates from the large libraries in the drug discovery efforts.

4.4 Conclusions

In this work, an integrated computational approach was employed to design and identify new peptides derived from an hIAPP sequence ($HSSNN_{18\text{-}22}$) that displayed highly promising inhibitory activity against hIAPP aggregation. The molecular docking studies and MD simulations of the top hit peptides HSSQN and HSSNQ displayed higher binding affinity to hIAPP monomer as compared to the parent native sequence $HSSNN_{18\text{-}22}$ of hIAPP monomer. HSSQN and HSSNQ bind to hIAPP monomer with a binding free energy of –21.25 ± 4.90 and –19.73 ± 3.10 kcal/mol, respectively, which is significantly higher as compared to hIAPP-HSSNN complex (–11.90 ± 4.12 kcal/mol). Notably, HSSQN binds to L12, F15, and Y37 of hIAPP monomer that play a critical role in hIAPP aggregation. The RMSD and R_g analyses highlights increased structural stability of hIAPP monomer on the addition of designed pentapeptides. Remarkably, the residues of the aggregation-prone regions ($hIAPP_{8–20}$ and $hIAPP_{20–29}$) of hIAPP monomer fluctuate at markedly lower values in the presence of HSSQN as compared to other pentapeptides, which indicates the higher conformational stability of hIAPP−HSSQN complex. The content of the non aggregation-prone helical conformation was notably increased in hIAPP monomer with a concomitant decrease in the coil content on the incorporation of HSSQN, and HSSNQ, which indicates a lower aggregation propensity of hIAPP monomer. Moreover, a notable increase in the helical content of the amyloidogenic region A8−S20 of hIAPP monomer was observed in the presence of HSSQN and HSSNQ, which depict the potential of designed pentapeptides as inhibitors of hIAPP aggregation. This is in coherence with clustering analysis that depicted a higher sampling of helical conformation in the central member of the highest populated clusters of hIAPP-HSSQN and hIAPP-HSSNQ complexes as compared to hIAPP alone. The hydrogen bond and SASA analyses depicted the stable binding of the HSSQN and HSSNQ with hIAPP monomer. It is worth noting that the intramolecular side chain-side chain contacts were significantly decreased in the hIAPP monomer on the incorporation of HSSQN and HSSNQ, which depict their tendency to block hIAPP aggregation. The computationally designed peptides, HSSQN and HSSNQ, emerged as

new, simple, and efficient inhibitors of hIAPP aggregation and encourage further experimental validation.

4.5 References

1. Ke, P.C.; Zhou, R.; Serpell, L.C.; Riek, R.; Knowles, T.P.; Lashuel, H.A.; Gazit, E.; Hamley, I.W.; Davis, T.P.; Fändrich, M.; Otzen, D.E. Half a century of amyloids: past, present and future. *Chem. Soc. Rev.* **2020**, *49*, 5473–5509.

2. (a) Nguyen, P.H.; Ramamoorthy, A.; Sahoo, B.R.; Zheng, J.; Faller, P.; Straub, J.E.; Dominguez, L.; Shea, J.E.; Dokholyan, N.V.; De Simone, A.; Ma, B. Amyloid oligomers: A joint experimental/computational perspective on Alzheimer's disease, Parkinson's disease, type II diabetes, and amyotrophic lateral sclerosis. *Chem. Rev.* **2021**, *121*, 2545–2647; (b) Ilie, I.M.; Caflisch, A. Simulation studies of amyloidogenic polypeptides and their aggregates. *Chem. Rev.* **2019**, *119*, 6956–6993; (c) Ramamoorthy, A. Insights into protein misfolding and amyloidogenesis. *Phys. Chem. Chem. Phys.* **2013**, *15*, 8867−8867; (d) Dobson, C. M. Protein folding and misfolding. *Nature* **2003**, *426*, 884−890.

3. Karran, E.; Mercken, M.; Strooper, B. D. The amyloid cascade hypothesis for Alzheimer's disease: an appraisal for the development of therapeutics. *Nat. Rev. Drug Discov.* **2011**, *10*, 698−712.

4. (a) Jurgens, C. A.; Toukatly, M. N.; Fligner, C. L.; Udayasankar, J.; Subramanian, S. L.; Zraika, S., Aston-Mourney, K.; Carr, D.B.; Westermark, P.; Westermark, G.T.; Kahn, S.E. β−cell loss and β−cell apoptosis in human type 2 diabetes are related to islet amyloid deposition. *Am. J. Pathol.* **2011**, *178*, 2632−2640; (b) Wei, L.; Jiang, P.; Xu, W.; Li, H.; Zhang, H.; Yan, L.; Chan-Park, M.B.; Liu, X.W.; Tang, K.; Mu, Y.; Pervushin, K. The molecular basis of distinct aggregation pathways of islet amyloid polypeptide. *J. Biol. Chem.* **2011**, *286*, 6291−6300; (c) Haataja, L.; Gurlo, T.; Huang, C. J.; Butler, P. C. Islet amyloid in type 2 diabetes, and the toxic oligomer hypothesis. *Endocr. Rev.* **2008**, *29*, 303−316.

5. (a) Lorenzo, A.; Razzaboni, B.; Weir, G.C.; Yankner, B.A. Pancreatic islet cell toxicity of amylin associated with type−2 diabetes mellitus. *Nature* **1994**, *368*, 756−60; (b) Kapurniotu, A. Amyloidogenicity and cytotoxicity of islet amyloid polypeptide. *Biopolymers* **2001**, *60*, 438−459; (c) Cooper, G. J.; Willis, A. C.; Clark, A.; Turner, R. C.; Sim, R. B.; Reid, K. B. Purification and characterization of a peptide from amyloid-rich pancreases of type 2 diabetic patients. *Proc. Natl. Acad. Sci. U.S.A.* **1987**, *84*, 8628−8632.

6. (a) Potter, K.J.; Abedini, A.; Marek, P.; Klimek, A.M.; Butterworth, S.; Driscoll, M.; Baker, R.; Nilsson, M.R.; Warnock, G.L.; Oberholzer, J.; Bertera, S. Islet amyloid deposition limits the viability of human islet grafts but not porcine islet grafts. *Proc. Natl Acad. Sci. U.S.A.* **2010**, *107*, 4305−4310; (b) Höppener, J. W. M.; Lips, C. J. M. Role of islet amyloid in type 2 diabetes mellitus. *Int. J. Biochem. Cell Biol.* **2006**, *38*, 726−736.

7. (a) Habchi, J.; Tompa, P.; Longhi, S.; Uversky, V.N. Introducing protein intrinsic disorder. *Chem. Rev.* **2014**, *114*, 6561–6588; (b) Guo, A.Z.; Fluitt, A.M.; de Pablo, J.J. Early-stage human islet amyloid polypeptide aggregation: Mechanisms behind dimer

formation. *J. Chem. Phys*. **2018**, *149*, 025101; (c) Cao, Q.; Boyer, D.R.; Sawaya, M.R.; Ge, P.; Eisenberg, D.S. Cryo-EM structure and inhibitor design of human IAPP (amylin) fibrils. *Nat. Struct. Mol. Biol*. **2020**, *27*, 653–659.

8. Soong, R.; Brender, J. R.; Macdonald, P. M.; Ramamoorthy, A. Association of highly compact type II diabetes related islet amyloid polypeptide intermediate species at physiological temperature revealed by diffusion NMR spectroscopy. *J. Am. Chem. Soc*. **2009**, *131*, 7079−7085.

9. Lapidus, L. J. Understanding protein aggregation from the view of monomer dynamics. *Mol. Biosyst*. **2013**, *9*, 29−35.

10. (a) Mishra, R.; Geyer, M.; Winter, R. NMR spectroscopic investigation of early events in IAPP amyloid fibril formation. *ChemBioChem* **2009**, *10*, 1769−1772; (b) Vaiana, S. M.; Best, R. B.; Yau, W. M.; Eaton, W. A.; Hofrichter, J. Evidence for a partially structured state of the amylin monomer. *Biophys. J*. **2009**, *97*, 2948−2957; (c) Vaiana, S. M.; Ghirlando, R.; Yau, W. M.; Eaton, W. A.; Hofrichter, J. Sedimentation studies on human amylin fail to detect low-molecular-weight oligomers. *Biophys. J*. **2008**, *94*, L45−L47; (d) Kayed, R.; Bernhagen, J.; Greenfield, N.; Sweimeh, K.; Brunner, H.; Voelter, W.; Kapurniotu, A. Conformational transitions of islet amyloid polypeptide (IAPP) in amyloid formation in vitro. *J. Mol. Biol*. **1999**, *287*, 781−796.

11. (a) Milardi, D.; Pappalardo, M.; Pannuzzo, M.; Grasso, D. M.; La Rosa, C. The role of the Cys2−Cys7 disulfide bridge in the early steps of Islet amyloid polypeptide aggregation: A molecular dynamics study. *Chem. Phys. Lett*. **2008**, *463*, 396−399; (b) Dupuis, N. F.; Wu, C.; Shea, J. E.; Bowers, M. T. The amyloid formation mechanism in human IAPP: dimers have β−strand monomer−monomer interfaces. *J. Am. Chem. Soc*. **2011**, *133*, 7240−7243; (c) Miller, C.; Zerze, G. H.; Mittal, J. Molecular simulations indicate marked differences in the structure of amylin mutants, correlated with known aggregation propensity. *J. Phys. Chem. B* **2013**, *117*, 16066−16075; (d) Murphy, R. D.; Conlon, J.; Mansoor, T.; Luca, S.; Vaiana, S. M.; Buchete, N. V. Conformational dynamics of human IAPP monomers. *Biophys. Chem.* **2012**, *167*, 1−7.

12. (a) Qiao, Q.; Bowman, G. R.; Huang, X. Dynamics of an intrinsically disordered protein reveal metastable conformations that potentially seed aggregation. *J. Am. Chem. Soc*. **2013**, *135*, 16092−16101; (b) Laghaei, R.; Mousseau, N.; Wei, G. Effect of the disulfide bond on the monomeric structure of human amylin studied by combined Hamiltonian and temperature replica exchange molecular dynamics simulations. *J. Phys. Chem. B* **2010**, *114*, 7071−7077.

13. (a) Yonemoto, I. T.; Kroon, G. J.; Dyson, H. J.; Balch, W. E.; Kelly, J. W. Amylin proprotein processing generates progressively more amyloidogenic peptides that initially sample the helical state. *Biochemistry* **2008**, *47*, 9900−9910; (b) Cort, J. R.; Liu, Z.; Lee, G. M.; Huggins, K. N. L.; Janes, S.; Prickett, K.; Andersen, N. H. Solution state structures of human pancreatic amylin and pramlintide. *Protein Eng. Des. Sel*. **2009**, *22*, 497−513.

14. Berhanu, W. M.; Masunov, A. E. Full length amylin oligomer aggregation: insights from molecular dynamics simulations and implications for design of aggregation inhibitors. *J. Biomol. Struct. Dyn*. **2014**, *32*, 1651–1669.

15. (a) Zhao, L.; Xin, Y.; Li, Y.; Yang, X.; Luo, L.; Meng, F. Ultraeffective inhibition of amyloid fibril assembly by nanobody–gold nanoparticle conjugates. *Bioconjug. Chem.* **2019**, *30*, 29−33; (b) Cabaleiro-Lago, C.; Lynch, I.; Dawson, K. A.; Linse, S. Inhibition of IAPP and IAPP (20−29) fibrillation by polymeric nanoparticles. *Langmuir* **2010**, *26*, 3453−3461.

16. Wang, M.; Sun, Y.; Cao, X.; Peng, G.; Javed, I.; Kakinen, A.; Davis, T.P.; Lin, S.; Liu, J.; Ding, F.; Ke, P.C. Graphene quantum dots against human IAPP aggregation and toxicity in vivo. *Nanoscale* **2018**, *10*, 19995−20006.

17. (a) Xin, Y.; Wang, X.; Luo, L.; & Meng, F. Conformation-dependent manipulation of human islet amyloid polypeptide fibrillation by shiitake-derived lentinan. *ACS Appl. Mater. Interfaces* **2018**, *10*, 31069−31079; (b) Tang, Y.; Zhang, D.; Zhang, Y.; Liu, Y.; Gong, X.; Chang, Y.; Ren, B.; Zheng, J. Introduction and fundamentals of human islet amyloid polypeptide inhibitors. *ACS Appl. Bio Mater*. **2020**, *3*, 8286−8308; (c) Saravanan, M.S.; Ryazanov, S.; Leonov, A.; Nicolai, J., Praest, P., Giese, A., Winter, R., Khemtemourian, L., Griesinger, C.; Killian, J. A. The small molecule inhibitor anle145c thermodynamically traps human islet amyloid peptide in the form of non-cytotoxic oligomers. *Sci. Rep*. **2019**, *9*, 19023.

18. (a) Liang, C. Q.; Li, Y. M. Peptides for disrupting and degrading amyloids. *Curr. Opin. Chem. Biol.* **2021**, *64*, 124−130; (b) Armiento, V.; Spanopoulou, A.; Kapurniotu, A. Peptide-based molecular strategies to interfere with protein misfolding, aggregation, and cell degeneration. *Angew. Chem. Int. Ed.* **2020**, *59*, 3372−3384; (c) Saini, R. K.; Goyal, D.; Goyal, B. Targeting human islet amyloid polypeptide aggregation and toxicity in type 2 diabetes: an overview of peptide-based inhibitors. *Chem. Res. Toxicol*. **2020**, *33*, 2719−2738; (d) Mitra, A.; Sarkar, N. Sequence and structure-based peptides as potent amyloid inhibitors: A review. *Arch. Biochem. Biophys*. **2020**, *695*, 108614.

19. (a) Abioye, R.O.; Okagu, O.D.; Udenigwe, C.C. Disaggregation of islet amyloid polypeptide fibrils as a potential anti-fibrillation mechanism of tetrapeptide TNGQ. *Int. J. Mol. Sci.* **2022**, *23*, 1972; (b) Fraczyk, A.; Janczewski, L.; Wasko, J.; Rozniakowski, K.; Galecki, K.; Kaminski, Z.J.; Kolesinska, B. Non-aggregating amylin fragments as an inhibitor of the aggregation process of susceptible to aggregation fragments 18–22, 23–27, and 33–37 of hormone. *Chem. Biodivers*. **2021**, *18*, e2100034.

20. Roy, R.; Paul, S. hIAPP-amyloid-core derived D-Peptide prevents hIAPP aggregation and destabilizes its protofibrils. *J. Phys. Chem. B* **2022** *126*, 822−839.

21. Rozniakowski, K.; Fraczyk, A.; Galecki, K.; Wietrzyk, J.; Filip-Psurska, B.; Fraczyk, J.; Kaminski, Z.J.; Kolesinska, B. New human islet amyloid polypeptide fragments susceptible to aggregation. *Chem. Biodivers*. **2020**, *17*, e2000501.

22. (a) Glenner, G. G.; Eanes, E. D.; Wiley, C. A. Amyloid fibrils formed from a segment of the pancreatic islet amyloid protein. *Biochem. Biophys. Res. Commun*. **1988**, *155*,

608−614; (b) Westermark, P.; Engström, U.; Johnson, K. H.; Westermark, G. T.; Betsholtz, C. Islet amyloid polypeptide: pinpointing amino acid residues linked to amyloid fibril formation. *Proc. Natl. Acad. Sci. U. S. A.* **1990**, *87*, 5036−5040; (c) Moriarty, D. F.; Raleigh, D. P. Effects of sequential proline substitutions on amyloid formation by human amylin20−29. *Biochemistry* **1999**, *38*, 1811−1818.

23. Gilead, S.; Gazit, E. Inhibition of amyloid fibril formation by peptide analogues modified with α-aminoisobutyric acid. *Angew. Chem. Int. Ed.* **2004**, *43*, 4041−4044.

24. (a) Albrecht, E.; Jones, H.; Gaeta, L. S. L.; Prickett, K. S.; Beaumont, K. **1996**, US005588953A; b) Fezoui, Y.; Soto-Jara, C. **2004**, WO 2004/083243 A1.

25. Goyal, D.; Shuaib, S.; Mann, S.; Goyal, B. Rationally designed peptides and peptidomimetics as inhibitors of amyloid-β (Aβ) aggregation: potential therapeutics of Alzheimer's disease. *ACS Comb. Sci.* **2017**, *19*, 55−80.

26. (a) Rehman, A.U.; Khurshid, B.; Ali, Y.; Rasheed, S.; Wadood, A.; Ng, H.L.; Chen, H.F.; Wei, Z.; Luo, R.; Zhang, J. Computational approaches for the design of modulators targeting protein-protein interactions. *Expert Opin. Drug Discov*. **2023**, *18*, 315−333; (b) Delaunay, M.; Ha-Duong, T. Computational tools and strategies to develop peptide-based inhibitors of protein-protein interactions. *Computational Peptide Science: Methods and Protocols*. New York, NY: Springer U.S. **2021**, 205−230; (c) Jana, S.; Singh, S. K. Identification of human tau-tubulin kinase 1 inhibitors: An integrated e-pharmacophore-based virtual screening and molecular dynamics simulation. *J. Biomol. Struct. Dyn*. **2020**, *38*, 886–900; (d) Kumar, A.; Srivastava, G.; Negi, A. S.; Sharma, A. Docking, molecular dynamics, binding energy-MM-PBSA studies of naphthofuran derivatives to identify potential dual inhibitors against BACE-1 and GSK-3β. *J. Biomol. Struct. Dyn*. **2019**, *37*, 275–290; (e) Manoharan, P.; Ghoshal, N. Fragment-based virtual screening approach and molecular dynamics simulation studies for identification of BACE1 inhibitor leads. *J. Biomol. Struct. Dyn.* **2018**, *36*, 1878–1892; (f) Kesari, P.; Pratap, S.; Dhankhar, P.; Dalal, V.; Mishra, M.; Singh, P. K.; Chauhan, H.; Kumar, P. Structural characterization and *in-silico* analysis of *Momordica charantia* 7S globulin for stability and ACE inhibition. Sci. Rep. **2020**, *10*, 1160.

27. (a) Chandrasekhar, G.; Srinivasan, E.; Nandhini, S.; Pravallika, G.; Sanjay, G.; Rajasekaran, R. Computer aided therapeutic tripeptide design, in alleviating the pathogenic proclivities of nocuous α-synuclein fibrils. *J. Biomol. Struct. Dyn.* **2023**, DOI: 10.1080/07391102.2023.2194003; (b) Luan, B.; Huynh, T. Crystal-structures-guided design of fragment-based drugs for inhibiting the main protease of SARS-CoV-2. *Proteins Struct. Funct. Bioinf.* **2022**, *90*, 1081−1089; (c) Jarmuła, A.; Zubalska, M.; Stępkowski, D. Consecutive aromatic residues are required for improved efficacy of β-sheet breakers. *Int. J. Mol. Sci.* **2022**, *23*, 5247; (d) VK, P.; Rath, S. P.; Abraham, P. Computational designing of a peptide that potentially blocks the entry of SARS-CoV, SARS-CoV-2 and MERS-CoV. *PloS One* **2021**, *16*, e0251913; (e) Kanchi, P. K.; Dasmahapatra, A. K. Enhancing the binding of the β-sheet breaker peptide LPFFD to the amyloid-β fibrils by aromatic modifications: A molecular dynamics simulation

study. *Comput. Biol. Chem*. **2021**, *92*, 107471; (f) Han, Y.; Král, P. Computational design of ACE2-based peptide inhibitors of SARS-CoV-2. *ACS Nano* **2020**, *14*, 5143−5147.

28. Schrödinger Release 2018-1: Maestro, Schrödinger, LLC, New York, NY, **2018**.

29. Nanga, R. P.; Brender, J. R.; Vivekanandan, S.; Ramamoorthy, A. Structure and membrane orientation of IAPP in its natively amidated form at physiological pH in a membrane environment. *Biochim. Biophys. Acta*. **2011**, *1808*, 2337–2342.

30. Trott, O.; Olson, A. J. AutoDock vina: improving the speed and accuracy of docking with a new scoring function, efficient optimization and multithreading. *J. Comput. Chem*. **2010**, *31*, 455–461.

31. Dallakyan, S.; Olson, A. J. Small-molecule library screening by docking with PyRx. *Methods Mol. Biol*. **2015**, *1263*, 243–250.

32 Kumari, R.; Kumar, R.; Open Source Drug Discovery Consortium; Lynn, A. g_mmpbsa: A GROMACS tool for high-throughput MM-PBSA calculations. *J. Chem. Inf. Model*. **2014**, *54*, 1951−1962.

33. Genheden, S.; Ryde, U. The MM/PBSA and MM/GBSA methods to estimate ligand binding affinities. *Expert Opin. Drug Discov.* **2015**, *10*, 449–461.

34. (a) Kaur, A.; Goyal, D.; Goyal, B. An α-helix mimetic oligopyridylamide, ADH-31, modulates $A\beta_{42}$ monomer aggregation and destabilizes protofibril structures: Insights from molecular dynamics simulations. *Phys. Chem. Chem. Phys.* **2020**, *22*, 28055–28073; (b) Shuaib, S.; Saini, R. K.; Goyal, D.; Goyal, B. Insights into the inhibitory mechanism of dicyanovinyl-substituted J147 derivative against $A\beta_{42}$ aggregation and protofibril destabilization: A molecular dynamics simulation study. *ChemistrySelect* **2017**, *2*, 1645–1657.

35. Huang, K.; Luo, S.; Cong, Y.; Zhong, S.; Zhang, J. Z. H.; Duan, L. An accurate free energy estimator: based on MM/PBSA combined with interaction entropy for protein–ligand binding affinity. *Nanoscale* **2020**, *12*, 10737–10750.

36. (a) Xie, L.; Luo, Y.; Lin, D.; Xi, W.; Yang, X.; Wei, G. The molecular mechanism of fullerene-inhibited aggregation of Alzheimer's β-amyloid peptide fragment. *Nanoscale* **2014**, *6*, 9752−9762; (b) Zhang, T.; Xu, W.; Mu, Y.; Derreumaux, P. Atomic and dynamic insights into the beneficial effect of the 1,4-Naphthoquinon-2-yl-L-tryptophan inhibitor on Alzheimer's Aβ1–42 dimer in terms of aggregation and toxicity. *ACS Chem. Neurosci.* **2014**, *5*, 148−159; (c) Novick, P. A.; Lopes, D. H.; Branson, K. M.; Esteras-Chopo, A.; Graef, I. A.; Bitan, G.; Pande, V. S. Design of β-amyloid aggregation inhibitors from a predicted structural motif. *J. Med. Chem.* **2012**, *55*, 3002−3010; (d) Best, R. B.; Buchete, N.-V.; Hummer, G. Are current molecular dynamics force fields too helical? *Biophys. J.* **2008**, *9*, L07–L09.

37. (a) Hou, T.; Wang, J.; Li, Y.; Wang, W. Assessing the performance of the MM/PBSA and MM/GBSA Methods. 1. The accuracy of binding free energy calculations based on molecular dynamics simulations. *J. Chem. Inf. Model.* **2011**, *51*, 69−82; (b) Maffucci,

I.; Contini, A. Explicit ligand hydration shells improve the correlation between MM-PB/GBSA binding energies and experimental activities. *J. Chem. Theory Comput.* **2013**, *9*, 2706−2717.

38. Abraham, M. J.; Murtola, T.; Schulz, R.; Páll, S.; Smith, J. C.; Hess, B.; Lindahl, E. GROMACS: High performance molecular simulations through multi–level parallelism from laptops to supercomputers. *SoftwareX* **2015**, *1–2*, 19–25.

39. Lindorff-Larsen, K.; Piana, S.; Palmo, K.; Maragakis, P.; Klepeis, J. L.; Dror, R. O.; Shaw, D. E. Improved side-chain torsion potentials for the Amber ff99SB protein force field. *Proteins Struct. Funct. Bioinf.* **2010**, *78*, 1950–1958.

40. (a) Piana, S.; Lindorff-Larsen, K.; Shaw, D.E. How robust are protein folding simulations with respect to force field parameterization? *Biophys. J.* **2011**, *100*, L47–L49; (b) Best, R.B.; Hummer, G. Optimized molecular dynamics force fields applied to the helix-coil transition of polypeptides. *J. Phys. Chem. B* **2009**, *113*, 9004–9015; (c) Lindorff-Larsen, K.; Maragakis, P.; Piana, S.; Eastwood, M.P.; Dror, R.O.; Shaw, D.E. Systematic validation of protein force fields against experimental data. *PLoS One* **2012**, *7*, e32131; (d) Peng, E.; Todorova, N.; Yarovsky, I. Effects of forcefield and sampling method in all-atom simulations of inherently disordered proteins: Application to conformational preferences of human amylin. *PLoS One* **2017**, *12*, e0186219.

41. Mark, P.; Nilsson, L. Structure and dynamics of the TIP3P, SPC, and SPC/E water models at 298 K. *J. Phys. Chem. A* **2001**, *105*, 9954−9960.

42. (a) Deserno, M.; Holm, C. How to mesh up Ewald sums. I. A theoretical and numerical comparison of various particle mesh routines. *J. Chem. Phys*. **1998**, *109*, 7678−7693; (b) Deserno, M.; Holm, C. How to mesh up Ewald sums. II. An accurate error estimate for the particle-particle-particlemesh algorithm. *J. Chem. Phys*. **1998**, *109*, 7694−7701.

43. Bussi, G.; Donadio, D.; Parrinello, M. Canonical sampling through velocity rescaling. *J. Chem. Phys*. **2007**, *126*, 014101.

44. Parrinello, M.; Rahman, A. Polymorphic transitions in single crystals: A new molecular dynamics method. *J. Appl. Phys*. **1981**, *52*, 7182−7190.

45. Humphrey, W.; Dalke, A.; Schulten, K. VMD – Visual Molecular Dynamics. *J. Mol. Graphics* **1996**, *14*, 33−38.

46. W.L. DeLano, The PyMOL molecular graphics system, http://www.pymol.org, 2002.

47. Kabsch, W.; Sander, C. Dictionary of protein secondary structure: pattern recognition of hydrogen-bonded and geometrical features. *Biopolymers* **1983**, *22*, 2577−2637.

48. (a) Chandra, A. Effects of ion atmosphere on hydrogen-bond dynamics in aqueous electrolyte solutions. *Phys. Rev. Lett*. **2000**, *85*, 768−771; (b) Paul, S.; Chandra, A. Hydrogen bond properties and dynamics of liquid-vapor interfaces of aqueous methanol solutions. *J. Chem. Theory Comput.* **2005**, *1*, 1221−1231; (c) Pal, S.; Paul, S. Understanding the role of reline, a natural DES, on temperature-induced conformational

changes of C-Kit G quadruplex DNA: A molecular dynamics study. *J. Phys. Chem. B* **2020**, *124*, 3123−3136.

49. (a) Daura, X.; Antes, I.; van Gunsteren, W. F.; Thiel, W.; Mark, A. E. The effect of motional averaging on the calculation of NMR-derived structural properties. *Proteins Struct. Funct. Bioinf.* **1999**, *36*, 542–555; (b) Daura, X.; Gademann, K.; Jaun, B.; Seebach, D.; van Gunsteren, W. F.; Mark, A. E. Peptide folding: when simulation meets experiment. *Angew. Chem. Int. Ed*. **1999**, *38*, 236–240.

50. Lao, Z.; Chen, Y.; Tang, Y.; Wei, G. Molecular dynamics simulations reveal the inhibitory mechanism of dopamine against human islet amyloid polypeptide (hIAPP) aggregation and its destabilization effect on hIAPP protofibrils. *ACS Chem. Neurosci.* **2019**, *10*, 4151−4159.

51. (a) Padrick, S. B.; Miranker, A. D. Islet amyloid polypeptide: identification of long-range contacts and local order on the fibrillogenesis pathway. *J. Mol. Biol*. **2001**, *308*, 783−794; (b) Marek, P.; Abedini, A.; Song, B.; Kanungo, M.; Johnson, M. E.; Gupta, R.; Zaman, W.; Wong, S. S.; Raleigh, D. P. Aromatic interactions are not required for amyloid fibril formation by islet amyloid polypeptide but do influence the rate of fibril formation and fibril morphology. *Biochemistry* **2007**, *46*, 3255−3261; (c) Bouzakraoui, S.; Mousseau, N. Structural and thermodynamical properties of early human amylin oligomers using replica exchange molecular dynamics: mutation effect of three key residues F15, H18 and F23. *Phys. Chem. Chem. Phys*. **2017**, *19*, 31290−31299.

52. Li, X.; Lao, Z.; Zou, Y.; Dong, X.; Li, L.; Wei, G. Mechanistic insights into the co-aggregation of Aβ and hIAPP: an all-atom molecular dynamic study. *J. Phys. Chem. B* **2021**, *125*, 2050−2060.

53. Kumari, A.; Sharma, R.; Shrivastava, N.; Somvanshi, P.; Grover, A. Bleomycin modulates amyloid aggregation in β-amyloid and hIAPP. *RSC Adv*. **2020**, *10*, 25929−25946.

54. (a) Goldsbury, C.; Goldie, K.; Pellaud, J.; Seelig, J.; Frey, P.; Müller, S.A.; Kistler, J.; Cooper, G.J.S.; Aebi, U. Amyloid fibril formation from full-length and fragments of amylin. *J. Struct. Biol*. **2000**, *130*, 352−362; (b) Sedman, V. L.; Allen, S.; Chan, W. C.; Davies, M. C.; Roberts, C. J.; Tendler, S. J.; Williams, P. M. Atomic force microscopy study of human amylin (20-29) fibrils. *Protein Pept. Lett*. **2005**, *12*, 79−83; (c) Zhang, S.; Andreasen, M.; Nielsen, J.T.; Liu, L.; Nielsen, E.H.; Song, J.; Ji, G.; Sun, F.; Skrydstrup, T.; Besenbacher, F.; Nielsen, N.C. Coexistence of ribbon and helical fibrils originating from $hIAPP_{20–29}$ revealed by quantitative nanomechanical atomic force microscopy. *Proc. Natl Acad. Sci. U.S.A.* **2013**, *110*, 2798−2803; (d) Scrocchi, L.A.; Ha, K.; Chen, Y.; Wu, L.; Wang, F.; Fraser, P.E. Identification of minimal peptide sequences in the (8–20) domain of human islet amyloid polypeptide involved in fibrillogenesis. *J. Struct. Biol*. **2003**, *141*, 218−227.

55. Tran, L.; Ha-Duong, T. Effect of post-translational amidation on islet amyloid polypeptide conformational ensemble: Implications for its aggregation early steps. *Int. J. Mol. Sci*. **2016**, *17*, 1896.

56. Dass, R.; Mulder, F.A.A.; Nielsen, J.T. ODiNPred: comprehensive prediction of protein order and disorder. *Sci. Rep.* **2020**, *10*, 14780.

57. (a) Luo, Z.; Gao, G.; Ma, Z.; Liu, Q.; Gao, X.; Tang, X.; Gao, Z.; Li, C.; Sun, T. Cichoric acid from witloof inhibit misfolding aggregation and fibrillation of hIAPP. *Int. J. Biol. Macromol*. **2020**, *148*, 1272−1279; (b) Tran, L.; Ha-Duong, T. Effect of post-translational amidation on islet amyloid polypeptide conformational ensemble: Implications for its aggregation early steps. *Int. J. Mol. Sci*. **2016**, *17*, 1896; (c) Apostolidou, M.; Jayasinghe, S.A.; Langen, R. Structure of α-helical membrane-bound human islet amyloid polypeptide and its implications for membrane-mediated misfolding. *J. Biol. Chem.* **2008**, *283*, 17205−17210.

58. Qi, R.; Luo, Y.; Ma, B.; Nussinov, R.; Wei, G. Conformational distribution and α−helix to β−sheet transition of human amylin fragment dimer. *Biomacromolecules* **2014**, *15*, 122−131.

59. Patil, S. M.; Xu, S.; Sheftic, S. R.; Alexandrescu, A. T. Dynamic α-helix structure of micelle-bound human amylin. *J. Biol. Chem*. **2009**, *284*, 11982−11991.

60. Li, H.; Luo, Y.; Derreumaux, P.; Wei, G. Effects of the RGTFEGKF inhibitor on the structures of the transmembrane fragment 70−86 of glycophorin A: an all-atom molecular dynamics study. *J. Phys. Chem. B* **2010**, *114*, 1004−1009.

61. Tian, H.; Ketkar, R.; Tao, P. ADMETboost: a web server for accurate ADMET prediction. *J. Mol. Model.* **2022**, 28, 408.

62. Xiong, G.; Wu, Z.; Yi, J.; Fu, L.; Yang, Z.; Hsieh, C.; Yin, M.; Zeng, X.; Wu, C.; Lu, A.; et al. ADMETlab 2.0: An integrated online platform for accurate and comprehensive predictions of ADMET properties. *Nucleic. Acids Res.* **2021**, *49*, W5–W14.

Chapter 5

Identification of new pentapeptides as potential inhibitors of amyloid–β42 aggregation using virtual screening and molecular dynamics simulations

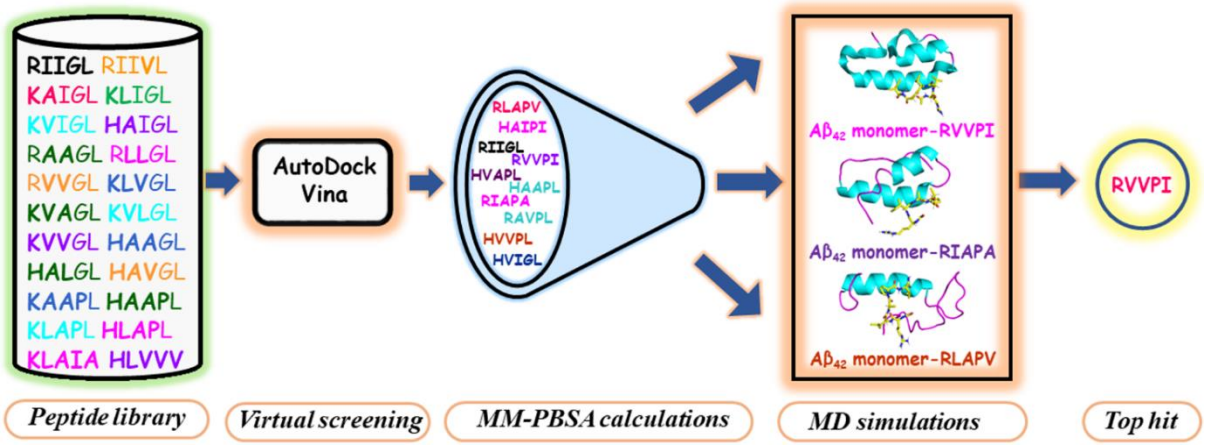

In our present study we investigated the effect of modified peptides on the Aβ42 aggregation using molecular dynamics (MD) simulations. The RIIGL peptide was substituted up to the five positions with similar amino acids to generate the peptide library. We performed molecular docking of 912 pentapeptide analogues of RIIGL followed by MM-PBSA (molecular mechanics Poisson-Boltzmann surface area) calculations of best 10 peptides from docking. The best inhibitors have been chosen from MD were those containing arginine i.e., RVVPI, RIAPA and RLAPV contributed strong binding with Aβ42 monomer than the reference peptide RIIGL. The RVVPI and RIAPA peptides resulting in increase in helical content and decrease in β–sheet content of Aβ42 monomer structure.

Kaur, A.; Goyal, B. Identification of new pentapeptides as potential inhibitors of amyloid–β42 aggregation using virtual screening and molecular dynamics simulations. *J. Mol. Graph. Model.* **2023**, 108558.

5.1 Introduction

Alzheimer's disease (AD) is the most common kind of dementia, predicted to account for 60–70% of all dementia cases.[1] About 55 million people suffer from dementia worldwide and the number of cases is generously increasing on daily basis.[2] The patients experiencing AD have symptoms like diminished memory, falling apart language, and issues like visual impairment.[3] In AD pathogenesis, neurotoxic amyloid-β (Aβ) self-assembly is the major event which is consequently a central point of study.[4] The modulation or inhibition of Aβ aggregation has been attempted using a variety of strategies to slow or reverse the disease progression, including stabilizing its native state,[5] avoiding the generation of on-pathway oligomers, inhibiting fibril elongation, and disaggregating already formed amyloid aggregates.[6] The major Aβ monomers are $A\beta_{40}$ and $A\beta_{42}$, and $A\beta_{42}$ is affirmed to have a higher affinity for aggregation and neurotoxicity than $A\beta_{40}$.[7] Studies show that monomeric $A\beta_{42}$ experiences a conformational transition of its underlying secondary structure.[8] The Aβ is at first in an irregular coil or helix conformation and consequently changes into β–sheet conformation. This change produces oligomeric species, which have a higher percentage of β–sheet structures. A previous study proposes that the arrangement of β–sheets drives the amyloid self-aggregation procedure.[8b] A complete understanding of the molecular mechanism of the conformational transition of Aβ monomer is important for the advancement of therapeutic procedures for AD.[9]

The helix (13–26) region of the Aβ peptide is of primary interest as a crucial central hydrophobic core (CHC), and KLVFF (16–20) fragment covered in this core region can undergo self-assembly and bind to full-length Aβ.[10] Nerelius and co-workers highlighted that targeting the central helix region of $A\beta_{42}$ with ligands disrupts the process of *in vitro* aggregation and stabilizes the helix conformation.[5] *In vivo* studies of the Drosophila Melanogaster model reported that ligand binding to the central helix decreases toxicity mediated by $A\beta_{42}$ in AD. Juneja et al. showed that central helix stabilization contributes to the inhibition of toxic intermediates formation and $A\beta_{42}$ aggregation.[11] The stabilization of α-helix results in the prevention of conformational conversion, which, in turn, blocks the formation of oligomeric and fibril species responsible for Aβ cytotoxicity.

The Aβ aggregation inhibitors have attracted significant attention as potential therapeutic candidates to cure or delay the onset of AD.[12] Among various inhibitors, peptide-based inhibitors displayed good potential as anti-aggregation agents due to their low cytotoxicity,

promising biocompatibility, high target affinity, and specificity.[3, 13, 14] As Aβ monomers undergo self-assembly to form toxic oligomers and aggregates, the peptide fragments derived from wild-type Aβ monomer have been employed as inhibitors of Aβ aggregation.[13c, 15] Samani et al. investigated the influence of terminal groups and halogenation of KLVFF on its activity against Aβ aggregation and highlighted that iodinated peptide with an amine at the N-terminus and amide at the C-terminus displayed maximum inhibitory activity against Aβ aggregation.[16] Several studies highlighted the key role of the hydrophobic C-terminal region of Aβ in its self-assembly and various inhibitors derived from the C-terminal region of Aβ have been explored as anti-aggregation agents against Aβ aggregation.[17]

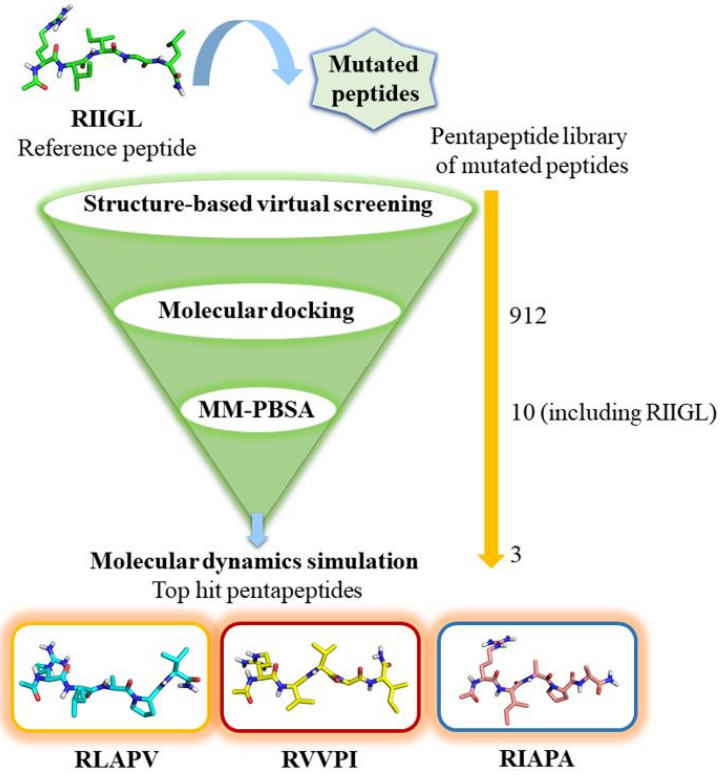

Figure 5.1: Workflow of computational screening protocol used in this work to identify potential inhibitors of $A\beta_{42}$ aggregation from the pentapeptide library based on reference peptide RIIGL.

Harkány et al. reported propionyl-Ile-Ile-Gly-Leu amide (Pr-IIGL) derived from the C-terminal region (31–35) of Aβ peptide as an inhibitor of $A\beta_{42}$ aggregation.[18] Pr-IIGL protected glial cells from cytotoxicity induced by $A\beta_{42}$ aggregates, however, it displayed neurotoxicity. Fülöp et al. modified Pr-IIGL by replacing propionyl with arginine to afford a new pentapeptide $RIIGL_a$, which is not neurotoxic and blocked Aβ amyloid formation as well as reduced the

cytotoxicity caused by Aβ aggregates.[19] The transmission electron microscopy (TEM) images depicted the formation of mature fibers of length 2–3 μm when the $A\beta_{42}$ monomer was incubated alone, whereas the fibril formation was completely inhibited when RIIGL was incorporated in $A\beta_{42}$ monomer. Notably, the cell viability of SHSY-5Y neuroblastoma cells was increased from 39% in $A\beta_{42}$ monomer alone to 84% when the $A\beta_{42}$ monomer was co-incubated with RIIGL. Thus, RIIGL can be employed as a lead motif for designing new Aβ aggregation inhibitors and its rational modification offers an opportunity to enhance its inhibitory activity against $A\beta_{42}$ aggregation.

In the present study, an integrated computational protocol was applied to screen a designed library of 912 pentapeptides based on the RIIGL (**Figure 5.1**). The top hit pentapeptides against $A\beta_{42}$ aggregation were shortlisted from the designed library using molecular docking-based virtual screening and binding free energy calculations. Further, the stability of $A\beta_{42}$ monomer-pentapeptide complexes was evaluated using molecular dynamics (MD) simulations. The study provides insights into the binding interactions between $A\beta_{42}$ monomer and pentapeptides, which will offer motivation for future experimental investigation of these peptides as potential therapeutic candidates against $A\beta_{42}$ aggregation in AD.

Table 5.1: Single amino acid mutated pentapeptides generated from RIIGL.

Amino acids of reference peptide	Nature of side chain	Amino acids with similar side chains	Peptides with one amino acid mutation
R	Basic, polar	K, H	**K**IIGL, **H**IIGL
I	Aliphatic, non-polar	A, L, V	R**A**IGL, R**L**IGL, R**V**IGL
I	Aliphatic, non-polar	A, L, V	RI**A**GL, RI**L**GL, RI**V**GL
G	Neutral, non-polar	P, V, I	RII**P**L, RII**V**L, RII**I**L
L	Aliphatic, non-polar	A, I, V	RIIG**A**, RIIG**I**, RIIG**V**

5.2 Computational details

5.2.1 Computational design of pentapeptides as inhibitors of $A\beta_{42}$ aggregation

A library of 912 pentapeptides was created by mutations at different positions of RIIGL using Maestro software (**Table 5.1–5.5**).[20] The amino acids have been classified into different groups based on the side chain similarity (**Table 5.1**). The common chemical properties and characteristics of the side chains were considered during amino acid grouping. The amino acids in RIIGL were replaced with amino acids of the same group.

Table 5.2: Pentapeptide sequences generated by mutating two amino acid residues in RIIGL.

Combination	Mutant peptides
1,2	**KA**IGL KLIGL KVIGL HAIGL **HL**IGL HVIGL
1,3	**KIA**GL KILGL KIVGL HIAGL **HIL**GL HIVGL
1,4	**KII**PL KIIVL KIIIL HIIPL HIIVL **HIII**L
1,5	**K**IIG**A** KIIGI **KIIGV** HIIGA **HIIGI** **H**IIG**V**
2,3	R**AA**GL RLLGL RVVGL RALGL R**LA**GL R**VL**GL R**AV**GL R**LV**GL R**VA**GL
2,4	R**AIP**L RLIVL RVIVL RAIVL RLIPL RVIPL R**AII**L R**LII**L R**VII**L
2,5	R**A**IG**A** RLIGI RVIGV RAIGI **RLIGV** R**V**IG**A** R**A**IG**V** R**L**IG**A** R**V**IG**I**
3,4	RI**AP**L RI**LV**L RI**VI**L RI**AV**L RI**LI**L RI**VP**L RI**AI**L RI**LP**L RI**VV**L
3,5	RI**A**G**A** RI**L**G**I** RI**V**G**V** RI**L**G**I** RI**V**G**V** RI**A**G**A** RI**V**G**V** RI**A**G**A** RI**L**G**I**
4,5	RII**PA** RII**VI** RII**IV** RII**PI** RII**VV** RII**IA** RII**PV** RII**VA** RII**II**

Table 5.3: Pentapeptide sequences generated by mutating three amino acid residues in RIIGL.

Combination	Mutant peptides
1,2,3	**KAA**GL **KAL**GL **KAV**GL **KLA**GL **KLL**GL **KLV**GL **KVA**GL **KVL**GL **KVV**GL **HAA**GL **HAL**GL **HAV**GL **HLA**GL **HLL**GL **HLV**GL **HVA**GL **HVL**GL **HVV**GL
1,2,4	**KAI**PL **KAI**VL **KAII**L **KLI**PL **KLI**VL **KLII**L **KVI**PL **KVI**VL **KVII**L **HAI**PL **HAI**VL **HAII**L **HLI**PL **HLI**VL **HLII**L **HVI**PL **HVI**VL **HVII**L
1,2,5	**KA**IG**A** **KA**IG**I** **KA**IG**V** **KL**IG**A** **KL**IG**I** **KL**IG**V** **KV**IG**A** **KV**IG**I** **KV**IG**V** **HA**IG**A** **HA**IG**I** **HA**IG**V** **HL**IG**A** **HL**IG**I** **HL**IG**V** **HV**IG**A** **HV**IG**I** **HV**IG**V**
1,3,4	**KIAP**L **KILP**L **KIVP**L **KIAV**L **KILV**L **KIVV**L **KIAI**L **KILI**L **HIAP**L **HILP**L **HIVP**L **HIAV**L **HILV**L **HIVV**L **HIAI**L **HILI**L **KIVI**L **HIVI**L
1,3,5	**KIAGA** **KIAGI** **KIAGV** **KILGA** **KILGI** **KILGV** **KIVGA** **KIVGI** **KIVGV** **HIAGA** **HIAGI** **HIAGV** **HILGA** **HILGI** **HILGV** **HIVGA** **HIVGI** **HIVGV**

1,4,5	**K**II**PA** **K**II**VA** **K**II**IA** **K**II**PI** **K**II**VI** **K**II**II** **K**II**PV** **K**II**VV** **K**II**IV** **H**II**VA** **H**II**IA** **H**II**PI** **H**II**VI** **H**II**II** **H**II**PV** **H**II**VV** **H**II**IV** **H**II**PA**
2,3,4	R**AAP**L R**AAV**L R**AAI**L R**ALP**L R**ALV**L R**ALI**L R**AVP**L R**AVV**L R**AVI**L R**LAP**L R**LAV**L R**LAI**L R**LLP**L R**LLV**L R**LLI**L R**LVP**L R**LVV**L R**LVI**L R**VAP**L R**VAV**L R**VAI**L R**VLP**L R**VLV**L R**VLI**L R**VVP**L R**VVV**L R**VVI**L
2,3,5	R**AAG**A R**AAG**I R**AAG**V R**ALG**A R**ALG**I R**ALG**V R**AVG**A R**AVG**I R**AVG**V R**LAG**A R**LAG**I R**LAG**V R**LLG**A R**LLG**I R**LLG**V R**LVG**A R**LVG**I R**LVG**V R**VAG**A R**VAG**I R**VAG**V R**VLG**A R**VLG**I R**VLG**V R**VVG**A R**VVG**I R**VVG**V
2,4,5	R**A**I**PA** R**A**I**VA** R**A**II**A** R**A**I**PI** R**A**I**VI** R**A**II**I** R**A**I**PV** R**A**I**VV** R**A**II**V** R**L**I**PA** R**L**I**PI** R**L**I**PV** R**L**I**VA** R**L**I**VI** R**L**I**VV** R**L**II**A** R**L**II**I** R**L**II**V** R**V**I**PA** R**V**I**PI** R**V**I**PV** R**V**I**VA** R**V**I**VI** R**V**I**VV** R**V**II**A** R**V**II**I** R**V**II**V**
3,4,5	RI**APA** RI**API** RI**APV** RI**AVA** RI**AVI** RI**AVV** RI**AIA** RI**AII** RI**AIV** RI**LPA** RI**LPI** RI**LPV** RI**LVA** RI**LVI** RI**LVV** RI**LIA** RI**LII** RI**LIV** RI**VPA** RI**VPI** RI**VPV** RI**VVA** RI**VVI** RI**VVV** RI**VIA** RI**VII** RI**VIV**

Table 5.4: Pentapeptide sequences generated by mutating four amino acid residues in RIIGL.

Combination	Mutant peptides
1,2,3,4	**KAAP**L **HAAP**L **KAAV**L **HAAV**L **KAAI**L **HAAI**L **KLAP**L **HLAP**L **KLAV**L **HLAV**L **KLAI**L **HLAI**L **KLLP**L **HLLP**L **KLLV**L **HLLV**L **KLLI**L **HLLI**L **KVAP**L **HVAP**L **KVAV**L **HVAV**L **KVAI**L **HVAI**L **KVLP**L **HVLP**L **KVLV**L **HVLV**L **KVLI**L **HVLI**L **KVVP**L **HVVP**L **KVVV**L **HVVV**L **KVVI**L **HVVI**L **KALP**L **HALP**L **KALV**L **HALV**L **KALI**L **HALI**L **KAVP**L **HAVP**L **KAVV**L **HAVV**L **KAVI**L **HAVI**L **KLVP**L **HLVP**L **KLVV**L **HLVV**L **KLVI**L **HLVI**L
1,2,3,5	**KAAG**A **KAAG**I **KAAG**V **HAAG**A **HAAG**I **HAAG**V **KALG**A **KALG**I **KALG**V **HALG**A **HALG**I **HALG**V **KAVG**A **KAVG**I **KAVG**V **HAVG**A **HAVG**I **HAVG**V **KLAG**A **KLAG**I **KLAG**V **HLAG**A **HLAG**I **HLAG**V **KLLG**A

	KLLGI KLLGV HLLGA HLLGI HLLGV KLVGA KLVGI KLVGV HLVGA HLVGI HLVGV KVAGA KVAGI KVAGV HVAGA HVAGI HVAGV KVLGA KVLGI KVLGV HVLGA HVLGI HVLGV KVVGA KVVGI KVVGV HVVGA HVVGI HVVGV
1,2,4,5	**KAIPA KAIPI KAIPV HAIPA HAIPI HAIPV KAIVA KAIVI KAIVV HAIVA HAIVI HAIVV KAIIA KAIII KAIIV HAIIA HAIII HAIIV KLIPA KLIPI KLIPV HLIPA HLIPI HLIPV KLIVA KLIVI KLIVV HLIVA HLIVI HLIVV KLIIA KLIII KLIIV HLIIA HLIII HLIIV KVIPA KVIPI KVIPV HVIPA HVIPI HVIPV KVIVA KVIVI KVIVV HVIVA HVIVI HVIVV KVIIA KVIII KVIIV HVIIA HVIII HVIIV**
1,3,4,5	**KIAPA KIAPI KIAPV HIAPA HIAPI HIAPV KIAVA KIAVI KIAVV HIAVA HIAVI HIAVV KIAIA KIAII KIAIV HIAIA HIAII HIAIV KILPA KILPI KILPV HILPA HILPI HILPV KILVA KILVI KILVV HILVA HILVI HILVV KILIA KILII KILIV HILIA HILII HILIV KIVPA KIVPI KIVPV HIVPA HIVPI HIVPV KIVVA KIVVI KIVVV HIVVA HIVVI HIVVV KIVIA KIVII KIVIV HIVIA HIVII HIVIV**
2,3,4,5	**RAAPA RAAPV RAAPI RAAVA RAAVV RAAVI RAAIA RAAIV RAAII RALPA RALPI RALPV RALVA RALVI RALVV RALIA RALII RALIV RAVPA RAVPI RAVPV RAVVA RAVVI RAVVV RAVIA RAVII RAVIV RLAPA RLAPI RLAPV RLAVA RLAVI RLAVV RLAIA RLAII RLAIV RLLPA RLLPI RLLPV RLLVA RLLVV RLLIA RLLII RLLIV RLVPA RLVPI RLVPV RLVVA RLVVV RLVIA RLVII RLVIV RVAPA RVAPI RVAPV RVAVA RVAVI RVAVV RVAIA RVAII RVAIV RVLPA RVLPI RVLPV RVLVA RVLVI RVLVV RVLIA RVLII RVLIV RVVPA RVVPI RVVPV RVVVA RVVVI RVVVV RVVIA RVVII RVVIV RLVVI RLLVI**

Table 5.5: Pentapeptide sequences generated by mutating five amino acid residues in RIIGL.

Combination	Mutant peptides
1,2,3,4,5	**KAAPA KAAPI KAAPV HAAPA HAAPI HAAPV KAAVA KAAVI KAAVV HAAVA HAAVI HAAVV KAAIA KAAII KAAIV HAAIA HAAII HAAIV KALPA KALPI KALPV HALPA HALPI HALPV KALVA KALVI KALVV HALVA HALVI HALVV KALIA KALII KALIV HALIA HALII HALIV KAVPA KAVPI KAVPV HAVPA HAVPI HAVPV KAVVA KAVVI KAVVV HAVVA HAVVI HAVVV KAVIA KAVII KAVIV HAVIA HAVII HAVIV KLAPA KLAPI KLAPV HLAPA HLAPI HLAPV KLAVA KLAVI KLAVV HLAVA HLAVI HLAVV KLAIA KLAII KLAIV HLAIA HLAII HLAIV KLLPA KLLPI KLLPV HLLPA HLLPI HLLPV KLLVA KLLVI KLLVV HLLVA HLLVI HLLVV KLLIA KLLII KLLIV HLLIA HLLII HLLIV KLVPA KLVPI KLVPV HLVPA HLVPI HLVPV KLVVA KLVVI KLVVV HLVVA HLVVI HLVVV KLVIA KLVII KLVIV HLVIA HLVII HLVIV KVAPA KVAPI KVAPV HVAPA HVAPI HVAPV KVAVA KVAVI KVAVV HVAVA HVAVI HVAVV KVAIA KVAII KVAIV HVAIA HVAII HVAIV KVLPA KVLPI KVLPV HVLPA HVLPI HVLPV KVLVA KVLVI KVLVV HVLVA HVLVI HVLVV KVLIA KVLII KVLIV HVLIA HVLII HVLIV KVVPA KVVPI KVVPV HVVPA HVVPI HVVPV KVVVA KVVVI KVVVV HVVVA HVVVI HVVVV KVVIA KVVII KVVIV HVVIA HVVII HVVIV**

5.2.2 Virtual screening of the designed pentapeptide library

The single amino acid in RIIGL was replaced with other amino acids present in the same group, which leads to the generation of 14 single amino acid mutated pentapeptides (**Table 5.1**). The RIIGL and single amino acid mutated pentapeptides were docked to $A\beta_{42}$ monomer (PDB ID: 1IYT)[21] to evaluate their binding affinity with the $A\beta_{42}$ monomer. The initial structures of the $A\beta_{42}$ monomer along with its amino acid sequence and RIIGL are shown in **Figure 5.2**. The pentapeptides displaying higher binding affinity with $A\beta_{42}$ monomer as compared to RIIGL were retained in the library. Similarly, two, three, four, and five amino acids were mutated in RIIGL to generate mutated pentapeptides and docked with $A\beta_{42}$ monomer. The mutated

peptides displaying higher binding affinity with $A\beta_{42}$ monomer as compared to RIIGL were retained in the library for further screening.

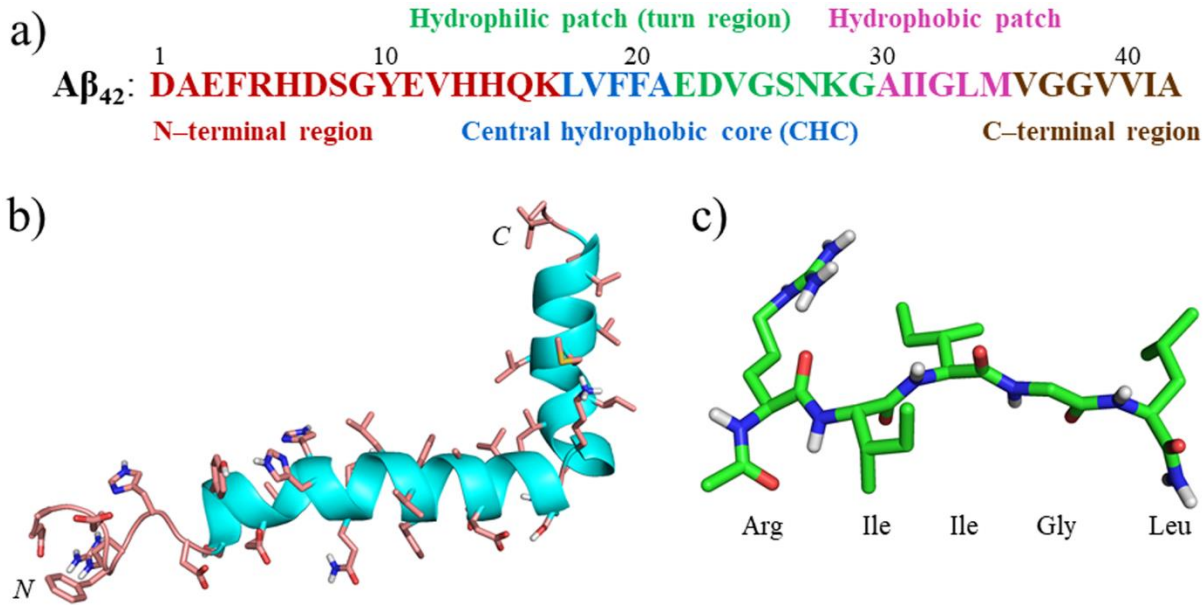

Figure 5.2: Sequence of $A\beta_{42}$ peptide with the key regions shown in different colours (panel a). The $A\beta_{42}$ monomer (PDB ID: 1IYT) and the reference peptide RIIGL are shown in the cartoon (panel b) and stick representation (panel c), respectively.

The PDBQT files for the $A\beta_{42}$ monomer and pentapeptides were prepared using PyRx.[22] The designed library was screened for potential peptide inhibitors of $A\beta_{42}$ aggregation using AutoDock Vina[23] assembled in the PyRx virtual screening tool.[24] The dimensions of the grid box were kept wide enough to cover the $A\beta_{42}$ monomer–pentapeptide complex. The exhaustiveness of the global search space was kept at 100. A root-mean-square deviation (RMSD) tolerance of 0.2 nm was applied to cluster the docked $A\beta_{42}$ monomer–pentapeptide poses followed by their ranking based on the binding energy.

5.2.3 Evaluation of binding free energy between Aβ42 monomer and pentapeptides using molecular mechanics Poisson-Boltzmann surface area (MM-PBSA)

The MM-PBSA method was utilized to further screen top hit pentapeptides obtained from the binding energy analysis using molecular docking. The top ten docked $A\beta_{42}$ monomer-pentapeptide complexes were subjected to energy minimization and 500 ps NVT followed by NPT equilibration. After MD simulations, the resulting structures were subjected to a binding free energy analysis between $A\beta_{42}$ monomer and pentapeptides by employing the MM-PBSA

method using the g_mmpbsa tool.[25, 26] The relative binding free energy was evaluated for the $A\beta_{42}$ monomer-pentapeptide complexes. The relative binding affinities determined by MM-PBSA are acceptable, however, it overvalues the absolute binding free energy.[27] Thus, the conformational entropy contribution has been ignored.[28] For each system, the conformational snapshots saved at 10 ps intervals from the 20 ns MD trajectories were used for the MM–PBSA analysis. The best three pentapeptides were chosen for their assessment against $A\beta_{42}$ aggregation using MD simulations. In addition, MD simulations of $A\beta_{42}$ monomer alone and $A\beta_{42}$ monomer–RIIGL were performed to assess the inhibitory potential of the shortlisted pentapeptides against $A\beta_{42}$ aggregation.

Table 5.6: Details of the MD simulated systems.

System	Simulation time (ns)[b]	Dimensions (nm) of the simulation box	N_w[c]
$A\beta_{42}$ monomer[a]	200	7.6 × 7.6 × 7.6	14608
$A\beta_{42}$ monomer–RIIGL complex	200	7.6 × 7.6 × 7.6	14590
$A\beta_{42}$ monomer–RLAPV complex	200	7.6 × 7.6 × 7.6	14581
$A\beta_{42}$ monomer–RVVPI complex	200	7.6 × 7.6 × 7.6	14578
$A\beta_{42}$ monomer–RIAPA complex	200	7.6 × 7.6 × 7.6	14585

[a]$A\beta_{42}$ monomer (PDB ID: 1IYT); [b]The GROMOS54a7 force field and SPC water model are used for MD simulations. [c]Number of water molecules added in the simulation box

5.2.4 MD simulation protocols

MD simulations were employed to visualize the conformational changes in the $A\beta_{42}$ monomer in the absence and presence of the top three pentapeptides obtained from MM-PBSA analysis. The GROMACS 5.0.1[29] was used for MD simulations. The GROMOS96 54a7 force field[30] was chosen for MD simulations as it displays good α–β–coil symmetry, stabilized secondary structure elements, and depicts closeness between observed and primary data of *J*–coupling ($^3J_{NH–H\alpha}$) constants.[31, 32] Recent studies have employed the GROMOS96 54a7 force field to explore the conformational dynamics of peptides and proteins.[33] The details of all the systems used for MD simulations are presented in **Table 5.6**. The systems were solvated by a simple point charge (SPC) water model in a cubic box of dimensions 7.6 nm × 7.6 nm × 7.6 nm. The five systems $A\beta_{42}$ monomer, $A\beta_{42}$ monomer–RIIGL, $A\beta_{42}$ monomer–RLAPV, $A\beta_{42}$ monomer–RVVPI, and $A\beta_{42}$ monomer–RIAPA were solvated with 14608, 14590, 14581, 14578, and 14585 SPC water molecules, respectively (**Table 5.6**). In each system, 0.15 M NaCl was added in the cubic box along with the required number of Na^+ and Cl^- counter ions to keep the system

overall neutral at physiological pH.[34] The periodic boundary conditions were applied in all simulations. The protonation states of the amino acids were assigned at the physiological pH. All bonds involving hydrogen atoms of $A\beta_{42}$ monomer were constrained using the LINCS algorithm,[35] and bonds within water were constrained by the SETTLE algorithm.[36] The particle mesh Ewald (PME) approach was used to calculate long-range electrostatic interactions and a cut-off of 1.0 nm was used to evaluate short-range van der Waals interactions.[37] The systems were energy minimized and equilibrated for 500 ps at 300 K under *NVT*, and then for 500 ps in *NPT* conditions. To maintain the desired temperature (300 K) and pressure (1 atm), the V-scaling method[38] and a Parrinello-Rahman barostat[39] have been employed, respectively. The MD simulations were run for 200 ns for all systems with a time interval of 10 ps.

The NMR chemical shifts of Cα and Cβ atoms of the central member of the conformational cluster with the highest population of $A\beta_{42}$ monomer were calculated by SHIFTX2[40] and compared with $A\beta_{42}$ monomer experimental chemical shifts.[41] The scalar *J*–coupling ($^3J_{NH\text{-}H\alpha}$) constants were calculated by evaluating the dihedral angles ϕ and ψ using the Karplus equation.[42] The parameter set was used in which A= 6.4, B= –1.4, and C= 1.9.[43] The GROMACS tools, visual molecular dynamics (VMD),[44] and PyMOL[45] were used to analyze the conformational ensembles from MD simulations. The MD ensembles were clustered using a cut-off of 0.15 nm over the backbone atoms by employing Daura et al. algorithm.[46] The structural alterations in the $A\beta_{42}$ monomer structure were analyzed using RMSD and radius-of-gyration (R_g) by employing gmx rms, and gmx gyrate, respectively. The center of mass (COM) distance between two residues was evaluated by gmx distance. The gmx hbond tool was used to determine hydrogen bonds. A hydrogen bond was considered if the distance between a donor atom (D) and an acceptor atom (A) is no larger than 0.35 nm and the angle of D–H---A is no less than 150º. The Dictionary of Secondary Structure of Proteins (DSSP) was utilized to assess the secondary structure contents of $A\beta_{42}$ monomer in the absence and presence of pentapeptides.[47] The free energy landscape (FEL) and binding free energy analysis were performed as reported in our previous studies.[48] The gmx sham was used to construct FEL which is defined as:

$$G_{(\mathrm{PC1,\ PC2})} = -k_B\, T \ln P_{(\mathrm{PC1,\ PC2})}$$

where G is the Gibbs free energy, k_B is the Boltzmann constant, T is the absolute temperature and $P_{(PC1, PC2)}$ is the probability distribution of systems along PC. The Origin 9.0 package was used to plot FEL.

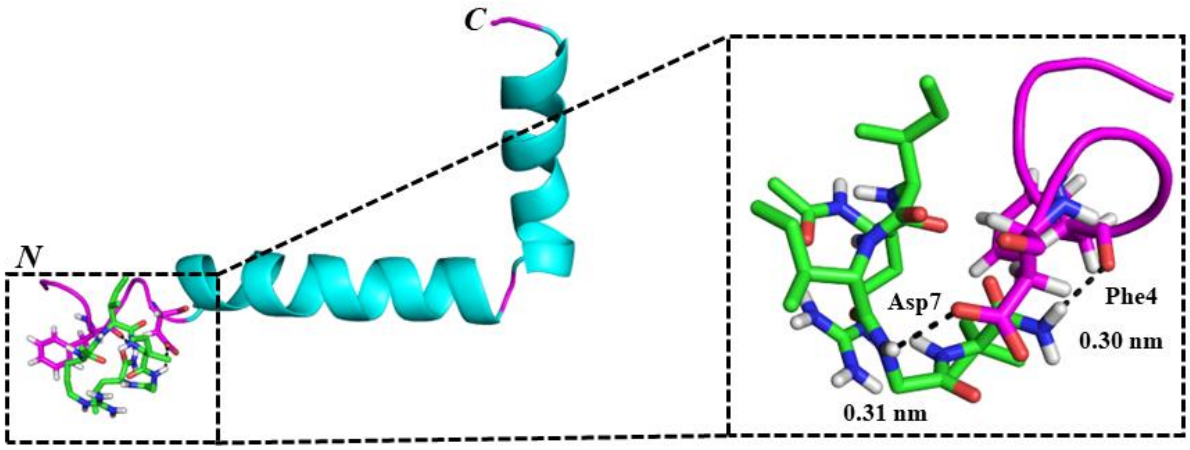

Figure 5.3: Docked pose of reference peptide RIIGL with $A\beta_{42}$ monomer is shown. The hydrogen bonds between $A\beta_{42}$ monomer and RIIGL are shown in the magnified view.

5.3 Result and discussion

5.3.1 Molecular docking and estimation of binding free energy of $A\beta_{42}$ monomer-pentapeptide complexes

The binding affinity and key interactions of computationally designed pentapeptides with $A\beta_{42}$ monomer were evaluated using molecular docking. The pentapeptides displayed binding energy with $A\beta_{42}$ monomer in the range −3.6 to −5.8 kcal/mol and ~23% of pentapeptides depict binding energy higher than RIIGL (–4.6 kcal/mol). RIIGL forms hydrogen bonds with Phe4 (0.30 nm) and Asp7 (0.31 nm) of $A\beta_{42}$ monomer (**Figure 5.3**).

Table 5.7: Binding free energies (kcal/mol) of the shortlisted pentapeptides with $A\beta_{42}$ monomer.

Pentapeptide	Binding free energy (kcal/mol)						
	$\Delta G_{binding}{}^{a}$	ΔE_{vdW}	$\Delta E_{elec.}$	$\Delta E_{MM}{}^{b}$	ΔG_{ps}	ΔG_{nps}	$\Delta G_{solv}{}^{c}$
RLAPV	-55.80	-30.40	-49.18	-79.18	27.51	-3.72	23.79
RVVPI	-46.32	-29.30	-64.09	-93.39	50.90	-3.80	47.10
RIAPA	-44.26	-29.39	-103.35	-132.74	92.82	-4.20	88.62
RIIGL	-41.29	-19.98	-78.61	-98.59	60.20	-2.90	57.30
RAVPL	-35.21	-19.00	-71.26	-90.26	57.82	-2.72	55.10
HVIGL	-24.80	-36.09	-1.97	-38.06	17.67	-4.40	13.27
HAIPV	-20.62	-30.47	-1.50	-31.97	15.11	-3.71	11.40

HAAPL	-19.98	-35.67	-7.90	-43.57	27.84	-4.25	23.58
HVVPL	-17.71	-37.55	-8.07	-45.62	32.37	-4.45	27.92
HVAPL	-14.82	-22.00	-2.04	-24.04	11.63	-2.41	9.22
HAIPI	-13.14	-32.44	-10.32	-42.76	33.76	-4.13	29.63

[a] $\Delta G_{binding} = \Delta E_{MM} + \Delta G_{solv}$; [b] $\Delta E_{MM} = \Delta E_{vdW} + \Delta E_{elec}$; [c] $\Delta G_{solv} = \Delta G_{ps} + \Delta G_{nps}$

The top ten pentapeptides were shortlisted from the designed library of 912 pentapeptides based on the binding affinity with Aβ$_{42}$ monomer (**Figure 5.4**). The molecular docking analyses highlighted that proline containing pentapeptides displayed higher binding energy with Aβ$_{42}$ monomer as compared to RIIGL, which is consistent with the results reported by Kanchi et al. that depicts the enhanced ability of the KLVFFPPPPP peptide for the destabilization of Aβ protofibrils as compared to KLVFF.[49]

To provide detailed insight into the key interactions between Aβ$_{42}$ monomer and the top ten pentapeptides, the binding free energies of Aβ$_{42}$ monomer-pentapeptide complexes were evaluated. The pentapeptides RLAPV, RVVPI, and RIAPA bind to Aβ$_{42}$ monomer with a binding free energy of –55.80, –46.32, and –44.26 kcal/mol, respectively, which is significantly higher compared to Aβ$_{42}$ monomer-RIIGL (–41.29 kcal/mol) (**Table 5.7**). The binding free energy analysis depicted that pentapeptides containing arginine bind more strongly with Aβ$_{42}$ monomer as compared to histidine-containing pentapeptides due to electrostatic interactions of arginine with negatively charged residues of Aβ$_{42}$ monomer.

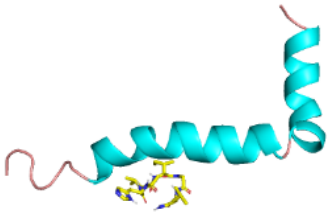

HVIGL (–5.8 kcal/mol)

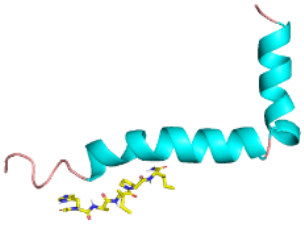

HAIPI (–5.7 kcal/mol)

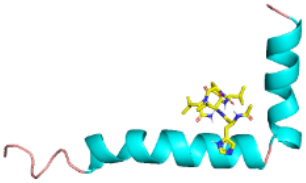

HVVPL (–5.7 kcal/mol)

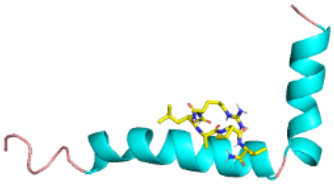

RLAPV (–5.7 kcal/mol)

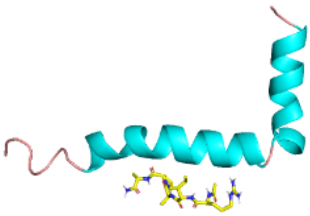

HVAPL (–5.6 kcal/mol)

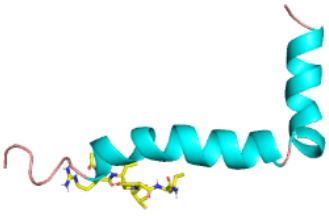

RIAPA (–5.6 kcal/mol)

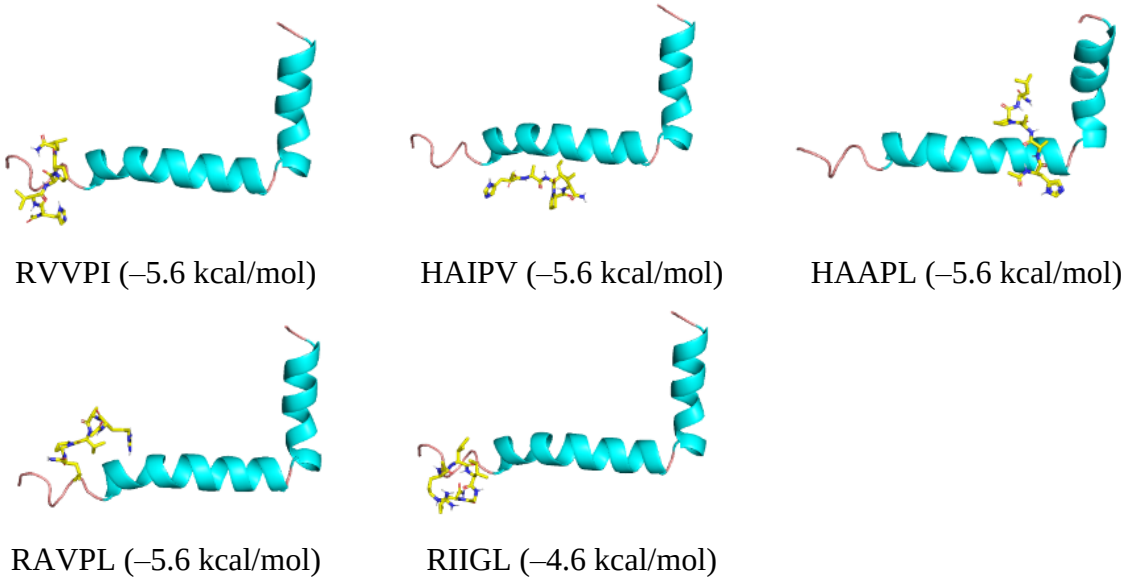

Figure 5.4: Docked poses of the top ten pentapeptides and reference peptide RIIGL with $A\beta_{42}$ monomer (PDB ID: 1IYT). The $A\beta_{42}$ monomer is in cartoon and pentapeptides are in sticks. The binding energy values evaluated using AutoDock Vina are expressed in kcal/mol.

5.3.2 Interaction of pentapeptides with $A\beta_{42}$ monomer: charged residues (Asp and Glu) of $A\beta_{42}$ monomer contribute significantly to the binding with pentapeptides

The residue-wise binding free energy was evaluated and the binding free energy values are reported in kcal/mol (**Figure 5.5**). RIIGL preferentially binds to D1 (–3.2), E3 (–3.2), D7 (–4.5), E11 (–6.5), E22 (–2.2), and D23 (–6.5) of $A\beta_{42}$ monomer (**Figure 5.5a**). RLAPV bind to D1 (–3.2), E3 (–2.6), D7 (–3.4), E11 (–4.7), E22 (–8.1), D23 (–5.2), I31 (–2.2) of $A\beta_{42}$ monomer (**Figure 5.5b**). The $A\beta_{42}$ residues D1 (–3.9), E3 (–3.9), D7 (–3.3), E11 (–4.9), E22 (–3.2), D23 (–5.4), contribute significantly to binding with RVVPI (**Figure 5.5c**), whereas $A\beta_{42}$ residues D1 (–4.0), E3 (–5.7), D7 (–5.7), E11 (–4.5), E22 (–5.5) and D23 (–3.7) contributed considerably in the binding to RIAPA (**Figure 5.5d**). The RIIGL, RLAPV, RIAPA, and RVVPI bind to the CHC region (17–21), E22, and D23 of $A\beta_{42}$ monomer, which play a key role in $A\beta_{42}$ aggregation and its associated cytotoxicity.[50] The arginine of pentapeptides displayed strong electrostatic interactions with the E22 and D23 of $A\beta_{42}$ monomer (**Figure 5.5**), which is consistent with Liu et al. that reported strong electrostatic interactions between negatively charged residues (D1, E3, E11, E22, and D23) of $A\beta_{42}$ monomer with the lysine of KLVFF inhibitor.[51] The binding free energy analysis revealed that intermolecular electrostatic interactions govern the binding of pentapeptides with $A\beta_{42}$ monomer.

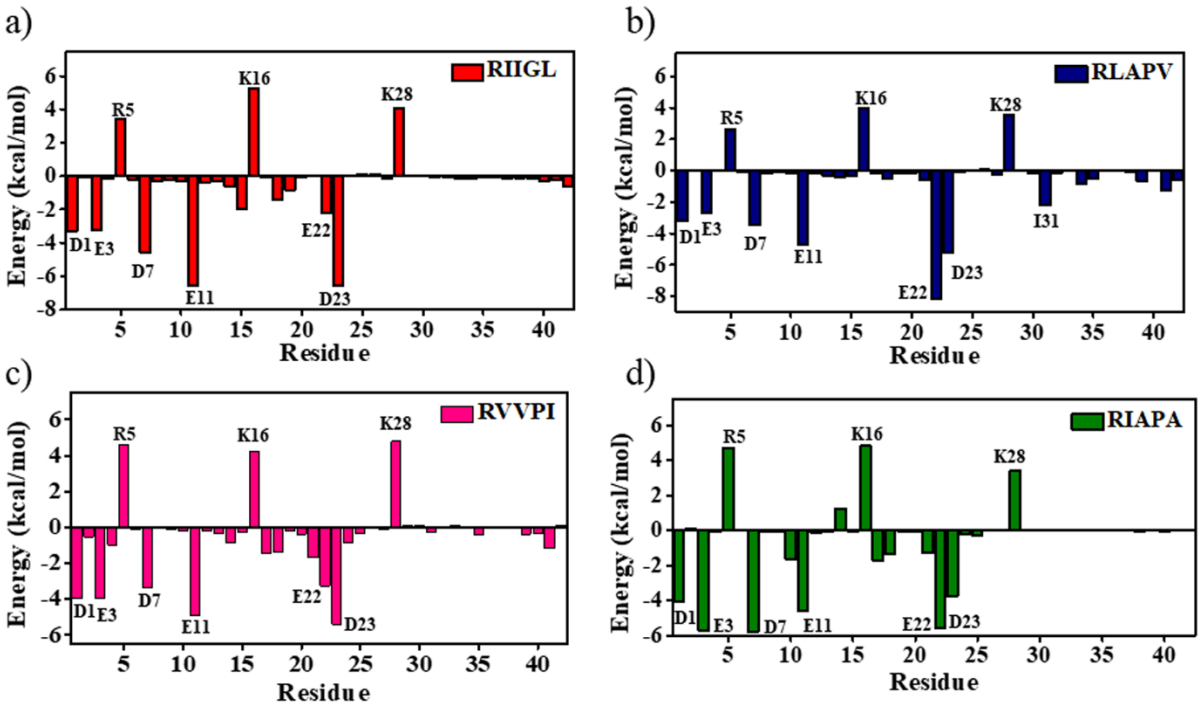

Figure 5.5: Contribution of each residue of $A\beta_{42}$ monomer towards binding with the lead pentapeptides. The $A\beta_{42}$ residues with the most favourable (< –1.0 kcal/mol) and unfavourable (>1.0 kcal/mol) contribution in the binding with pentapeptides are labeled.

The residue-wise binding free energy highlighted that RLAPV displayed hydrophobic contacts with I31, L34, M35, V39, and I41 of $A\beta_{42}$ monomer, whereas a higher number of residues A2, F4, L17, F20, A21, V24, G25, V39, V40, I41 of $A\beta_{42}$ monomer were involved in the hydrophobic contacts with RVVPI. In the case of RIAPA, the residues L17, A21, V24, and G25 of $A\beta_{42}$ monomer displayed hydrophobic contacts. The hydrophobic contacts between the $A\beta_{42}$ monomer and pentapeptides result in the formation of a U-shaped structure with more accessibility of the hydrophilic residues to the solvent and result in the lower sampling of β–sheet conformation (**Figure 5.5**). This is consistent with Wang et al.,[52] which highlighted hydrophobic contacts between $A\beta_{42}$ monomer and flavonoids induce U-shaped structure in $A\beta_{42}$ monomer with no sampling of the β–sheet conformation. Notably, the maximum number of hydrophobic contacts were observed in RVVPI and the representative conformation of the most-populated microstate in $A\beta_{42}$ monomer-RVVPI displayed the formation of a U-shaped structure (**Figure 5.11**) and hence resulting in a reduced aggregation propensity of $A\beta_{42}$ monomer on the incorporation of RVVPI.

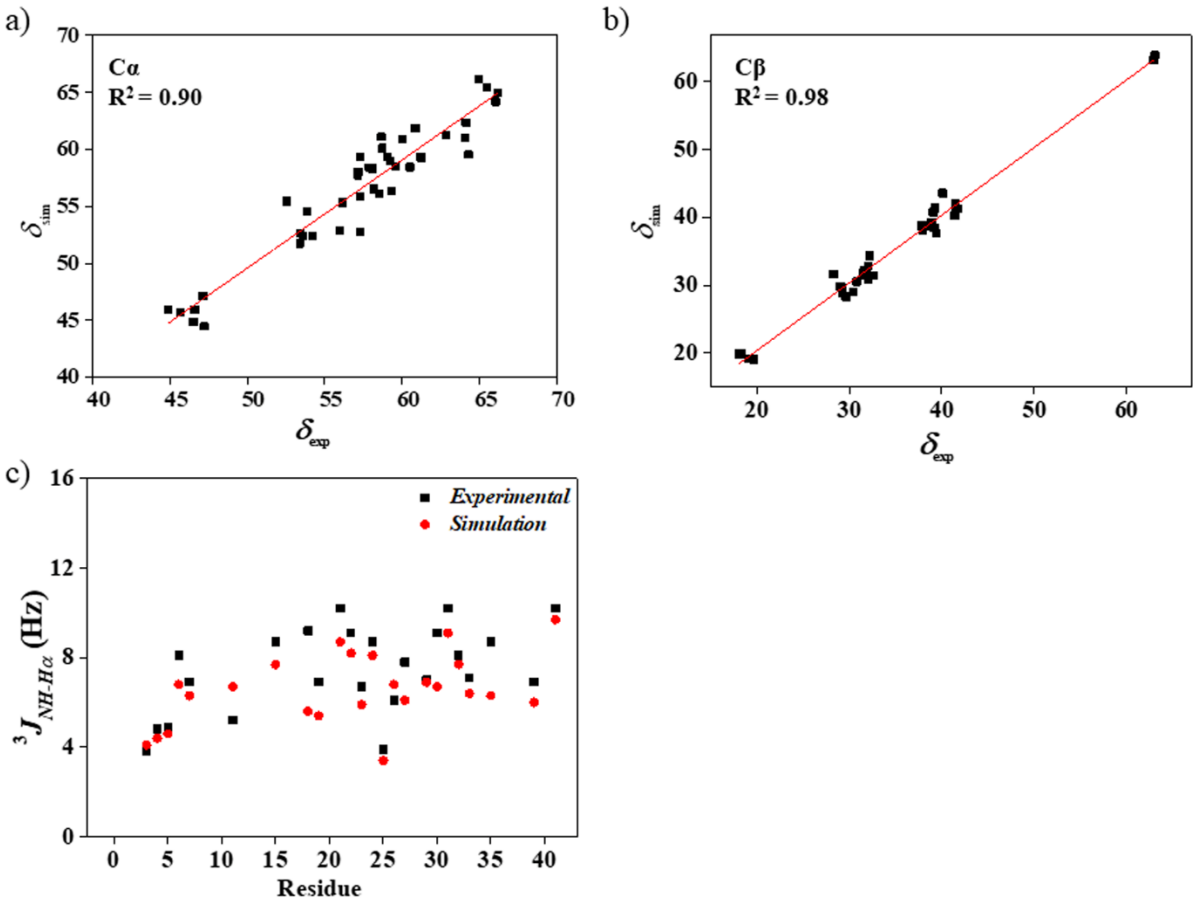

Figure 5.6: Correlation between simulated and experimental NMR chemical shifts for Cα, Cβ atoms of Aβ$_{42}$ monomer (panels a, and b, respectively). The unit of chemical shift is ppm. Comparison of computational and experimental NMR *J*-coupling constants ($^3J_{HN\text{-}H\alpha}$) of Aβ$_{42}$ monomer (panel c).

To investigate whether the conformational ensembles from MD simulations match the experimental data, the NMR chemical shifts have been evaluated. A significant correlation was observed between simulated (δ_{sim}) and experimental (δ_{exp}) primary chemical shifts for Cα (R^2= 0.90) and Cβ atoms (R^2= 0.98) of Aβ$_{42}$ monomer (**Figure 5.6a, b**), which indicates that Aβ$_{42}$ monomer conformational ensemble produced by MD simulations is in close agreement with the experimental data. Additionally, the ensemble-averaged $^3J_{NH\text{-}H\alpha}$ values evaluated from the MD simulation data display good agreement with experimental $^3J_{NH\text{-}H\alpha}$ values (**Figure 5.6c**).[53]

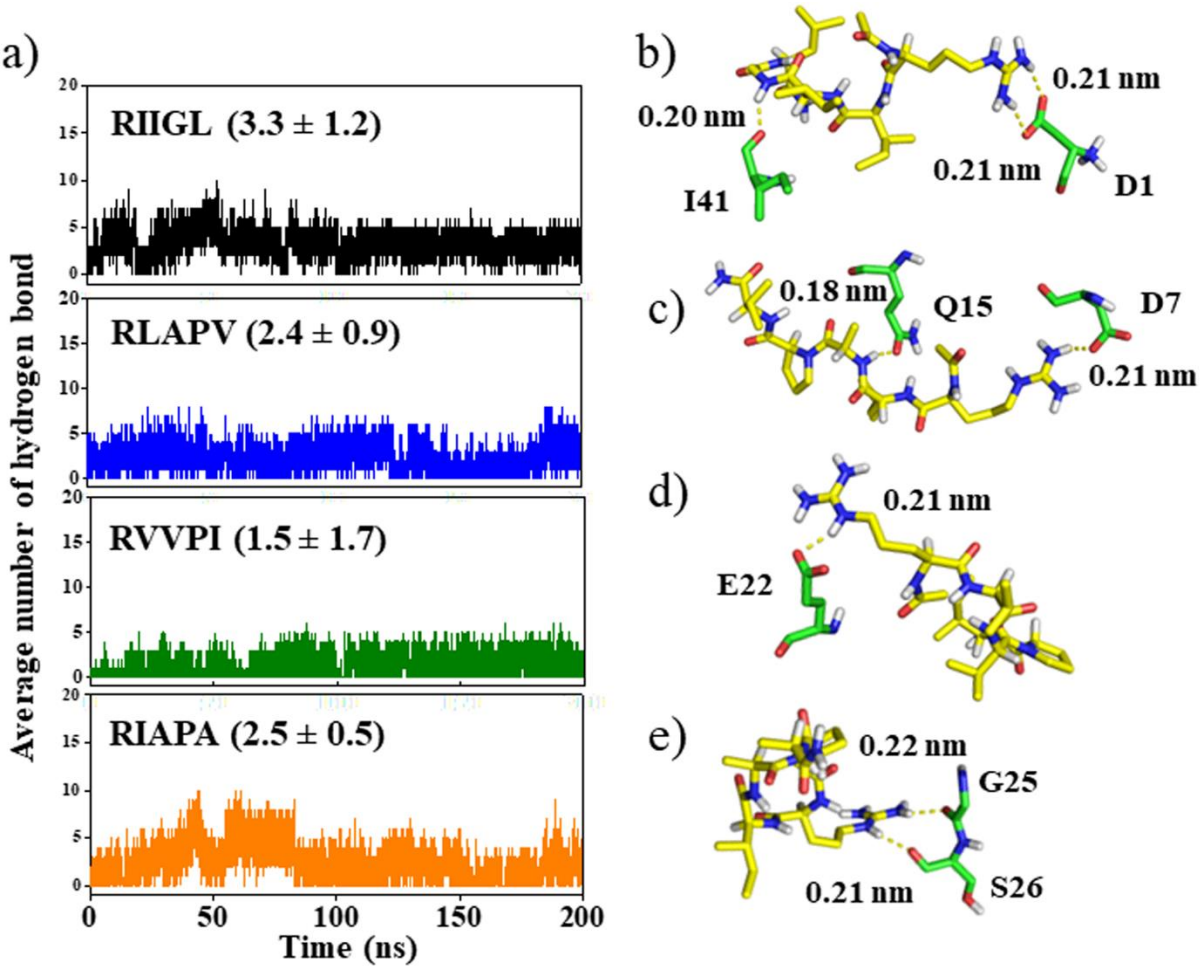

Figure 5.7: Number of hydrogen bonds between $A\beta_{42}$ monomer and pentapeptides during simulation (panel a). Snapshots of hydrogen bond interactions of $A\beta_{42}$ monomer with RIIGL, RLAPV, RVVPI, and RIAPA are shown in panels (b-e), respectively.

To analyze the stability of the $A\beta_{42}$ monomer-pentapeptide complexes, hydrogen bond analysis was performed (**Figure 5.7**). The average number of hydrogen bonds was noted to be 3.3 ± 1.2, 2.4 ± 0.9, 1.5 ± 1.7, and 2.5 ± 0.5 for $A\beta_{42}$ monomer-RIIGL, $A\beta_{42}$ monomer-RLAPV, $A\beta_{42}$ monomer-RVVPI, and $A\beta_{42}$ monomer-RIAPA, respectively, which indicate the stability of the $A\beta_{42}$ monomer-pentapeptide complexes. RVVPI displayed a hydrogen bond with E22 of $A\beta_{42}$ monomer (**Figure 5.7d**), which is reported for its key role in the $A\beta_{42}$ aggregation and its associated toxicity.[54] The hydrogen bond analysis is consistent with our earlier finding (**Figure 5.7c**) that highlights the notable contribution of E22 (–3.27 kcal/mol) in binding with RVVPI.

5.3.3 Pentapeptides bind to $A\beta_{42}$ monomer to form a stable complex

For Aβ$_{42}$ monomer, RMSD fluctuate at a higher value after 170 ns and then steadily attained a stable plateau (**Figure 5.8a**). The average RMSD of Aβ$_{42}$ monomer display limited change in presence of pentapeptides that indicates stable binding of the pentapeptides with the Aβ$_{42}$ monomer. The average value of RMSD for Aβ$_{42}$ monomer was noted to be 0.99 ± 0.06 nm. The average RMSD changes to 1.12 ± 0.02, 1.09 ± 0.09, and 1.13 ± 0.03 nm for Aβ$_{42}$ monomer–RIIGL, Aβ$_{42}$ monomer–RVVPI, and Aβ$_{42}$ monomer–RIAPA respectively, whereas the average RMSD is 0.99 ± 0.08 nm for Aβ$_{42}$ monomer–RLAPV. The RMSD of Aβ$_{42}$ monomer–RVVPI and Aβ$_{42}$ monomer–RLAPV complexes were less as compared to Aβ$_{42}$ monomer–RIIGL, which indicates higher structural stability of Aβ$_{42}$ monomer–RVVPI and Aβ$_{42}$ monomer–RLAPV complexes.

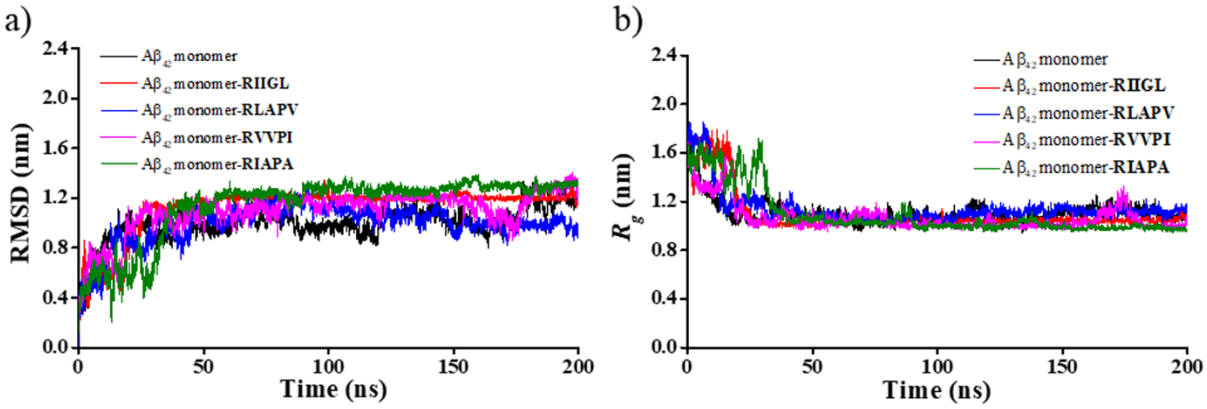

Figure 5.8: RMSD (panel a) and R_g (panel b) of Aβ$_{42}$ monomer in the absence and presence of pentapeptides.

At the start of the simulation, a relatively high value of R_g was noted in all systems that fall to lower values within 50 ns and then attained equilibrium (**Figure 5.8b**). The average value of R_g for Aβ$_{42}$ monomer, Aβ$_{42}$ monomer–RIIGL, Aβ$_{42}$ monomer–RLAPV, Aβ$_{42}$ monomer–RVVPI, and Aβ$_{42}$ monomer–RIAPA was noted to be 1.10 ± 0.02, 1.09 ± 0.05, 1.13 ± 0.04, 1.06 ± 0.05, and 1.09 ± 0.06 nm, respectively. The average R_g of Aβ$_{42}$ monomer in the presence of RIIGL, RVVPI, and RIAPA has marginally lower values as compared to Aβ$_{42}$ monomer alone, which indicates the stability of Aβ$_{42}$ monomer-pentapeptide complexes. The repeat simulations (simulations 2 and 3) with varying initial velocities for Aβ$_{42}$ monomer displayed almost similar RMSD and R_g patterns as noted in simulation 1 (**Figure 5.9a, b**), which reflects the reproducibility of conformational ensembles.

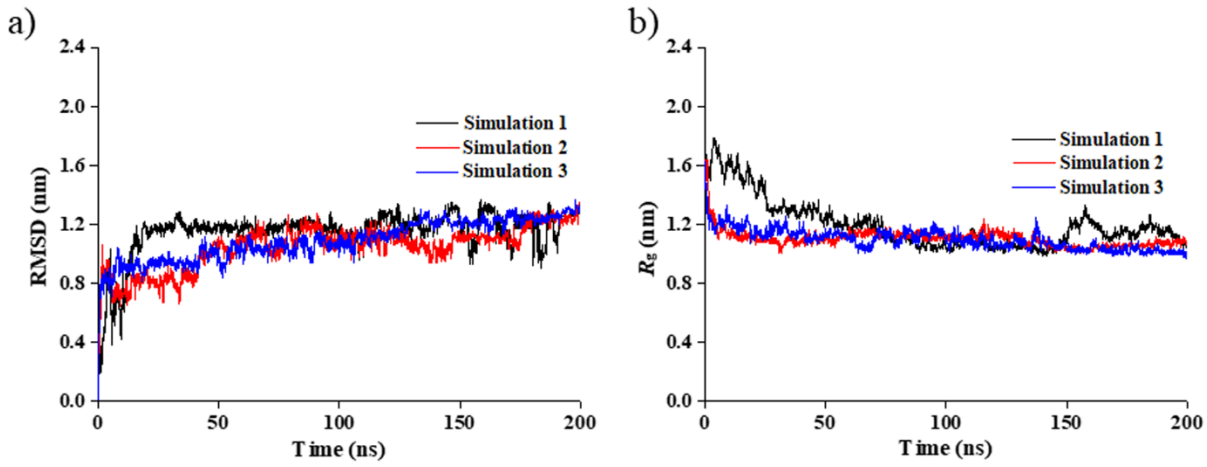

Figure 5.9: RMSD and R_g of repeat simulations of $A\beta_{42}$ monomer are shown in panels a, and b, respectively.

Further, residue-based RMSF for Cα atoms of $A\beta_{42}$ monomer and $A\beta_{42}$ monomer-pentapeptide complexes was evaluated to analyze the flexibility and local dynamics of $A\beta_{42}$ monomer (**Figure 5.10**). Reduced fluctuations were noted in residues 1–5, 8, 11–28 for $A\beta_{42}$ monomer–RIIGL, 1–19, 21–22, 26 for $A\beta_{42}$ monomer–RLAPV, and 13–19, 21–24 for $A\beta_{42}$ monomer–RIAPA (**Figure 5.10a, b, d**). The residues 1–2, 5, 8, 12-16 in the N-terminal, 17–21 in the CHC, 22–27, 30, and 40–42 in the C-terminal regions of $A\beta_{42}$ monomer display lower atomic fluctuations on the incorporation of RVVPI (**Figure 5.10c**). The RMSF analysis depicted reduced fluctuations of ~57% residues in $A\beta_{42}$ monomer–RVVPI complex as compared to other complexes, which indicate higher $A\beta_{42}$ structural stability in presence of RVVPI.

5.3.4 Effect of pentapeptides on the conformational sampling of $A\beta_{42}$ monomer and secondary structure analysis

The conformational clustering algorithm is commonly used as a data mining method to screen massive MD ensembles into a compact size.[55] The total number of microstates for $A\beta_{42}$ monomer was noted to be 88 and the number decreased to 84, 64, 48, and 63 for $A\beta_{42}$ monomer–RIIGL, $A\beta_{42}$ monomer–RLAPV, $A\beta_{42}$ monomer–RVVPI, and $A\beta_{42}$ monomer–RIAPA, respectively (**Table 5.8**), which indicates higher conformational stability of $A\beta_{42}$ peptide in the presence of pentapeptides. Remarkably, the number of microstates was reduced from 88 in $A\beta_{42}$ monomer to 48 in $A\beta_{42}$ monomer–RVVPI, which depicts conformational homogeneity in $A\beta_{42}$ monomer on the incorporation of RVVPI. The percentage population of m_1 was noted to be 34.5% in $A\beta_{42}$ monomer and the occupancy increased to 62.3%, 48.4%, 89.1%, and 50.4% in $A\beta_{42}$ monomer–RIIGL, $A\beta_{42}$ monomer–RLAPV, $A\beta_{42}$ monomer–

RVVPI, and $A\beta_{42}$ monomer–RIAPA, respectively. The increased sampling in the m_1 depicts more homogeneity in the conformational ensemble of $A\beta_{42}$ monomer in the presence of pentapeptides.

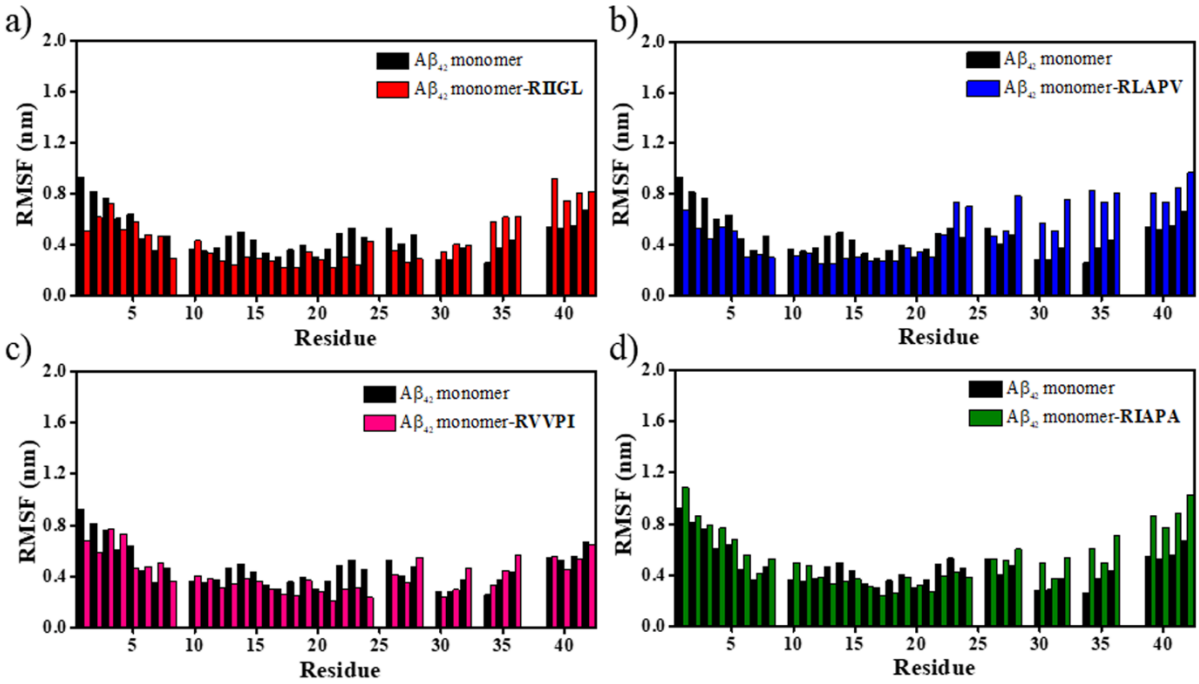

Figure 5.10: RMSFs in $A\beta_{42}$ monomer with and without pentapeptides.

The visual inspection of microstates m_1 and m_3 of $A\beta_{42}$ monomer depict coil conformation at the C-terminal region. Notably, microstate m_2 sampled β–sheet at the C-terminus of $A\beta_{42}$ monomer, which is consistent with Khatua et al. that highlighted the existence of β–sheet at the C-terminus of $A\beta_{42}$ monomer in the representative conformation extracted from the most-populated microstate.[56] In contrast, no β–sheet conformation was observed in the three most-populated microstates of $A\beta_{42}$ monomer-pentapeptide complexes, which depict prevention of the conformational conversion from random coil/helix to β-sheet in the $A\beta_{42}$ monomer in the presence of pentapeptides.

Table 5.8: Conformational clustering analysis of $A\beta_{42}$ monomer alone and in the presence of pentapeptides.

System	No. of microstates	Percentage population of three most-populated microstates		
		m_1	m_2	m_3
$A\beta_{42}$ monomer	88	34.5	19.1	14.6
$A\beta_{42}$ monomer–RIIGL	84	62.3	3.2	2.8
$A\beta_{42}$ monomer–RLAPV	64	48.4	14.7	13.9

$A\beta_{42}$ monomer–RVVPI	48	89.1	4.9	1.2
$A\beta_{42}$ monomer–RIAPA	63	50.4	19.2	0.8

Among shortlisted pentapeptides, RVVPI displayed a remarkably high tendency to induce the helical content in $A\beta_{42}$ monomer. The representative structures of the three highest-populated microstates of $A\beta_{42}$ monomer–RVVPI displayed helix as the most dominant conformation (**Figure 5.11**). Notably, enhanced sampling of the helical conformation in the E3–S26 and K28–V40 regions of $A\beta_{42}$ monomer was observed in m_1 (percentage population: 89.1%) of $A\beta_{42}$ monomer–RVVPI complex (**Figure 5.11**). Thus, conformational clustering analysis depicted a homogeneous conformational ensemble and enhanced sampling of the helical content in $A\beta_{42}$ monomer in presence of RVVPI.

Previous studies reported that $A\beta_{42}$ monomer with preliminary α–helix or random coil structure changes into β–sheet structures, which is a key step in Aβ fibrillogenesis.[57] The $A\beta_{42}$ monomer possessing β–sheet rich structures will subsequently self-assemble into different types of aggregates.[58] To characterize the inhibitory effect of pentapeptides on the conformational conversion of $A\beta_{42}$ monomer, the secondary structure analysis of $A\beta_{42}$ monomer with and without pentapeptides was performed (**Figure 5.12, Table 5.9**). In the case of $A\beta_{42}$ monomer, the sampling of β–sheet conformation was observed in the N-terminal (residues 7–9) and C-terminal regions (residues 38–40) after ~85 ns (Fig. 8a). This is consistent with Wang et al.,[52] which reported the sampling of the β-sheet structures in the C-terminal region (residues 30–31 and 37–38) of $A\beta_{42}$ monomer. Another study reported the existence of a short β-sheet structure in the C-terminal region (residues 36–37) of $A\beta_{42}$ monomer.[57b]

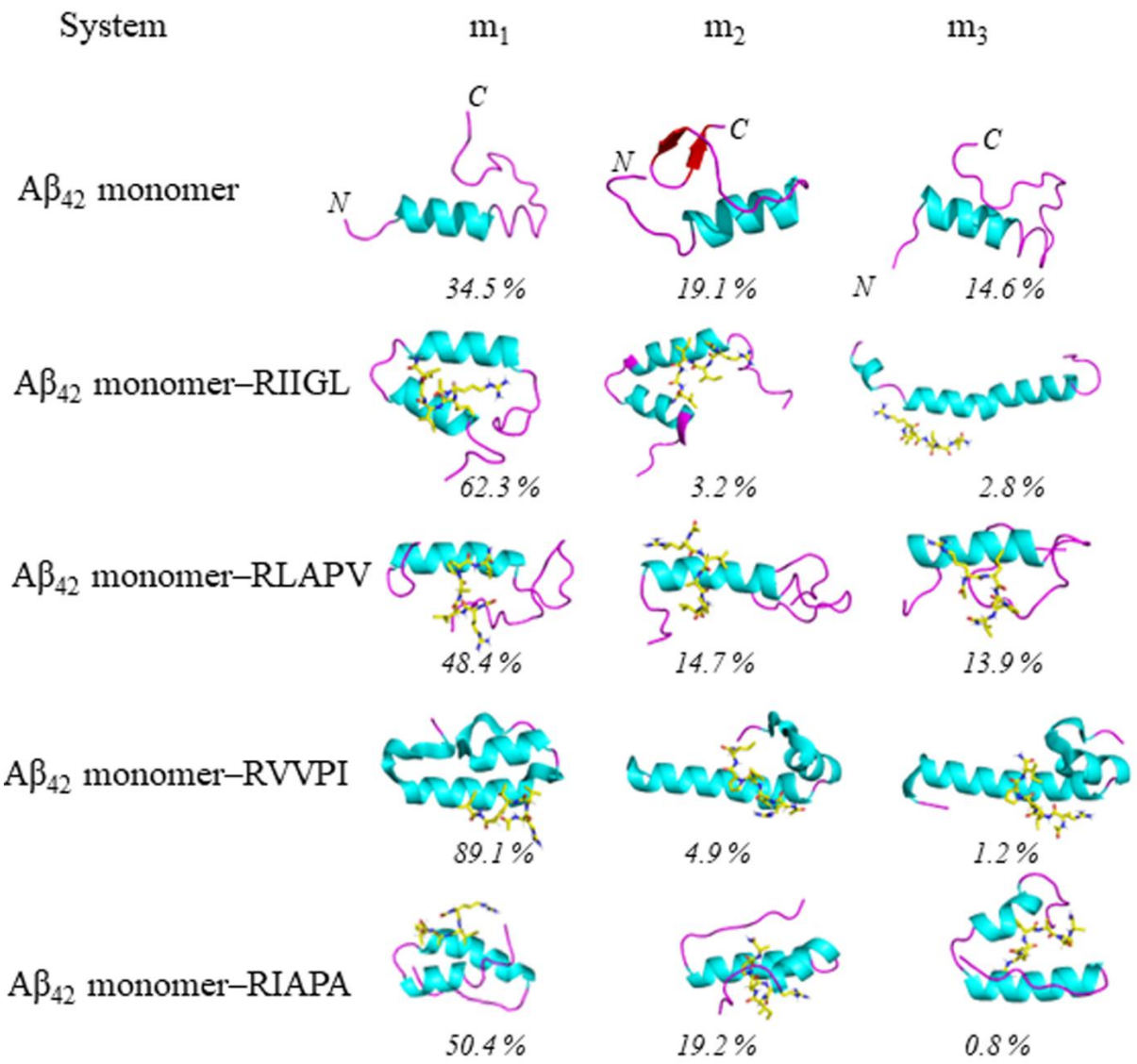

Figure 5.11: Conformational clustering analysis of $A\beta_{42}$ monomer alone and in the presence of pentapeptides. The central members of the three most-populated microstates along with their populations are shown in the cartoon models.

The contents of the helix, β–sheet, coil, bend and turn conformations for $A\beta_{42}$ monomer were noted to be 42.2 ± 3.9, 8.5 ± 2.8, 26.1 ± 3.4, 15.4 ± 4.1, and 8.2 ± 2.5%, respectively (**Table 5.9**). Fang et al. reported 45.28 ± 2.42 helix, 5.20 ± 2.68 % β–sheet, 24.69 ± 4.58 coil, 14.91 ± 4.91 bend, 9.92 ± 6.06 turn contents in $A\beta_{42}$ monomer,[59] which is almost identical to the secondary structure content noted for $A\beta_{42}$ monomer in the present study. Notably, the β-sheet content sampled in $A\beta_{42}$ monomer is consistent with Wang et al.[52] which reported ~7% β-sheet content in the conformational ensemble of $A\beta_{42}$ monomer.

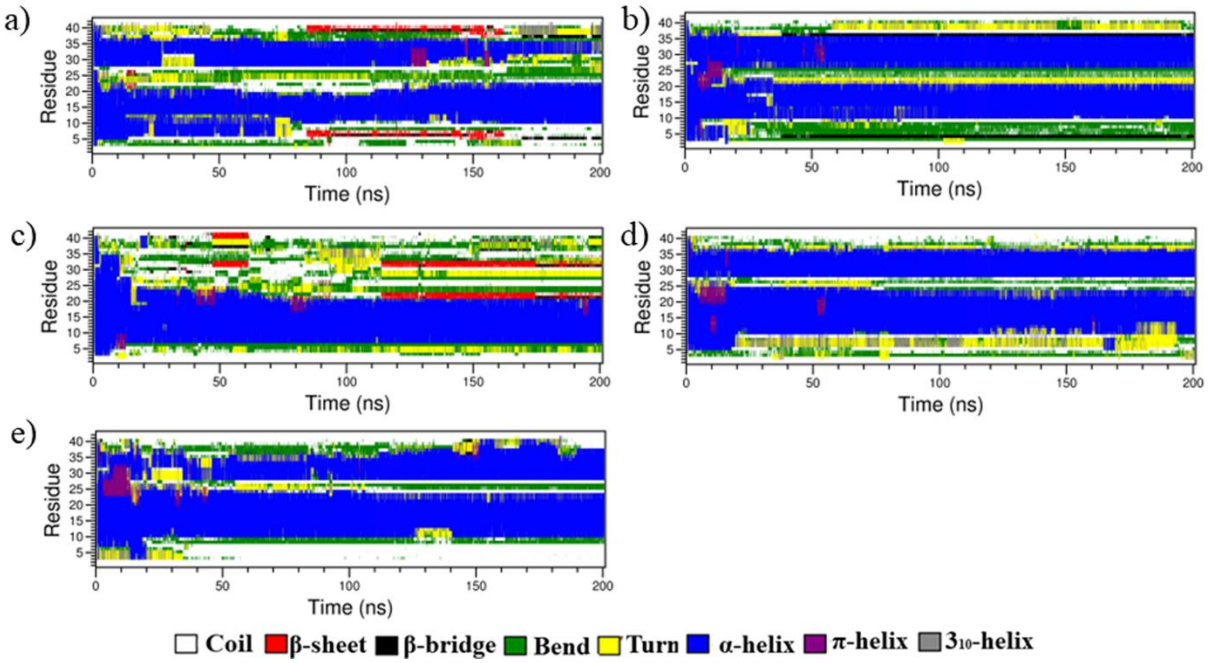

Figure 5.12: Variations in the secondary structure occupancies of $A\beta_{42}$ monomer alone (panel a) and in the presence of RIIGL (panel b), RLAPV (panel c), RVVPI (panel d), and RIAPA (panel e). The secondary structures are color-coded as shown underneath.

The helical content was increased from 42.2 ± 3.9 in $A\beta_{42}$ monomer to 52.3 ± 2.4, 57.6 ± 4.4, and 56.8 ± 3.9% on the incorporation of RIIGL, RVVPI, and RIAPA, respectively, which indicate reduced aggregation propensity of $A\beta_{42}$ monomer on the incorporation of pentapeptides. In comparison to 8.5 ± 2.8% β–sheet content sampled in the $A\beta_{42}$ monomer, the β–sheet content decreased to 4.6 ± 1.3% in $A\beta_{42}$ monomer–RIIGL and 5.4 ± 1.8% in $A\beta_{42}$ monomer–RLAPV, and interestingly, no β–sheet was sampled in $A\beta_{42}$ monomer–RVVPI and $A\beta_{42}$ monomer–RIAPA complexes. Notably, the β–sheet structure is present in the C-terminal region for $A\beta_{42}$ monomer–RIIGL and in the residues (21-23, 31, 32) of $A\beta_{42}$ monomer–RLAPV complex. Interestingly, no β–sheet conformations in $A\beta_{42}$ monomer were observed in the presence of RVVPI and RIAPA (**Table 5.9**). A notable increase in the helical and no sampling of β–sheet in $A\beta_{42}$ peptide on the addition of RVVPI and RIAPA highlight the preservation of native helical/random coil structure of $A\beta_{42}$ peptide.

Table 5.9: Secondary structure compositions of the simulated systems.

Secondary structure component	$A\beta_{42}$ monomer	$A\beta_{42}$ monomer–RIIGL	$A\beta_{42}$ monomer–RLAPV	$A\beta_{42}$ monomer–RVVPI	$A\beta_{42}$ monomer–RIAPA
helix[a]	42.2 ± 3.9	52.3 ± 2.4	38.7 ± 4.2	57.6 ± 4.4	56.8 ± 3.9

β–sheet[b]	8.5 ± 2.8	4.6 ± 1.3	5.4 ± 1.8	0.0 ± 0.0	0.0 ± 0.0
Coil	26.1 ± 3.4	18.1 ± 2.6	27.6 ± 2.8	24.5 ± 3.6	28.4 ± 2.9
Bend	15.4 ± 4.1	16.3 ± 3.2	18.2 ± 4.3	9.8 ± 3.9	8.6 ± 3.3
Turn	8.2 ± 2.5	8.9 ± 1.8	10.8 ± 2.1	8.4 ± 2.4	6.9 ± 1.4

[a]helix is the sum of α–, π– and 3_{10} helix ; [b]β–sheet is the sum of β–strand and β–bridge

5.3.5 Impact of pentapeptides on the intra-residue interactions, D23–K28 salt bridge, and solvent-accessible surface area (SASA) of $A\beta_{42}$ monomer

A comparison between the intramolecular side-chain contacts observed in $A\beta_{42}$ monomer and $A\beta_{42}$ monomer–pentapeptides complexes highlights significant changes in the side-chain contacts of the residues of N-terminal, CHC, mid-domain, and C-terminal regions (**Figure 5.13**). In the $A\beta_{42}$ monomer, side-chain contacts were observed between the N-terminal and CHC (17-21) regions. Notably, the mid-domain (26-32) residues interacted with the C-terminal (34-42) residues of $A\beta_{42}$ monomer. Previous studies reported that the interactions between CHC/mid-domain and C-terminal regions play an important role in the early self-assembly of $A\beta_{42}$ monomer.[60] The side-chain contacts between CHC/mid-domain and C-terminal regions in the $A\beta_{42}$ monomer disappear with the addition of RIIGL. On the incorporation of RVVPI in $A\beta_{42}$ monomer, the side chain contacts between the mid-domain (26-32) and C-terminal (34-42) regions were significantly reduced highlighting the lower aggregation propensity of $A\beta_{42}$ monomer in the presence of RVVPI. We note that the intra-residue contacts between N-terminal (1-7) and N-terminal/CHC regions observed in $A\beta_{42}$ monomer become less abundant in $A\beta_{42}$ monomer–RIAPA.

On the incorporation of RLAPV in the $A\beta_{42}$ monomer, few side-chain contacts were noted between N-terminal (1-9) and C-terminal (34-40) regions. However, the contacts between CHC (17-22)/mid-domain (26-32) and C-terminal (34-42) regions were reduced, although to a lesser extent as compared to RVVPI, in the $A\beta_{42}$ monomer on the incorporation of RLAPV highlighting the lower aggregation propensity of $A\beta_{42}$ monomer on the addition of RLAPV.

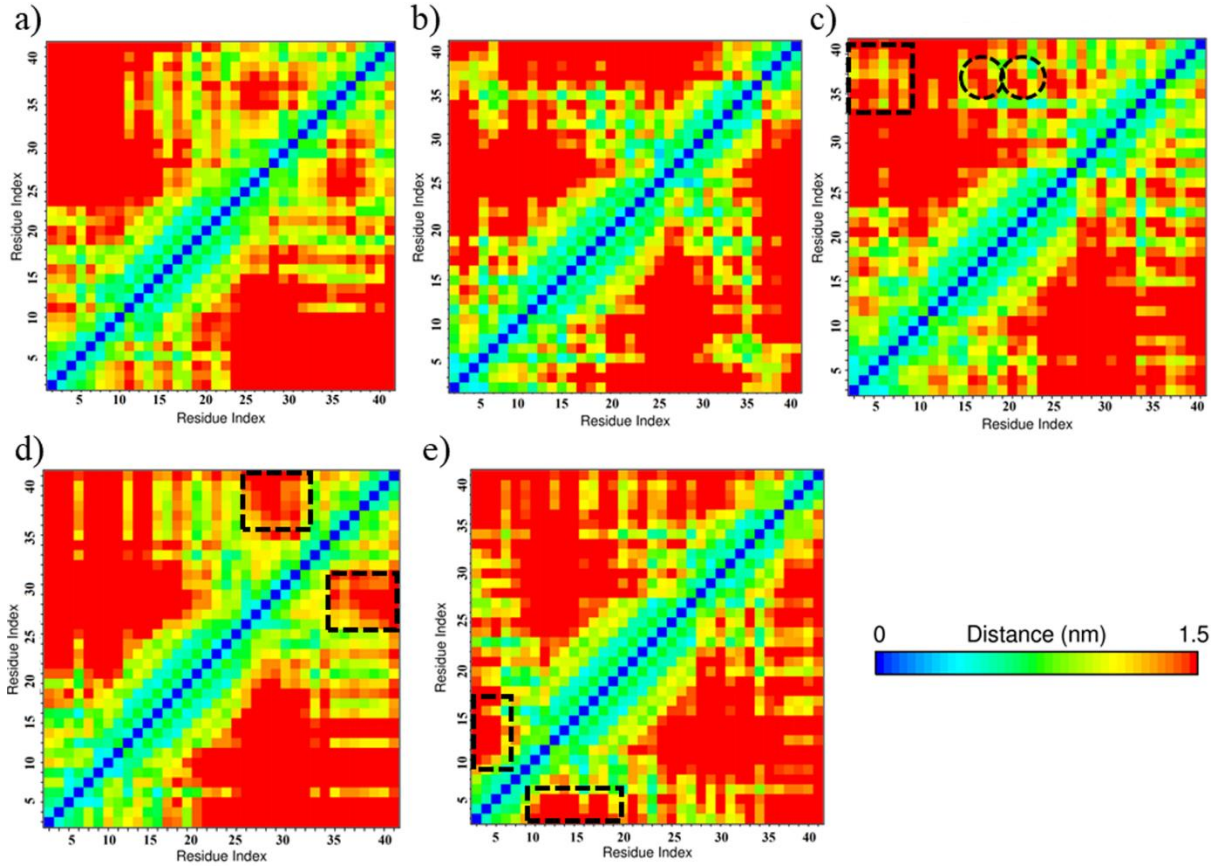

Figure 5.13: Side chain-side chain contacts between $A\beta_{42}$ residues in $A\beta_{42}$ monomer, $A\beta_{42}$ monomer–RIIGL, $A\beta_{42}$ monomer–RLAPV, $A\beta_{42}$ monomer–RVVPI, and $A\beta_{42}$ monomer–RIAPA are shown in panel (a-e), respectively.

The SASA was evaluated to examine the hydrophobic contacts in $A\beta_{42}$ monomer in the absence and presence of pentapeptides (**Figure 5.14a**). The residue-wise SASA analysis highlighted lower SASA values of the hydrophobic residues of $A\beta_{42}$ monomer in the presence of pentapeptides. In comparison to $A\beta_{42}$ monomer alone, the following hydrophobic residues displayed lower SASA values in the $A\beta_{42}$ monomer–pentapeptides complexes: (*i*) F4, I31, M35, V36 for $A\beta_{42}$ monomer–RIIGL (*ii*) I31, V40 for $A\beta_{42}$ monomer–RLAPV (*iii*) F4, F20, V24, A30, L34, V40 for $A\beta_{42}$ monomer–RVVPI, and (*iv*) F20, V24, A30, L34 for $A\beta_{42}$ monomer–RIAPA. The decrease in the SASA of hydrophobic residues on the incorporation of pentapeptides highlights the low propensity of $A\beta_{42}$ monomer for the self-aggregation to form neurotoxic oligomers. In the case of $A\beta_{42}$ monomer–RVVPI, the maximum number of hydrophobic residues displayed lower SASA as compared to $A\beta_{42}$ monomer, which indicates the significant inhibitory potential of RVVPI against $A\beta_{42}$ aggregation.

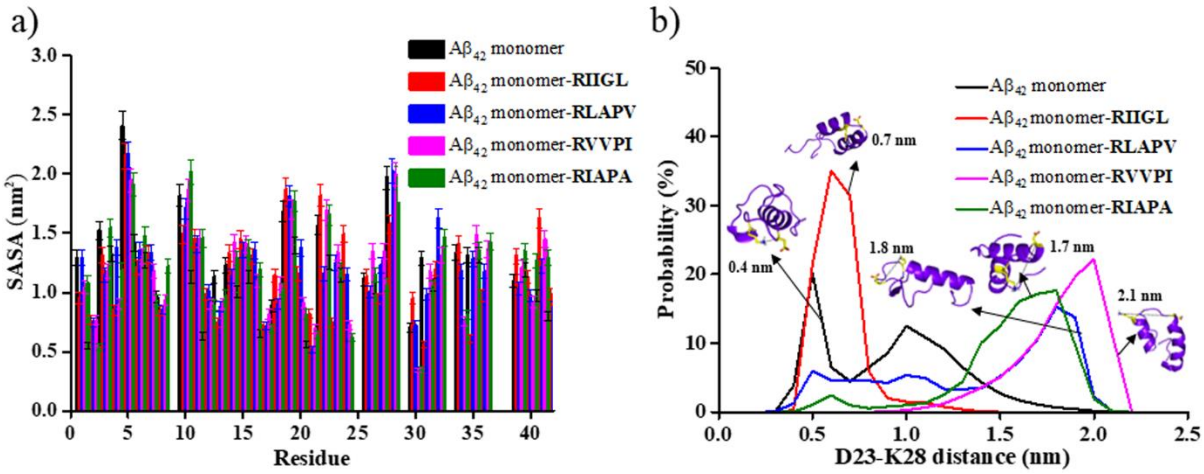

Figure 5.14: Residue-wise SASA (panel a) and the probability of D23-K28 salt bridge interaction (panel b) in the Aβ42 monomer with and without pentapeptides.

The intramolecular D23–K28 salt bridge in Aβ42 monomer is considered to be involved in oligomer stability and Aβ42 fibril formation.[61] Previous studies reported that the stability of the D23–K28 salt bridge plays a key role in the conformation conversion and fibrillation of Aβ42 monomer.[62] To analyze whether the interaction between Aβ42 monomer and pentapeptide affects the formation of the D23–K28 salt bridge, the interatomic distance between Cγ (D23)–Nξ (K28) was evaluated (Fig. 10b). Previous studies reported that a salt bridge is formed when the distance between Cγ (D23)–Nξ (K28) is less than 0.50 nm.[63] The distance distribution curve depicted a peak at 0.40 nm having a high probability and another peak at ~0.90 nm with a low probability in Aβ42 monomer. The distance peak at ~0.40 nm indicates D23–K28 salt bridge interaction (**Figure 5.14b**). In the case of Aβ42 monomer–RIIGL, the percentage population of conformations having salt bridge interaction between D23 and K28 increased significantly at distance greater than 0.50 nm. Notably, only one distant peak centered at 2.1 nm was observed in Aβ42 monomer–RVVPI, whereas two distant peaks centered at 1.7 nm and 0.6 nm were noted in Aβ42 monomer–RIAPA, which, in turn, depicts the disruption of salt bridge interaction and hence, lower aggregation propensity of Aβ42 monomer in the presence of RVVPI and RIAPA.

5.3.6 Impact of pentapeptides on FEL of Aβ42 monomer

To examine the conformational states of the Aβ42 monomer and Aβ42 monomer–pentapeptide complexes, Gibbs FEL was plotted using the first two principal components, *i.e.*, PC1 and PC2 as reaction coordinates, along with free energy as the third reaction coordinate. In the FEL map,

the meta-stable conformational states are represented by cyan and green regions, and the free energy minima are represented by purple area (**Figure 5.15**). The FEL of $A\beta_{42}$ monomer was noted to be broader than $A\beta_{42}$ monomer–pentapeptide complexes, which indicates higher conformational heterogeneity.

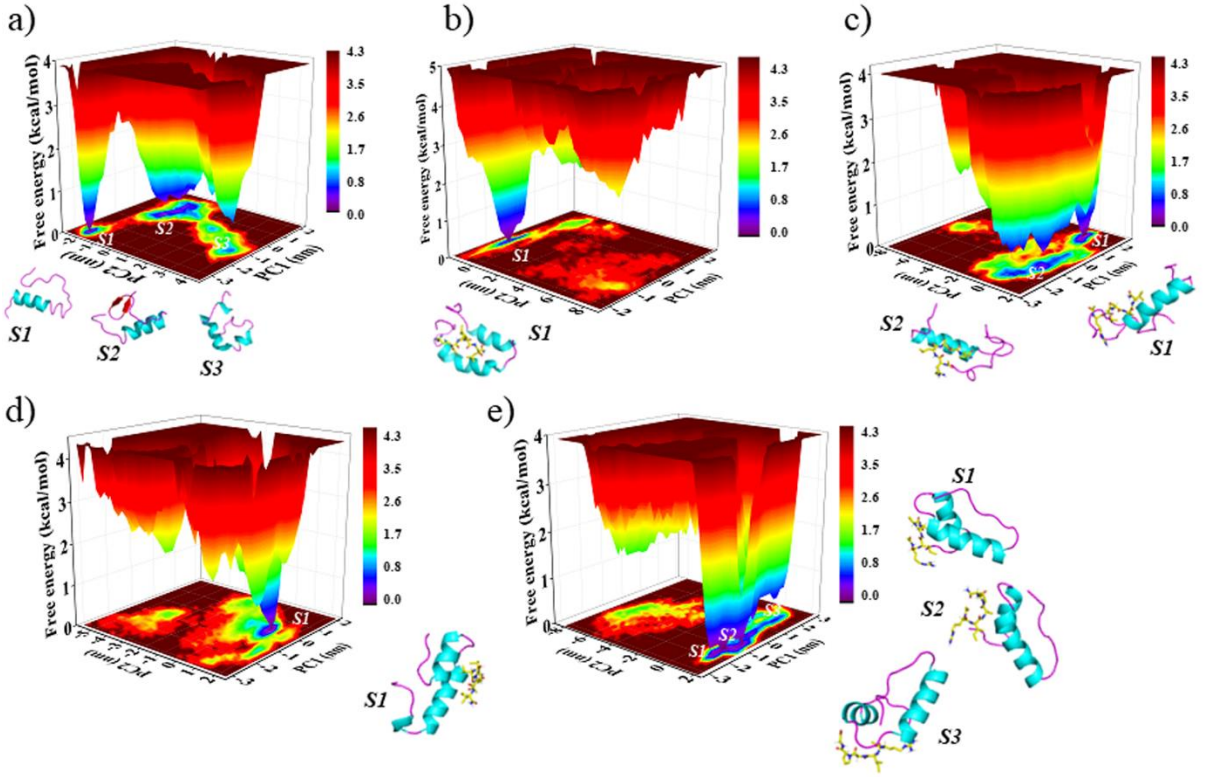

Figure 5.15: FEL of $A\beta_{42}$ monomer alone (panel a) and in the presence of RIIGL (panel b), RLAPV (panel c), RVVPI (panel d), and RIAPA (panel e). The minimum energy conformations extracted from the FEL are depicted in the cartoon.

In comparison to the three minimum energy basins in $A\beta_{42}$ monomer, a single dominant minimum energy basin was noted in $A\beta_{42}$ monomer–RIIGL, and $A\beta_{42}$ monomer–RVVPI complexes (**Figure 5.15b, d**), which, in turn, highlight less conformational diversity in $A\beta_{42}$ monomer on the incorporation of RIIGL and RVVPI.

The secondary structural statistics of the minimum energy conformation derived from the FEL of the simulated systems are listed in **Table 5.10**. For $A\beta_{42}$ monomer, the minimum energy conformation *S1–S3* sampled 30–31% helix, 6–11% β–sheet, 28–31% coil, 15–21% bend, and 13–18% turn content. Notably, enhanced sampling of helix conformation (52–55%) was observed in the energetically favoured conformations of $A\beta_{42}$ monomer–RIIGL, $A\beta_{42}$ monomer–RVVPI, and $A\beta_{42}$ monomer–RIAPA complexes (**Fig. 5.15b, d, e**). The β–sheet

content is noted to be 5% for *S1* conformation in $A\beta_{42}$ monomer–RIIGL and, 10% and 5% for *S1* and *S2* conformation, respectively, in $A\beta_{42}$ monomer–RLAPV. Remarkably, a complete absence of β–sheet content was observed in $A\beta_{42}$ monomer–RVVPI and $A\beta_{42}$ monomer–RIAPA complexes (**Table 5.10**), which depict the prevention of conformational transition of $A\beta_{42}$ monomer in the presence of RVVPI and RIAPA. The absence of the β–sheet and notably higher sampling of helical conformation lower the aggregation propensity of $A\beta_{42}$ monomer in the presence of RVVPI and RIAPA.

Table 5.10: Secondary structure composition of the representative conformations extracted from the FEL of simulated systems.

Model system	conformation	helix[b]	β-sheet[a]	coil	bend	turn
$A\beta_{42}$ monomer	*S1*	30	11	31	15	13
	S2	30	6	25	21	18
	S3	31	8	28	15	18
$A\beta_{42}$ monomer–RIIGL	*S1*	52	5	14	24	5
$A\beta_{42}$ monomer–RLAPV	*S1*	33	10	19	24	14
	S2	33	5	26	17	19
$A\beta_{42}$ monomer–RVVPI	*S1*	52	0	26	10	12
$A\beta_{42}$ monomer–RIAPA	*S1*	55	0	29	12	4
	S2	52	0	33	7	8
	S3	52	0	31	12	5

[a]β–sheet is the sum of β–strand and β-bridge; [b]helix is the sum of α–, π– and 3_{10} helix

5.4 Conclusions

A library of 912 pentapeptides was generated by mutating the amino acids in RIIGL using computational methods. The molecular docking-based virtual screening followed by binding free energy calculations by MM-PBSA predicted RLAPV, RVVPI, and RIAPA as strong binders to $A\beta_{42}$ monomer as well as stabilizing $A\beta_{42}$ monomer in the helical conformation. The binding free energy analysis revealed that intermolecular electrostatic interactions govern the binding of pentapeptides with $A\beta_{42}$ monomer, and pentapeptides containing arginine bind more strongly with $A\beta_{42}$ monomer as compared to histidine-containing pentapeptides due to electrostatic interactions of arginine with negatively charged residues of $A\beta_{42}$ monomer. The secondary structure analysis highlighted that the β–sheet content decreased to 4% in $A\beta_{42}$ monomer–RIIGL and 5% in $A\beta_{42}$ monomer–RLAPV as compared to 8% sampled in the $A\beta_{42}$ monomer, and interestingly, no β–sheet was sampled in $A\beta_{42}$ monomer–RVVPI and $A\beta_{42}$

monomer–RIAPA complexes. The minimum energy conformation derived from the FEL highlighted the complete absence of β–sheet content in $A\beta_{42}$ monomer–RVVPI and $A\beta_{42}$ monomer–RIAPA complexes, which depict the prevention of conformational transition of $A\beta_{42}$ monomer in the presence of RVVPI and RIAPA. The MD simulations predicted RVVPI and RIAPA as potential inhibitors of $A\beta_{42}$ aggregation. In the future, experimental studies of top hit pentapeptides as therapeutic candidates against $A\beta_{42}$ aggregation should further corroborate the computational findings.

5.5 References

1. (a) Abbott, A. Could drugs prevent Alzheimer's? These trials aim to find out. *Nature* **2022**, *603*, 216–219; (b) Cummings, J.; Lee, G.; Nahed, P.; Kambar, M. E. Z. N.; Zhong, K.; Fonseca, J.; Taghva, K. Alzheimer's disease drug development pipeline: 2022, *Alzheimer's Dementia* **2022**, *8*, No. e12295; (c) Huang, L-K.; Chao, S-P.; Hu, C-J.; Clinical trials of new drugs for Alzheimer disease, *J. Biomed. Sci*. **2020**, *27*, 18.

2. Gauthier, S.; Rosa-Neto, P.; Morais, J. A.; Webster, C. World Alzheimer Report 2021: Journey through the diagnosis of dementia, London, England: Alzheimer's Disease International. 2021.

3. Ryan, P.; Patel, B.; Makwana, V.; Jadhav, H. R.; Kiefel, M.; Davey, A.; Reekie, T. A.; Rudrawar, S.; Kassiou, M. Peptides, peptidomimetics, and carbohydrate–peptide conjugates as amyloidogenic aggregation inhibitors for Alzheimer's disease. *ACS Chem. Neurosci.* **2018**, *9*, 1530–1551.

4. Holtzman, D. M. Alzheimer's disease: Moving towards a vaccine. *Nature*, **2008**, *454*, 418–420.

5. Nerelius, C.; Sandegren, A.; Sargsyan, H.; Raunak, R.; Leijonmarck, H.; Chatterjee, U.; Fisahn, A.; Imarisio, S.; Lomas, D. A.; Crowther, D. C.; Strömberg, R. α-Helix targeting reduces amyloid-β peptide toxicity. *Proc. Natl. Acad. Sci. U.S.A.* **2009**, *106*, 9191–9196.

6. (a) Tonali, N.; Dodero, V. I.; Kaffy, J.; Hericks, L.; Ongeri, S.; Sewald, N. Real-time BODIPY-binding assay to screen inhibitors of the early oligomerization process of Aβ1–42 peptide. *ChemBioChem* **2020**, *21*, 1129–1135; (b) Tonali, N.; Kaffy, J.; Soulier, J. L.; Gelmi, M. L.; Erba, E.; Taverna, M.; Heijenoort, C. van; Ha-Duong, T.; Ongeri, S. Structure-activity relationships of β-hairpin mimics as modulators of amyloid β-peptide aggregation. *Eur. J. Med. Chem*. **2018**, *154*, 280–293; (c) Pellegrino, S.; Tonali, N.; Erba, E.; Kaffy, J.; Taverna, M.; Contini, A.; Taylor, M.; Allsop, D.; Gelmi, M. L.; Ongeri, S. β-Hairpin mimics containing a piperidine–pyrrolidine scaffold modulate the β-amyloid aggregation process preserving the monomer species. *Chem. Sci.* **2017**, *8*, 1295–1302; (d) Kaffy, J.; Brinet, D.; Soulier, J. L.; Correia, I.; Tonali, N.; Fera, K. F.; Iacone, Y.; Hoffmann, A. R.; Khemtémourian, L.; Crousse, B.; Taylor, M. Designed glycopeptidomimetics disrupt protein–protein interactions mediating amyloid β-peptide aggregation and restore neuroblastoma cell viability. *J. Med. Chem*. **2016**, *59*, 2025–2040.

7. (a) Bernstein, S. L.; Dupuis, N. F.; Lazo, N. D.; Wyttenbach, T.; Condron, M. M.; Bitan, G.; Teplow, D. B.; Shea, J. E.; Ruotolo, B. T.; Robinson, C. V.; Bowers, M. T. Amyloid-β protein oligomerization and the importance of tetramers and dodecamers in the aetiology of Alzheimer's disease. *Nat. Chem*. **2009**, *1*, 326–331; (b) Economou, N. J.; Giammona, M. J.; Do, T. D.; Zheng, X.; Teplow, D. B.; Buratto, S. K.; Bowers, M. T. Amyloid β-protein assembly and Alzheimer's disease: dodecamers of $A\beta_{42}$, but not of $A\beta_{40}$, seed fibril formation. *J. Am. Chem. Soc*. **2016**, *138*, 1772–1775; (c) Lee, S. J. C.; Nam, E.; Lee, H. J.; Savelieff, M. G.; Lim, M. H. Towards an understanding of amyloid-β oligomers: characterization, toxicity mechanisms, and inhibitors. *Chem. Soc. Rev.* **2017**, *46*, 310–323; (d) Yan, Y.; Wang, C. $A\beta_{42}$ is more rigid than $A\beta_{40}$ at the C terminus: implications for Aβ aggregation and toxicity. *J. Mol. Biol.* **2006**, *364*, 853–862.

8. (a) Nguyen, P.; Derreumaux, P. Understanding amyloid fibril nucleation and Aβ oligomer/drug interactions from computer simulations. *Acc. Chem. Res*. **2014**, *47*, 603–611; (b) Zhuang, W.; Sgourakis, N. G.; Li, Z. Y.; Garcia, A. E.; Mukamel, S. Discriminating early stage $A\beta_{42}$ monomer structures using chirality-induced 2DIR spectroscopy in a simulation study. *Proc. Natl. Acad. Sci. U.S.A*. **2010**, *107*, 15687–15692.

9. (a) Baweja, L.; Balamurugan, K.; Subramanian, V.; Dhawan, A. Effect of graphene oxide on the conformational transitions of amyloid β peptide: A molecular dynamics simulation study. *J. Mol. Graph. Model*. **2015**, *61*, 175–185; (b) Gera, J.; Szogi, T.; Bozso, Z.; Fulop, L.; Barrera, E. E.; Rodriguez, A. M.; Enriz, R.D. Searching for improved mimetic peptides inhibitors preventing conformational transition of amyloid-β_{42} monomer. *Bioorg. Chem.* **2018**, *81*, 211–221; (c) Liu, F. F.; Ji, L.; Zhang, L.; Dong, X. Y.; Sun, Y. Molecular basis for polyol–induced protein stability revealed by molecular dynamics simulations. *J. Chem. Phys.* **2010**, *132*, 225103; (d) Shen, H. C.; Ding, J. Y.; Li, L.; Liu, F. F. Effect of Y220C mutant on the conformational transition of p53C probed by molecular dynamics simulation. *Acta. Phys. Sin*. **2016**, *32*, 2620–2627; (e) Shuaib, S.; Goyal, B. Scrutiny of the mechanism of small molecule inhibitor preventing conformational transition of amyloid β_{42} monomer: Insights from molecular dynamics simulations. *J. Biomol. Struct. Dyn*. **2018**, *36*, 663–678.

10. (a) Mager, P. P.; Reinhardt, R.; Fischer, K. Molecular simulation to aid in the understanding of the Aβ(1–42) peptide of Alzheimer's disease. *Mol. Simul*. **2001**, *26*, 367–379; (b) Tjernberg, L. O.; Naslund, J.; Lindqvist, F.; Johansson, J.; Karlstrom, A. R.; Thyberg, J.; Nordstedt, C. Arrest of β-amyloid fibril formation by a pentapeptide ligand. *J. Biol. Chem*. **1996**, *271*, 8545–8548; (c) Tjernberg, L. O.; Lilliehook, C.; Callaway, D. J.; Naslund, J.; Hahne, S.; Thyberg, J.; Nordstedt, C. Controlling amyloid β-peptide fibril formation with protease-stable ligands. *J. Biol. Chem*. **1997**, *272*, 12601–12605; (d) Watanabe, K.; Nakamura, K.; Akikusa, S.; Okada, T.; Kodaka, M.; Konakahara, T.; Okuno, H. Inhibitors of fibril formation and cytotoxicity of β-amyloid peptide composed of KLVFF recognition element and flexible hydrophilic disrupting element. *Biochem. Biophys. Res. Commun*. **2002**, *290*, 121–124; (e) Watanabe, K.; Segawa, T.; Nakamura, K.; Kodaka, M.; Konakahara, T.; Okuno, H. Identification of the molecular interaction site of amyloid β peptide by using a fluorescence assay. *J. Pept. Res*. **2001**, *58*, 342–346.

11. Juneja, A.; Ito, M.; Nilsson, L. Implicit solvent models and stabilizing effects of mutations and ligands on the unfolding of the amyloid β-peptide central helix. *J. Chem. Theory Comput.* **2013**, *9*, 834–846.

12. (a) Chen, Y.; Li, X.; Zhan, C.; Lao, Z.; Li, F.; Dong, X.; Wei, G. A comprehensive insight into the mechanisms of dopamine in disrupting Aβ protofibrils and inhibiting Aβ aggregation. *ACS Chem. Neurosci*. **2021**, *12*, 4007−4019; (b) Gong, Y.; Zhan, C.; Zou, Y.; Qian, Z.; Wei, G.; Zhang, Q. Serotonin and melatonin show different modes of action on $A\beta_{42}$ protofibril destabilization. *ACS Chem. Neurosci*. **2021**, *12*, 799–809; (c) Zhang, Y.; Zhang, D.; Tang, Y.; Ren, B.; Liu, F.; Xu, L.; Chang, Y.; Zheng, J. Aromadendrin: A dual amyloid promoter to accelerate fibrillization and reduce cytotoxicity of both amyloid−β and hIAPP. *Mater. Adv*. **2020**, *1*, 1241−1252; (d) Zhan, C.; Chen, Y.; Tang, Y.; Wei, G. Green tea extracts EGCG and EGC display distinct mechanisms in disrupting

$A\beta_{42}$ protofibril. *ACS Chem. Neurosci*. **2020**, *11*, 1841–1851; (e) Fan, Q.; Liu, Y.; Wang, X.; Zhang, Z.; Fu, Y.; Liu, L.; Wang, P.; Ma, H.; Ma, H.; Seeram, N. P.; Zheng, J.; Zhou, F. Ginnalin a inhibits aggregation, reverses fibrillogenesis, and alleviates cytotoxicity of amyloid−β(1−42). *ACS Chem. Neurosci*. **2020**, *11*, 638–647; (f) Kaushik, A. C.; Kumar, A.; Peng, Z.; Khan, A.; Junaid, M.; Ali, A.; Bharadwaj, S.; Wei, D.-Q. Evaluation and validation of synergistic effects of amyloid-beta inhibitor–gold nanoparticles complex on Alzheimer's disease using deep neural network approach. *J. Mater. Res*. **2019**, *34*, 1845−1853; (g) Hou, S.; Gu, R.-X.; Wei, D.-Q. Inhibition of β–amyloid channels with a drug candidate wgx–50 revealed by molecular dynamics simulations. *J. Chem. Inf. Model*. **2017**, *57*, 2811–2821; (h) Fan, H.-M.; Gu, R.-X.; Wang, Y.-J.; Pi, Y.-L.; Zhang, Y.-H.; Xu, Q.; Wei, D.-Q. Destabilization of Alzheimer's $A\beta_{42}$ protofibrils with a novel drug candidate wgx–50 by molecular dynamics simulations. *J. Phys. Chem. B* **2015**, *119*, 11196−11202; (i) Tang, M.; Wang, Z.; Zhou, Y.; Xu, W.; Li, S.; Wang, L.; Wei, D.-Q.; Qiao, Z. A novel drug candidate for Alzheimer's disease treatment: gx–50 derived from *Zanthoxylum Bungeanum*. *J. Alzheimer's Dis*. **2013**, *34*, 203–213.

13. (a) Ren, B.; Tang, Y.; Zhang, D.; Liu, Y.; Zhang, Y.; Chen, H.; Hu, R.; Zhang, M.; Zheng, J. Conformational-specific self-assembled peptides as dual-mode, multi-target inhibitors and detectors for different amyloid proteins. *J. Mater. Chem. B* **2022**, *10*, 1754−1762; (b) Wang, L.; Wang, N.; Zhang, W.; Cheng, X.; Yan, Z.; Shao, G.; Wang, Xi.; Wang, R.; Fu, C. Therapeutic peptides: current applications and future directions. *Sig. Transduct. Target. Ther*. **2022**, *7*, 48; (c) Goyal, D.; Shuaib, S.; Mann, S.; Goyal, B. Rationally designed peptides and peptidomimetics as inhibitors of amyloid–β (Aβ) aggregation: Potential therapeutics of Alzheimer's disease. *ACS Comb. Sci*. **2017**, *19*, 55−80.

14. (a) Bhattacharjee, S.; Bhattacharyya, R. PRFF peptide mimic interferes with toxic fibrin–$A\beta_{42}$ interaction by emulating the Aβ binding interface on fibrinogen. *ACS Chem. Neurosci*. **2021**, *12*, 4144–4152; (b) Lei, L.; Zou, Z.; Liu, J.; Xu, Z.; Fu, Y.; Tian, Y.; Zhang, W. Multifunctional peptide-assembled micelles for simultaneously reducing amyloid–β and reactive oxygen species. *Chem. Sci*. **2021**, *12*, 6449; (c) Roy, R.; Pradhan, K.; Khan, J.; Das, G.; Mukherjee, N.; Das, D.; Ghosh, S. Human serum albumin-inspired glycopeptide-based multifunctional inhibitor of amyloid–β toxicity. *ACS Omega* **2020**, *5*, 18628–18641; (d) Mondal, P.; Khan, J.; Gupta, V.; Ghosh, S. *In silico* approach for designing potent neuroprotective hexapeptide. *ACS Chem. Neurosci*. **2019**, *10*, 3018–3030.

15. Mitra, A.; Sarkar, N. Sequence and structure-based peptides as potent amyloid inhibitors: a review. *Arch. Biochem. Biophys*. **2020**, *695*, 108614–108624.

16. Khalili Samani, E.; Mofid, M. R.; Malakoutikhah, M. The effect of terminal groups and halogenation of KLVFF peptide on its activity as an inhibitor of β-amyloid aggregation. *J. Pept. Sci*. **2020**, *26*, e3227.

17. (a) Jarrett, J. T.; Berger, E. P.; Lansbury, P. T. The carboxy terminus of the β amyloid protein is critical for the seeding of amyloid formation: implications for the pathogenesis of Alzheimer's disease. *Biochemistry* **1993**, 32, 4693–4697; (b) Bansal, S.; Maurya, I. K.; Yadav, N.; Thota, C. K.; Kumar, V.; Tikoo, K.; Chauhan, V. S.; Jain, R. C-terminal fragment, $A\beta_{32–37}$, analogues protect against Aβ aggregation-induced toxicity. *ACS*

Chem. Neurosci. **2016**, *7*, 615–623; (c) Fradinger, E. A.; Monien, B. H.; Urbanc, B.; Lomakin, A.; Tan, M.; Li, H.; Spring, S. M.; Condron, M. M.; Cruz, L.; Xie, C. W.; Benedek, G. B. C-terminal peptides coassemble into $A\beta_{42}$ oligomers and protect neurons against $A\beta_{42}$-induced neurotoxicity. *Proc. Natl. Acad. Sci. U.S.A.* **2008**, *105*, 14175–14180; (d) Li, H.; Rahimi, F.; Bitan, G. Modulation of amyloid β-protein (Aβ) assembly by homologous C-terminal fragments as a strategy for inhibiting aβ toxicity. *ACS Chem. Neurosci*. **2016**, *7*, 845–856; (e) Dutta, M.; Mattaparthi, V. S. K. A comparative study to elucidate the inhibitory mechanism of a 6-mer fragment of amyloid-beta 42 peptide as a potential therapeutic in Alzheimer's disease. *Curr. Sci*. **2018**, *114*, 1207–1213.

18. Harkany, T.; Abraham, I.; Laskay, G.; Timmerman, W.; Jost, K.; Zarandi, M.; Penke, B.; Nyakas, C.; Luiten, P. G. Propionyl-IIGL tetrapeptide antagonizes β-amyloid excitotoxicity in rat nucleus basalis. *Neuroreport* **1999**, *10*, 1693–1698.

19. Fülöp, L.; Zarándi, M.; Datki, Z.; Soós, K.; Penke, B. β-Amyloid-derived pentapeptide RIIGLa inhibits $A\beta_{1-42}$ aggregation and toxicity. *Biochem. Biophys. Res. Commun*. **2004**, *324*, 64–69.

20. Schrödinger Release2018–1: Maestro, Schrödinger, LLC, New York, NY, 2018.

21. Crescenzi, O.; Tomaselli, S.; Guerrini, R.; Salvadori, S.; D'Ursi, A. M.; Temussi, P. A.; Picone, D. Solution structure of the Alzheimer amyloid β–peptide (1–42) in an apolar microenvironment–Similarity with a virus fusion domain. *Eur. J. Biochem*. **2002**, *269*, 5642–5648.

22. Dallakyan, S.; Olson, A. J. Small-molecule library screening by docking with PyRx. *Methods Mol. Biol.* **2015**, *1263*, 243–250.

23. Trott, O.; Olson, A. J. AutoDock vina: improving the speed and accuracy of docking with a new scoring function, efficient optimization and multithreading. *J. Comput. Chem.* **2010**, *31*, 455–461.

24. (a) Jones, C. L.; Njomen, E.; Sjogren, B.; Dexheimer, T. S.; Tepe, J. J. Small molecule enhancement of 20s proteasome activity targets intrinsically disordered proteins. *ACS Chem. Biol.* **2017**, *12*, 2240–2247; (b) Shaker, B.; Yu, M. S.; Lee, J.; Lee, Y.; Jung, C.; Na, D. User guide for the discovery of potential drugs via protein structure prediction and ligand docking simulation. *J. Microbiol.* **2020**, *58*, 235–244; (c) de Sousa, A. C. C.; Combrinck, J. M.; Maepa, K.; Egan, T. J. Virtual screening as a tool to discover new β–haematin inhibitors with activity against malaria parasites. *Sci. Rep.* **2020**, *10*, 3374.

25. Kumari, R.; Kumar, R.; Lynn, A. g_mmpbsa—A GROMACS tool for high–throughput MM–PBSA calculations. *J. Chem. Inf. Model.* **2014**, *54*, 1951–1962.

26. Genheden, S.; Ryde, U. The MM/PBSA and MM/GBSA methods to estimate ligand-binding affinities. *Expert Opin. Drug Discov.* **2015**, *10*, 449–461.

27. Huang, K.; Luo, S.; Cong, Y.; Zhong, S.; Zhang, J. Z. H.; Duan, L. An accurate free energy estimator: based on MM/PBSA combined with interaction entropy for protein–ligand binding affinity. *Nanoscale* **2020**, *12*, 10737–10750.

28. (a) Xie, L.; Luo, Y.; Lin, D.; Xi, W.; Yang, X.; Wei, G. The molecular mechanism of fullerene-inhibited aggregation of Alzheimer's β-amyloid peptide fragment. *Nanoscale* **2014**, *6*, 9752−9762; (b) Zhang, T.; Xu, W.; Mu, Y.; Derreumaux, P. Atomic and dynamic insights into the beneficial effect of the 1,4-Naphthoquinon-2-yl-L-tryptophan inhibitor on Alzheimer's Aβ1–42 dimer in terms of aggregation and toxicity. *ACS Chem. Neurosci.* **2014**, *5*, 148−159; (c) Zhang, T.; Zhang, J.; Derreumaux, P.; Mu, Y. Molecular mechanism of the inhibition of EGCG on the Alzheimer $A\beta_{1-42}$ dimer. *J. Phys. Chem. B* **2013**, *117*, 3993−4002; (d) Novick, P. A.; Lopes, D. H.; Branson, K. M.; Esteras-Chopo, A.; Graef, I. A.; Bitan, G.; Pande, V. S. Design of β-amyloid aggregation inhibitors from a predicted structural motif. *J. Med. Chem.* **2012**, *55*, 3002−3010; (e) Best, R. B.; Buchete, N. V.; Hummer, G. Are current molecular dynamics force fields too helical? *Biophys. J.* **2008**, *9*, L07–L09.

29. Abraham, M. J.; Murtola, T.; Schulz, R.; Páll, S.; Smith, J. C.; Hess, B.; Lindahl, E. GROMACS: High performance molecular simulations through multi–level parallelism from laptops to supercomputers. *SoftwareX* **2015**, *1–2*, 19–25.

30. Lin, Z. X.; Gunsteren, W. F. Refinement of the application of the GROMOS 54A7 force field to β–peptides. *J. Comput. Chem.* **2013**, *34*, 2796−2805.

31. (a) Jia, L.; Wang, W.; Yan, Y.; Hu, R.; Sang, J.; Zhao, W.; Wang, Y.; Wei, W.; Cui, W.; Yang, G.; Lu, F.; Zheng, J.; Liu, F. General aggregation-induced emission probes for amyloid inhibitors with dual inhibition capacity against amyloid β–protein and α–synuclein. *ACS Appl. Mater. Interfaces* **2020**, *12*, 31182–31194; (b) Xing, X.; Liu, C.; Ali, A.; Kang, B.; Li, P.; Ai, H. Novel disassembly mechanisms of sigmoid $A\beta_{42}$ protofibrils by introduced neutral and charged drug molecules. *ACS Chem. Neurosci.* **2020**, *11*, 45−56.

32. Somavarapu, A. K.; Kepp, K. P. The dependence of amyloid–β dynamics on protein force fields and water models. *ChemPhysChem* **2015**, *16*, 3278–3289.

33. (a) Gupta, S.; Dasmahapatra, A. K. Destabilization potential of phenolics on Aβ fibrils: Mechanistic insights from molecular dynamics simulation. *Phys. Chem. Chem. Phys.* **2020**, *22*, 19643–19658; (b) Pal, S.; Banerjee, S.; Kumar, A.; Prabhakaran, E. N. H–bond surrogate-stabilized shortest single-turn α–helices: sp^2 constraints and residue preferences for the highest α–helicities. *ACS Omega* **2020**, *5*, 13902–13912.

34. (a) Pasieka, A.; Panek, D.; Szałaj, N.; Espargaró, A.; Więckowska, A.; Malawska, B.; Sabaté, R.; Bajda, M. Dual inhibitors of amyloid−β and tau aggregation with amyloid−β disaggregating properties: Extended *in cellulo*, *in silico*, and kinetic studies of multifunctional anti-Alzheimer's agents. *ACS Chem. Neurosci.* **2021**, *12*, 2057−2068; (b) Brown, A. M.; Bevan, D. R. Molecular dynamics simulations of amyloid β−peptide (1−42): Tetramer formation and membrane interactions. *Biophys. J.* **2016**, *111*, 937–949.

35. Hess, B.; Bekker, H.; Berendsen, H. J. C.; Fraaije, J. G. E. M. LINCS: A linear constraint solver for molecular simulations. *J. Comput. Chem.* **1997**, *18*, 1463–1472.

36. Miyamoto, S.; Kollman, P. A. Settle: An analytical version of the SHAKE and RATTLE algorithm for rigid water models. *J. Comput. Chem.* **1992**, *13*, 952–962.

37. Essmann, U.; Perera, L.; Berkowitz, M. L.; Darden, T.; Lee, H.; Pedersen, L. G. A smooth particle mesh ewald method. *J. Chem. Phys.* **1995**, *103*, 8577.

38. Bussi, G.; Donadio, D.; Parrinello, M. Canonical sampling through velocity rescaling. *J. Chem. Phys.* **2007**, *126*, 014101.

39. Parrinello, M.; Rahman, A. Polymorphic transitions in single crystals: A new molecular dynamics method. *J. Appl. Phys.* **1981**, *52*, 7182.

40. (a) Han, B.; Liu, Y.; Ginzinger, W. S.; Wishart, S. D. SHIFTX2: Significantly improved protein chemical shift prediction. *J. Biomol. NMR* **2011**, *50*, 43–57; (b) Neal, S.; Nip, A. M.; Zhang, H.; Wishart, D. S. Rapid and accurate calculation of protein ^{1}H, ^{13}C and ^{15}N chemical shifts. *J. Biomol. NMR* **2003**, *26*, 215–240.

41. (a) Hou, L.; Shao, H.; Zhang, Y.; Li, H.; Menon, N. K.; Neuhaus, E. B.; Brewer, J. M.; Byeon, I. J. L.; Ray, D. G.; Vitek, M. P.; Iwashita, T. Solution NMR studies of the Aβ (1− 40) and Aβ (1− 42) peptides establish that the Met35 oxidation state affects the mechanism of amyloid formation. *J. Am. Chem. Soc.* **2004**, *126*, 1992–2005; (b) Walti, M. A.; Orts, J.; Vogeli, B.; Campioni, S.; Riek, R. Solution NMR studies of recombinant Aβ (1–42): from the presence of a micellar entity to residual β-Sheet structure in the soluble species. *ChemBioChem* **2015**, *16*, 659–669.

42. Karplus, M. Vicinal proton coupling in nuclear magnetic resonance. *J. Am. Chem. Soc.* **1963**, *85*, 2870–2871.

43. Pardi, A.; Billeter, M.; Wüthrich, K. Calibration of the angular dependence of the amide proton-Cα proton coupling constants, ^{3}JHNα, in a globular protein: use of ^{3}JHNα for identification of helical secondary structure. *J. Mol. Biol*. **1984**, *180*, 741−751.

44. Humphrey, W.; Dalke, A.; Schulten, K. VMD – Visual Molecular Dynamics. *J. Mol. Graphics Modell.* **1996**, *14*, 33−38.

45. DeLano, W.L. The PyMOL molecular graphics system, http://www.pymol.org, 2002.

46. (a) Daura, X.; Antes, I.; van Gunsteren, W. F.; Thiel, W.; Mark, A. E. The effect of motional averaging on the calculation of NMR-derived structural properties. *Proteins: Struct. Funct. Genet.* **1999**, *36*, 542–555; (b) Daura, X.; Gademann, K.; Jaun, B.; Seebach, D.; van Gunsteren, W.F.; Mark, A. E. Peptide folding: when simulation meets experiment. *Angew. Chem. Int. Ed.* **1999**, *38*, 236–240.

47. Kabsch, W.; Sander, C. Dictionary of protein secondary structure: pattern recognition of hydrogen–bonded and geometrical features. *Biopolymers* **1983**, *12*, 2577–2637.

48. (a) Kaur, A.; Goyal, D.; Goyal, B. An α-helix mimetic oligopyridylamide, ADH-31, modulates $A\beta_{42}$ monomer aggregation and destabilizes protofibril structures: Insights from molecular dynamics simulations. *Phys. Chem. Chem. Phys.* **2020**, *22*, 28055–28073; (b) Shuaib, S.; Saini, R. K.; Goyal, D.; Goyal, B. Insights into the inhibitory mechanism of dicyanovinyl-substituted J147 derivative against $A\beta_{42}$ aggregation and protofibril destabilization: a molecular dynamics simulation study. *ChemistrySelect* **2017**, *2*, 1645–1657.

49. Kanchi, P. K.; Dasmahapatra, A. K. Destabilization of the Alzheimer's amyloid-β peptide by a proline-rich β-sheet breaker peptide: a molecular dynamics simulation study. *J. Mol. Model.* **2021**, *27*, 356–369.

50. (a) Jamasbi, E.; Wade, J.D.; Separovic, F.; Hossain, M.A. Amyloid beta (Aβ) peptide and factors that play important roles in Alzheimer's disease. *Curr. Med. Chem.* **2016**, *23*, 884–892; (b) Morimoto, A.; Irie, K.; Murakami, K.; Masuda, Y.; Ohiga–shi, H.; Nagao, M.; Fukuda, H.; Shimizu, T.; Shirasawa, T. Analysis of the secondary structure of β–amyloid($A\beta_{42}$) fibrils by systematic proline replacement. *J. Biol. Chem.* **2004**, *279*, 52781–52788; (c) Hsu, F.; Park, G.; Guo, Z. F. Key residues for the formation of $A\beta_{42}$ amyloid fibrils. *ACS Omega* **2018**, *3*, 8401–8407.

51. Liu, F.; Du, W.; Sun, Y.; Zheng, J.; Dong, X. Atomistic characterization of binding modes and affinity of peptide inhibitors to amyloid–β protein. *Front. Chem. Sci. Eng.* **2014**, *8*, 433–444.

52. Wang, L.; Zeng, R.R.; Pang, X.Q.; Gu, Q.; Tan, W. The mechanisms of flavonoids inhibiting conformational transition of amyloid–β_{42} monomer: a comparative molecular dynamics simulation study. *RSC Adv.* **2015**, *5*, 66391–66402.

53. Paravastu, A. K.; Leapman, R. D.; Yau, W.-M.; Tycko, R. Molecular structural basis for polymorphism in Alzheimer's β–amyloid fibrils. *Proc. Natl. Acad. Sci. U.S.A.* **2008**, *105*, 18349−18354.

54. Perálvarez-Marín, A.; Mateos, L.; Zhang, C.; Singh, S.; Cedazo-Mínguez, A.; Visa, N.; Morozova-Roche, L.; Gräslund, A.; Barth, A. A. Influence of residue 22 on the folding, aggregation profile, and toxicity of the Alzheimer's amyloid β peptide. *Biophys. J.* **2009**, *97*, 277–285.

55. Kim, H.; Jang, C.; Yadav, D. K.; Kim, M. H. The comparison of automated clustering algorithms for resampling representative conformer ensembles with RMSD matrix. *J. Cheminform.* **2017**, *9*, 21.

56. Khatua, P.; Mondal, S.; Bandyopadhyay, S. Effects of metal ions on $A\beta_{42}$ peptide conformations from molecular simulation studies. *J. Chem. Inf. Model.* **2019**, *59*, 2879–2893.

57. (a) Barrow, C. J.; Yasuda, A.; Kenny, P. T.; Zagorski, M. G. Solution conformations and aggregational properties of synthetic amyloid β–peptides of Alzheimer's disease. Analysis of circular dichroism spectra. *J. Mol. Biol.* **1992**, *225*, 1075–1093; (b) Liu, F. F.; Dong, X. Y.; He, L.; Middelberg, A. P.; Sun, Y. Molecular insight into conformational transition of amyloid β–peptide 42 inhibited by (–)–epigallocatechin–3–gallate probed

by molecular simulations. *J. Phys. Chem. B* **2011**, *115*, 11879–11887; (c) Steckmann, T.; Bhandari, Y. R.; Chapagain, P. P.; Gerstman, B. S. Cooperative structural transitions in amyloid–like aggregation. *J. Chem. Phys.* **2017**, *46*, 135103.

58. Chiti, F.; Dobson, C. M. Protein misfolding, amyloid formation, and human disease: A summary of progress over the last decade. *Annu. Rev. Biochem.* **2017**, *86*, 27–68.

59. Fang, M.; Zhang, Q.; Wang, X.; Su, K.; Guan, P.; Hu, X. Inhibition mechanisms of (−)-epigallocatechin-3-gallate and genistein on amyloid-beta 42 peptide of Alzheimer's disease via molecular simulations. *ACS Omega* **2022**, *7*, 19665–19675.

60. (a) Yang, M.; Teplow, D. B. Amyloid β–protein monomer folding: free energy surfaces reveal alloform specific differences. *J. Mol. Biol.* **2008**, *384*, 450−464; (b) Urbanc, B.; Cruz, L.; Yun, S.; Buldyrev, S. V.; Bitan, G.; Teplow, D. B.; Stanley, H. E. *In silico* study of amyloid β–protein folding and oligomerization. *Proc. Natl. Acad. Sci. U.S.A.* **2004**, *101*, 17345–17350; (c) Coskuner, O.; Wise–Scira, O. Arginine and disordered amyloid–β peptide structures: molecular level insights into the toxicity in Alzheimer's disease. *ACS Chem. Neurosci.* **2013**, *4*, 1549–1558.

61. (a) Petkova, A. T.; Leapman, R. D.; Guo, Z. H.; Yau, W. M.; Mattson, M. P.; Tycko, R. Self–propagating, molecular–level polymorphism in Alzheimer's β–amyloid fibrils. *Science* **2005**, *307*, 262–265; (b) Tarus, B.; Straub, J. E.; Thirumalai, D. Dynamics of Asp23–Lys28 salt-bridge formation in $A\beta_{10–35}$ monomers. *J. Am. Chem. Soc.* **2006**, *128*, 16159–16168.

62. (a) Jahanbin, F.; Bozorgmehr, M. R.; Morsali, A.; Beyramabadi, S. A. The effect of different alcohols on the Asp23–Lys28 and Asp23–Ala42 salt bridges of the most effective peptide in Alzheimer's disease: Molecular dynamics viewpoints. *J. Mol. Graph. Model.* **2018**, *86*, 199–208; (b) Reddy, G.; Straub, J. E.; Thirumalai, D. Influence of preformed Asp23–Lys28 salt bridge on the conformational fluctuations of monomers and dimers of Aβ peptides with implications for rates of fibril formation. *J. Phys. Chem. B* **2009**, *113*, 1162–1172; (c) Sun, Y.; Xi, W.; Wei, G. Atomic–level study of the effects of O4 molecules on the structural properties of protofibrillar Aβ trimer: β–sheet stabilization, salt bridge protection, and binding mechanism. *J. Phys. Chem. B* **2015**, *119*, 2786–2794.

63. Yang, C.; Zhu, X.; Li, J.; Shi, R. Exploration of the mechanism for LPFFD inhibiting the formation of β-sheet conformation of Aβ (1-42) in water. *J. Mol. Model.* **2010**, *16*, 813–821.

Chapter 6

Exploring the impact of C-terminal based pentapeptides on the disassembly of pre-formed Aβ42 fibrils

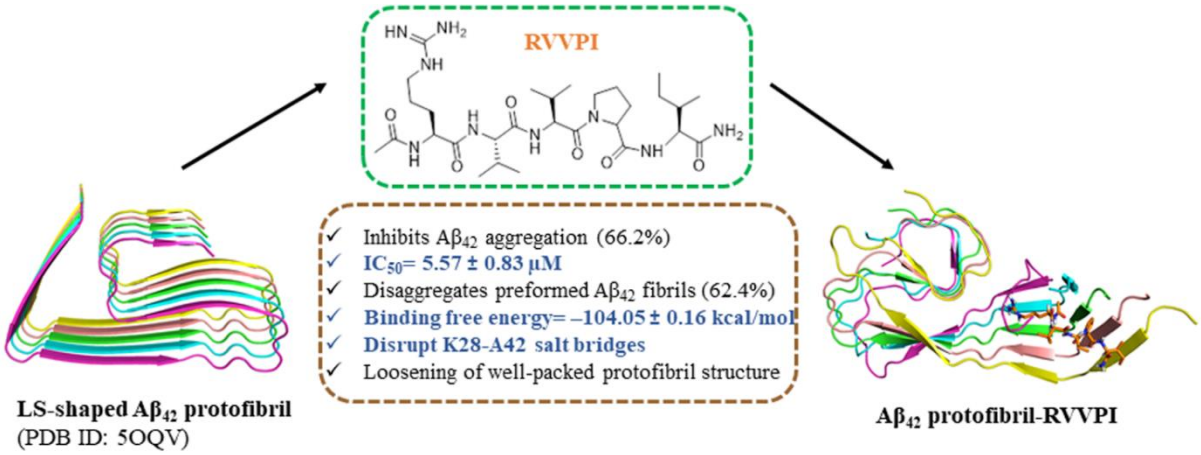

Rationally designed pentapeptide, RVVPI, displayed a more pronounced effect than RIIGL on the destabilization of the LS-shaped Aβ42 protofibril by reducing the sampling of β-sheets, lowering interchain hydrogen bonds, and disrupting K28-A42 salt bridges. ThT fluorescence results depicted that RVVPI exhibited significant inhibition of Aβ42 aggregation (Inhibition= 66.2%, IC_{50}= 5.57 ± 0.83 µM) and disassembly of pre-formed Aβ42 fibrils (62.4%).

6.1 Introduction

The misfolding of proteins and their subsequent aggregation to amyloids[1] are strongly correlated with several human amyloidosis like Alzheimer's disease (AD), amyotrophic lateral sclerosis, type II diabetes, Parkinson's disease *etc*.[2] AD is characterized as a progressive, chronic, prevalent in the geriatric population and widely pervasive neurodegenerative disorder, accounts for predominant portion of dementia cases globally, and its incidence is escalating at an uncontrollable pace.[3] Globally, ~55 million people are suffering with dementia with the prevision of becoming 78 million by 2030.[4]

The pathological hallmarks of AD comprises extracellular depositions of amyloid-β (Aβ)[5] and the intracellular formation of thread-like neurofibrillary tangles composed of tau protein.[6] The two Aβ isoforms, Aβ$_{40}$ and Aβ$_{42}$, are derived from the proteolysis of amyloid precursor protein (APP) by β- and γ-secretases in the amyloidogenic pathway.[7] The maturation of Aβ into fully developed fibrils is a nucleation-dependent comprising various steps that include the formation of protofibrils, neurotoxic soluble oligomers, and finally amyloid fibrils.[8] Increasing evidence suggests that initially formed soluble oligomeric assemblies of Aβ are the main cytotoxic species in AD.[9] Thus, strategies to halt or disrupt the generation of Aβ aggregates are effective therapeutic approaches against AD. These strategies involve hindering protein-protein interactions that lead to the formation of toxic Aβ aggregates or impeding the conformational shift of Aβ from its native disordered state to the aggregation susceptible β-sheet conformation.[10] Furthermore, the recent FDA approval of the humanized IgGI monoclonal antibody lecanemab for the treatment of AD in its initial stages has inspired the design and development of more efficacious inhibitors against Aβ aggregation.[11]

In recent decades, the development of peptide-based inhibitors against amyloid aggregation evoked significant interest due to their promising biocompatibility, low cytotoxicity, high target affinity, and specificity.[12,13] Particularly, arginine-rich peptides and peptides derived from the hydrophobic C-terminus of Aβ have been identified as potential modulators of Aβ aggregation.[12c,14] The literature studies depicted that the hydrophobic C-terminus of Aβ plays a dominant role in controlling its self-aggregation.[15] Benedek, Bitan and co-workers identified fragments Aβ(31-42) and Aβ(39-42) derived from the C-terminal region of Aβ as effective modulators of Aβ aggregation as well as cytotoxicity induced by Aβ aggregates.[16] Pike and co-workers reported that the Aβ$_{42}$ aggregation and its associated cytotoxicity was notably reduced on substituting M35 with Nle and replacing GLM(33-35) with VAA depicting key roles of these

residues in inducing Aβ aggregation and its associated cytotoxicity.[17] Jain et al. reported a hexapeptide (IGLMVG-NH_2) derived from C-terminal fragment Aβ(32-37) that completely alleviated the Aβ-mediated toxicity on the PC12 cells.[18]

Harkány et al. depicted propionyl-Ile-Ile-Gly-Leu amide (Pr-IIGL) derived from the tetrapeptide $Aβ_{31–34}$ region as an $Aβ_{42}$ aggregation inhibitor.[19] Pr-IIGL protected glial cells from $Aβ_{42}$ aggregates induced neurotoxicity, however, it displayed toxicity in neuroblastoma culture due to enhanced self-aggregation tendency imparted by the propionyl group. To avoid self-aggregation of Pr-IIGL, Fülöp et al. replaced the hydrophobic propionyl in Pr-IIGL with cationic arginine to yield $RIIGL_a$ with reduced self-aggregation propensity and increased solubility in aqueous media.[20] $RIIGL_a$ binds to neurotoxic Aβ aggregates and significantly reduced the cytotoxicity induced by fibrillar $Aβ_{42}$ in SHSY-5Y human neuroblastoma cells. Thus, RIIGL can be utilized as a tempting sequence to design Aβ aggregation modulators with enhanced efficacy.

In this regard, we previously employed a computational protocol comprising virtual screening, binding free energy calculations and molecular dynamics to screen top hit peptides from a designed library of 912 pentapeptides based on the RIIGL.[21] The integrated computational methodology predicted RVVPI and RIAPA as new peptides with notably enhanced ability to block $Aβ_{42}$ aggregation as compared to RIIGL.[21] However, the binding interactions of peptides (RIIGL, RVVPI, and RIAPA) on Aβ oligomers and their destabilization mechanism of Aβ protofibrils remains unclear. Thus, in this work, the ability of RIIGL, RVVPI, and RIAPA to destabilize $Aβ_{42}$ protofibril structure was illuminated by molecular dynamics (MD) simulations. To our best knowledge, no study illuminated the underlying mechanism of destabilization of cryo-EM resolved LS-shaped Aβ protofibrils (PDB ID: 5OQV) on the incorporation of RIIGL using MD simulations. To complement the computational results, the peptides were synthesized and their potential to block $Aβ_{42}$ aggregation and disaggregate $Aβ_{42}$ aggregates was evaluated using thioflavin T (ThT) and transmission electron microscopy (TEM). Furthermore, self-aggregation tendency of synthesized peptides RIIGL, RVVPI, RIAPA was evaluated using ThT and TEM assay.

6.2 Computational and experimental details

6.2.1 Molecular docking

The Aβ42 pentamer model chosen for molecular docking in this work is derived from the PDB ID: 5OQV.[22] For molecular docking of peptides with Aβ42 protofibril, the PDBQT files for both Aβ42 and peptides were generated using the PyRx tool.[23] Molecular docking was performed by AutoDock Vina.[24] The dimensions of the grid box were adjusted to encompass the Aβ42 protofibril-peptide complex. A search space exhaustiveness of 100 was selected to enhance the reliability of results. The docked poses of the peptides were clustered with an RMSD tolerance of 0.2 nm, and the poses were ranked according to their binding energy.

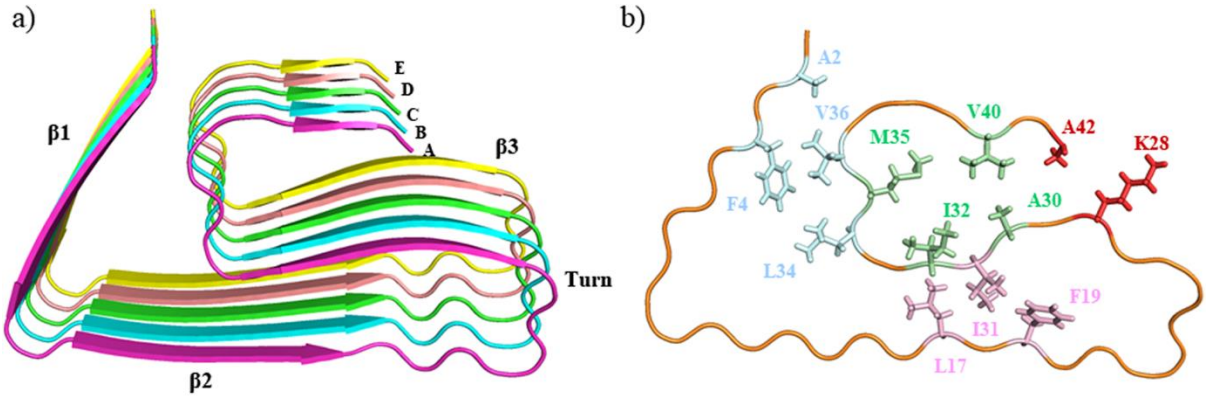

Figure 6.1: Cartoon representation of LS-shaped Aβ42 protofibril (PDB ID: 5OQV) depicting five chains denoted as A, B, C, D, and E (panel a). Structual details of a single chain of Aβ42 protofibril depicting hydrophobic core (core-1: A2, F4, L34 and V36; core-2: L17, F19 and I31; core-3: A30, I32, M35, and V40) and salt bridge (K28 and A42) residues (panel b).

6.2.2 MD simulations

The all-atom MD simulations were performed using GROMOS96 54a7 force field[25] in the presence of Simple Point Charge (SPC) water model[26] according to previous MD simulation studies[27] using GROMACS 5.0.1 package.[28] The GROMOS96 54a7 force field was chosen as it exhibits good α–β–coil symmetry and depict close proximity between observed and primary data of *J*–coupling ($^3J_{NH-H\alpha}$) constants.[29] Moreover, recent studies employed GROMOS96 54a7 force field to monitor the conformational changes in peptides.[30] To maintain electroneutrality, counter ions were included in the simulation box as required, and periodic boundary conditions were maintained throughout the simulations. The protonation states of amino acids were determined based on physiological pH. In each system, 150 mM NaCl was added in the cubic box with the requisite number of Na^+ and Cl^- ions to maintain electroneutrality at physiological pH. The MD simulations were executed employing the leap-frog stochastic dynamics integrator at a temperature of 310 K, and a relaxation time of 0.1 ps was applied. The bond lengths were constrained utilizing the LINCS algorithm.[31] The short-range van der Waals

forces were truncated at 1.0 nm, and long-range electrostatic forces were computed using the particle mesh Ewald (PME) method.[32] The systems were energy minimized using steepest descent algorithm followed by energy minimization employing conjugate gradient and then pre-equilibration for 500 ps in the *NVT* ensemble was conducted to ensure a constant temperature of 310 K.[33] In the subsequent stage, 500 ps simulation in the *NPT* ensemble was conducted using the Parrinello-Rahman barostat protocols[34] to ensure a constant temperature of 310 K and pressure of 1 atm. The simulations were run for 200 ns for each system with coordinates saving at a time step of 10 ps.

The trajectories from MD simulations were analyzed using a combination of Visual Molecular Dynamics (VMD),[35] GROMACS tools, and PyMOL.[36] For the initial assessment of the overall structural stability of the $A\beta_{42}$ protofibril with and without peptides, the gmx rms and gmx gyrate tools were employed to calculate the RMSD and R_g, respectively. To depict the stability of the salt bridges, the time occupancies of the salt bridges were assessed by determining the instances where the distances between the amino group of K28 and the carboxyl group of A42 were less than 0.32 nm. The impact of peptides on the secondary structure of $A\beta_{42}$ protofibril was assessed using the Dictionary of Secondary Structure of Proteins (DSSP) program by utilizing the gmx do_dssp tool.[37] The binding free energies of RIIGL, RVVPI, and RIAPA with $A\beta_{42}$ protofibril were computed by utilizing g_mmpbsa package[38] based on the molecular mechanics Poisson-Boltzmann surface area (MM-PBSA) method[39] according to our previous studies.[40] Furthermore, analysis of residue-specific binding free energy was conducted to evaluate the individual contributions of $A\beta_{42}$ protofibril residues in their interaction with peptides.

Table 6.1: System details for MD simulations.

System	Simulation time (ns)[b]	Box dimensions (nm)	SPC water molecules
control[a]	200 × 2	7.7 × 7.7 × 7.7	14517
RIIGL	200 × 1	7.7 × 7.7 × 7.7	14472
RVVPI	200 × 1	7.7 × 7.7 × 7.7	14477
RIAPA	200 × 1	7.7 × 7.7 × 7.7	14476

[a]control ($A\beta_{42}$ protofibril, PDB ID: 5OQV); [b]Simulations were performed using GROMOS96 54a7 force field with Simple Point Charge (SPC) water model

6.2.3 Solid-phase peptide synthesis

All chemicals were obtained from Sigma-Aldrich and were utilized as received without additional purification unless specifically indicated. Analytical-grade solvents were used for the synthesis without any additional purification. The solid-phase peptide synthesis (SPPS) method was employed for the synthesis of all peptides utilizing Fmoc-protected rink amide resin. The Fmoc-protected L-amino acids were utilized in the synthesis of peptides. The removal of Fmoc protection from rink amide resin was done using 35% piperidine in DMF. *In situ* activation of the Fmoc-protected amino acid was achieved by treating it with TBTU (6 equiv.) and DIPEA (6 equiv.) and then initial amino acid coupling to the resin was performed. Next, the amino acids were sequentially coupled, and Fmoc deprotection was performed using 35% piperidine in DMF. Subsequently, three equivalents each of Fmoc-protected amino acids, DIPEA, and HOBt were used as an activator base along with DMF as the solvent. The accomplishment of each coupling reaction was regularly confirmed through Kaiser's test. The steps of Fmoc removal and coupling were repeated using successive Fmoc-protected amino acids to generate the desired peptides attached to the resin. The synthesis of all sequences followed the same protocol. To release the synthesized peptides from the resin, a mixture of 5% water, 5% thioanisole, 82% TFA, 5% phenol, and 2.5% EDT (1,2-ethanedithiol) was used. The reaction proceeded with continuous shaking for 3 h using a vibrax shaker. After completion of the reaction, the resin suspension underwent filtration, and the collected filtrate was gradually added to cold diethyl ether to achieve thorough precipitation. Ultimately, the resulting precipitate was isolated through centrifugation at 4°C with a speed of 6000 rpm. To ensure purity, all peptides were purified utilizing a C-8 reversed-phase high-performance liquid chromatography (RP-HPLC) column. The characterization of the peptides was achieved through HRMS, and they were then stored in a freezer at –20°C for future applications.

6.2.4 Purification of peptides by HPLC and characterization

The preliminary purification of peptides (1 mg/mL) included dissolving them in a mixture of water and methanol (1:1; v/v), which was subsequently introduced into a preparative RP-HPLC system (Agilent Technologies 1260 Infinity series system). This process operated at 220 nm with a flow rate of 1 mL/min. The mobile-phase solvents A and B consisted of 0.1% TFA in acetonitrile (CH_3CN) and 0.1% TFA in water, respectively. The system was programmed to operate for 30 minutes, employing a linear gradient spanning from 10% to 70% of mobile-phase B. The pure peptide fractions were gathered and subsequently dissolved in a minimal

amount of t-butanol/water solution. The resulting solution underwent lyophilization, yielding a white powder with a fluffy texture.

Table 6.2: Data for the synthesized peptides, including sequence, structure, HRMS, and HPLC results.

Sequence	Mol. formula (Mol. weight)	HRMS data		HPLC data	
		Calcd.	Obsd.	t_R (min)	Purity (%)
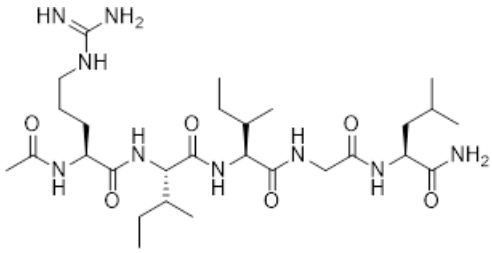 [Ac-Arg-Ile-Ile-Gly-Leu-NH_2]	$C_{28}H_{53}N_9O_6$ (611.4118)	612.4196	612.4199	3.57	100%
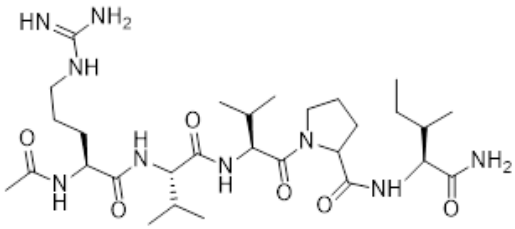 [Ac-Arg-Val-Val-Pro-Ile-NH_2]	$C_{29}H_{53}N_9O_6$ (623.8000)	624.4196	624.4197	3.48	100%
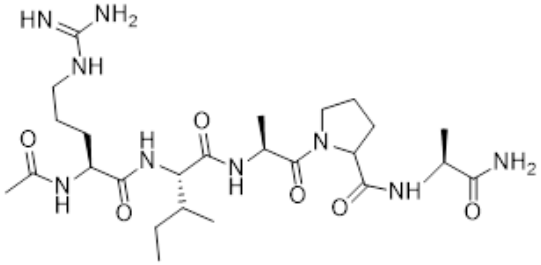 [Ac-Arg-Ile-Ala-Pro-Ala-NH_2]	$C_{25}H_{45}N_9O_6$ (567.6920)	568.3570	568.3586	3.52	95%

Analytical RP-HPLC (Thermo Scientific Dionex Ultimate 3000) was employed to assess the purity of peptides. This operated at 220 nm with a flow rate of 1 mL/min, employing the same mobile-phase solvent system as previously described. The system was operated for 10 minutes with a gradient ranging from 10% to 60% of mobile-phase B (0.1% TFA in water). The purity of the peptides was assessed and found to be in the range of 92% to 100% (**Table 6.2**). Subsequently, the peptides were characterized using high-resolution mass spectrometry (HRMS). HRMS (Q−Tof) m/z: calcd. For RIIGL ($C_{28}H_{53}N_9O_6$) $[M+H]^+$ 612.4196, found:

612.4199; HRMS (Q−Tof) m/z: calcd. For RVVPI ($C_{29}H_{53}N_9O_6$) $[M+H]^+$ 624.4196, found: 624.4197; HRMS (Q−Tof) m/z: calcd. For RIAPA ($C_{25}H_{45}N_9O_6$) $[M+H]^+$ 568.3570, found: 568.3586.

6.2.5 ThT assay

The detailed procedure of ThT assay was explained in our previous studies.[41] $A\beta_{42}$ was purchased from Anaspec and dissolved in 1,1,1,3,3,3-hexafluoro-2-propanol (HFIP). A stock solution of $A\beta_{42}$ (221.5 μM) was prepared by dissolving 0.1 mg of $A\beta_{42}$ peptide in 100 μL NaOH (10 mM) and the solution was stored at –20 °C. The stock solutions of synthesized peptides (2 mM) were prepared in DMSO. Simultaneously, a stock solution of ThT (1 mM) was made in 50 mM PBS buffer and was diluted to 200 μM.

For $A\beta_{42}$ aggregation assay, $A\beta_{42}$ (9 μL, 10 μM) and ThT (20 μL, 20 μM) with or without synthesized peptides (1:0, 1:0.25, 1:0.5, 1:1, 1:2, 1:4 and 1:6 molar ratio of $A\beta_{42}$:peptides) were diluted to 200 μL with 50 mM PBS buffer (pH 7.4) in 96 well plate and incubated at 37 °C for 24 h at constant agitation (180 rpm). For disaggregation of pre-formed $A\beta_{42}$ fibrils assay, $A\beta_{42}$ monomer was incubated at 37 °C for 24 h to generate fibrils, and later synthesized peptides were added to the aliquots of $A\beta_{42}$ fibrils and incubated for another 24 h under same conditions. SpectraMax M5^e spectrophotometer was utilized to measure the ThT emission intensities (excitation: 450 nm, emission: 485 nm). To determine the percentage inhibition the ThT emission data was fitted in the equation $(1–F_{sample}/F_{control})*100$.

6.2.6 Statistical analysis

All experiments were repeated and samples were analyzed in triplicate to ascertain the reproducibility of results. Graphs were generated using Microsoft Office Excel 2010, OriginPro 9.0, and GraphPad Prism 10. Data was presented as mean ± SEM.

6.2.7 TEM assay

TEM was employed to observe the fibrillary architect of $A\beta_{42}$ in the absence and presence of synthesized peptides. In this regard, $A\beta_{42}$ fibrils (10 μM) were co-incubated with peptides (20μM) in PBS buffer (50 mM) at 37 °C for 24 h. All the samples (2 μL) were dropcasted on carbon-coated copper grids (200 Mesh size) and then allowed to air dry for 30 minutes. Subsequently, all the grids were stained with a 1% potassium phosphotungstate (pH 7.2)

solution for 30 seconds and extra stain was drained with the use of kim wipes and allowed to dry at RT. The sample was loaded on the TEM grid holder and examined using a JEOL JEM-1400 microscope.

Table 6.3: Molecular docking analysis of pentapeptides with Aβ42 protofibril.

Peptide	AutoDock binding energy (kcal/mol)	Residues of Aβ42 protofibril participating in hydrogen bond interactions with pentapeptides		
		Residue	Atom[a]	Distance (nm)
RIIGL	–6.4	Glu22 (E)	NH:OC	0.28
		Asn27 (E)	CO:HN	0.19
RVVPI	–7.0	Phe20 (E)	CO:HN	0.24
		Glu22 (E)	CO:HN	0.30
		Lys28 (E)	CO:HN	0.23
RIAPA	–6.6	Phe20 (E)	NH:OC	0.30
		Glu22 (E)	CO:HN	0.23

[a]The atoms on the left correspond to Aβ42 protofibril, whereas on the right correspond to pentapeptides.

6.3 Results and discussion

6.3.1 Molecular docking of peptides with Aβ42 protofibril

The low molecular weight Aβ42 oligomers comprising tetramers, pentamers, and hexamers display enhanced toxicity to the neuronal cells and ultimately leads to synaptic dysfunction.[42] Thus, the ability of peptides (RIIGL, RVVPI, and RIAPA) to disassemble Aβ42 protofibril was investigated using pentamer derived from the cryo-EM Aβ42 fibrillar structure (PDB ID: 5OQV)[22] (**Figure 6.1**). The LS-shaped 5OQV structure constitute two intertwined protofibrils, tetramer and pentamer. The Aβ42 pentamer was chosen for molecular docking and MD simulations in this work as the importance of pentamer and hexamer oligomers was highlighted in previous studies. Cheon et al. performed MD simulations of Aβ peptide consisting of varying chain lengths (Number of chains= 1, 2, 3, 4, 5, 6, 7, 8, 10, and 12).[43] From the structures observed in the MD simulations, two characteristic oligomer sizes emerged, trimer and paranuclei, which generated distinct structural patterns during fibrillization. The study highlighted that Aβ17–42 pentamer and hexamer oligomers, called paranuclei, are potent on-pathway intermediates that are converted into U-shape fibrillar structures. The trimers and tetramers formed non-fibrillar oligomers, which primarily progress to off-pathway species.

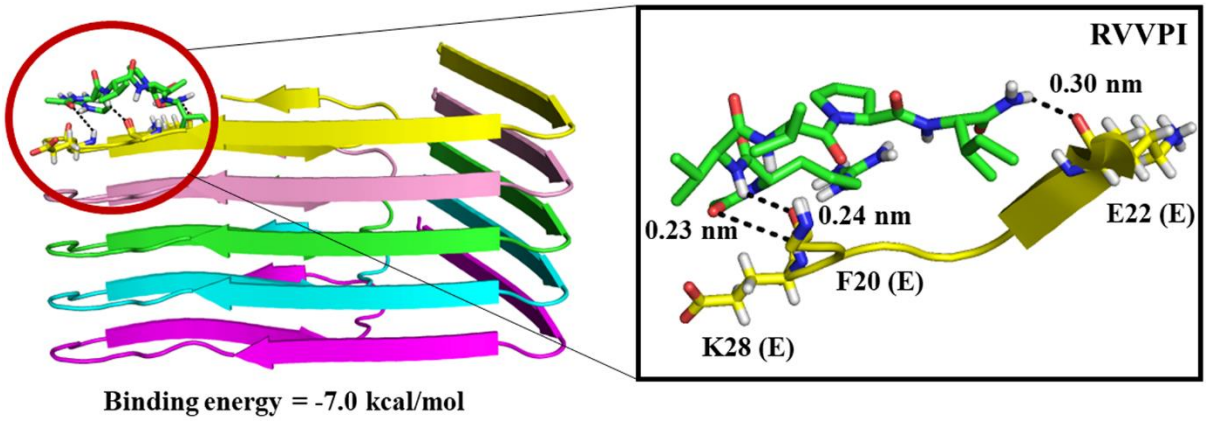

Figure 6.2: Docked pose of RVVPI with Aβ42 protofibril (PDB ID: 5OQV). The Aβ42 protofibril is shown in the cartoon and RVVPI is displayed in sticks. The magnified views depict the hydrogen bonds between RVVPI and Aβ42 protofibril residues in black dashed lines with distances in nm.

Bitan et al. employed biochemical, spectroscopic, and morphologic methods to investigate the initial oligomerization and assembly of Aβ40 and Aβ42.[44] The carefully prepared aggregate-free Aβ40 existed as monomers, dimers, trimers, and tetramers, in rapid equilibrium. In contrast, Aβ42 preferentially formed pentamer/hexamer units (paranuclei) that assembled further to form beaded superstructures similar to early protofibrils. The authors mentioned that operationally, the pentamer/hexamer units may be considered "paranuclei", because they represent an initial, and minimal, structural unit from which Aβ assemblies evolve and suggested that the paranuclei formed by Aβ42 may be important therapeutic targets. Wolff et al. highlighted that the smallest detectable species are pentamer or hexamer of Aβ42 in solution.[45]

The Aβ42 protofibril (PDB ID: 5OQV) has LS-sharped morphology and stabilize by K28-A42 salt bridges. Furthermore, three hydrophobic cores (core-1 comprising A2, F4, L34 and V36, core-2 consisting of L17, F19 and I31, and core-3 having A30, I32, M35, and V40) stabilize the protofibril structure.

The binding energy and key interactions of RIIGL, RVVPI, and RIAPA with Aβ42 protofibril were examined using molecular docking (**Figure 6.2** and **Figure 6.3**). RIIGL, RVVPI, and RIAPA bind favourably to Aβ42 protofibril with binding energies of –6.4, –7.0, and, –6.6 kcal/mol, respectively (**Table 6.3**). RIIGL displayed hydrogen bonds with Glu22 (0.28 nm) and Asn27 (0.19 nm) of chain E of Aβ42 protofibril (**Figure 6.3a**), whereas RVVPI interacted with Phe20 (0.24 nm), Glu22 (0.30 nm) and Lys28 (0.23 nm) of chain E of Aβ42 protofibril (Figure 2). RIAPA formed hydrogen bonds with Phe20 (0.30 nm) and Glu22 (0.23 nm) of chain E of Aβ42 protofibril (**Figure 6.3b**).

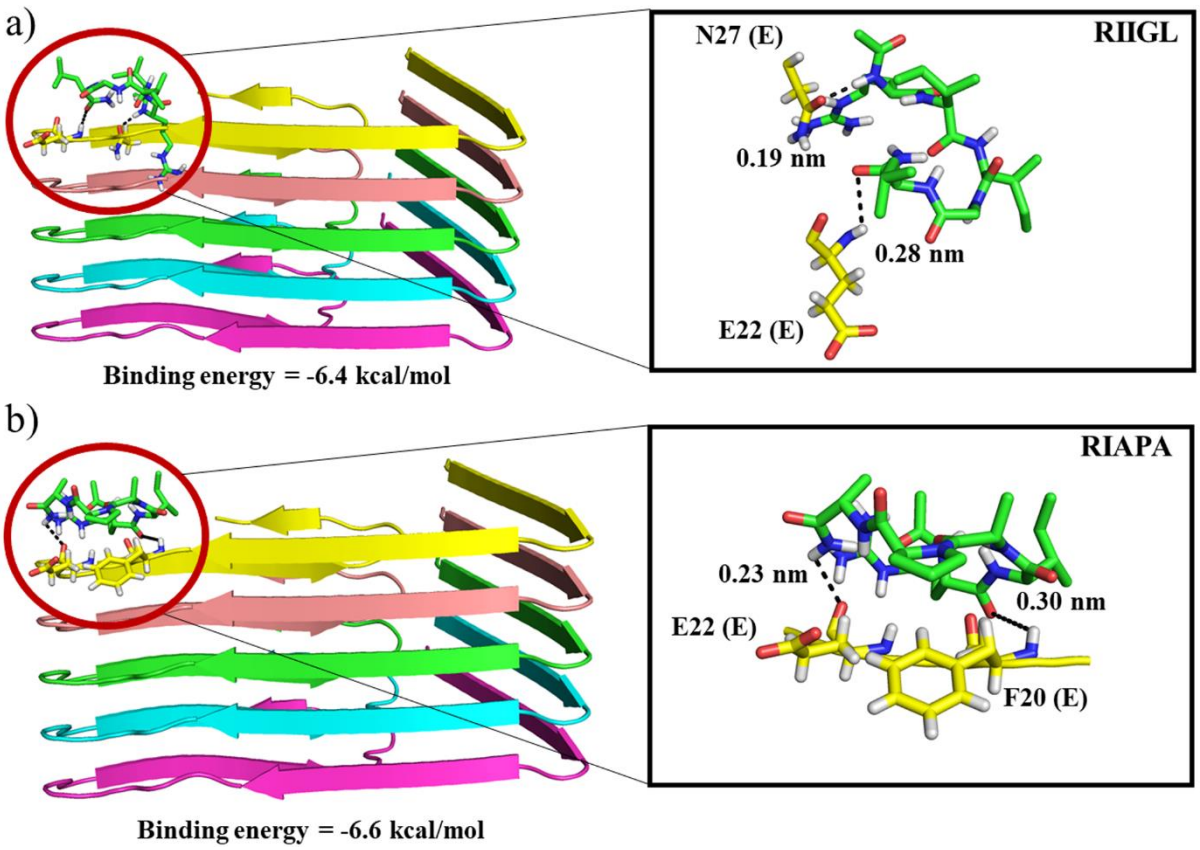

Figure 6.3: Docked poses of RIIGL and RIAPA with Aβ42 protofibril (PDB ID: 5OQV) are shown in panels a, and, b, respectively. The Aβ42 protofibril is shown in the cartoon, whereas peptides are displayed in the stick representation. The magnified views depict the hydrogen bonds between the peptides and Aβ42 protofibril residues in black dashed lines with distances in nm.

The Phe19 and Phe20 residues of aggregation-prone central hydrophobic core[46] (CHC) region of Aβ42 are involved in the favourable stacking interactions and provide structural stability to Aβ aggregates.[47] The hydrogen bond interactions of RVVPI and RIAPA with Phe20 of Aβ42 protofibril interrupts the interchain π–π interactions between Phe residues, which, in turn, leads to destabilization of protofibril structure. The molecular docking analysis depicted a stronger association of RVVPI with Aβ42 protofibril in comparison to RIIGL and RIAPA as evidenced by its lower binding energy and a higher number of hydrogen bonds.

Furthermore, the ability of peptides to destabilize the ordered structure of β-sheet rich Aβ42 protofibril was examined using MD simulations. Four systems isolated Aβ42 protofibril (designated as control) and Aβ42 protofibril-RIIGL (designated as RIIGL), Aβ42 protofibril-RVVPI (designated as RVVPI), and Aβ42 protofibril-RIAPA (designated as RIAPA) were employed for MD simulations (**Table 6.1**).

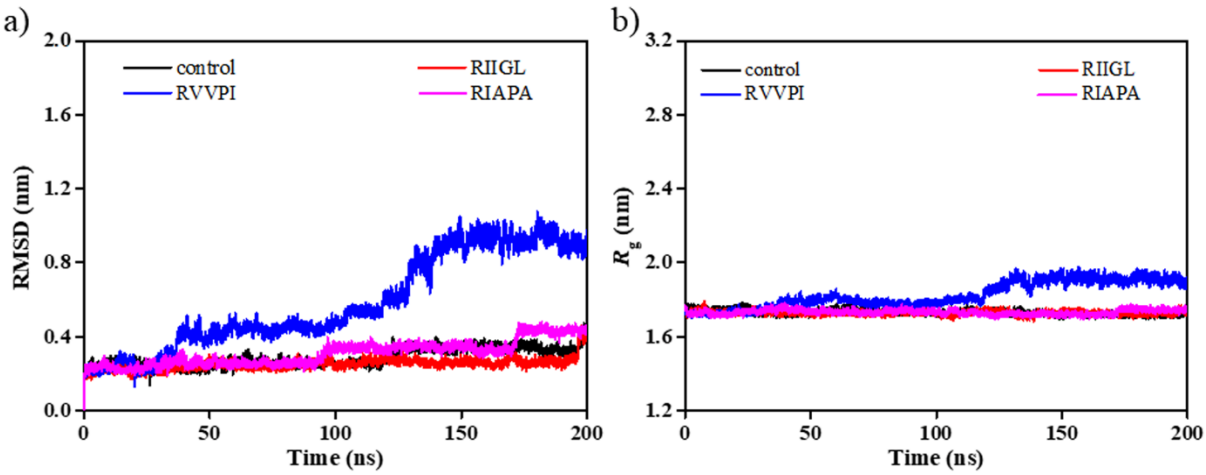

Figure 6.4: Variations in the RMSD (panel a) and R_g (panel b) with time (ns) for the simulated systems.

2.2 Structural stability of Aβ42 protofibril in the presence of peptides

The effect of peptides on the protofibril structural stability was examined using root-mean-square deviation (RMSD) (**Figure 6.4a**).[48] The average RMSD of control, RIIGL, RVVPI, and RIAPA are noted to be 0.30 ± 0.02, 0.31 ± 0.05, 0.60 ± 0.04, and 0.32 ± 0.06 nm, respectively. The average RMSD (0.30 ± 0.02 nm) of control is consistent with Dong et al.[49] which reported an RMSD of 0.27 nm for isolated Aβ42 protofibril (PDB ID: 5OQV). A notably higher value (0.60 ± 0.04 nm) was observed on the addition of RVVPI, which depicts a more pronounced structural perturbation effect of RVVPI on the stability of Aβ42 protofibril structure. The average value of radius-of-gyration (R_g) of control, RIIGL, RVVPI, and RIAPA are noted to be 1.73 ± 0.02, 1.74 ± 0.04, 1.82 ± 0.02, and, 1.74 ± 0.05 nm, respectively (**Figure 6.4b**). A higher R_g value of 1.82 ± 0.02 nm in the RVVPI as compared to 1.73 ± 0.02 nm in the control indicates the loosening of the well-packed chains in the protofibril. The repeat simulations with different intitial velocities depicts identical RMSD and R_g pattern, which highlight reliability of MD simulations (**Figure 6.5**).

RMSF measure the residues fluctuations in proteins and residues with high RMSF values indicate enhanced conformational fluctuations and flexibility.[50] The average RMSF of control, RIIGL, RVVPI, and RIAPA are noted to be 0.22 ± 0.02, 0.37 ± 0.03, 0.84 ± 0.01, and 0.38 ± 0.02 nm, respectively (**Figure 6.6a**).

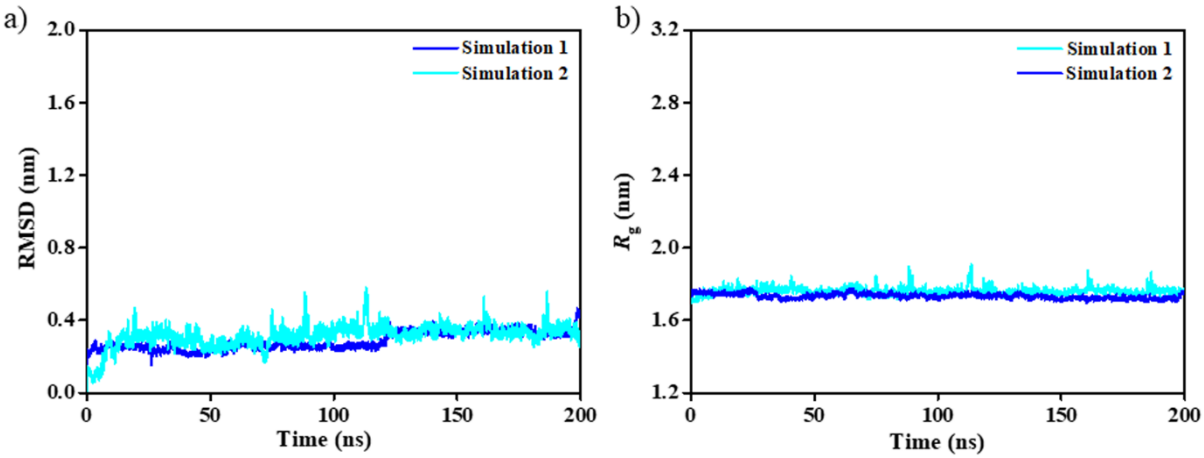

Figure 6.5: RMSD (panel a) and R_g (panel b) of repeat simulations of Aβ42 protofibril.

Notably, all residues of Aβ42 protofibril fluctuate at higher values on the addition of RVVPI, which depicts greater structural perturbation in the ordered structure of Aβ42 protofibril. Higher fluctuations were noted in all residues of Aβ42 protofibril except A42 in RIIGL, and Y10 and A21 in RIAPA, which highlighted distortion in the protofibril structure. This is consistent with Nie et al.,[51] which depicted notably higher conformational fluctuations in 36 residues in Aβ42 protofibril- epicatechin-3-gallate (ECG) system as compared to Aβ42 protofibril alone (PDB ID: 5OQV) leading to conformational distortion in the Aβ42 protofibril structure. Thus, RMSF analysis depicted notably enhanced conformational fluctuations in Aβ42 protofibril on the incorporation of peptides, however, RVVPI displays a more pronounced destabilization effect due to remarkably higher conformational fluctuations in protofibril structure than other peptides.

The SASA measure the solvent accessible surface area of a protein and higher value of SASA indicate more distortion in the native structure of a protein.[52] The average SASA of control, RIIGL, RVVPI, and RIAPA are noted to be 104.1 ± 0.08, 107.3 ± 0.11, 160.4 ± 0.15, and 113.4 ± 0.12 nm^2, respectively (**Figure 6.6b**). A noteworthy increase in SASA of Aβ42 protofibril from 104.1 ± 0.08 to 160.4 ± 0.15 nm^2 on the incorporation of RVVPI depicts higher accessibility of the solvent resulting from the distortion in the protofibril structure. The SASA analysis is in agreement with the observation that a comparable increase in SASA induced by arginine containing short peptides results in the destabilization of Aβ42 protofibril.[53]

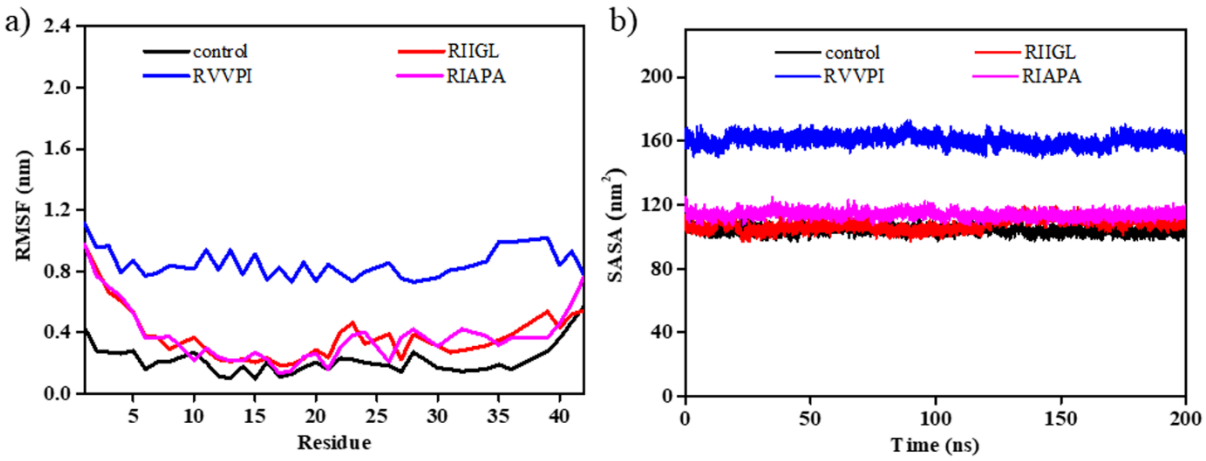

Figure 6.6: Residue-wise RMSF and variations in SASA during simulation in control, RIIGL, RVVPI, and RIAPA systems.

2.3 Conformational snapshots and interchain hydrogen bond analysis depicts structural perturbation of Aβ42 protofibril in the presence of peptides

To examine the destabilization of Aβ42 protofibril on the incorporation of peptides, conformational snapshots were visualized (**Figure 6.7**). During simulation, RVVPI displayed binding at chain E of Aβ42 protofibril (**Figure 6.7**). This binding pattern is noteworthy as recent studies emphasized that fibril structure growth is accelerated at the even edge attributed to the exposed CHC region.[54] Upon incorporation of RVVPI, Aβ42 protofibril undergoes extensive conformational changes especially extended β-strand conformations begin to disappear (**Figure 6.7**). Additionally, a visual examination revealed a reduction in β-sheet (β1) content of chains A and E of Aβ42 protofibril accompanied by a concomitant increase in coil content on the addition of RVVPI (**Figure 6.7**). Furthermore, the shortening of β-strands and disruption of LS morphology of Aβ42 protofibril on the addition of RVVPI depicts the loosening of Aβ42 protofibril chains resulting in the structural distortion of Aβ42 protofibril (**Figure 6.7**). In contrast, extended β-strands are comparatively more stable throughout the simulation in control and RIIGL systems (**Figure 6.7**). The LS-shaped morphology of Aβ42 protofibril remains intact in the RIIGL and RIAPA systems as compared to RVVPI (**Figure 6.7**), which depicts a higher destabilization potential of RVVPI.

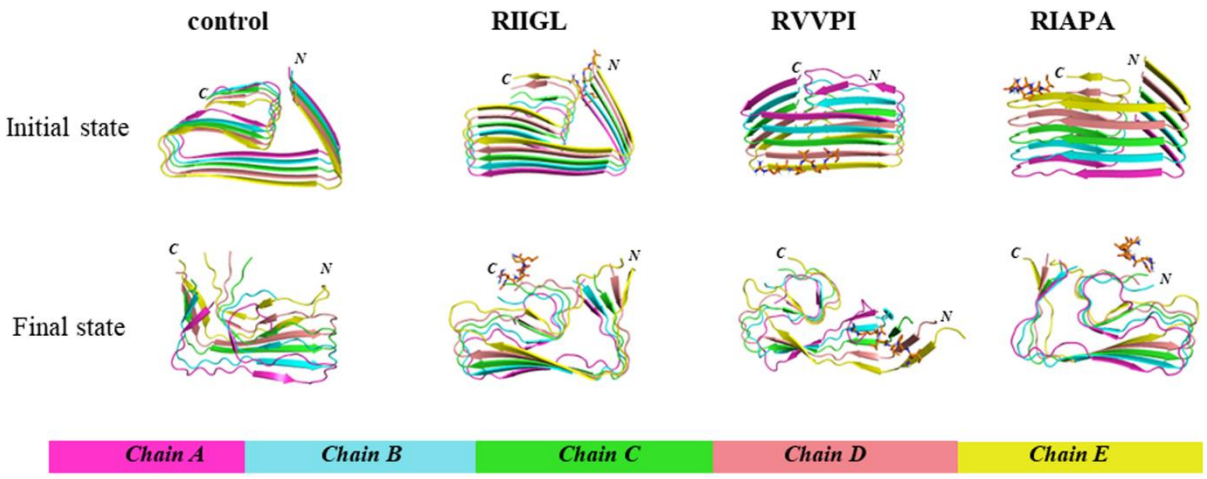

Figure 6.7: Conformational snapshots at different time intervals depicting the structural changes in Aβ42 protofibril.

The stability of Aβ42 protofibril relies on the interaction between different chains within the protofibril, facilitated by hydrogen bonds and hydrophobic contacts. The hydrogen bonds between neighbouring chains emerge as a pivotal factor in Aβ42 protofibril stability. The interchain hydrogen bonds in protofibril with and without peptides were evaluated (**Table 6.4**). In Aβ42 protofibril, the average hydrogen bonds between chains A−B, B−C, C−D, and D−E during simulation are noted to be 33.4, 34.4, 31.2, and 31.4, respectively.

Table 6.4: Average number of interchain hydrogen bonds in Aβ42 protofibril with and without pentapeptides during simulation.

System	Number of interchain hydrogen bonds			
	A-B	B-C	C-D	D-E
control	33.4	34.4	31.2	31.4
RIIGL	30.7	33.5	30.7	28.2
RVVPI	29.4	30.3	30.2	25.6
RIAPA	30.8	32.6	30.5	29.4

The binding of peptides has a notable effect on the interchain hydrogen bonds in Aβ42 protofibril. The average number of hydrogen bonds decreased from 33.4 to 29.4 in chain A-B, 34.4 to 30.3 in chain B-C, 31.2 to 30.2 in chain C-D, and 31.4 to 25.6 in chain D-E of Aβ42 protofibril on incorporating RVVPI, which indicates lower interchain interactions leading to the structural perturbation of Aβ42 protofibril. Notably, lower interchain hydrogen bonds between chain D-E in Aβ42 protofibril on the addition of RVVPI is consistent with the molecular docking analysis that highlighted the binding of RVVPI with the residues of chain E of Aβ42 protofibril. Among newly designed peptides RVVPI and RIAPA, the incorporation of RVVPI resulted in a larger decrease in the interchain hydrogen bonds in Aβ42 protofibril

(Table S2), which, in turn, depicts a higher ability of RVVPI to destabilize protofibril structure than RIAPA.

2.3 Impact of peptides on the β-sheet rich Aβ42 protofibril structure

To elucidate the effect of peptides on the structural destabilization of β-sheet rich protofibril, secondary structure occupancies were examined (**Table 6.5**). The content of β-sheet, coil, bend, and turn in control are noted to be 56.4 ± 0.5, 30.1 ± 0.4, 10.3 ± 0.8, and 1.2 ± 0.3, respectively. The β-sheet in control is consistent with Zhan et al.,[55] which reported β-sheet of 54.9 ± 1.0 % in Aβ42 protofibril (PDB ID: 5OQV).

Table 6.5: Secondary structure compositions for control, RIIGL, RVVPI, and RIAPA systems.

System	β–sheet[a]	coil	bend	turn	chain separator
control	56.4 ± 0.5	30.2 ± 0.4	10.2 ± 0.8	1.2 ± 0.3	2.00 ± 0.0
RIIGL	54.2 ± 0.5	32.6 ± 0.7	10.2 ± 0.2	1.0 ± 0.2	2.00 ± 0.0
RVVPI	53.4 ± 0.9	33.4 ± 0.5	10.2 ± 0.4	1.0 ± 0.1	2.00 ± 0.0
RIAPA	53.8 ± 0.5	33.0 ± 0.8	10.2 ± 0.3	1.0 ± 0.2	2.00 ± 0.0

[a]β–sheet = β–strand + β–bridge

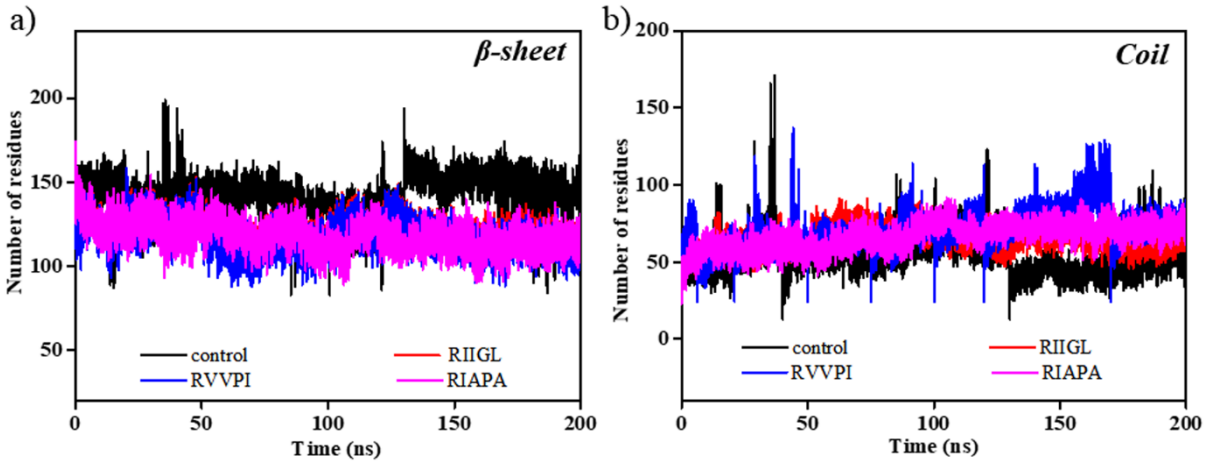

Figure 6.8: Variations in the number of Aβ42 protofibril residues adopting β-sheet (panel a) and coil (panel b) during simulation in control, RIIGL, RVVPI, and RIAPA systems.

The probability of β-sheet structure decreased from 56.4 ± 0.5 in control to 54.1 ± 0.5 in RIIGL, 53.4 ± 0.9 in RVVPI, and 53.9 ± 0.5 in RIAPA, while the sampling of random coil conformation increased from 30.1 ± 0.4 in control to 32.7 ± 0.7 in RIIGL, 33.3 ± 0.5 in RVVPI, and 33.0 ± 0.8 in RIAPA. The lower β-sheet content leads to the loosening of the well packed protofibril chains followed by distortion in its overall structure that is consistent with the β-sheet rich Aβ oligomers converting into amorphous, off-pathway species on the incorporation

of resveratrol and epigallocatechin gallate (EGCG).[56] Apart from β-sheet and random coil, other secondary structures such as bend, turn, and chain separator were quite similar in the four systems (**Table 6.5**). The $A\beta_{42}$ protofibril undergoes accelerated disorganization in the presence of RVVPI marked by lower residues adopting β-sheet conformation with a concomitant increase in the residues sampling coil conformation (**Figure 6.8**). The decrease in the β-sheet with a concomitant increase in coil confirms a hindrance to the formation of higher-order neurotoxic aggregates due to the distortion in the regular β-sheet structure of $A\beta_{42}$ protofibril.

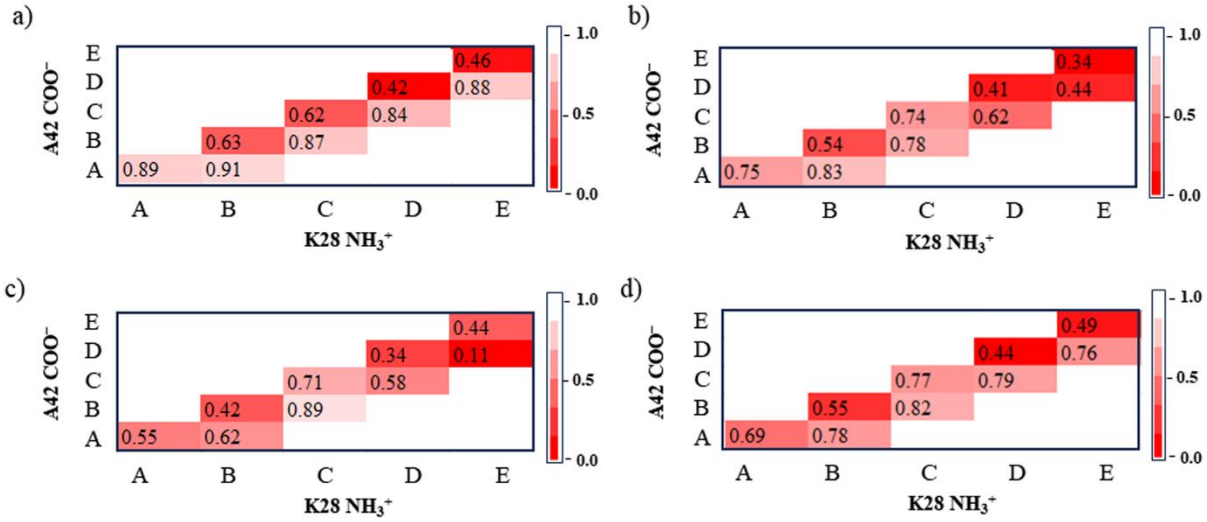

Figure 6.9: Probability of intrachain and interchain K28-A42 salt bridges in control, RIIGL, RVVPI, and RIAPA systems are shown in panels a-d, respectively. The A, B, C, D, and E in panels a-d refer to different chains in $A\beta_{42}$ protofibril.

2.4 Peptides significantly disrupt K28-A42 salt bridges in Aβ42 protofibril, and RVVPI displays a more pronounced disruptive ability

The U-shaped[57] $A\beta_{9\text{-}40}$, $A\beta_{1\text{-}40}$, and $A\beta_{17\text{-}42}$ protofibrils are stabilized by D23-K28 salt bridges, whereas K28-A42 salt bridges stabilize the S-shaped[57a,58] $A\beta_{11\text{-}42}$ and LS-shaped[Error! Bookmark not defined.] $A\beta_{1\text{-}42}$ protofibrils. To examine the effect of designed peptides on the stability of K28-A42 salt bridges in $A\beta_{42}$ protofibril, the probability of interchain and intrachain salt bridges between K28-A42 was examined on the incorporation of peptides (**Figure 6.9**). Salt bridges were considered to exist if the distance between the amino group of K28 and the carboxyl group of A42 was within a range of 0.32 nm.[59] In control, an average probability of 0.88 was noted for the interchain salt bridges involving K28 and A42 residues (**Table 6.6**). This is consistent with Gong et al., which reported an average probability of > 0.82 for interchain K28-A42 salt

bridges in the 5OQV protofibril model. However, the average probability of interchain salt bridges significantly decreased from 0.88 in control to 0.67 in RIIGL, 0.55 in RVVPI, and 0.79 in RIAPA (**Table 6.6**). Notably, disruption of interchain salt bridges in $A\beta_{42}$ protofibril is more pronounced in RVVPI as compared to other peptides, which is consistent with interchain hydrogen bond analysis highlighting the more pronounced effect of RVVPI to destabilize the protofibril structure. Furthermore, the probability of the interchain K28-A42 salt bridge in chain D-E was notably reduced from 0.88 in control to 0.11 in RVVPI (**Table 6.6**), which is consistent with the conformational snapshots depicting binding of RVVPI with the residues of chain D and E of $A\beta_{42}$ protofibril.

Table 6.6: Probability of interchain salt bridges between K28-A42 in the $A\beta_{42}$ protofibril in control, RIIGL, RVVPI, and RIAPA systems.

Interchain salt bridges (K28-A42)	Probability			
	control	RIIGL	RVVPI	RIAPA
A-B	0.91	0.83	0.62	0.78
B-C	0.87	0.78	0.89	0.82
C-D	0.84	0.62	0.58	0.79
D-E	0.88	0.44	0.11	0.76

Table 6.7: Probability of intrachain salt bridges between K28-A42 in the $A\beta_{42}$ protofibril in control, RIIGL, RVVPI, and RIAPA systems.

Intrachain salt bridges (K28-A42)	Probability			
	control	RIIGL	RVVPI	RIAPA
A-A	0.89	0.75	0.55	0.69
B-B	0.63	0.54	0.42	0.55
C-C	0.62	0.74	0.71	0.77
D-D	0.42	0.41	0.34	0.44
E-E	0.46	0.34	0.44	0.49

In addition to interchain K28-A42 salt bridges in $A\beta_{42}$ protofibril, the intrachain salt bridges are also affected by the incorporation of peptides (**Table 6.7**). The average probability of K28-A42 intrachain salt bridges was reduced from 0.60 in control to 0.55 in RIIGL and 0.49 in RVVPI, whereas it remains unaffected in RIAPA (**Table 6.7**). The K28-A42 salt bridge analysis depicted higher disruption of interchain salt bridges as compared to the intrachain salt bridges and the effect is more pronounced in the presence of RVVPI as compared to other peptides. Thus, RVVPI destabilizes the protofibril structure by disrupting K28-A42 salt bridges considered critical for protofibril stability.

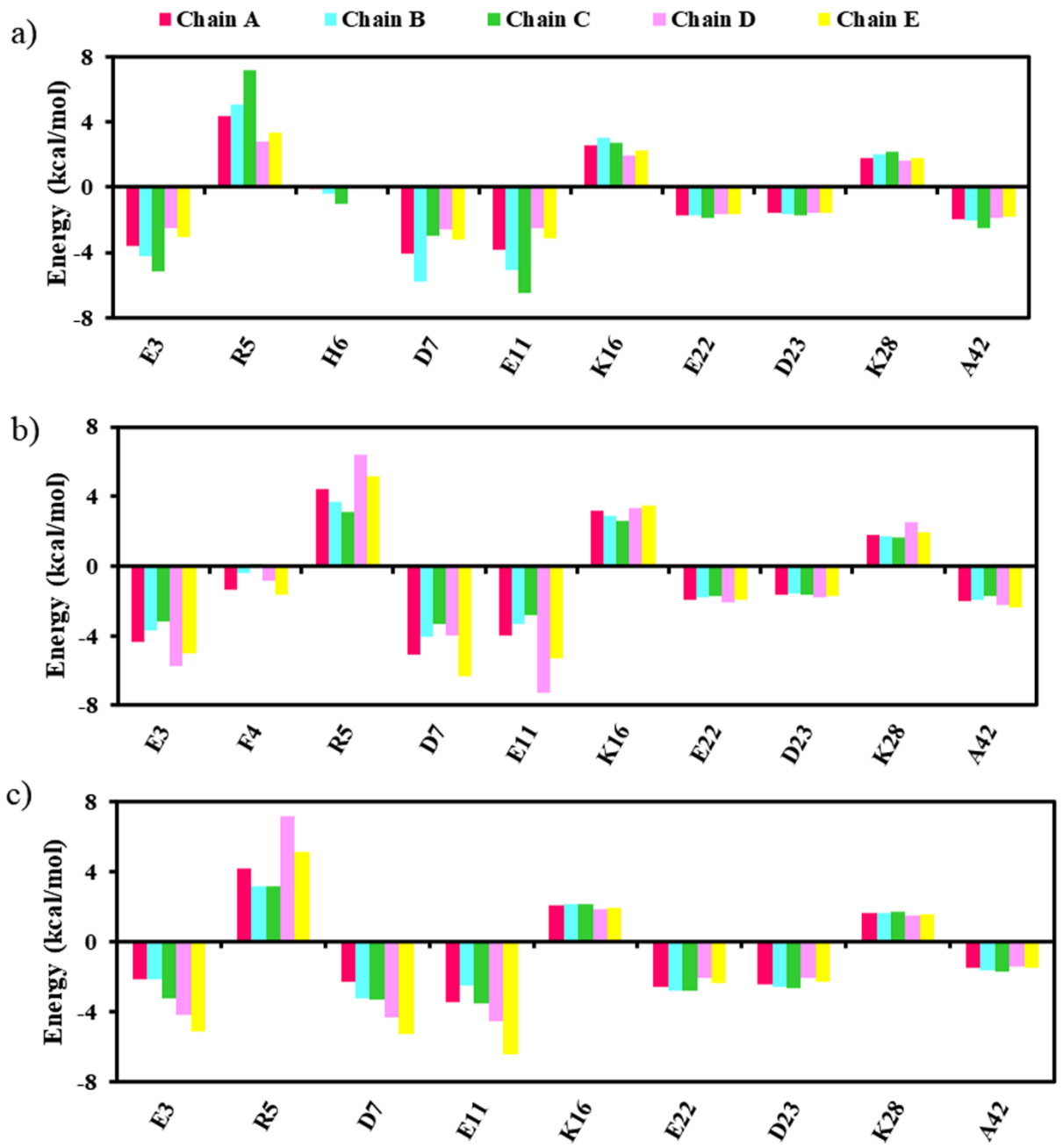

Figure 6.10: Residue-wise contribution of the different chains of the protofibril to the binding free energy (kcal/mol) of RIIGL (panel a), RVVPI (panel b), and RIAPA (panel c) with Aβ42 protofibril.

2.5 Electrostatic interactions govern the binding of peptides to Aβ42 protofibril

RIIGL, RVVPI, and RIAPA binds to Aβ42 protofibril with binding free energies of –95.77 ± 1.99, –104.05 ± 0.16, and –99.49 ± 0.03 kcal/mol (**Table 6.8**). The van der Waals and electrostatic interaction terms favour the binding of peptides to Aβ42 protofibril, whereas the polar solvation is unfavourable for the binding. Notably, the electrostatic interactions contributed significantly in the binding free energy as compared to the van der Waals

interactions (**Table 6.8**), which is due to the electrostatic interactions of arginine in the peptides with aspartic and glutamic acid residues of Aβ42 protofibril (**Figure 6.10**). Furthermore, the per-residue binding free energy of the Aβ42 protofibril residues with the peptides was evaluated (**Figure 6.10**).

RIIGL preferentially binds to D7 (–5.8), E11 (–5.1) of chain B and E3 (–5.2), E11(–6.5) of chain C of the Aβ42 protofibril (**Figure 6.10a**). The Aβ42 protofibril residues D7 (–5.1) of chain A, E3 (–5.8) and E11 (–7.3) of chain D, and E3 (–5.0), D7 (–6.3), and E11 (–5.3) of chain E contributed significantly to binding with RVVPI (**Figure 6.10b**), whereas E3 (–5.1), D7 (–5.3), and E11 (–6.4) of chain E of Aβ42 protofibril contributed in binding to RIAPA (**Figure 6.10c**). Thus, residue-wise free binding energy analysis highlights that charged residues influence Aβ42 protofibril-peptide interactions. Notably, we find that RVVPI displayed binding with a higher number of Aβ42 protofibril residues, which is consistent with its more pronounced destabilization of protofibril structure than other peptides.

Table 6.8: Binding free energy of pentapeptides with Aβ42 protofibril.

Energy terms (kcal/mol)	Aβ42 protofibril–RIIGL	Aβ42 protofibril–RVVPI	Aβ42 protofibril–RIAPA
ΔE_{vdW}	– 29.77 ± 3.12	–32.63 ± 3.77	–29.47 ± 0.09
ΔE_{elec}	–126.28 ± 6.56	–137.00 ± 9.46	–133.29 ± 10.07
ΔE_{MM}[a]	–156.05 ± 9.68	–169.63 ± 13.23	–162.77 ± 10.16
ΔG_{ps}	+64.15 ± 8.21	+69.60 ± 13.63	+65.94 ± 10.76
ΔG_{nps}	–3.87 ± 0.52	–4.02 ± 0.56	–2.66 ± 0.64
ΔG_{solv}[b]	+60.28 ± 7.69	+65.58 ± 13.07	+63.28 ± 10.13
$\Delta G_{binding}$[c]	–95.77 ± 1.99	–104.05 ± 0.16	–99.49 ± 0.03

[a] $\Delta E_{MM} = \Delta E_{vdW} + \Delta E_{elec}$; [b] $\Delta G_{solv} = \Delta G_{ps} + \Delta G_{nps}$; [c] $\Delta G_{binding} = \Delta E_{MM} + \Delta G_{solv}$

2.6 Synthesized peptides showed inhibition of Aβ42 aggregation

The inhibition of Aβ42 aggregation by the three selected peptides (RIIGL, RVVPI, and RIAPA) was monitored by the thioflavin T (ThT) fluorescence assay. ThT is widely employed to monitor Aβ aggregation, as it emits stronger fluorescence emission when bound to β-sheet-rich amyloid structures.[60] The experimental conditions including Aβ42, ThT concentration, and incubation time were first optimized prior to ThT assay. Under the optimized conditions, Aβ42 alone and in the presence of peptides (RIIGL, RVVPI, and RIAPA) at various stoichiometric ratios 1:0, 1:0.25, 1:0.5, 1:1, 1:2, 1:4, and 1:6 of Aβ42:peptides were incubated and results were plotted in **Figure 6.11a**. ThT data shows that synthesized peptides exhibited inhibition of Aβ42

aggregation in a dose-dependent manner. RIIGL, RVVPI, and RIAPA showed 47.1 %, 66.2%, and 51.6 %, respectively inhibition of Aβ42 aggregation at 1:2 molar ratio of Aβ42:peptides. Further increase in the concentration of peptides did not lead to significant improvement in the inhibition efficiency against Aβ42 aggregation. Among the synthesized peptides, RVVPI exhibited the highest inhibitory activity against Aβ42 aggregation, consistent with the results from the computational screening.[21] The IC_{50} values calculated for RIIGL, RVVPI, and RIAPA were 25.59 ± 0.71, 5.57 ± 0.83, and 15.88 ± 0.66 µM, respectively (**Figure 6.12**).

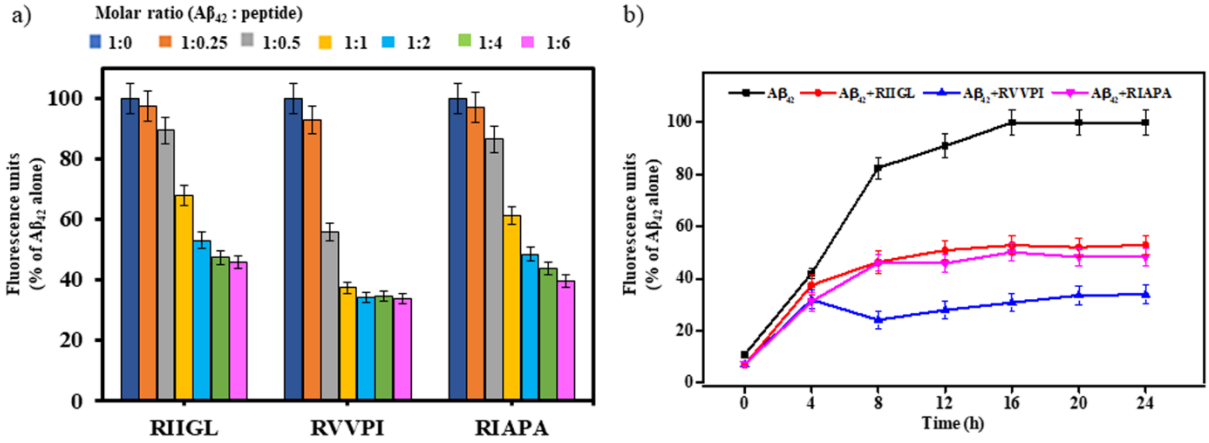

Figure 6.11: ThT assay: a) Inhibition of Aβ42 aggregation by synthesized peptides at various stoichiometric ratios (1:0, 1:0.25, 1:0.5, 1:1, 1:2, 1:4 and 1:6) of Aβ42:peptides after 24 h incubation at 37 °C with constant agitation, [Aβ42]= 10 µM; b) Time course of Aβ42 aggregation in the absence and presence of synthesized peptides, [Aβ42]= 10 µM and [peptides]= 20 µM. The experiments were performed in triplicate, and error bars represent the standard deviation.

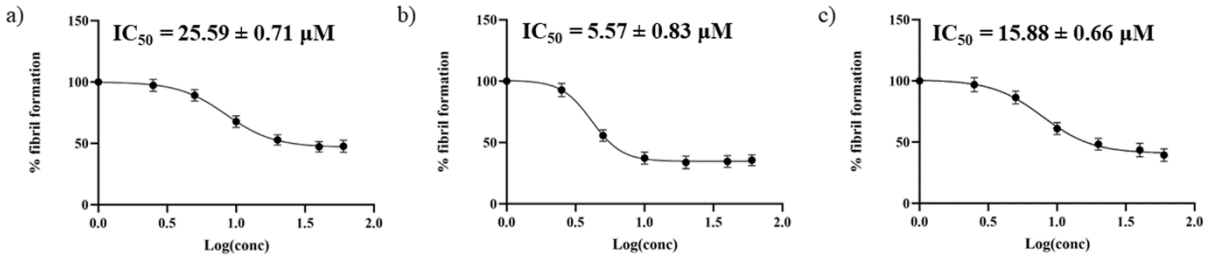

Figure 6.12: Dose-response curves of RIIGL (panel a), RVVPI (panel b), and RIAPA (panel c) against Aβ42 aggregation to determine their respective IC_{50} values.

The changes in ThT fluorescence were noted at various time interval for Aβ42 alone and in the presence of synthesized peptides (**Figure 6.11b**). The increase in ThT emission intensity indicated the aggregation of Aβ42. A growth curve for Aβ42 fibrillation showed a saturation phase at nearly 16 h of incubation. In the absence of RIIGL, RVVPI, and RIAPA peptides, the enhancement in ThT emission intensity was high for neat Aβ_{42}, however, Aβ_{42} aggregation was inhibited in the presence of peptides (inhibition efficiency RVVPI > RIAPA > RIIGL).

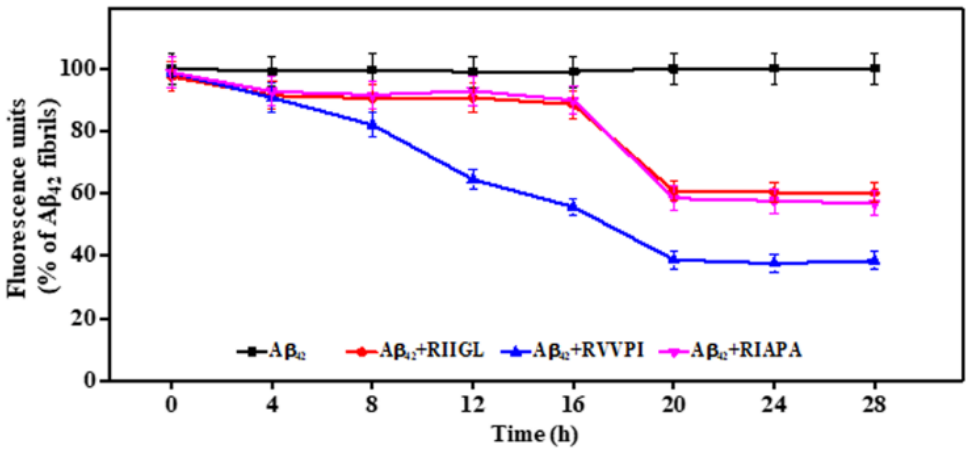

Figure 6.13: Kinetic ThT assay: disaggregation of pre-formed Aβ42 aggregates by RIIGL, RVVPI, and RIAPA at [Aβ42]= 10 μM, [peptides]= 20 μM. The experiments were performed in triplicate, and error bars represent the standard deviation.

2.7 Synthesized peptides showed disaggregation of preformed Aβ42 aggregates

In addition, the peptides were tested to examine their ability to disassemble the pre-formed Aβ42 fibrils by ThT assay (**Figure 6.13**). In this regard, fibrillation was allowed to proceed for 24 h, at this time point a 2-fold molar excess of either peptide (RIIGL, RVVPI, and RIAPA) were added and incubated for future 24 h. In the kinetic Aβ42 disaggregation assay, RIIGL and RIAPA showed moderate activity in dissolving the pre-formed aggregates with disaggregating efficiency of 39.7 %, and 42.4 %, respectively (**Figure 6.13**). Among the synthesized peptides, RVVPI was most efficient (62.4%) in disaggregating the pre-formed Aβ42 aggregates, consistent with the computational results.

Furthermore, TEM was performed to study the fibrillary architecture of Aβ42 aggregates in the absence and presence of peptides (RIIGL, RVVPI, and RIAPA) [**Figure 6.14 (a-e)**]. Dense amyloid fibrils were seen in the TEM image of Aβ42 alone after 24 h of incubation (**Figure 6.14b**) as compared to Aβ42 at 0 h (**Figure 6.14a**). Notably, a significant decrease in the amount and length of fibrils was seen when pre-formed Aβ42 fibrils were co-incubated with RVVPI (**Figure 6.14d**). The ThT and TEM studies highlighted the efficiency of RVVPI in the disassembly of pre-formed Aβ42 fibrils.

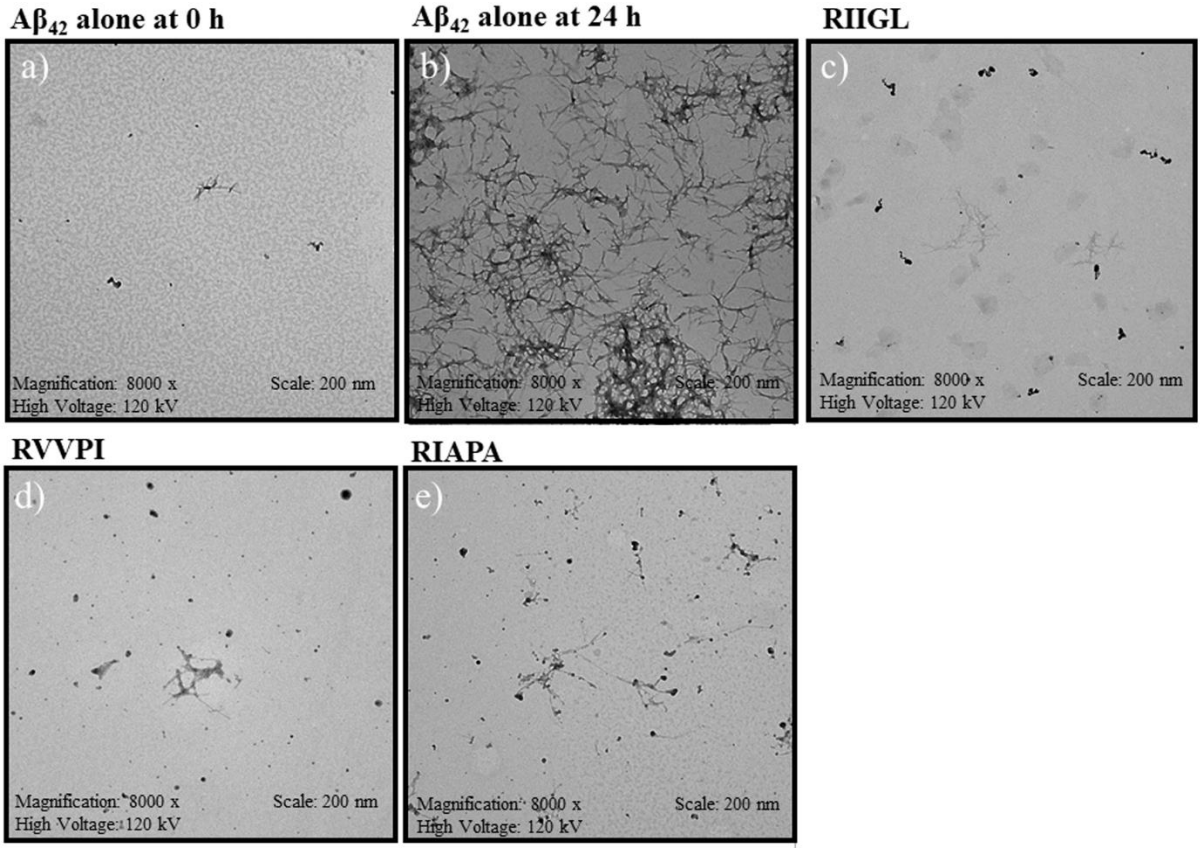

Figure 6.14: TEM images: a) Aβ42, 0 h; b) Aβ42, 24 h; c) Aβ42 aggregates+RIIGL, 24 h; d) Aβ42 aggregates+RVVPI, 24 h; e) Aβ42 aggregates +RIAPA, 24 h. Scale bar: 200 nm, [Aβ42]= 10 μM, [peptides]= 20 μM.

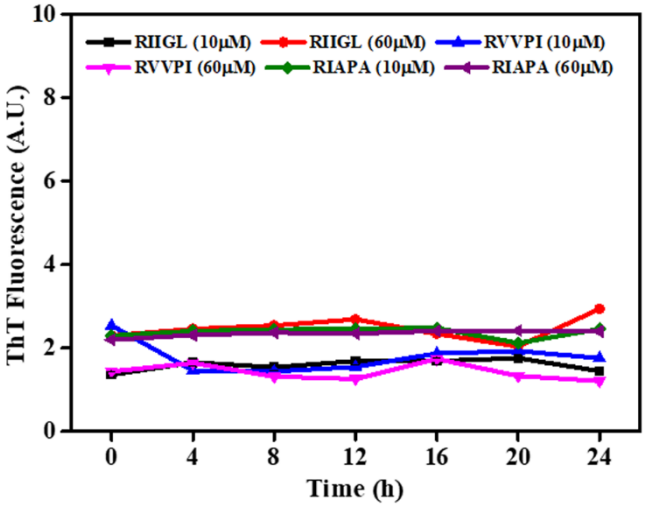

Figure 6.15: ThT assay: self-aggregation tendency of the synthesized peptides at different concentrations in PBS buffer at pH= 7.4.

The observed better efficiency of RVVPI and RIAPA to disaggregate the pre-formed Aβ$_{42}$ aggregates as compared to RIIGL was attributed to the incorporation of proline in their sequences. The literature reports highlighted that the insertion of a proline in synthetic peptides leads to enhanced ability to impede fibril formation.[61] Specifically, the unique structural properties of proline, including its ability to impose rigidity by constraining the backbone dihedral angle (ϕ), contribute to its effectiveness in disrupting β-sheet formation. Arginine has been widely employed as an aggregation suppressor in various previously published papers.[62] Furthermore, the distinct amino acid compositions of RIIGL, RVVPI, and RIAPA influence their hydrophobicity and interaction with Aβ$_{42}$ aggregates. RVVPI displayed highest inhibitory activity against Aβ_{42} aggregation due to higher hydrophobic character that was consistent with its greater van der Waals interaction (–32.63 ± 3.77 kcal/mol) contribution to the total binding free energy to Aβ$_{42}$ protofibril as compared to RIAPA (–29.47 ± 0.09 kcal/mol) noted in the computational studies (**Table 6.8**).

Additionally, the self-aggregation propensity of the synthesized peptides (RIIGL, RVVPI, and RIAPA) was assessed by ThT and TEM assay. In this regard, RIIGL, RVVPI, and RIAPA were incubated at varying molar concentrations for 24 h at 37 °C, and ThT emission intensity was monitored at various time points (**Figure 6.15**). No enhancement in ThT emission intensity was observed even after incubating RIIGL, RVVPI, and RIAPA for 24 h, indicating that synthesized peptides do not exhibit self-aggregation in solution. The TEM images of RIIGL, RVVPI, and RIAPA peptides at t= 0 h and after 24 h incubation were procured [**Figure 6.16(a-f)**]. The TEM images for all peptides after 24 h incubation showed no fibrillar structures, indicating that the peptides do not undergo aggregation. The results corroborate previous findings by Fülöp et al. which demonstrated that RIIGL does not self-aggregate even after incubation for 6 days.[20] These results suggested that the synthesized peptides do not self-aggregate in solution, which is much required for the success of these constructs as drug candidates.

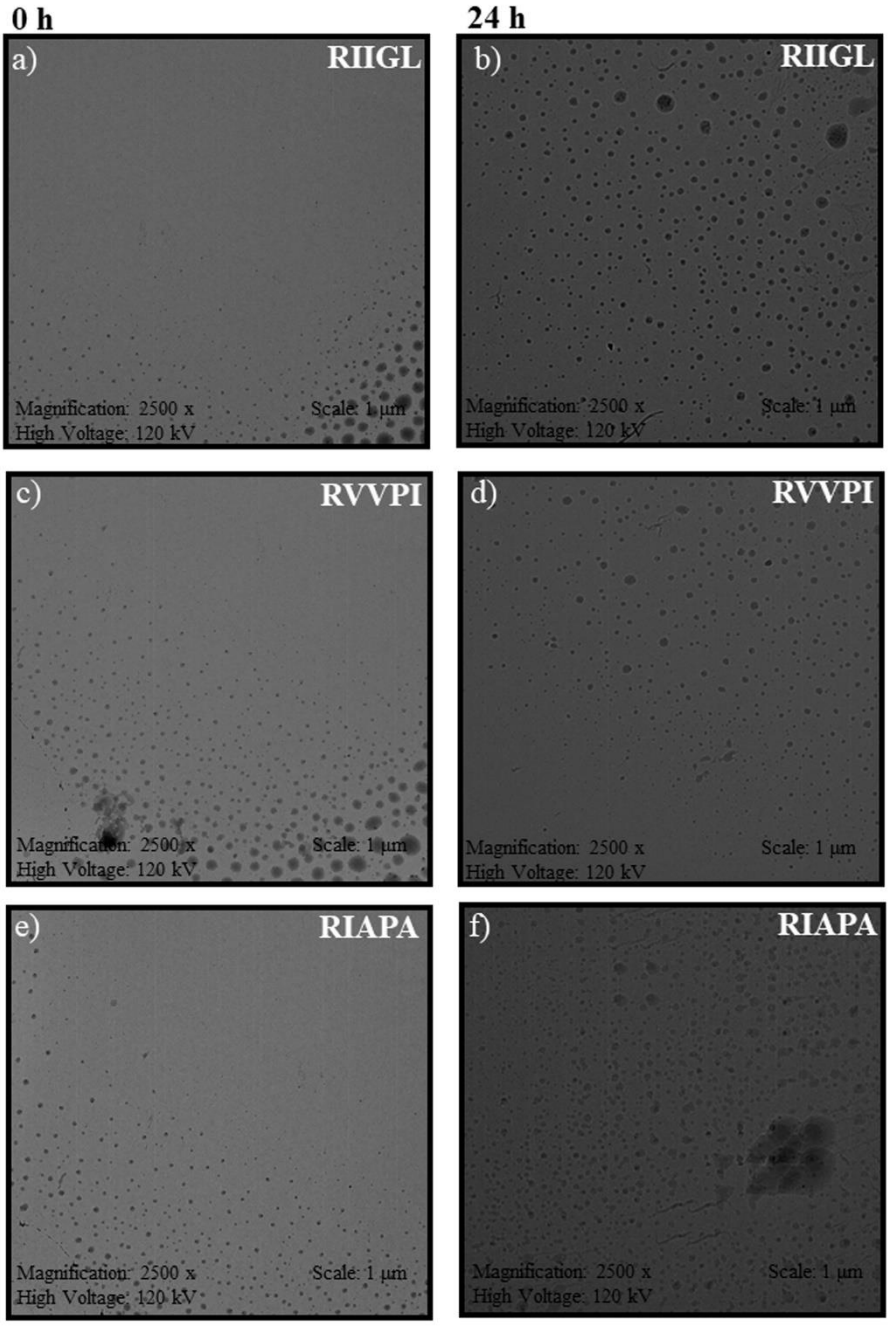

Figure 6.16: TEM images, [peptides]= 40 µM at 37 °C for 24 h constant agitation a) RIIGL t= 0 h; b) RIIGL t= 24 h; c) RVVPI t= 0 h; d) RVVPI, t= 24 h; e) RIAPA t= 0 h; f) RIAPA, t= 24 h. Scale bar: 1 µm.

6.4 Conclusion

In this work, MD simulations, ThT, and TEM studies have been performed to examine the ability of newly designed pentapeptides (RVVPI and RIAPA) to disaggregate pre-formed $A\beta_{42}$ aggregates. RIIGL, RVVPI, and RIAPA binds favourably to $A\beta_{42}$ protofibril with binding free

energies of –95.77 ± 1.99, –104.05 ± 0.16, –99.49 ± 0.03 kcal/mol, respectively, with the major contribution from the electrostatic interactions. A remarkably high RMSD and RMSF in Aβ$_{42}$ protofibril was noted in the presence of RVVPI than other peptides depicting higher structural perturbation and distortion in the protofibril structure. RVVPI displayed a more pronounced effect on the protofibril destabilization by reducing the sampling of β-sheets, lowering interchain hydrogen bonds, and disrupting K28-A42 salt bridges. The ThT fluorescence results depicted that RVVPI exhibited the highest inhibitory activity (Inhibition= 66.2%, IC_{50}= 5.57 ± 0.83 μM) against Aβ$_{42}$ aggregation and enhanced efficiency (62.4%) in the disassembly of pre-formed Aβ_{42} fibrils, which corroborated well with computational findings. The observed better efficiency of RVVPI to disaggregate the pre-formed Aβ$_{42}$ aggregates was due to the presence of proline and higher hydrophobic character. The study highlights a new peptide, RVVPI, derived from the C-terminal of Aβ$_{42}$ as a promising inhibitor of Aβ$_{42}$ aggregation and disassembly of the pre-formed Aβ_{42} fibrils, which, in turn, raises the tempting possibility that this sequence could prove to be a lead motif for designing effective antagonists of Aβ aggregation. Furthermore, the study illuminates the molecular mechanism by which RIIGL, RVVPI, and RIAPA destabilize Aβ$_{42}$ protofibril, which will be beneficial for the design of therapeutic candidates against other disease-related protein assemblies.

6.5 References

1. (a) Li, D.; Liu, C. Molecular rules governing the structural polymorphism of amyloid fibrils in neurodegenerative diseases, *Structure*, **2023**, *31*, 1335–1347; (b) Scheres, S.H.; Ryskeldi-Falcon, B.; Goedert, M. Molecular pathology of neurodegenerative diseases by cryo-EM of amyloids. *Nature* **2023**, *621*, 701–710; (c) Linse, S.; Knowles, T. Amyloids and protein aggregation, *Chem. Sci.*, **2023**, *14*, 6491–6492; (d) Buell, A. K. Stability matters, too–the thermodynamics of amyloid fibril formation. *Chem. Sci.* **2022**, *13*, 10177–10192.

2. (a) Nguyen, P. H.; Ramamoorthy, A.; Sahoo, B. R.; Zheng, J.; Faller, P.; Straub, J. E.; Dominguez, L.; Shea, J. E.; Dokholyan, N. V.; De Simone, A.; Ma, B. Amyloid oligomers: A joint experimental/computational perspective on Alzheimer's disease, Parkinson's disease, type II diabetes, and amyotrophic lateral sclerosis. *Chem. Rev*. **2021**, *121*, 2545−2647; (b) Oasa, S.; Kouznetsova, V. L.; Tiiman, A.; Vukojević, V.; Tsigelny, I. F.; Terenius, L. Small molecule decoys of aggregation for elimination of Aβ-peptide toxicity. *ACS Chem. Nerosci*. **2023**, *14*, 1575–1584; (c) (c) Lacham-Hartman, S.; Moshe, R.; Ben-Zichri, S.; Shmidov, Y.; Bitton, R.; Jelinek, R.; Papo, N. APPI-derived cyclic peptide enhances Aβ$_{42}$ aggregation and reduces Aβ$_{42}$-mediated membrane destabilization and cytotoxicity. *ACS Chem. Nerosci*. **2023**, *14*, 3385–3397; (d) Soto, C.; Pritzkow, S. Protein misfolding, aggregation, and conformational strains in neurodegenerative diseases. *Nat. Neurosci.* **2018**, *21*, 1332–1340; (e) Iadanza, M.G.; Jackson, M.P.; Hewitt, E.W.; Ranson, N.A.; Radford, S.E. A new era for understanding amyloid structures and disease. *Nat. Rev. Mol. Cell Biol.* **2018**, *19*, 755–773.

3. (a) Hippius, H.; Neundörfer, G. The discovery of Alzheimer's disease. *Dialogues Clin. Neurosci.* **2003**, *5*, 101−108; (b) Alzheimer, A. Über Eine Eigenartige Erkrankung Der Hirnrinde. *Allg. Zschr. Psychiat. Psych. gerichtl. Med.*, 1907, **64**, 146−148; (c) Goedert, M.; Spillantini, M.G. A century of Alzheimer's disease. *Science*, **2006**, *314*, 777−781; (d) Grøntvedt, G.R.; Schröder, T.N.; Sando, S.B.; White, L.; Bråthen, G.; Doeller, C.F. Alzheimer's disease. *Curr. Biol*. **2018**, *28*, R645–R649; (e) Y. L. Han, H. H. Yin, C. Xiao, M. T. Bernards, Y. He, Y. X. Guan, *ACS Chem. Neurosci*. **2023**, *14*, 4051–4061.

4. (a) Alzheimer's Disease International. https://www.alzint.org/about/dementia-facts-figures/ (access date: February 25, 2024); (b) https://www.who.int/news-room/fact-sheets/detail/dementia (access date: February 25, 2024).

5. (a) Ono, K. Alzheimer's disease as oligomeropathy. *Neurochem. Int.*, **2018**, *119*, 57–70; (b) Murphy, M.P.; LeVine III, H. Alzheimer's disease and the amyloid–β peptide. *J. Alzheimer's Dis.* **2010**, *19*, 311–323; (c) Stancu, I. C.; Vasconcelos, B.; Terwel, D.; Dewachter, I. Models of β-amyloid induced Tau-pathology: the long and "folded" road to understand the mechanism. *Mol. Neurodegener*. **2014**, *9*, 1−14.

6. (a) Sierra-Fonseca, J.A.; Gosselink, K.L. Tauopathy and neurodegeneration: A role for stress. *Neurobiol. Stress* **2018**, *9*, 105−112; (b) Šimić, G.; Babić Leko, M.; Wray, S.; Harrington, C.; Delalle, I.; Jovanov-Milošević, N.; Bažadona, D.; Buée, L.; De Silva, R.; Di Giovanni, G.; Wischik, C. Tau protein hyperphosphorylation and aggregation in Alzheimer's disease and other tauopathies, and possible neuroprotective strategies. *Biomolecules* **2016**, *6*, 6; (c) Nisbet, R.M.; Polanco, J.C.; Ittner, L.M.; Götz, J. Tau aggregation and its interplay with amyloid–β. *Acta. Neuropathol.* **2015**, *129*, 207–220.

7. (a) Hardy, J.; Selkoe, D. J. The amyloid hypothesis of Alzheimer's disease: progress and problems on the road to therapeutics. *Science* **2002**, *297*, 353−356; (b) Haass, C.; Selkoe, D. J. Soluble protein oligomers in neurodegeneration: lessons from the Alzheimer's amyloid β-peptide. *Nat. Rev. Mol. Cell Biol*. **2007**, *8*, 101−112; (c) Hamley, I.W. The amyloid beta peptide: a chemist's perspective. Role in Alzheimer's and fibrillization. *Chem. Rev.* **2012**, *112*, 5147–5192; (d) Mattson, M.P. Cellular actions of beta-amyloid precursor protein and its soluble and fibrillogenic derivatives. *Physiol. Rev.* **1997**, *77*, 1081–1132.

8. (a) Michaels, T. C.; Šarić, A.; Habchi, J.; Chia, S.; Meisl, G.; Vendruscolo, M.; Dobson, C. M.; Knowles, T. P. Chemical kinetics for bridging molecular mechanisms and macroscopic measurements of amyloid fibril formation. *Annu. Rev. Phys. Chem*. **2018**, *69*, 273−298; (b) Xi, W.; Vanderford, E.K.; Hansmann, U.H. Out-of-register Aβ$_{42}$ assemblies as models for neurotoxic oligomers and fibrils. *J. Chem. Theory Comput.* **2018**, *14*, 1099−1110; (c) Xi, W.; Hansmann, U.H. Ring-like N-fold models of Aβ$_{42}$ fibrils. *Sci. Rep.* **2017**, *7*, 1−14; (d) Ahmed, M.; Davis, J.; Aucoin, D.; Sato, T.; Ahuja, S.; Aimoto, S.; Elliott, J.I.; Van Nostrand, W.E.; Smith, S.O. Structural conversion of neurotoxic amyloid–β$_{1–42}$ oligomers to fibrils. *Nat. Struct. Mol. Biol.* **2010**, *17*, 561−567.

9. (a) Walsh, D. M.; Selkoe, D. J. Aβ oligomers – a decade of discovery. *J. Neurochem*. **2007**, *101*, 1172–1184; (b) Hayden, E.; Teplow, D. Amyloid β-protein oligomers and Alzheimer's disease, *Alzheimer's Res. Ther*. **2013**, *5*, 60; (c) Winner, B.; Jappelli, R.; Maji, S. K.; Desplats, P. A.; Boyer, L.; Aigner, S.; Hetzer, C.; Loher, T.; Vilar, M.; Campioni, S.; Tzitzilonis, C.; Soragni, A.; Jessberger, S.; Mira, H.; Consiglio, A.; Pham, E.; Masliah, E.; Gage, F. H.; Riek, R. *In vivo* demonstration that α-synuclein oligomers are toxic. *Proc. Natl. Acad. Sci. U. S. A.* **2011**, *108*, 4194−4199; (d) Kayed, R.; Head, E.; Thompson, J. L.; McIntire, T. M.; Milton, S. C.; Cotman, C. W.; Glabe, C. G. Common structure of soluble amyloid oligomers implies common mechanism of pathogenesis. *Science* **2003**, *300*, 486−489.

10. (a) Chen, Y.; Li, X.; Zhan, C.; Lao, Z.; Li, F.; Dong, X.; Wei, G. A comprehensive insight into the mechanisms of dopamine in disrupting Aβ protofibrils and inhibiting Aβ aggregation. *ACS Chem. Neurosci.* **2021**, *12*, 4007−4019; (b) Gong, Y.; Zhan, C.; Zou, Y.; Qian, Z.; Wei, G.; Zhang, Q. Serotonin and melatonin show different modes of action on Aβ42 protofibril destabilization. *ACS Chem. Neurosci.* **2021**, *12*, 799–809; (c) Zhang, Y.; Zhang, D.; Tang, Y.; Ren, B.; Liu, F.; Xu, L.; Chang, Y.; Zheng, J. Aromadendrin: a dual amyloid promoter to accelerate fibrillization and reduce cytotoxicity of both amyloid-β and hIAPP. *Mater. Adv.* **2020**, *1*, 1241−1252; (d) Zhan, C.; Chen, Y.; Tang, Y.; Wei, G. Green tea extracts EGCG and EGC display distinct mechanisms in disrupting Aβ42 protofibril. *ACS Chem. Neurosci.* **2020**, *11*, 1841−1851; (e) Fan, Q.; Liu, Y.; Wang, X.; Zhang, Z.; Fu, Y.; Liu, L.; Wang, P.; Ma, H.; Ma, H.; Seeram, N.P.; Zheng, J. Ginnalin A inhibits aggregation, reverses fibrillogenesis, and alleviates cytotoxicity of amyloid β (1–42). *ACS Chem. Neurosci.* **2020**, *11*, 638−647; (f) Doig, A. J. Peptide inhibitors of β-amyloid aggregation. *Curr. Opin. Drug Discov. Dev*. **2007**, *10*, 533–539; (g) Yang, C.; Zhu, X.; Li, J.; Shi, R. Exploration of the mechanism for LPFFD inhibiting the formation of β-sheet conformation of Aβ(1–42) in water. *J. Mol. Model*. **2010**, *6*, 813–821; (h) Gestwicki, J. E.; Crabtree, G. R.; Graef, I. A. Harnessing chaperons to generate small molecule inhibitors of amyloid β aggregation. *Science* **2004**, *306*, 865–869.

11. (a) McDade, E.; Cummings, J.L.; Dhadda, S.; Swanson, C.J.; Reyderman, L.; Kanekiyo, M.; Koyama, A.; Irizarry, M.; Kramer, L.D.; Bateman, R.J. Lecanemab in patients with early Alzheimer's disease: Detailed results on biomarker, cognitive, and clinical effects from the randomized and open-label extension of the phase 2 proof-of-concept study. *Alzheimers Res. Ther.* **2022**, *14*, 191; (b) Van Dyck, C.H.; Swanson, C.J.; Aisen, P.; Bateman, R.J.; Chen, C.; Gee, M.; Kanekiyo, M.; Li, D.; Reyderman, L.; Cohen, S.; Froelich, L. Lecanemab in early Alzheimer's disease. *N. Engl. J. Med*., **2023**, *388*, 9–21.

12. (a) Ren, B.; Tang, Y.; Zhang, D.; Liu, Y.; Zhang, Y.; Chen, H.; Hu, R.; Zhang, M.; Zheng, J. Conformational-specific self-assembled peptides as dual-mode, multi-target inhibitors and detectors for different amyloid proteins. *J. Mater. Chem. B* **2022**, *10*, 1754−1762; (b) Wang, L.; Wang, N.; Zhang, W.; Cheng, X.; Yan, Z.; Shao, G.; Wang, Xi.; Wang, R.; C. Fu, R. Therapeutic peptides: current applications and future directions. *Sig. Transduct. Target. Ther.* **2022**, *7*, 48; (c) Armiento, V.; Spanopoulou, A.; Kapurniotu, A. Peptide-based molecular strategies to interfere with protein misfolding, aggregation, and cell degeneration. *Angew. Chem. Int. Ed*. **2020**, *59*, 3372−3384; (d) Ryan, P.; Patel, B.; Makwana, V.; Jadhav, H.R.; Kiefel, M.; Davey, A.; Reekie, T.A.; Rudrawar, S.; Kassiou, M. Peptides, peptidomimetics, and carbohydrate–peptide conjugates as amyloidogenic aggregation inhibitors for Alzheimer's disease. *ACS Chem. Neurosci.*, **2018**, *9*, 1530–1551; (e) Goyal, D.; Shuaib, S.; Mann, S.; Goyal, B. Rationally designed peptides and peptidomimetics as inhibitors of amyloid–β (Aβ) aggregation: Potential therapeutics of Alzheimer's disease. *ACS Comb. Sci.* **2017**, *19*, 55−80.

13. (a) Bhattacharjee, S.; Bhattacharyya, R. PRFF peptide mimic interferes with toxic fibrin–Aβ$_{42}$ interaction by emulating the Aβ binding interface on fibrinogen. *ACS Chem. Neurosci.* **2021**, *12*, 4144–4152; (b) Lei, L.; Zou, Z.; Liu, J.; Xu, Z.; Fu, Y.; Tian, Y.; Zhang, W. Multifunctional peptide-assembled micelles for simultaneously reducing amyloid–β and reactive oxygen species. *Chem. Sci.* **2021**, *12*, 6449; (c) Roy, R.; Pradhan, K.; Khan, J.; Das, G.; Mukherjee, N.; Das, D.; Ghosh, S. Human serum albumin-inspired glycopeptide-based multifunctional inhibitor of amyloid–β toxicity. *ACS Omega* **2020**, *5* 18628–18641; (d) Mondal, P.; Khan, J.; Gupta, V.; Ghosh, S. *In silico* approach for designing potent neuroprotective hexapeptide. *ACS Chem. Neurosci*. **2019**, *10*, 3018–3030.

14. (a) Rajasekhar, K.; Madhu, C.; Govindaraju, T. Natural tripeptide-based inhibitor of multifaceted amyloid β toxicity. *ACS Chem. Nerosci*. **2016**, *7*, 1300–1310; (b) Kim, J. R.; Murphy, R. M. Mechanism of accelerated assembly of β-amyloid filaments into fibrils by KLVFFK. *Biophys J*. **2004**, *86*, 3194–3203; (c) Kumar, J.; Namsechi, R.; Sim, V. L. Structure-based peptide design to modulate amyloid beta aggregation and reduce cytotoxicity. *PLoS ONE* **2015**, *10*, e0129087; (d) Soto, C.; Kindy, M. S.; Baumann, M.; Frangione, B. Inhibition of Alzheimer's amyloidosis by peptides that prevent β-sheet conformation. *Biochem Biophys Res Commun*. **1996**, *226*, 672–680; (e) Wang, F.; Zhou, X. L.; Yang, Q. G. A peptide that binds specifically to the β-amyloid of Alzheimer's disease: selection and assessment of anti-β-amyloid neurotoxic effects. *PLoS ONE* **2011**, *6*, e27649; (f) Bett. C. K.; Serem, W. K.; Fontenot, K. R.; Hammer, R. P.; Garno, J. C. Effects of peptides derived from terminal modifications of the Aβ central hydrophobic core on Aβ fibrillization. *ACS Chem Nerosci*. **2010,** *1*, 661–678; (g) Rajasekhar, K.; Suresh, S. N.; Manjithaya, R.; Govindaraju, T. Rationally designed peptidomimetic modulators of Aβ toxicity in Alzheimer's disease. *Sci Rep*. **2015**, *5*, 8139–8148; (h) Zhang, L.; Yagnik, G.; Peng, Y. Kinetic studies of inhibition of the amyloid beta (1–42)

aggregation using a ferrocene-tagged β-sheet breaker peptide. *Anal Biochem*. **2013**, *434*, 292–299; (i) Bruinsma, I. B.; Karawajczyk, A.; Schaftenaar, G.; de Waal, R. M. W.; Verbeek, M. M.; van Delft, F. L. A rational design to create hybrid β-sheet breaker peptides to inhibit aggregation and toxicity of amyloid-β. *Med. Chem. Commun*. **2011**, *2*, 60−64.

15. Jarrett, J. T.; Berger, E. P.; Lansbury Jr, P. T. The Carboxy Terminus of the β Amyloid Protein is Critical for the Seeding of Amyloid Formation: Implications for the Pathogenesis of Alzheimer's Disease. *Biochemistry* **1993**, *32,* 4693–4697.

16. Fradinger, E. A.; Monien, B. H.; Urbanc, B.; Lomakin, A.; Tan, M.; Li, H.; Spring, S. M.; Condron, M. M.; Cruz, L.; Xie, C.-W.; Benedek, G. B.; Bitan G. C-Terminal Peptides Coassemble into Aβ$_{42}$ Oligomers and Protect Neurons Against Aβ$_{42}$-Induced Neurotoxicity. *Proc. Natl. Acad. Sci.* U.S.A. **2008**, *105*, 14175–14180.

17. (a) Pike, C. J.; Walencewicz-Wasserman, A. J.; Kosmoski, J.; Cribbs, D. H.; Glabe, C. G.; Cotman, C. W. Structure-Activity Analyses of β-Amyloid Peptides: Contributions of the β25-35 Region to Aggregation and Neurotoxicity. *J. Neurochem.* **1995**, *64*, 253–265. (b) Pike, C. J.; Burdick, D.; Walencewicz–Wasserman, A. J.; Glabe, C. G.; Cotman, C. W. Neurodegeneration Induced by β-amyloid Peptides In Vitro: The Role of Peptide Assembly State. *J. Neurosci.* **1993**, *13*, 1676–1687.

18. Bansal, S.; Maurya I. K.; Yadav, N.; Thota, C. K.; Kumar, V.; Tikoo, K.; Chauhan, V. S.; Jain, R. C-terminal fragment, Aβ$_{32-37}$, analogues protect against Aβ aggregation-induced toxicity. *ACS Chem. Neurosci*. **2016**, *7,* 615–623.

19. Harkany, T.; ÁbraháAm, I.; Laskay, G.; Timmerman, W.; Jost, K.; Zarándi, M.; Penke, B.; Nyakas, C.; Luiten, P.G. Propionyl-IIGL tetrapeptide antagonizes β-amyloid excitotoxicity in rat nucleus basalis. *Neuroreport* **1999**, *10*, 1693–1698.

20. Fülöp, L.; Zarándi, M.; Datki, Z.; Soós, K.; Penke, B. β-Amyloid-derived pentapeptide RIIGLa inhibits Aβ1–42 aggregation and toxicity. *Biochem. Biophys. Res. Commun*. **2004**, *324,* 64–69.

21. Kaur, A.; Goyal, B. Identification of new pentapeptides as potential inhibitors of amyloid–β42 aggregation using virtual screening and molecular dynamics simulations. *J. Mol. Graph. Model*. **2023**, 108558.

22. Gremer, L.; Schölzel, D.; Schenk, C.; Reinartz, E.; Labahn, J.; Ravelli, R.B.; Tusche, M.; Lopez-Iglesias, C.; Hoyer, W.; Heise, H.; Willbold, D. Fibril structure of amyloid-β (1–42) by cryo–electron microscopy. *Science* **2017**, *358*, 116–119.

23. Dallakyan, S.; Olson, A. J. Small-molecule library screening by docking with PyRx. *Methods Mol. Biol.* **2015**, *1263*, 243–250.

24. Trott, O.; Olson, A. J. AutoDock vina: improving the speed and accuracy of docking with a new scoring function, efficient optimization and multithreading. *J. Comput. Chem.* **2010**, *31*, 455–461.

25. (a) Lin, Z.; van Gunsteren, W.F. Refinement of the application of the GROMOS 54A7 force field to β-peptides. *J. Comput. Chem.* **2013**, *34*, 2796–2805; (b) Huang, W., Lin,

Z.; van Gunsteren, W.F. Validation of the GROMOS 54A7 force field with respect to β-peptide folding *J. Chem. Theory Comput.* **2011**, *7*, 1237–1243; (c) Schmid, N., Eichenberger, A.P., Choutko, A., Riniker, S., Winger, M., Mark, A.E.; van Gunsteren, W.F. Definition and testing of the GROMOS force-field versions 54A7 and 54B7. *Eur. Biophys. J.* **2011**, *40*, 843–856.

26. Berendsen, H.J.; Postma, J.P.; van Gunsteren, W.F.; Hermans, J. Interaction models for water in relation to protein hydration. *Intermolecular Forces*. Dordrecht, Netherland: Reidel. **1981**, 331–342.

27. (a) Jia, L.; Wang, W.; Yan, Y.; Hu, R.; Sang, J.; Zhao, W.; Wang, Y.; Wei, W.; Cui, W.; Yang, G.; Lu, F. General aggregation-induced emission probes for amyloid inhibitors with dual inhibition capacity against amyloid β-protein and α-synuclein. *ACS Appl. Mater. Interfaces* **2020**, *12*, 31182–31194; (b) Xing, X.; Liu, C.; Ali, A.; Kang, B.; Li, P.; Ai, H. Novel disassembly mechanisms of sigmoid Aβ$_{42}$ protofibrils by introduced neutral and charged drug molecules. *ACS Chem. Neurosci.* **2020**, *11*, 45−56.

28. (a) Abraham, M. J.; Murtola, T.; Schulz, R.; Páll, S.; Smith, J. C.; Hess, B.; Lindahl, E. GROMACS: High performance molecular simulations through multi–level parallelism from laptops to supercomputers. *SoftwareX* **2015**, *1–2*, 19–25; (b) Van Der Spoel, D.; Lindahl, E.; Hess, B.; Groenhof, G.; Mark, A.E.; Berendsen, H.J. GROMACS: fast, flexible, and free. *J. Comput. Chem.* **2005**, *26*, 1701–1718.

29. Somavarapu, A. K.; Kepp, K. P. The dependence of amyloid–β dynamics on protein force fields and water models. *ChemPhysChem* **2015**, *16*, 3278–3289.

30. (a) Gupta, S.; Dasmahapatra, A. K. Destabilization potential of phenolics on Aβ fibrils: Mechanistic insights from molecular dynamics simulation. *Phys. Chem. Chem. Phys.* **2020**, *22*, 19643–19658; (b) Pal, S.; Banerjee, S.; Kumar, A.; Prabhakaran, E. N. H–bond surrogate-stabilized shortest single-turn α–helices: sp^2 constraints and residue preferences for the highest α–helicities. *ACS Omega* **2020**, *5*, 13902–13912.

31. Hess, B.; Bekker, H.; Berendsen, H. J. C.; Fraaije, J. G. E. M. LINCS: A linear constraint solver for molecular simulations. *J. Comput. Chem.* **1997**, *18*, 1463–1472.

32. (a) Essmann, U.; Perera, L.; Berkowitz, M. L.; Darden, T.; Lee, H.; Pedersen, L. G. A smooth particle mesh ewald method. *J. Chem. Phys.* **1995**, *103*, 8577–8593; (b) Darden, T., York, D.; Pedersen, L. The effect of long-range electrostatic interactions in simulations of macromolecular crystals–a comparison of the ewald and truncated list methods. *J. Chem. Phys.*, 1993, **98**, 10089–10092.

33. Bussi, G.; Donadio, D.; Parrinello, M. Canonical sampling through velocity rescaling. *J. Chem. Phys.* **2007**, *126*, 014101.

34. Parrinello, M.; Rahman, A. Polymorphic transitions in single crystals: A new molecular dynamics method. *J. Appl. Phys.* **1981**, *52*, 7182.

35. Humphrey, W.; Dalke, A.; Schulten, K. VMD – Visual Molecular Dynamics. *J. Mol. Graphics Modell*. **1996**, *14*, 33−38.

36. DeLano, W.L. The PyMOL molecular graphics system, http://www.pymol.org, 2002.

37. Kabsch, W.; Sander, C. Dictionary of protein secondary structure: pattern recognition of hydrogen–bonded and geometrical features. *Biopolymers* **1983**, *12*, 2577–2637.

38. Kumari, R.; Kumar, R.; Lynn, A. g_mmpbsa−A GROMACS tool for high-throughput MM-PBSA calculations. *J. Chem. Inf. Model*. **2014**, *54*, 1951−1962.

39. Genheden, S.; Ryde, U. The MM/PBSA and MM/GBSA methods to estimate ligand-binding affinities. *Expert Opin. Drug Discov.* **2015**, *10*, 449–461.

40. (a) Kaur, A.; Goyal, D.; Goyal, B. An α-helix mimetic oligopyridylamide, ADH-31, modulates Aβ$_{42}$ monomer aggregation and destabilizes protofibril structures: Insights from molecular dynamics simulations. *Phys. Chem. Chem. Phys.* **2020**, *22*, 28055–28073; (b) Shuaib, S.; Saini, R.K.; Goyal, D.; Goyal, B. Insights into the inhibitory mechanism of dicyanovinyl-substituted J147 derivative against Aβ$_{42}$ aggregation and protofibril destabilization: A molecular dynamics simulation study. *ChemistrySelect* **2017**, *2*, 1645–1657.

41. Kaur, A.; Mann, S.; Kaur, A.; Priyadarshi, N.; Goyal, B.; Singhal, N.K.; Goyal, D. Multi-target-directed triazole derivatives as promising agents for the treatment of Alzheimer's disease. *Bioorg. Chem.* **2019**, *87*, 572−584.

42. (a) Sackmann, C.; Hallbeck, M. Oligomeric amyloid−β induces early and widespread changes to the proteome in human iPSC-derived neurons. *Sci. Rep.* **2020**, *10*, 6538−6550; (b) Cline, E. N.; Bicca, M. A.; Viola, K. L.; Klein, W. L. The amyloid-oligomer hypothesis: Beginning of the third decade. *J. Alzheimers Dis.* **2018**, *64*, S567–S610; (c) Sengupta, U.; Nilson, A. N.; Kayed, R. The role of amyloid−β oligomers in toxicity, propagation, and immunotherapy. *EbioMedicine* **2016**, *6*, 42–49.

43. Cheon, M.; Kang, M.; Chang, I. Polymorphism of fibrillar structures depending on the size of assembled Aβ$_{17–42}$ peptides. *Sci. Rep*. **2016**, *6*, 38196.

44. Bitan, G.; Kirkitadze, M.D.; Lomakin, A.; Vollers, S.S.; Benedek, G.B.; Teplow, D.B. Amyloid β-protein (Aβ) assembly: Aβ40 and Aβ42 oligomerize through distinct pathways. *Proc. Natl. Acad. Sci. U.S.A.* **2003**, *100*, 330–335.

45. Wolff, M.; Zhang-Haagen, B.; Decker, C.; Barz, B.; Schneider, M.; Biehl, R.; Radulescu, A.; Strodel, B.; Willbold, D.; Nagel-Steger, L. Aβ$_{42}$ pentamers/hexamers are the smallest detectable oligomers in solution. *Sci. Rep*. **2017**, *7*, 2493.

46. Jarrett, J.T.; Berger, E.P.; Lansbury Jr, P.T. The carboxy terminus of the amyloid protein is critical for the seeding of amyloid formation: Implications for the pathogenesis of Alzheimer's disease. *Biochemistry* **1993**, *32*, 4693–4697.

47. (a) Kumar, J.; Namsechi, R.; Sim, V. L. Structure-based peptide design to modulate amyloid beta aggregation and reduce cytotoxicity. *PLoS One* **2015**, *10*, e0129087; (b) Inouye, H.; Gleason, K.A.; Zhang, D.; Decatur, S.M.; Kirschner, D.A. Differential effects of Phe19 and Phe20 on fibril formation by amyloidogenic peptide Aβ$_{16–22}$ (Ac–KLVFFAE–NH$_2$). *Proteins Struct. Funct. Bioinf.* **2010**, *78*, 2306–2321; (c) Mager, P.P.; Fischer, K. Simulation of the Lipophilic and Antigenic Cores of the Aβ (1–42) Peptide of Alzheimer's Disease. *Mol. Simul.* **2001**, *27*, 237–242; (d) Jarmuła, A.; Zubalska, M.; Stępkowski, D. Consecutive aromatic residues are required for improved efficacy of β-

sheet breakers. *Int. J. Mol. Sci.* **2022**, *23*, 5247; (e) Watanabe, K.; Segawa, T.; Nakamura, K.; Kodaka, M.; Okuno, H.; Konakahara, T. Identification of the molecular interaction site of amyloid β peptide by using a fluorescence assay *J. Pept. Res.* **2001**, *58*, 342–346; (f) Jarmuła, A.; Ludwiczak, J.; Stępkowski, D. β-sheet breakers with consecutive phenylalanines: Insights into mechanism of dissolution of β-amyloid fibrils. *Proteins Struct. Funct. Bioinf.* **2021**, *89*, 762–780.

48. Cheng, X.; Ivanov, I. Molecular dynamics. *Comput. Toxicol*. **2012**, *1*, 243–285.

49. Dong, X.; Tang, Y.; Zhan, C.; Wei, G. Green tea extract EGCG plays a dual role in Aβ$_{42}$ protofibril disruption and membrane protection: A molecular dynamic study. *Chem. Phys. Lipids* **2021**, *234*, 105024.

50. Fuglebakk, E.; Echave, J.; Reuter, N. Measuring and comparing structural fluctuation patterns in large protein datasets. *Bioinformatics* **2012**, *28*, 2431–2440.

51. Nei, R.Z.; Zhang, S.S.; Yan, X.K.; Feng, K.; Lao, Y.J.; Bao, Y.R. Molecular insights into the structure destabilization effects of ECG and EC on the Aβ protofilament: An all-atom molecular dynamics simulation study. *Int. J. Biol. Macromol.* **2023**, *253*, 127002.

52. Berhanu, W.M.; Hansmann, U.H. Side-chain Hydrophobicity and the Stability of Aβ$_{16–22}$ Aggregates. *Protein Sci*. **2012**, *21*, 1837–1848.

53. Barale, S. S.; Parulekar, R. S.; Fandilolu, P. M.; Dhanavade, M. J.; Sonawane, K. D. Molecular insights into destabilization of Alzheimer's Aβ protofibril by arginine containing short peptides: a molecular modeling approach. *ACS Omega* **2019**, *4*, 892–903.

54. W. Han, K. Schulten, *J. Am. Chem. Soc.* **2014**, *136*, 12450– 12460.

55. Zhan, C.; Chen, Y.; Tang, Y.; Wei, G. Green tea extracts EGCG and EGC display distinct mechanisms in disrupting Aβ$_{42}$ protofibril. *ACS Chem. Neurosci*. **2020**, *11*, 1841–1851.

56. Li, F.; Zhan, C.; Dong, X.; Wei, G. Molecular mechanisms of resveratrol and EGCG in the inhibition of Aβ$_{42}$ aggregation and disruption of Aβ 42 protofibril: Similarities and differences. *Phys. Chem. Chem. Phys.* **2021**, *23*, 18843–18854.

57. (a) Grasso, G.; Rebella, M.; Muscat, S.; Morbiducci, U.; Tuszynski, J.; Danani, A.; Deriu, M.A. Conformational dynamics and stability of U-shaped and S-shaped amyloid–β assemblies. *Int. J. Mol. Sci.* **2018**, *19*, 571; (b) Cheon, M.; Hall, C.K.; Chang, I. Structural conversion of Aβ$_{17–42}$ peptides from disordered oligomers to U-shape protofilaments *via* multiple kinetic pathways. *PLoS Comput. Biol.* **2015**, *11*, e1004258; (c) Paravastu, A.K.; Leapman, R.D.; Yau, W.M.; Tycko, R. Molecular structural basis for polymorphism in Alzheimer's β-amyloid fibrils. *Proc. Natl. Acad. Sci. U.S.A.* **2008**, *105***,** 18349–18354**.**

58. (a) Colvin, M.T.; Silvers, R.; Ni, Q.Z.; Can, T.V.; Sergeyev, I.; Rosay, M.; Donovan, K.J.; Michael, B.; Wall, J.; Linse, S.; Griffin, R.G. Atomic resolution structure of monomorphic Aβ$_{42}$ amyloid fibrils. *J. Am. Chem. Soc.* **2016**, *138*, 9663–9674; (b) Xiao, Y.; Ma, B.; McElheny, D.; Parthasarathy, S.; Long, F.; Hoshi, M.; Nussinov, R.; Ishii, Y. Aβ (1–42) fibril structure illuminates self–recognition and replication of amyloid in Alzheimer's disease. *Nat. Struct. Mol. Biol.* **2015**, *22*, 499–505; (c) Nguyen, P.H.;

Derreumaux, P. An S-shaped Aβ$_{42}$ cross-β hexamer embedded into a lipid bilayer reveals membrane disruption and permeability. *ACS Chem. Neurosci.* **2023**, *14*, 936–946.

59. (a) Donald, J.E.; Kulp, D.W.; DeGrado, W.F. Salt bridges: Geometrically specific, designable interactions. *Proteins: Struct. Funct. Genet*. **2011**, *79*, 898–915; (b) Musafia, B.; Buchner, V.; Arad, D. Complex salt bridges in proteins: statistical analysis of structure and function. *J. Mol. Biol*. **1995**, *254*, 761–770; (c) Kumar, S.; Nussinov, R. Close-range electrostatic interactions in proteins. *ChemBioChem* **2002**, *3*, 604–617.

60. Nilsson, M.R. Techniques to study amyloid fibril formation *in vitro*. *Methods* **2004**, *34*, 151−160.

61. (a) Soto, C. M.; Kindy, S.; Baumann, M.; Frangione, B. Inhibition of Alzheimer's amyloidosis by peptides that prevent β-sheet conformation. *Biochem. Biophys. Res. Commun*. **1996**, *226*, 672–680; (b) Viet, M. H.; Ngo, S. T.; Lam, N. S.; Li, M. S. Inhibition of aggregation of amyloid peptides by beta-sheet breaker peptides and their binding affinity. *J. Phys. Chem. B* **2011**, *115*, 7433–7446; (c) Li, S. C.; Goto, N. K.; Williams, K. A.; Derer, C. M. α-helical, but not β-sheet, propensity of Proline is determined by peptide environment. *Proc. Natl. Acad. Sci. U. S. A*. **1996**, *93*, 6676–6681.

62. (a) Das, U.; Hariprasad, G.; Ethayathulla, A. S.; Manral, P.; Das, T. K.; Pasha, S.; Mann, A.; Ganguli, M.; Verma, A. K.; Bhat, R.; Chandrayan, S. K.; Ahmed, S.; Sharma, S.; Kaur, P.; Singh, T. P.; Srinivasan, A. Inhibition of protein aggregation: supramolecular assemblies of arginine hold the key. *PloS One* **2007**, *2*, 1176; (b) Shukla, D.; Trout, B. L. Interaction of arginine with proteins and the mechanism by which it inhibits aggregation. *J. Phys. Chem. B* **2010**, *114*, 13426–13438.

Spectras

a)

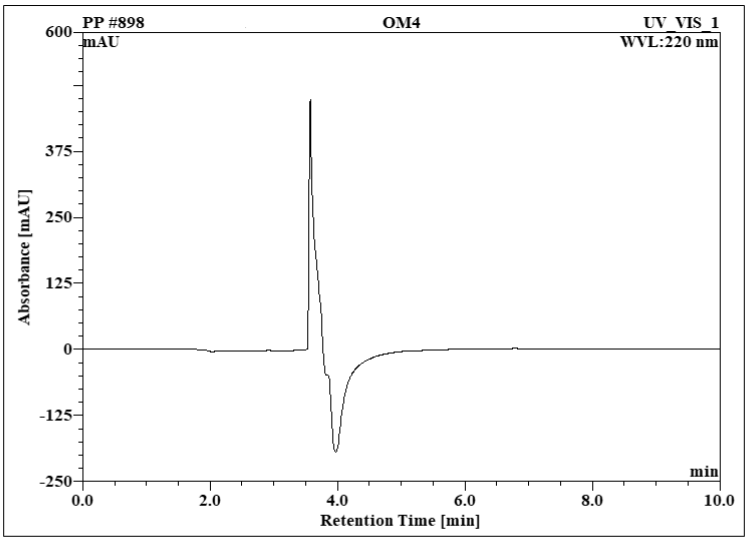

No.	Ret.Time	Peak Name	Height	Area	Rel.Area	Amount	Type
	min		mAU	mAU*min	%		
1	3.57	n.a.	488.283	52.374	100.00	n.a.	BMB*
Total:			488.283	52.374	100.00	0.000	

b)

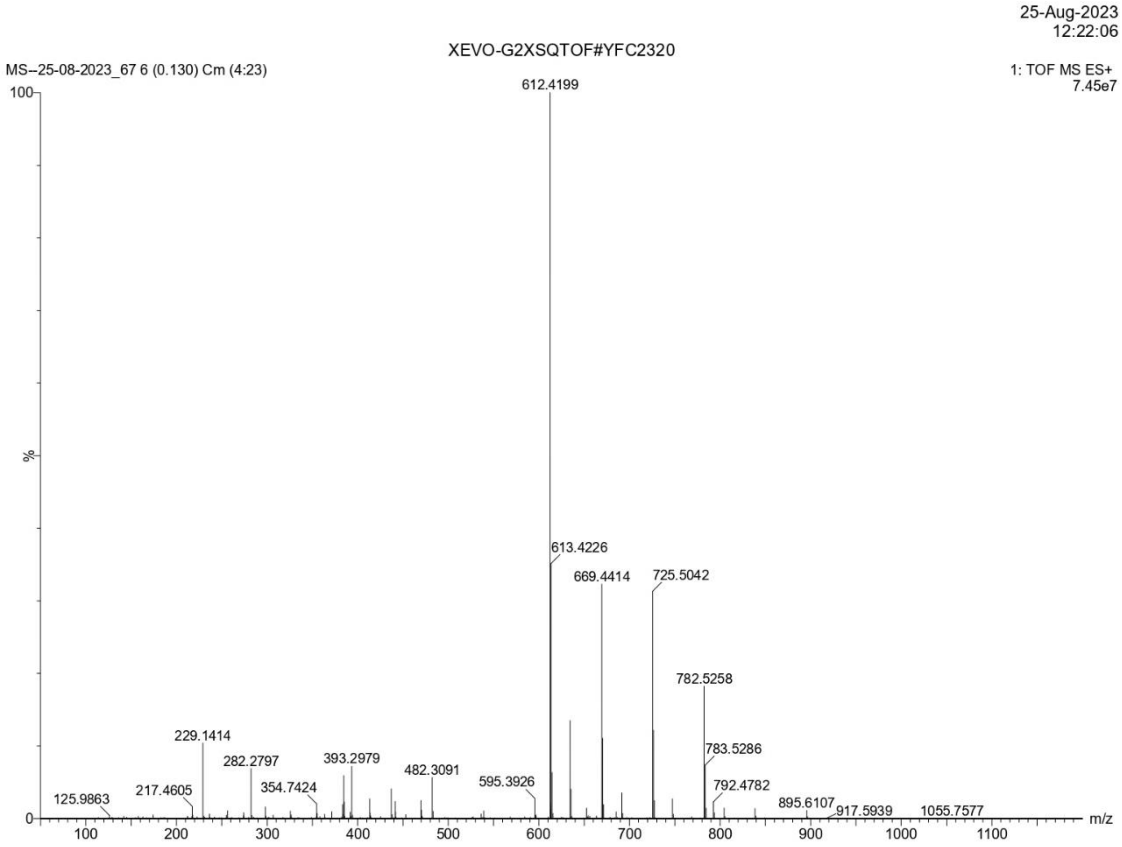

HPLC chromatogram (panel a) and HRMS (panel b) of RIIGL.

a)

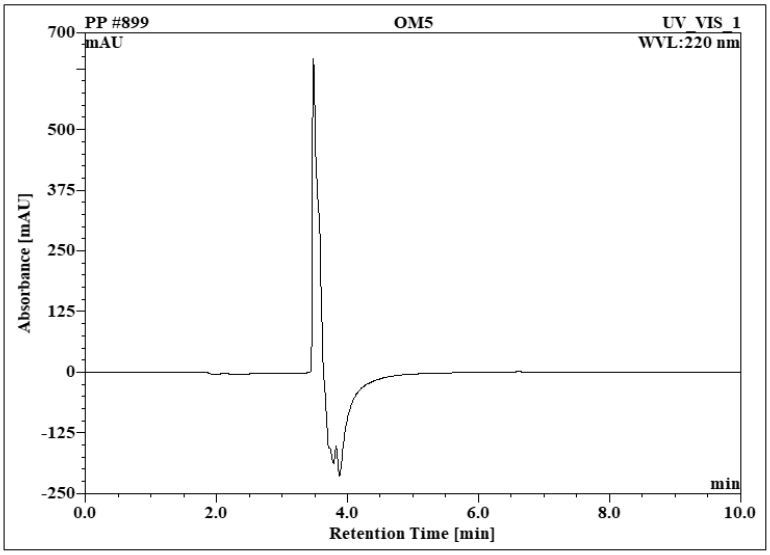

No.	Ret.Time	Peak Name	Height	Area	Rel.Area	Amount	Type
	min		mAU	mAU*min	%		
1	3.48	n.a.	633.796	60.017	100.00	n.a.	BMB*
Total:			633.796	60.017	100.00	0.000	

b)

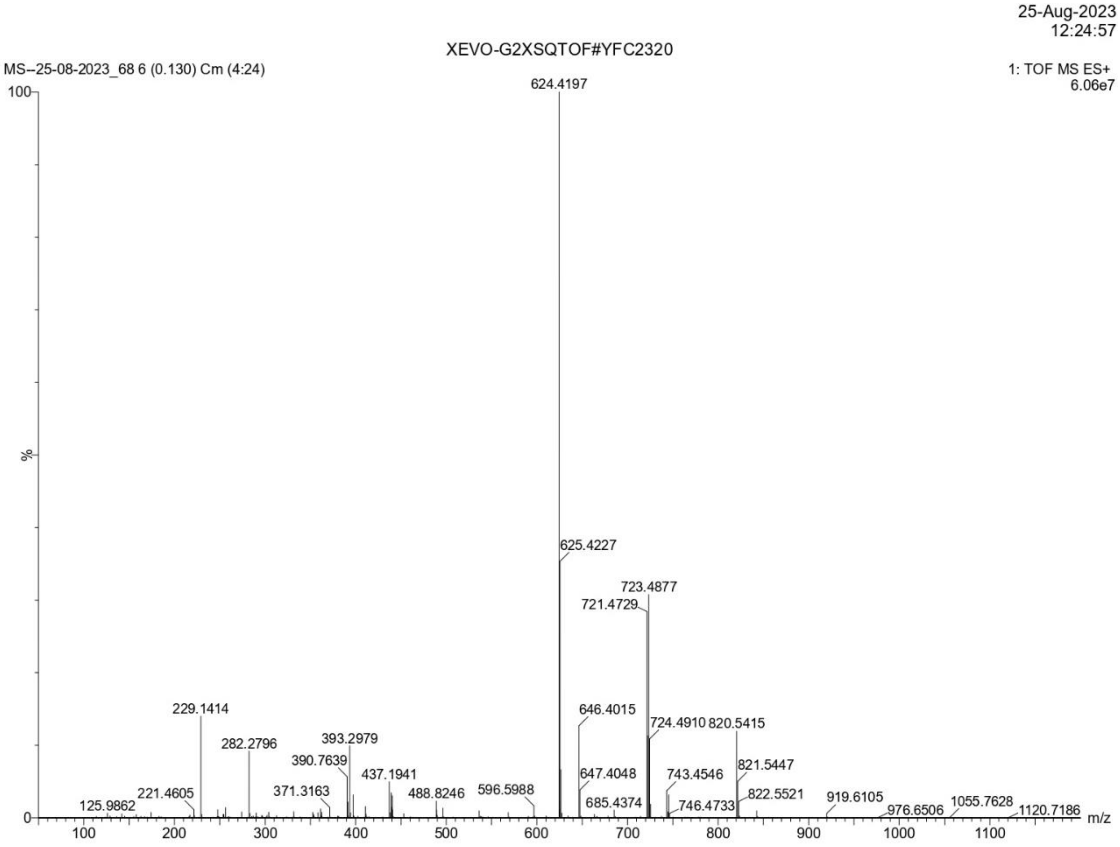

HPLC chromatogram (panel a) and HRMS (panel b) of RVVPI.

a)

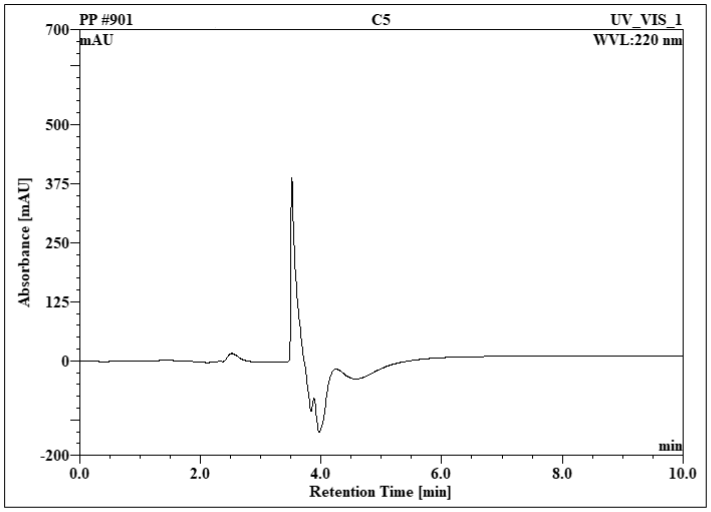

No.	Ret.Time	Peak Name	Height	Area	Rel.Area	Amount	Type
	min		mAU	mAU*min	%		
1	2.67	n.a.	0.521	1.874	5.07	n.a.	BM *
2	3.52	n.a.	388.935	35.094	94.93	n.a.	MB*
Total:			389.456	36.968	100.00	0.000	

b)

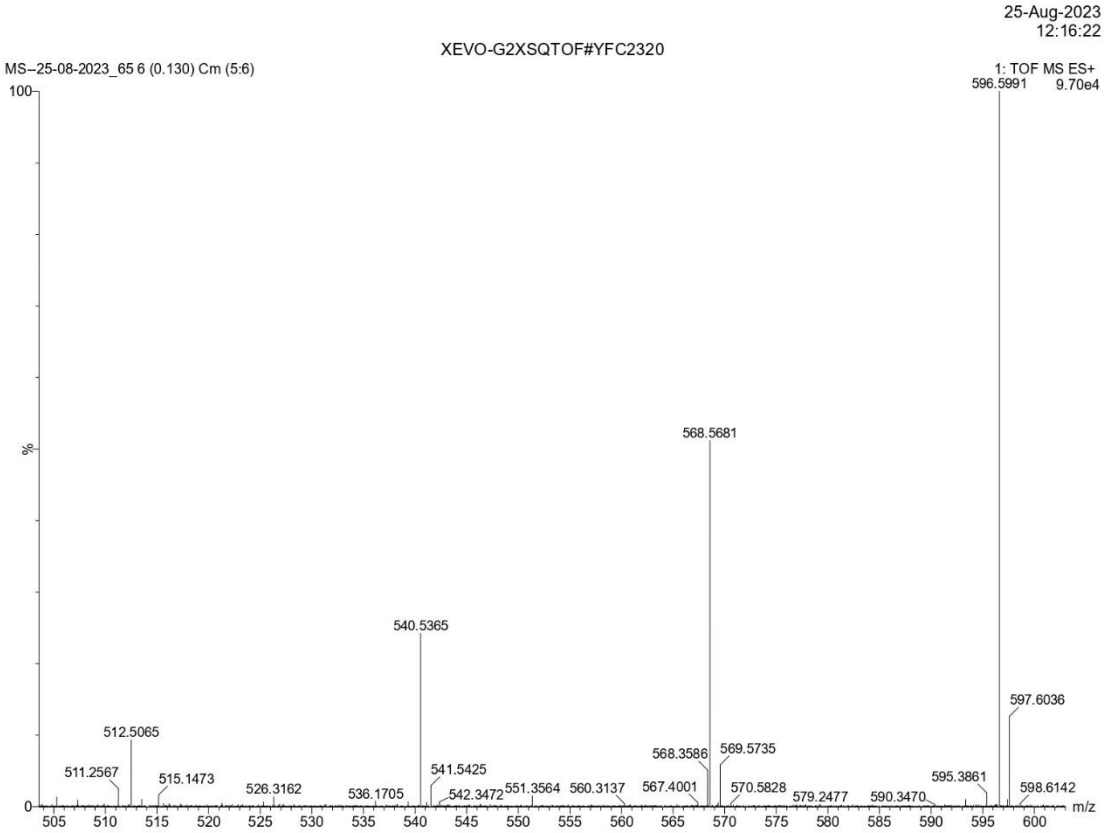

HPLC chromatogram (panel a) and HRMS (panel b) of RIAPA.

Chapter 7

Summary and conclusions

The misfolding of proteins and their subsequent aggregation to amyloids are strongly correlated with several human amyloidoses like Alzheimer's disease (AD), amyotrophic lateral sclerosis, type 2 diabetes (T2D), Parkinson's disease, *etc*. One of the pathological hallmarks of T2D is the presence of fibrillar amyloid deposits and soluble oligomers formed by the aggregation of human islet amyloid polypeptide (hIAPP). The pathological hallmarks of AD comprise extracellular depositions of amyloid-β (Aβ) and the intracellular formation of thread-like neurofibrillary tangles composed of tau protein.

Increasing evidence suggests that initially formed soluble oligomeric assemblies of hIAPP and Aβ are the main cytotoxic species in T2D and AD. The experimental characterization of the toxic oligomers is a significant challenge due to the heterogeneity and transient nature of the oligomeric assemblies. The rational design of inhibitors against oligomeric assemblies involved in protein aggregation-derived diseases will be greatly aided by the structural, dynamic, and mechanistic insights from computational studies. Despite extensive experimental research on protein aggregation-derived diseases, the starting point for the oligomeric assemblies and subsequent fibril formation has been not fully understood. In this regard, molecular dynamics (MD) simulation results in the present thesis will be beneficial to illuminate the molecular mechanism of amyloid aggregation and the inhibitory mechanism of peptide inhibitors against amyloid aggregation in T2D and AD.

The thesis is organized in the following manner: the comprehensive overview of amyloids, mechanism of amyloid formation, hallmarks of T2D and AD, and recent literature related to peptide-based inhibitors hIAPP and $A\beta_{42}$ aggregation, underlying causes of T2D and AD were reviewed in Chapter 1. Chapter 2 presented the details of computational approaches and biophysical methods used in the present thesis. The various MD analysis tools, solid phase peptide synthesis protocol, and description of biophysical assays used to evaluate the inhibitory activity of peptides against $A\beta_{42}$ aggregation are described.

Chapter 3 presented the molecular mechanism of the inhibition of hIAPP aggregation in the presence of ANFLVH using MD simulations. MD simulation analysis highlighted that ANFLVH prevented the conformational transition of hIAPP by stabilizing the native helical conformation. The binding free energy analysis by the molecular mechanics Poisson–Boltzmann surface area (MM-PBSA) method highlighted favourable binding ($\Delta G_{binding}$= – 49.90 ± 0.67 kcal/mol) of ANFLVH with hIAPP and depicted a significant contribution of the

van der Waals interaction term (ΔE_{vdW}= –46.33 ± 0.32 kcal/mol) in the stability of the hIAPP-ANFLVH complex. The per-residue binding free energy highlighted that ANFLVH strongly interacted with His18 of hIAPP, which has been reported as a key residue in mediating the hIAPP self-assembly process (**Figure 7.1**).

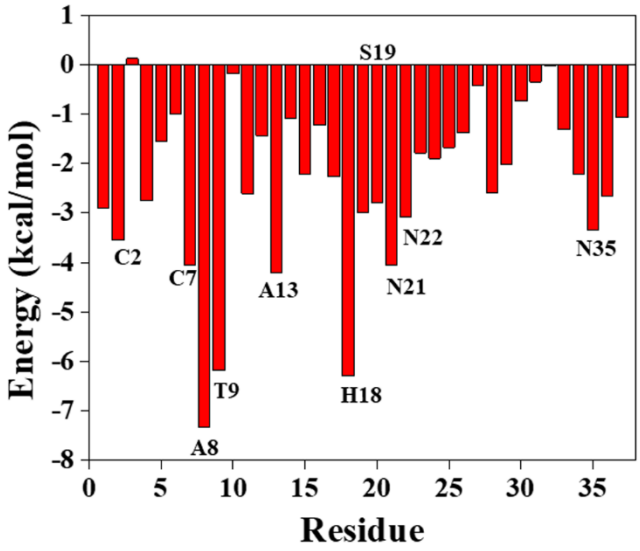

Figure 7.1: The binding free energy (kcal/mol) contribution of each residue of hIAPP in the hIAPP-ANFLVH complex is shown.

The percentage population of the three most-populated microstates for hIAPP was 65.4%, 13.6%, and 5.8% as compared to 76.8%, 9.4%, and 3.0%, respectively, in the hIAPP-ANFLVH complex. An increase in the percentage population of $\mathbf{m_1}$ of the hIAPP-ANFLVH complex was observed, which highlights higher conformational homogeneity of hIAPP in the presence of ANFLVH (**Figure 7.2**). The conformational clustering analysis of the conformational ensemble highlighted that ANFLVH significantly inhibited the formation of aggregation-prone β-sheet conformation by reducing β-sheet content and stabilizing the helical conformation in the hIAPP monomer. This work sheds light on the inhibitory mechanism of ANFLVH against hIAPP aggregation at the atomic level.

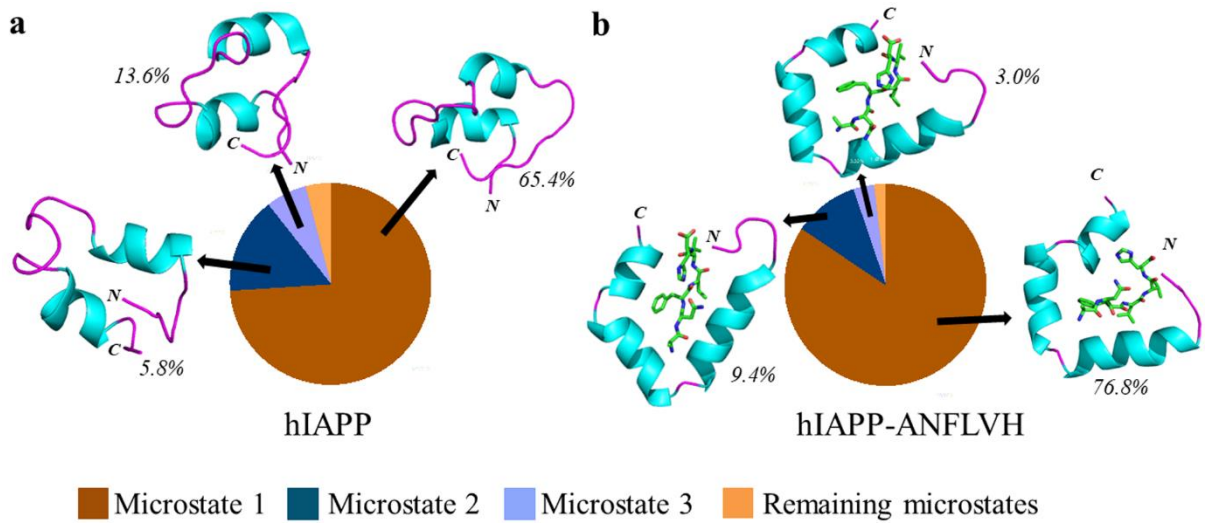

Figure 7.2: The representative conformations of the three most-populated microstates (**m_1**, **m_2**, and **m_3**) of hIAPP and hIAPP-ANFLVH complex are shown in the cartoon representation. The percentage population of corresponding microstates is shown underneath the structure.

Chapter 4 demonstrated a successful structure-based virtual screening approach to understand prospective interactions of peptide-based inhibitors with hIAPP protein throughout this chapter. The library of pentapeptides based on fragment $HSSNN_{18\text{-}22}$ was designed and assessed for their efficacy in blocking hIAPP aggregation using an integrated computational screening approach. The top hit pentapeptides against hIAPP aggregation were shortlisted from the designed library using molecular docking-based virtual screening and binding free energy calculations.

The binding free energy calculations identified HSSQN and HSSNQ as top hits that bind to hIAPP monomer with a binding affinity of –21.25 ± 4.90 and –19.73 ± 3.10 kcal/mol, respectively. The sampling of the non aggregation-prone helical conformation was notably increased from 23.5 ± 3.0 in hIAPP monomer to 38.1 ± 3.6, and 33.8 ± 3.0% on the incorporation of HSSQN, and HSSNQ, respectively, which indicate reduced aggregation propensity of hIAPP monomer.

A remarkable increase in the helical content in the residues N3−L12 and V17−F23 of hIAPP monomer was observed on the incorporation of HSSQN (**Figure 7.3**). Upon HSSNQ binding, the propensity of residues C2−A8 of hIAPP monomer to sample coil conformation was significantly decreased and the probability of helical content was increased in the F15−F23 region of hIAPP monomer (**Figure 7.3**). An overall increase in helical content in the amyloidogenic region A8−S20 was observed in the presence of HSSQN and HSSNQ.

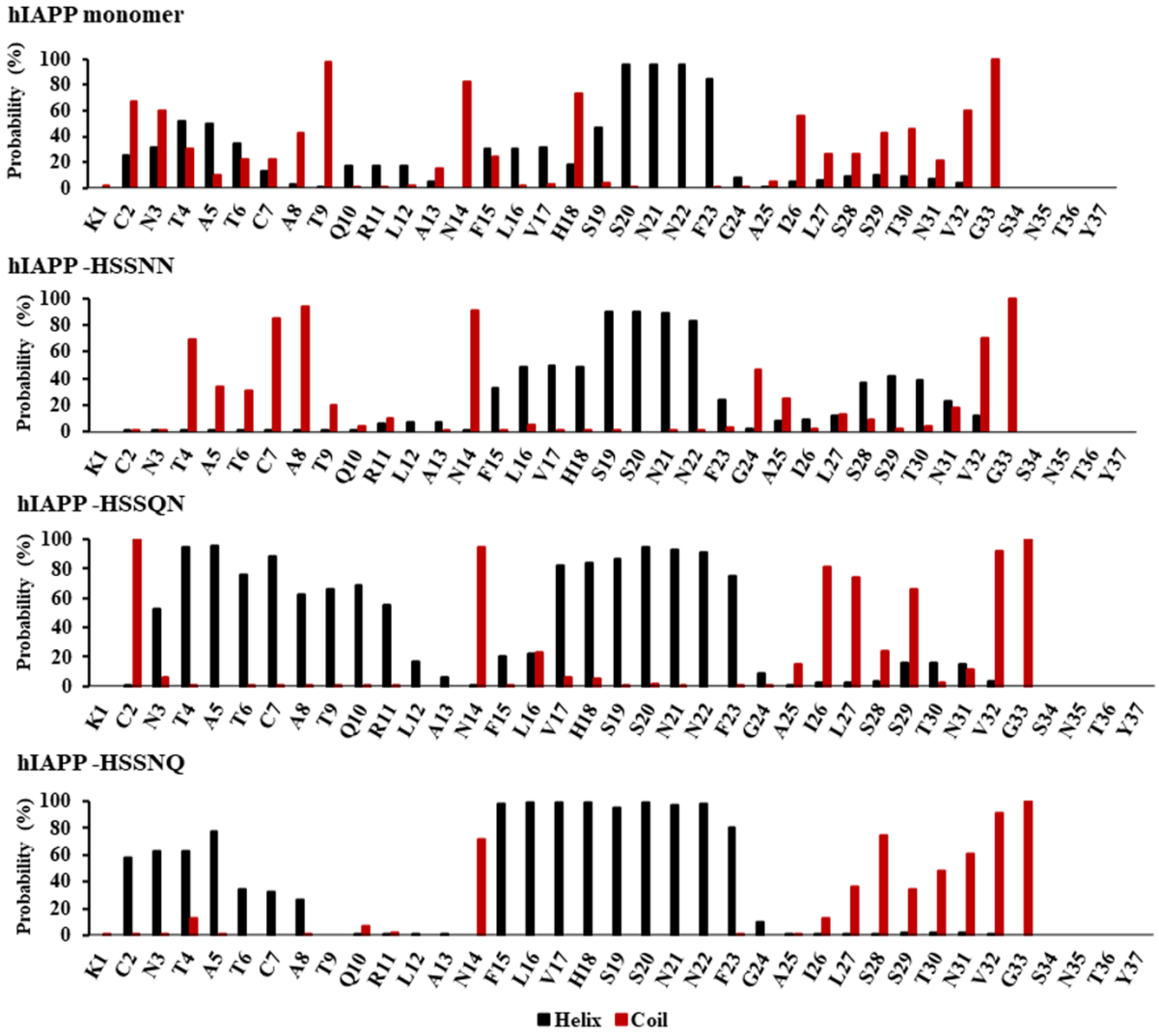

Figure 7.3: Residue-wise helix and coil content in hIAPP alone and hIAPP-pentapeptide complexes.

The most-populated cluster in hIAPP−HSSQN constituted 97.40% population and sampled helical conformations in the regions T6−L16, H18−S28, and N31−N35 of hIAPP monomer. The visual inspection depicts that hIAPP monomer sampled coiled conformation with short helix structures (**Figure 7.4**). Increased sampling of the helix conformation in the central member of the highest populated cluster of hIAPP-pentapeptide complexes was observed.

The MD simulations highlighted that glutamine in HSSNQ and HSSQN contributed to strong binding with hIAPP monomer as compared to HSSNN and enhanced the sampling of the helix in hIAPP monomer, which depicts their tendency to block hIAPP aggregation. The computationally designed peptides, HSSQN and HSSNQ, emerged as new, simple, and efficient inhibitors of hIAPP aggregation and encourage further experimental validation.

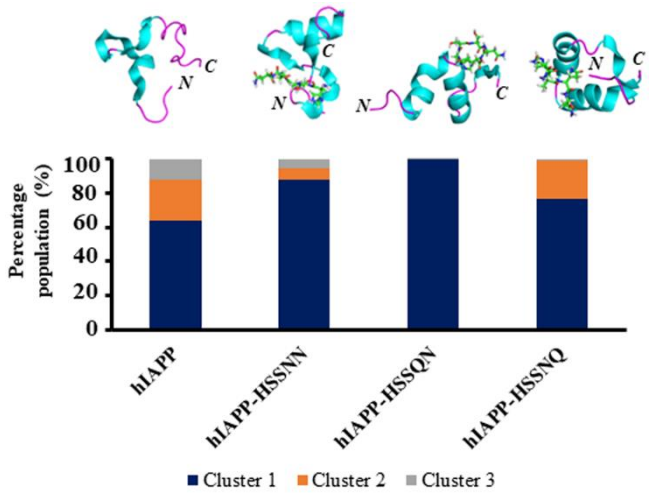

Figure 7.4: Percentage population and the central member of the highest populated cluster in hIAPP monomer, hIAPP-HSSNN, hIAPP-HSSQN, and hIAPP-HSSNQ complexes.

Chapter 5 highlights the potential to discover a new peptide-based drug that could perturb $A\beta_{42}$ aggregation. A library of 912 pentapeptides was designed based on the RIIGL sequence and these peptides were assessed for their efficacy in blocking $A\beta_{42}$ aggregation using an integrated computational protocol (**Figure 7.5**). The top hit pentapeptides against $A\beta_{42}$ aggregation were shortlisted from the designed library using molecular docking-based virtual screening and binding free energy calculations.

Table 7.1: Secondary structure compositions of the simulated systems.

Secondary structure component	$A\beta_{42}$ monomer	$A\beta_{42}$ monomer–RIIGL	$A\beta_{42}$ monomer–RLAPV	$A\beta_{42}$ monomer–RVVPI	$A\beta_{42}$ monomer–RIAPA
helix[a]	42.2 ± 3.9	52.3 ± 2.4	38.7 ± 4.2	57.6 ± 4.4	56.8 ± 3.9
β–sheet[b]	8.5 ± 2.8	4.6 ± 1.3	5.4 ± 1.8	0.0 ± 0.0	0.0 ± 0.0
Coil	26.1 ± 3.4	18.1 ± 2.6	27.6 ± 2.8	24.5 ± 3.6	28.4 ± 2.9
Bend	15.4 ± 4.1	16.3 ± 3.2	18.2 ± 4.3	9.8 ± 3.9	8.6 ± 3.3
Turn	8.2 ± 2.5	8.9 ± 1.8	10.8 ± 2.1	8.4 ± 2.4	6.9 ± 1.4

[a]helix is the sum of α–, π– and 3_{10} helix ; [b]β–sheet is the sum of β–strand and β–bridge

The binding free energy calculations by MM-PBSA predicted RLAPV, RVVPI, and RIAPA as strong binders to $A\beta_{42}$ monomer. The residue-wise binding free energy predicted hydrophobic contacts between $A\beta_{42}$ monomer and top-hit pentapeptides, which resulted in the formation of a U-shaped structure with more accessibility of the hydrophilic residues to the solvent. On the incorporation of RVVPI in $A\beta_{42}$ monomer, the side chain contacts between the mid-domain

(26-32) and C-terminal (34-42) regions were significantly reduced highlighting the lower aggregation propensity of $A\beta_{42}$ monomer in the presence of RVVPI.

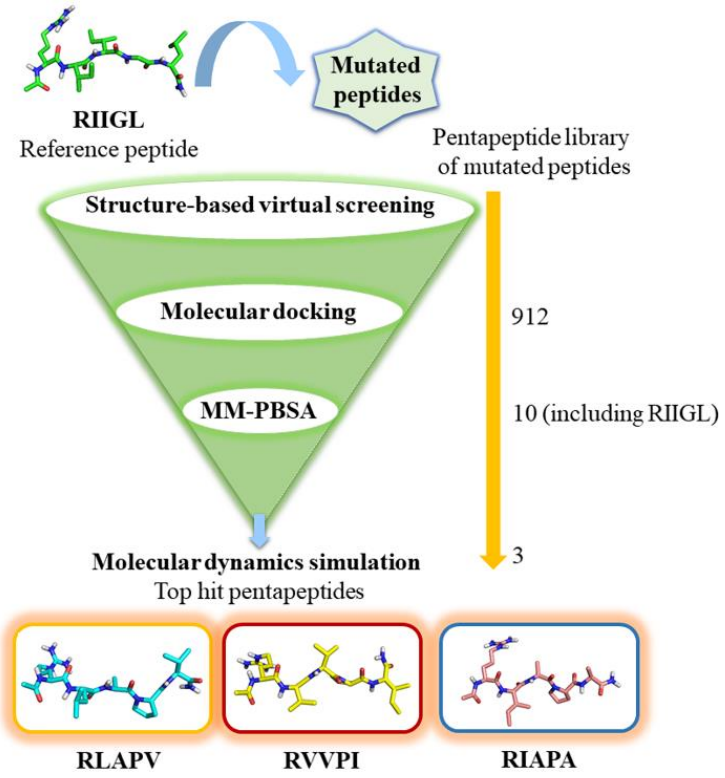

Figure 7.5: Integrated computational screening protocol used to identify potential inhibitors of $A\beta_{42}$ aggregation from the pentapeptide library based on reference peptide RIIGL.

The helical content was increased from 42.2 ± 3.9 in $A\beta_{42}$ monomer to 52.3 ± 2.4, 57.6 ± 4.4, and 56.8 ± 3.9% on the incorporation of RIIGL, RVVPI, and RIAPA, respectively, which indicate reduced aggregation propensity of $A\beta_{42}$ monomer on the incorporation of pentapeptides (**Table 7.1**). In comparison to 8.5 ± 2.8% β–sheet content sampled in the $A\beta_{42}$ monomer, the β–sheet content decreased to 4.6 ± 1.3% in $A\beta_{42}$ monomer–RIIGL and 5.4 ± 1.8% in $A\beta_{42}$ monomer–RLAPV, and interestingly, no β–sheet was sampled in $A\beta_{42}$ monomer–RVVPI and $A\beta_{42}$ monomer–RIAPA complexes.

In the $A\beta_{42}$ monomer–RVVPI system, the maximum number of hydrophobic residues displayed lower SASA as compared to $A\beta_{42}$ monomer, which indicates the significant inhibitory potential of RVVPI against $A\beta_{42}$ aggregation (**Figure 7.6a**). Also, only one distant peak centered at 2.1 nm was observed in $A\beta_{42}$ monomer–RVVPI complex which depicts the disruption of salt bridge interaction on the incorporation of RVVPI (**Figure 7.6b**).

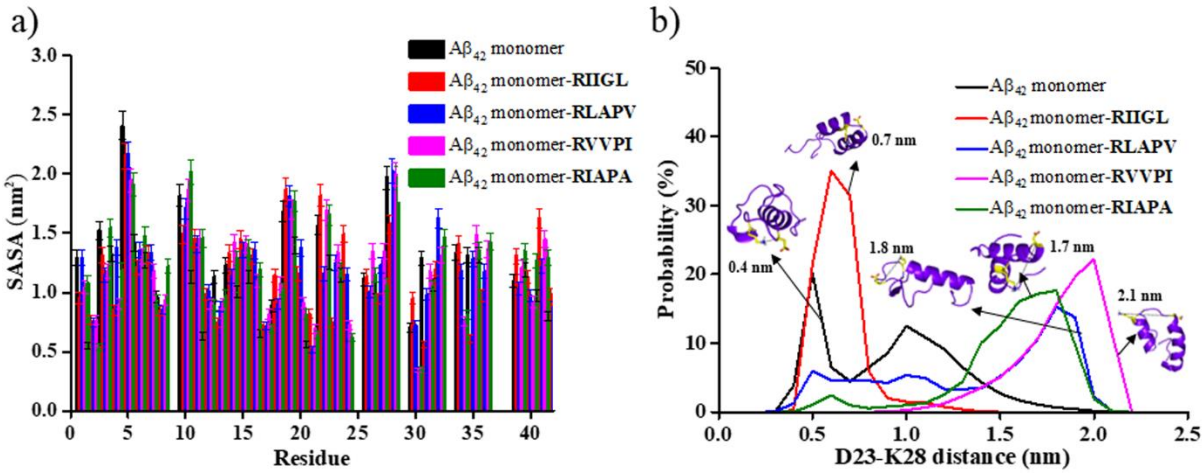

Figure 7.6: Residue-wise SASA (panel a) and the probability of D23-K28 salt bridge interaction (panel b) in the Aβ42 monomer with and without pentapeptides.

The integrated computational methodology predicted RVVPI and RIAPA as new peptides with notably enhanced ability to block Aβ42 aggregation as compared to RIIGL. The MD simulations highlighted that the incorporation of proline and arginine in pentapeptides contributed to their strong binding with Aβ42 monomer and inhibition of the conformational conversion of Aβ42 monomer to aggregation-prone structures.

In chapter 6, the disruptive ability of pentapeptides (RIIGL, RVVPI, and RIAPA) on Aβ42 protofibril was examined using MD simulations and *in vitro* studies. The residue-wise free binding energy analysis highlighted that charged residues influence Aβ42 protofibril-pentapeptide interactions. Notably, RVVPI displays a more pronounced destabilization effect than other peptides due to higher conformational fluctuations, and disruption of K28-A42 salt bridges in Aβ42 protofibril. To corroborate the computational findings, the pentapeptides were synthesized and their inhibitory activity against Aβ42 aggregation and disaggregation of pre-formed Aβ42 aggregates was evaluated using thioflavin T (ThT) and transmission electron microscopy (TEM) studies. Among the synthesized peptides, RVVPI exhibited the highest inhibitory activity (Inhibition= 66.2%, IC_{50}= 5.57 ± 0.83 μM) against Aβ42 aggregation consistent with the computational results (**Figure 7.7a**). Remarkably, RVVPI displayed ~4.5 fold lower IC_{50} value as compared to the Aβ42 C-terminal derived RIIGL. The results of ThT and TEM highlighted the enhanced efficiency of RVVPI (62.4%) in the disassembly of pre-formed Aβ_{42} fibrils than other peptides (**Figure 7.7b**). Moreover, synthesized peptides do not self-assemble under experimental conditions, which is much required for their success as amyloid aggregation inhibitors. The combined *in silico* and *in vitro* studies in this work

identified a new pentapeptide, RVVPI, as an efficient modulator of Aβ$_{42}$ aggregation and disassembly of pre-formed Aβ$_{42}$ aggregates.

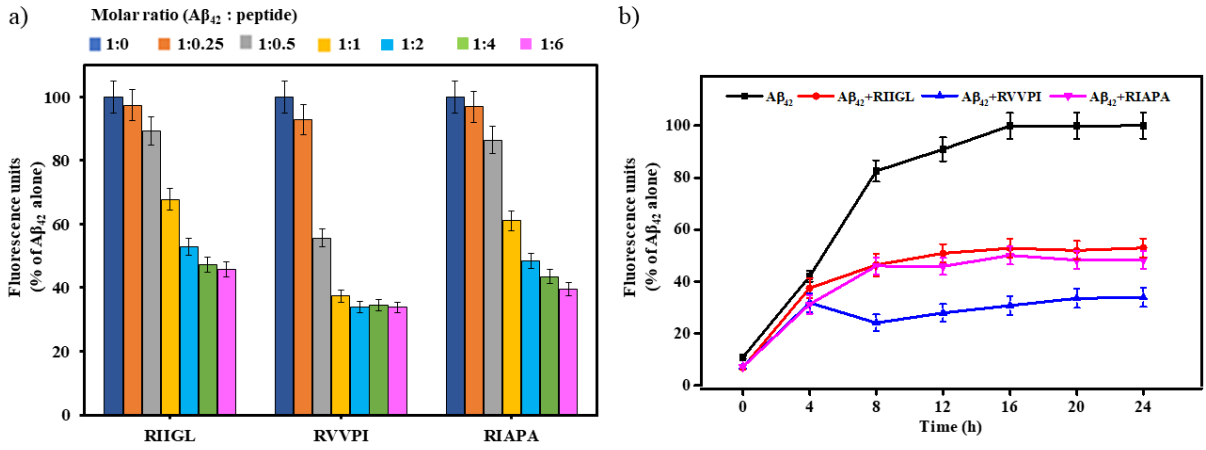

Figure 7.7: a) Assessment of Aβ$_{42}$ aggregation inhibition using ThT fluorescence assay at various stoichiometric ratios (1:0, 1:0.25, 1:0.5, 1:1, 1:2, 1:4, and 1:6) of Aβ$_{42}$:peptides after a 24-hour incubation at 37 °C with constant agitation, where [Aβ$_{42}$]= 10 μM. b) The graph of kinetic ThT fluorescence assay with [Aβ$_{42}$]= 10 μM and [peptides]= 20 μM. Each experiment was conducted in triplicate, and error bars indicate the standard deviation of the emission measurement.

The observed better efficiency of RVVPI to disaggregate the pre-formed Aβ$_{42}$ aggregates was due to the presence of proline and higher hydrophobic character. The study highlights a new peptide, RVVPI, as a potential inhibitor of Aβ$_{42}$ aggregation and disassembly of the pre-formed Aβ$_{42}$ fibrils. Furthermore, the study illuminates the molecular mechanism by which RIIGL, RVVPI, and RIAPA destabilize Aβ$_{42}$ protofibril.

Various neurodegenerative and non-neurodegenerative diseases have been linked to protein aggregation. Protein aggregation-derived diseases are still poorly understood and there are currently no effective therapies. Recent studies have shown that early-stage soluble oligomers are more toxic as compared to mature fibrils. Thus, strategies to halt or disrupt the generation of hIAPP and Aβ aggregates are effective therapeutic approaches against T2D and AD. Among various inhibitors, peptide-based inhibitors displayed good potential as anti-aggregation agents due to their low cytotoxicity, promising biocompatibility, high target affinity, and specificity.

The present thesis work explored the binding modes and inhibitory mechanism of peptide inhibitors against hIAPP and Aβ$_{42}$ aggregation. Additionally, the work reported in this thesis illuminates the molecular mechanism by which peptides (RIIGL, RVVPI, and RIAPA)

destabilize $A\beta_{42}$ protofibril, which will be beneficial for the design of therapeutic candidates against other disease-related protein assemblies. The insights from MD simulations will increase our understanding of the key interactions of potent inhibitors with hIAPP and $A\beta_{42}$ peptides, which, in turn, will contribute to the design and development of more potent inhibitors against multifactorial T2D and AD.

Furthermore, an integrated computational protocol was applied to identify top-hit peptides as potential inhibitors against hIAPP and $A\beta_{42}$ aggregation. Notably, a new peptide, RVVPI, derived from the C-terminal of $A\beta_{42}$ was identified as a promising inhibitor of $A\beta_{42}$ aggregation and disassembly of the pre-formed $A\beta_{42}$ fibrils using combined *in silico* and *in vitro* studies, which, in turn, raises the tempting possibility that this sequence could prove to be a lead motif for designing effective antagonists of Aβ aggregation.

List of Publications

1. Kaur, A.; Goyal, B. Deciphering the inhibitory mechanism of hIAPP-derived fragment peptide against hIAPP aggregation in type 2 diabetes. *ChemistrySelect* **2020**, *5*, 13341–13350. (Impact factor: 2.1)

2. Kaur, A.; Goyal, B. Identification of new pentapeptides as potential inhibitors of amyloid–β42 aggregation using virtual screening and molecular dynamics simulations. *J. Mol. Graph. Model.* **2023**, *124*, 108558. (Impact factor: 2.9)

3. Kaur, A.; Goyal, B. *In silico* design and identification of new peptides for mitigating hIAPP aggregation in type 2 diabetes. *J. Biomol. Struct. Dyn.* **2023**, DOI: 10.1080/07391102.2023.2254411. (Impact factor: 4.4)

4. Kaur, A.; Mankoo, O. K.; Diksha, D.; Priyadarshi, N.; Goyal, D.; Singhal, N. K.; Goyal, B. Exploring the impact of C-terminal based pentapeptides on the disassembly of $A\beta_{42}$ fibrils (Submitted for publication)

List of conferences and workshops

1. *Oral presentation* on the topic "Molecular insights into the inhibitory mechanism of a hexapeptide inhibitor against hIAPP aggregation in type 2 diabetes" at 2nd International Conference in collaboration with University of Florence, Italy on *Application of Biotechnology in Industry and Society* (ABIS-2019) held at NIT Jalandhar, Punjab, India (November 14-16, **2019**).

2. *Oral presentation* on the topic "Inhibition of hIAPP aggregation in type 2 diabetes by a peptide inhibitor derived from hIAPP sequence: A molecular dynamics simulation study" at *International Conference on Biosciences and Biotechnology* (ICBB-2019) held at LPU Jalandhar, Punjab, India (November 4-5, **2019**).

3. Participated in the workshop on *Mastering The Publishing Process* held virtually by Department of Science & Technology and American Chemical Society (July 28, **2020**).

4. Participated in webinar on *Altered Lifestyle: Neurological and Cardiovascular Complications* organized by NIPER Ahmedabad, Gujrat, India (September 11, **2020**).

5. Participated in *INDO-US seminar on Drivers of Future Pharmaceuticals* organized by Department of Pharmaceutics at NIPER Ahmedabad, Gujrat, India (June 09, **2023**).